Spontaneous Emission in Nanophotonics

Spontaneous Emission in Nanophotonics

a dissertation presented
by
Adi Pick
to
The Department of Physics

in partial fulfillment of the requirements
for the degree of
Doctor of Philosophy
in the subject of
Physics

Harvard University
Cambridge, Massachusetts
August 2017

Thesis advisor: Professor Steven Johnson Adi Pick

Spontaneous Emission in Nanophotonics

Abstract

In this thesis, we present semi-analytic theories of radiation noise in nanophotonic devices, which utilize new numerical software for solving light equations in nano-structures, combined with thermodynamic tools for including radiation noise. The first part of the thesis focuses on noise in lasers. Our formulation produces a formula for the width of the central spectral peaks ("the linewidth") in single- and multimode lasers, as well as formulas for the sidepeaks, which arise due to relaxation oscillations. Our formulas contain almost all previously known effects and find new nonlinear and multimode corrections in complicated nanophotonic structures. We verify our theory with brute-force simulations of the semiclassical Maxwell–Bloch equations, augmented with random sources representing radiation noise. Moreover, we extend our theory of laser noise and include amplified spontaneous emission (ASE) near the lasing threshold. In the second part of the thesis, we discuss spontaneous emission at exceptional points (EPs)—exotic degeneracies in non-Hermitian systems. Our theory extends beyond spontaneous emission to any light–matter interaction described by the local density of states (e.g., absorption, thermal emission, and nonlinear frequency conversion). Whereas traditional spontaneous-emission theories imply infinite enhancement factors at EPs, we derive finite bounds on the enhancement, proving maximum enhancement of 4 in passive systems with second-order EPs and significantly larger enhancements (exceeding 400×) in gain-aided and higher-order EP systems. Finally, we demonstrate an application of our theory to higher-harmonic generation in nonlinear media with EPs.

To Matilda, my one and only cat,

I am sorry I had to leave you. I hope you are still happy and alive...

"About your cat, Mr. Schrödinger—I have good news and bad news."

Contents

Acknowledgments

First and foremost, I would like to thank Steven Johnson, my advisor. I can safely say that every time I walked into his office during the five years that I spent in his group, I learned something new and neat about math, physics, numerical analysis, music, politics, or English. It was a privilege to be around someone who almost always knew what the right answer should be, even when it was not obvious how to get there. Quite exceptionally, Steven was involved in all the messy details that go into calculations, not just in the results, and was always willing to teach me how to solve, write, code, or present my work. The pleasant atmosphere during our meetings, seminars, and "Johnson jam sessions" made my MIT days something that I will always cherish.

On my first day in the group, Steven introduced me to Alejandro Rodriguez; then, a postdoc at Harvard and, today, a Princeton Professor. Alejandro helped me make my "baby steps" in the field of nanophotonics. He helped me set up my first MEEP code and introduced me to the topic of radiation noise. Throughout my PhD, he kept bringing up cool ideas for projects and, in general, always helped me get things done. Alejandro introduced me to Zin Lin from Harvard, a fruitful collaboration which lead to Ch. 8 of this thesis. He also introduced me to Chinmay Khandekar and Weiliang Lin, collaborations which produced three additional papers, which are not included in this thesis.

Soon after starting to work on noise in lasers, Steven introduced me to Prof. Doug Stone from Yale. Doug helped me "turn my math into physics" and put it in the context and terminology of the laser literature. I thank Doug for being fully involved in the writing process, for greatly improving the content and readability of our papers, and for advertising our work at conferences. Doug introduced me to Alex Cerjan, who was one of my closest colleagues during this PhD. I thank Alex for replying the dozens or hundreds of emails that I sent him, for endless discussions about what really goes on inside a laser, and for helping me dig through my lengthy derivations in search for missing factors of 2π's and $\hbar$'s.

I would also like to thank a few people at Harvard who helped me make this PhD

happen: prof. Amir Yacoby, for his valuable academic advice throughout my PhD, prof. Eric Heller, for agreeing to be on my PhD committee, prof. Mikhail Lukin and prof. Susanne Yelin for introducing me to the field of optics, prof. Melissa Franklin, for being much more than just a department head, caring for my well-being and helping me find my way in this department, and Lisa Cacciabaudo and Shirley Entzminger for their warm, dedicated, and professional help with various bureaucratic and financial issues that arose due to my special status as a hybrid Harvard-MIT student.

This work would not have been possible without the support of past and current members of the jdj group. In particular, I would likt to thank Bo Zhen, for thorough discussions on the physics of exceptional points and coupled-mode theory, for revisiting figures and manuscripts, and for (somewhat ironically) introducing me to some Israeli students and professors who work on similar topics at the Technion. Also to Owen Miller for helping me with every possible question, looking through derivations and brainstorming computational details, Chia (Wade) Hsu, for his valuable help on almost any research question I had, Aristeidies, for helping me deal with long and terrifying calculations and also with small and scary mice, and David Liu, for being a great fellow grad student and for guiding me through his SALT code, which is used in the first part of the thesis. I would also like to thank Prof. Marin Soljacic, for being involved in the work on exceptional points and to Ido Kaminer, Tena Dubcek, and Nick Rivera from Marin's group, for letting me join a cool project on two-photon lasers, which is not included in this thesis. I would also like to thank Felipe Hernandez for working with us on a mathematical question that came up during our work on exceptional points, and proposing a beautiful solution, which appears in the appendix of this thesis.

Last but not least, I would like to thank my husband, Tal, and baby Or for helping me keep the right balance between work and everything else, and thank the Pick family, Terry King, and Claire Shindler for their moral support, which I definitely needed during the many "ups and downs" that I encountered.

Chapter 1

Introduction

This thesis presents a theory of light in micro-structured lasers and resonators. Traditional optics started developing in the 17th century, attempting to explain everyday phenomena like dispersion, interference, reflection, and refraction [1]. Over the next two centuries, physicists and mathematicians established the relation between electromagnetic fields and the charges and currents which produce them and, in 1865, James Clerk Maxwell gathered these understandings and presented a unified electromagnetic theory [2, 3], which could explain all the *classical* optical phenomena known to date. But there remained questions that could not be answered classically, including the interaction of light with small objects like electrons. The answer came in 1917, in Einstein's paper on the *quantum theory* of radiation [4], where he predicted that an excited atom could return to a lower energy state via *spontaneous emission* of a photon. Moreover, Einstein showed that when light passed through an excited atom, it could *stimulate the emission* of more light. Three decades later, when Schawlow and Townes were trying to figure out ways to generate short-wavelength radiation, they recalled Einstein's idea. Based on the 1917 paper, they proposed a technique for light amplification by stimulated emission of radiation [5] or, as we call it today, *the laser*.

The first lasers where "large" (centimeter-scale) devices with relatively simple structures. Over the years, the advent of semiconductors and progress in fabrication tech-

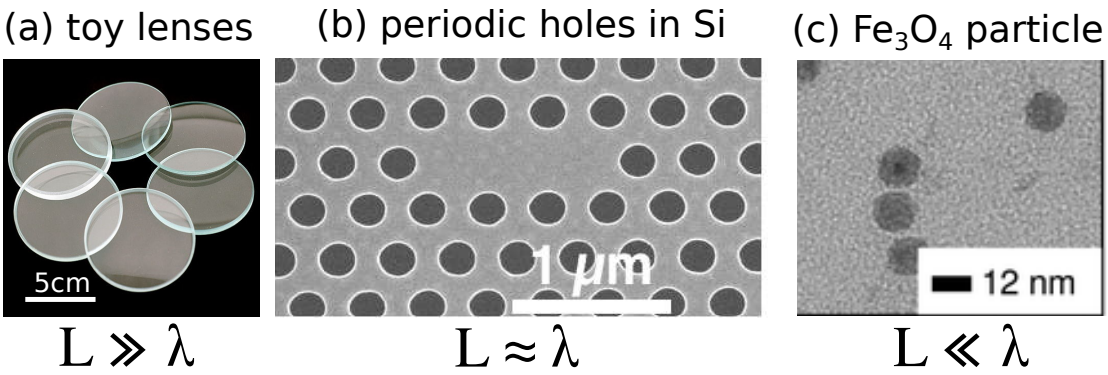

Figure 1.1: Optical length scales: (a) Toy lenses, where $L \gg \lambda$, are in the short-wavelength regime and can be modeled using ray optics. (b) Modern cavities, like periodically structured arrays of holes in silicon, have features of size comparable to the wavelength, $L \approx \lambda$, and hence the full wave nature comes into play. (c) Nano-scale particles, for which $L \ll \lambda$, can be treated using Rayleigh theory.

nology produced "small" (sub-micrometer scale) optical devices, sometimes with fine and complicated features. Theoretical approaches for modeling optical systems vary depending on the system's length scale, L, compared to the wavelength of radiation, λ. Three regimes (of large, intermediate, and small systems) are shown in Fig. 1.1. Systems which are much larger than the wavelength ($L \gg \lambda$) are accurately described in the framework of ray optics [6]. Some examples are lenses in sunglasses and toy magnifying glasses (Fig. 1.1a). In the opposite regime, systems which are much smaller than the wavelength ($L \ll \lambda$, Fig. 1.1c) are described by Rayleigh theory, which amounts to approximating the scatteres by point-like dipole sources [7]. For example, Rayleigh theory famously explains how white sunlight turns blue when scattering off of the molecules in the earth's atmosphere [8]. The intermediate regime—when the structure size is comparable to the wavelength—is the most involved from a theoretical viewpoint, and this is precisely the regime of *nanophotonics* [9] ($L \approx \lambda$, Fig. 1.1b). In this regime, simplistic approximations typically fail and wave phenomena, like interference and multiple

scattering, come into play.

When simplified analytic approaches fail, one usually resorts to numerical solutions. However, some problems, like analyzing the spectral properties of spontaneous emission in nanophotonic structures, are so complex that it quickly becomes intractable to solve them with brute-force methods. A modern approach to solve such problems is to develop semi-analytic theories, which can utilize existing numerical tools to analyze nanophotonic devices, and that is the subject of this thesis.

1.1 The laser noise spectrum

The first problem we address in this thesis is the noise spectrum of nanophotonic lasers. Lasers, in the most naive description, produce light of a single color. However, more realistically, when laser light passes through a spectrometer, the spectral peak is always smeared, and its width is called *the linewidth* (see Fig. 1.2a). The fundamental process responsible for this broadening is spontaneous emission.[§] [11] (Although the lasing process should amplify stimulated emission, excited atoms in the laser also produce spontaneous emission noise.) The fundamental laser linewidth was first computed by Schawlow and Townes, in the original laser proposal [5]. Over the years, a long list of corrections were found [12], such as the Petermann correction [13], associated with radiation leaking out of the cavity, the Henry α factor [14], which is an order-of-magnitude correction in semiconductor lasers, and the incomplete-inversion correction [15], due to partial excitation of the atoms in the laser (called the *gain medium*). Traditional laser theory has two main shortcomings: First, the correction factors are usually derived

[§]Semiclassically, one can think of spontaneous emission as a stochastic field produced by random currents. While the currents appear as sources in the *classical* Maxwell's equations, their correlations are determined *quantum mechanically* [10].

as separate effects, but this is not true in general (for example, the Henry α factor is modified in open cavities with a non-trivial Petermann factor). Secondly, most theories do not take into account the spatial variations in the laser field and, in that sense, are "zero-dimensional".

In Ch. 3, we remedy these problems.[†] Starting directly from the most general semi-classical Maxwell–Bloch equations [see Eqs. (2.20)–(2.22) below], we obtain a general linewidth formula [Eq. (3.3)], which contains all previously known corrections, while accurately treating the inhomogeniety in the field. Our formula reduces to the traditional formula in the appropriate limits, and predicts new order-of-magnitude corrections in complex microcavities. In Ch. 4, we validate this formula using brute-force simulations of the stochastic Maxwell–Bloch equations. In contrast to our analytic formula, brute-force simulations cannot handle arbitrary three-dimensional structures,[§] but they are still useful for verification.

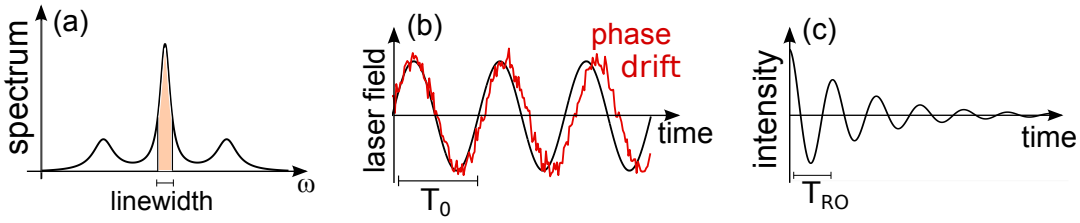

Figure 1.2: (a) The laser noise spectrum consists of a central peak at the laser frequency and possibly weak and broad sidebands. (b) The field of a single-color laser is sinusoidal (black curve). Consequently, its spectrum contains only the central peak at the oscillation frequency, $\omega_0 = 2\pi/T_0$. The peak is broadened by spontaneous emission, which produces phase drifts (red curve). (c) More generally, the atoms can respond non-instantaneously to deviations of the field from steady state. This causes relaxation oscillations at frequency $\omega_{\mathrm{RO}} = 2\pi/T_{\mathrm{RO}}$, which produce sidepeaks in the spectrum.

[†]The results of this work were published in [16] and [17], and are reviewed in [12].

[§]The laser equations [Eqs. (2.20)–(2.22)] are partial differential equations whose solution requires keeping track of multiple fields and involves multiple time scale, making them particularly computationally demanding [18].

In chapters 5 and 6 we discuss more features of the laser spectrum (Fig. 1.2a). In Ch. 5, we derive a formula for spectral sidepeaks [Eq. (5.3)]. In the most naive picture of a laser, the nonlinear interaction between the laser field and the atoms stabilizes the laser field at a steady state; That produces a single-color laser with sinusoidal field and a Lorentzian-shaped spectrum (Fig. 1.2b). More generally however, when the relaxation rates of the field and atoms are comparable, perturbations from the steady state relax via *relaxation oscillations* (Fig. 1.2c) and that produces spectral sidepeaks. The sidepeak spectrum was first studied by Vahala and Yariv in semiconductor lasers [19], and a formula for the sidepeaks was derived in [20] (using phenomenological rate equations). We generalize these results, starting from the more accurate Maxwell–Bloch equations, and find that the sidepeaks depend on three spatially averaged "α factors" (each with different weights). We demonstrate our new results with numerical examples. Finally, in Ch. 6, we address a peculiar feature, which appears in most standard linewidth formulas: The linewidth scales inversely with the laser intensity, and blows up when extrapolated to the point of operation where the laser is turned on (the *laser threshold*). We remedy this problem by incorporating into our theory spontaneous emission which has been amplified by the laser atoms [technically called *amplified spontaneous emission* (ASE)]. That produces a non-zero threshold intensity and a finite result for the threshold linewidth (Fig. 6.1). Similar to the linewidth problem, our approach generalizes earlier results [21] and makes new predictions for highly-inhomogeneous and multimode lasers, which were previously inaccessible.[†]

[†]In another project, lead by people from the Rodriguez group at Princeton, we exploited new powerful numerical tools to study ASE from arbitrary composite bodies. The results were published in [22].

1.2 Controlling light emission with exceptional points

The last two chapters of the thesis apply not only to lasers but, more generally, to *electromagnetic resonators*, which is just a fancy name for bodies that can trap light in a small region for a long time [23]. Resonances are ubiquitous in optics, with applications including light confinement [24], frequency selection [25], frequency conversion [26], and "stopping light" [27]. In particular, resonances can be used to control spontaneous (and stimulated) emission rates.[§] In optics, this idea is attributed to Edward Mills Purcell [29], for showing that when placing an emitter inside a resonator, its emission rate is enhanced by a factor, which scales inversely with the resonator volume while scaling linearly with the amount of time the light spends in the resonator before leaking out. This principle is illustrated schematically in Fig. 1.3a-b. Purcell's work initiated an entire industry aimed at developing *small* and *low-loss* resonators, which are nowadays widely used in medical [30] and military [31] applications. State-of-the-art cavities can enhance spontaneous emission rates by six orders of magnitude [32].

These impressive achievements motivated the search for new resonant structures with special optical properties. Particularly interesting are systems with "exceptional points" (EPs), which occur in open systems (Fig. 1.3c) when two or more resonances merge and have precisely the same frequency and field distribution [33, 34]. (Formally speaking, such systems are described by non-Hermitian *defective matrices*—$N \times N$ matrices with less than N eigenvectors which, therefore, do not have a complete basis of eigenvectors.)

[§]More generally, resonant interaction of emitters with their environment appear in many fields of physics. An intuitive example can be found at concert halls: the opera singer (the emitter) sings and the glass (the resonator) breaks. Specifically, the idea of tailoring the environment in order to control emission is most easily explained in the context of antenna theory: *the same current radiates a different amount of power depending on the surrounding geometry* [28].

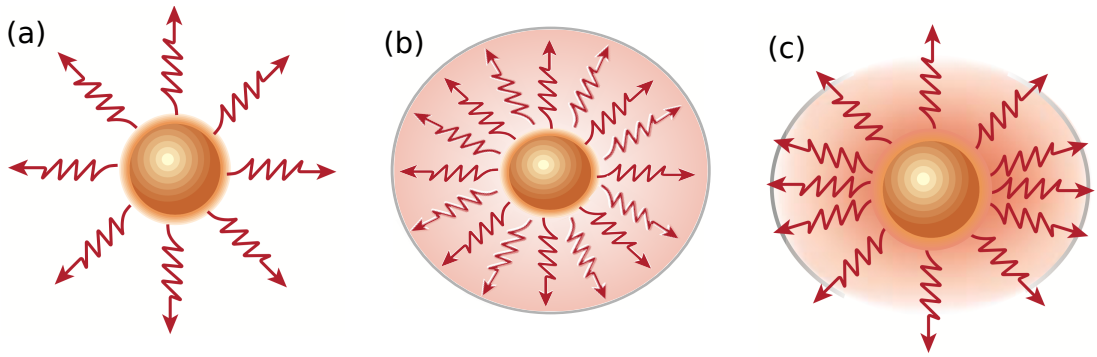

Figure 1.3: Purcell enhancement of spontaneous emission. By placing an emitter inside a resonator (b,c), its spontaneous emission rate is enhanced compared to the rate of emission in free space (a). The enhancement factor depends on whether the cavity is closed (b) or open (c). [(a) and (c) borrowed from [43]].

Recently, EPs have been found experimentally in a variety of systems [35, 36, 37],[†] enabling to explore their intriguing properties, such as unconventional lasing behavior [39], non-trivial topological properties [40], and loss-induced transparency [41]. In regard to spontaneous emission, EPs are seemingly peculiar: while standard formulas for spontaneous emission appear to diverge at EPs [42], experimental measurements find finite rates.

This apparent contradiction is remedied in the second part of the thesis. In Ch. 7, we present a theory of spontaneous emission near EPs.[§] By carefully adding the emission rates of the two merging resonances, we show that the divergent components cancel, and we provide simple formulas for the "corrected Purcell enhancement" at EPs [Eqs. (7.9) and (7.10)]. Although it was previously known how to regularize similar divergences at EPs in a general linear-algebra context [46], it was not well understood in the optics

[†]During my PhD, I was involved in a project lead by people from the Soljacic group at MIT, where we experimentally observed a new type of EPs: rings of EPs in periodically patterned Si_3N_4 slabs. The results were published in [38].

[§]The results of this work were published in [44]. The algorithm we use to compute the limiting expressions at the EP is explained in our online manuscript [45].

community, leading authors to attribute false significance to the diverging "Petermann" factor at EPs [47, 48, 49]. Even theoretical descriptions that correctly captured the finite behavior [50] were not general (limited to one-dimensional systems and other simplifications). Most importantly, our work quantifies the amount of enhancement that one could potentially achieve with EPs, and shows that by adding gain (e.g., from excited atoms), systems with EPs may exceed the traditional Purcell enhancement. In Ch. 8, we extend our theory to higher-order EPs, which from by merging more than two resonances.[†] In addition, we apply our theory to the problem of frequency conversion in nonlinear media with EPs.[§]

[†]The results were published in [51].
[§]Our manuscript can be found online at [52].

Chapter 2

Mathematical preliminaries

In the previous chapter, we introduced the topic of light emission in nanophpotonics from a layman's perspective. In this chapter, we complete all the technical details. A key point in our discussion is that lasers and resonators can exchange energy with their surrounding and are, therefore, open systems [53, 54]: light is lost, either radiatively (leaking through the resonator walls) or non-radiatively (getting absorbed by the medium), while it is also produced (via spontaneous or stimulated emission). Open systems are formally described by *non-Hermitian* operators [33] (Fig. 2.1). In Sec. 2.1, we present a non-Hermitian operator whose eigenmodes are the electromagnetic resonances: the operator-form of Maxwell's equations [23] [Eq. (2.4)]. Then, in Sec. 2.2, we move on to discuss lasers. We review the Maxwell–Bloch laser equations [55] [Eqs. (2.20)–(2.22)] and recast them in the form of a non-Hermitian eigenvalue problem [56, 57] [Eq. (3.50)]. In Sec. 2.3, we survey key results from thermodynamics (in particular, the fluctuation–dissipation theorem [58, 59]), which are used for computing the laser noise spectrum in the first part of the thesis. Finally, in Sec. 2.4, we define exceptional points [34]—a special kind of degenerate resonances that can exist in non-Hermitian systems, which are discussed in the second part of the thesis.

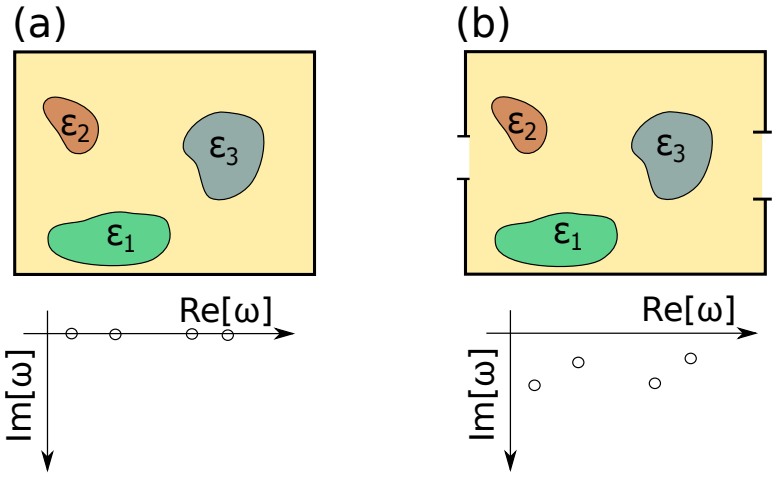

Figure 2.1: (a) Closed systems (top) are represented by Hermitian operators whose eigenfrequencies (ω_n) are real (bottom), while (b) open systems (top) are represented by non-Hermitian operators, whose eigenfrequencies are complex (bottom) and lie in the lower half of the complex-frequency plane. The imaginary part of the eigenfrequency determines the rate of decay of the resonance.

2.1 Electromagnetic resonances

Classical electromagnetism is governed by the four macroscopic Maxwell's equations: two divergence equations and two curl equations [3]. Our starting point in the formulation of electromagnetic resonances is the source-free frequency-domain curl equations,[§] which in SI units are [23]:

$$\begin{aligned} \nabla \times \mathbf{H} &= -i\omega\varepsilon_0\varepsilon(\mathbf{x})\mathbf{E} \\ \nabla \times \mathbf{E} &= i\omega\mu_0\mu(\mathbf{x})\mathbf{H}. \end{aligned} \tag{2.1}$$

[§]Note that at nonzero frequencies, the divergence equations, $\nabla \cdot (\varepsilon\mathbf{E}) = 0$ and $\nabla \cdot (\mu\mathbf{H}) = 0$, are automatically satisfied since the divergence of a curl vanishes, and we are never interested in electrostatics ($\omega = 0$) in this work.

These equations relate electric and magnetic vector fields ($\mathbf{E}$ and $\mathbf{H}$ respectively) in a non-dispersive medium with dielectric permittivity $\varepsilon(\mathbf{x})$ and magnetic permeability $\mu(\mathbf{x})$.[†] ε_0 and μ_0 are the vacuum permittivity and permeability. Since most materials do not have magnetic response at optical frequencies, we restrict the analysis to nonmagnetic media [with $\mu(\mathbf{x}) = 1$] [60].

By recasting Maxwell's equations [Eq. (2.1)] in the form of an eigenvalue problem, we can use many tools from quantum mechanics and linear algebra. To this end, we use the first equation in Eq. (2.1) to eliminate the magnetic field and substitute the result into the second equation. Introducing the vacuum speed of light, $c = 1/\sqrt{\varepsilon_0\mu_0}$, one obtains:

$$\tfrac{1}{\varepsilon(\mathbf{x})}\nabla \times \nabla \times \mathbf{E}(\mathbf{x}) = \left(\tfrac{\omega}{c}\right)^2 \mathbf{E}(\mathbf{x}). \tag{2.2}$$

Equation (2.2) determines the electric field $\mathbf{E}$, while the magnetic field $\mathbf{H}$ is related to $\mathbf{E}$ via Eq. (2.1). Electomagnetic resonances are formally defined as outgoing wave solutions of the eigenvalue problem [33]

$$\hat{\Theta}\mathbf{E}_n(\mathbf{x}) = \left(\tfrac{\omega_n}{c}\right)^2 \mathbf{E}_n(\mathbf{x}) \tag{2.3}$$

$$\hat{\Theta} \equiv \tfrac{1}{\varepsilon(\mathbf{x})}\nabla \times \nabla \times, \tag{2.4}$$

where the subscript n denotes the nth mode. Each resonance is associated with a (possibly) complex "eigenfrequency," ω_n, and "mode profile," $\mathbf{E}_n$. As mentioned above, we are interested in open systems, but we begin by reviewing the more familiar case of

[†]More generally, the permittivity and permeability may be frequency dependent [i.e., $\varepsilon(\mathbf{x}, \omega)$ and $\mu(\mathbf{x}, \omega)$] and that accounts for material dispersion, meaning that different wavelengths are associated with different phase velocities. For simplicity, we focus here on non-dispersive media and treat the more general case in Sec. 7.7.

closed systems.

2.1.1 Closed systems and Hermitian operators

In this section, we derive orthogonality relations in closed systems. Such relations are a key element in perturbation theory and coupled-mode theory, which we use in this thesis to obtain approximate solutions to problems that cannot be solved exactly. We begin by introducing the "conjugated inner product:" [61]

$$\langle \mathbf{F}, \mathbf{G} \rangle_\varepsilon \equiv \langle \mathbf{F}, \varepsilon \mathbf{G} \rangle \equiv \int \varepsilon(\mathbf{x}) \mathbf{F}^*(\mathbf{x}) \mathbf{G}(\mathbf{x}) dx \tag{2.5}$$

where "$*$" denotes complex conjugation. Since the inner product [Eq. (2.5)] is positive-definite when ε is real and positive [23],[§] we can use it and normalize the resonances:

$$\langle \mathbf{E}_n, \mathbf{E}_n \rangle_\varepsilon = 1 \tag{2.6}$$

Armed with the definition of the inner product [Eq. (2.5)] and the Maxwell operator ($\hat{\Theta}$), one defines the adjoint operator as: [62]

$$\langle \mathbf{F}, \hat{\Theta}^\dagger \mathbf{G} \rangle_\varepsilon \equiv \langle \hat{\Theta} \mathbf{F}, \mathbf{G} \rangle_\varepsilon \tag{2.7}$$

An operator, $\hat{\Theta}$, is *Hermitian* if it satisfies:

$$\hat{\Theta}^\dagger = \hat{\Theta}. \tag{2.8}$$

[§]A bilinear form is positive-definite if it satisfies the conditions: $\langle \mathbf{F}, \mathbf{F} \rangle \geq 0$ and $\langle \mathbf{F}, \mathbf{F} \rangle = 0$ if and only if $\mathbf{F} = 0$.

For example, in electromagnetism, Maxwell's operator, $\hat{\Theta}$, is Hermitian when ε is real (which is true in the absence of gain or material loss) and when there is no net flux through the boundaries (e.g., when the fields, $\mathbf{E}$ and $\mathbf{H}$, vanish at the boundaries of integration). We prove this property in the footnote.[†] Hermitian operators have the well-known properties: [23]

$$\text{Real eigenvalues} \qquad \omega_n^2 = (\omega_n^2)^* \tag{2.9}$$

$$\text{Orthogonal modes} \qquad \langle \mathbf{E}_m, \mathbf{E}_n \rangle_\varepsilon = \delta_{mn} \tag{2.10}$$

The first property implies that the eigenmodes oscillate sinusoidally (at frequency ω_n) without decay, as one would expect from energy conservation in closed systems. In the next section, we derive equivalent results for non-Hermitian systems. We prove Eqs. (2.9) and (2.10) in the footnote.[§]

[†]This can be seen by calculating: $\langle \mathbf{F}, \hat{\Theta}^\dagger \mathbf{G} \rangle_\varepsilon = \int \varepsilon(\mathbf{x}) \left[\varepsilon(\mathbf{x})^{-1} \nabla \times \nabla \times \mathbf{F}(\mathbf{x})\right]^* \mathbf{G}(\mathbf{x}) dx = \int \mathbf{F}^*(\mathbf{x}) \left[\nabla \times \nabla \times \mathbf{G}(\mathbf{x})\right] dx = \int \varepsilon(\mathbf{x}) \mathbf{F}^*(\mathbf{x}) \left[\varepsilon(\mathbf{x})^{-1} \nabla \times \nabla \times \mathbf{G}(\mathbf{x})\right] dx = \langle \mathbf{F}, \hat{\Theta} \mathbf{G} \rangle_\varepsilon$ The first equality follows from definition of the adjoint [Eq. (2.7)]. The second equality follows from integrating twice by parts, assuming that fields vanish at the boundaries of integration and that $\varepsilon^* = \varepsilon$. The third equality follows simply from rearranging the integrand, and the last equality follows from the definition of the inner product.

[§]**Proof of Eq. (2.9):** Using the eigenvalue equation [Eq. (2.4)] together with the normalization condition [Eq. (2.6)], the eigenvalues can be written as $\langle \mathbf{E}_n, \hat{\Theta} \mathbf{E}_n \rangle_\varepsilon = \left(\frac{\omega_n}{c}\right)^2 \langle \mathbf{E}_n, \mathbf{E}_n \rangle_\varepsilon = \left(\frac{\omega_n}{c}\right)^2$. So the first property follows from $\langle \mathbf{E}_n, \hat{\Theta} \mathbf{E}_n \rangle_\varepsilon = \langle \mathbf{E}_n, \hat{\Theta}^\dagger \mathbf{E}_n \rangle_\varepsilon = \langle \hat{\Theta} \mathbf{E}_n, \mathbf{E}_n \rangle_\varepsilon = \int \varepsilon (\hat{\Theta} \mathbf{E}_n)^* \mathbf{E}_n dx = \int \left(\varepsilon \mathbf{E}_n^* \hat{\Theta} \mathbf{E}_n\right)^* dx = \langle \mathbf{E}_n, \hat{\Theta} \mathbf{E}_n \rangle_\varepsilon^*$. The first equality uses the Hermiticity of $\hat{\Theta}$. The second equality uses the definition of the adjoint. The third uses the definition of the inner product, and the two last steps follow from rearranging the terms.

Proof of Eq. (2.10): The orthogonality relation is obtained by subtracting two equal quantities: $0 = \langle \mathbf{E}_m, \hat{\Theta} \mathbf{E}_n \rangle_\varepsilon - \langle \mathbf{E}_m, \hat{\Theta}^\dagger \mathbf{E}_n \rangle_\varepsilon = \langle \mathbf{E}_m, \hat{\Theta} \mathbf{E}_n \rangle_\varepsilon - \langle \hat{\Theta} \mathbf{E}_m, \mathbf{E}_n \rangle_\varepsilon = \langle \mathbf{E}_m, \left(\frac{\omega_n}{c}\right)^2 \mathbf{E}_n \rangle_\varepsilon - \langle \left(\frac{\omega_m^*}{c}\right)^2 \mathbf{E}_m, \mathbf{E}_n \rangle_\varepsilon = \left[\left(\frac{\omega_n}{c}\right)^2 - \left(\frac{\omega_m}{c}\right)^2\right] \langle \mathbf{E}_m, \mathbf{E}_n \rangle_\varepsilon$, The first equality follows from Hermiticity of $\hat{\Theta}$. The second follows from definition of the adjoint. The third, from the definition of the eigenvectors, and the last from realness of the eigenvalues. The result implies that either $\omega_n^2 = \omega_m^2$ or $\langle \mathbf{E}_m, \mathbf{E}_n \rangle_\varepsilon = 0$ which ,together with the normalization condition Eq. (2.6), proves Eq. (2.10).

2.1.2 Open systems and Non-Hermitian operators

Open systems are represented by non-Hermitian operators. [33] (For example, gain and absorption are described macroscopically by an imaginary dielectric permittivity, making $\hat{\Theta}$ non-Hermitian.[†]) In that case, the properties in Eqs. (2.9) and (2.10) are no longer true. The eigenfrequencies ω_n are generally complex and lie the lower part of the complex-frequency plane [63] (Fig. 2.1b, bottom). The imaginary part of ω_n determines the rate at which energy leaks out of the system.

In order to derive perturbation theory and coupled-mode theory for open systems, we need orthogonality relations that hold regardless of Hermiticity of the operators. We show in this section that such relations can be obtained by using the "unconjugated inner product:" [33]

$$(\mathbf{F}, \mathbf{G})_\varepsilon \equiv (\mathbf{F}, \varepsilon\mathbf{G}) \equiv \int \varepsilon(\mathbf{x})\mathbf{F}(\mathbf{x})\mathbf{G}(\mathbf{x})dx. \tag{2.11}$$

Note that this definition does not satisfy all the properties of the inner product and, in particular, it is not necessarily real. Using this definition, we introduce also the transposed operator $\hat{\Theta}^T$, defined as [62]

$$(\mathbf{F}, \hat{\Theta}^T\mathbf{G})_\varepsilon \equiv (\hat{\Theta}\mathbf{F}, \mathbf{G})_\varepsilon \tag{2.12}$$

In addition to the eigenvectors of $\hat{\Theta}$ (from here on called *right eigenevectors*), there is a set of eigenvectors of $\hat{\Theta}^T$ with the same eigenvalues (from here on called *left eigenev-*

[†]When revisiting the Hermiticity proof for closed system [see footnote after Eq. (2.8)], one finds that if $\varepsilon \neq \varepsilon^*$, then $\hat{\Theta} \neq \hat{\Theta}^\dagger$.

tors) [62]:

$$\hat{\Theta}\mathbf{E}_n^R(\mathbf{x}) = \left(\tfrac{\omega_n}{c}\right)^2 \mathbf{E}_n^R(\mathbf{x}) \tag{2.13}$$

$$\hat{\Theta}^T\mathbf{E}_n^L(\mathbf{x}) = \left(\tfrac{\omega_n}{c}\right)^2 \mathbf{E}_n^L(\mathbf{x}) \tag{2.14}$$

Similar to the Hermitian orthogonality relation [Eq. (2.9)], we obtain *biorthogonality relations* for non-Hermitian eigenmodes by subtracting two equal quantities:

$$\begin{aligned} 0 = (\mathbf{E}_m^L, \hat{\Theta}\mathbf{E}_n^R)_\varepsilon - (\hat{\Theta}\mathbf{E}_n^R, \mathbf{E}_m^L)_\varepsilon = (\mathbf{E}_m^L, \hat{\Theta}\mathbf{E}_n^R)_\varepsilon - (\mathbf{E}_n^R, \hat{\Theta}^T\mathbf{E}_m^L)_\varepsilon = \\ (\mathbf{E}_m^L, \left(\tfrac{\omega_n}{c}\right)^2 \mathbf{E}_n^R)_\varepsilon - (\mathbf{E}_n^R, \left(\tfrac{\omega_m}{c}\right)^2 \mathbf{E}_m^L)_\varepsilon = \left[\left(\tfrac{\omega_n}{c}\right)^2 - \left(\tfrac{\omega_m}{c}\right)^2\right](\mathbf{E}_m^L, \mathbf{E}_n^R)_\varepsilon, \end{aligned} \tag{2.15}$$

The first equality follows from the definition of the unconjugated inner product [Eq. (2.11)]. The second from the definition of the transpose. The third from the definition of left and right eigenvectors, and the last follows from rearranging the terms. The result implies that either $\omega_n^2 = \omega_m^2$ or $(\mathbf{E}_m^L, \mathbf{E}_n^R)_\varepsilon = 0$, which can be written alternatively as the

$$\text{Biorthogonality relation} \qquad (\mathbf{E}_m^L, \mathbf{E}_n^R)_\varepsilon = 0 \qquad \text{for n} \neq \text{m}. \tag{2.16}$$

Note that in contrast to the conjugated norm [Eq. (2.5)], we cannot normalize the unconjugated norm of a mode, $(\mathbf{E}_n^L, \mathbf{E}_n^R)_\varepsilon$, to 1, because it can vanish. In fact, it is not even obvious that the unconjugated norm is bounded. The eigenvectors, which correspond to complex "leaky" eigenfrequencies, diverge at infinite distance from the structure [in the sense that $\|\mathbf{E}_n^L(\mathbf{x})\|, \|\mathbf{E}_n^R(\mathbf{x})\| \to \infty$ when $\|\mathbf{x}\| \to \infty$] [64]. There are many approaches to overcome this issue. One possibility (borrowed from quantum field theory) is to use a "regulator," which amounts to introducing a decay factor inside the

integrand in Eq. (2.11), making the integrand finite while leaving the integral unaltered [65]. Another option, which is popular among computational theorists and is the method of our choice, is to place the so called "perfectly matched" layers (PML) [28] at a finite distance from the structure. The layers are designed to guarantee that the field decays to zero at large distances from the structure, while remains unchanged outside of the layers. In Sec. 7.8, we prove that with PML, the unconjugated norm is bounded.

Last, we mention that although we deal with problems that are not Hermitian, Maxwell's operator is complex-symmetric in most cases, which means that it is equal to its transpose: $\hat{\Theta} = \hat{\Theta}^T$.[§] It is a simple exercise to show that the following relations between left and right eigenvectors hold [44]:

$$\text{If } \hat{\Theta} = \hat{\Theta}^T \qquad \mathbf{E}_n^L = \varepsilon^{-1}\mathbf{E}_n^R \tag{2.17}$$

$$\text{If } \hat{\Theta} = \hat{\Theta}^\dagger \qquad \mathbf{E}_n^L = \varepsilon^{-1}(\mathbf{E}_n^R)^* \tag{2.18}$$

Note that the biorthogonality relation generalizes the notion of orthogonality of Hermitian eigenvectors, in the sense that when applying Eq. (2.16) to the eigenvectors of complex-symmetric Hermitian operators, one recovers the standard conjugated norm:

$$(\mathbf{E}_n^L, \mathbf{E}_m^R)_\varepsilon = \int \varepsilon \mathbf{E}_n^L \mathbf{E}_m^R = \int \varepsilon\varepsilon^{-1}(\mathbf{E}_m^R)^* \mathbf{E}_n^R = \langle \mathbf{E}_n^L, \mathbf{E}_m^R \rangle \tag{2.19}$$

[§]This can be seen by calculating: $(\mathbf{F}, \hat{\Theta}^T\mathbf{G})_\varepsilon = \int \varepsilon(\mathbf{x}) \left[\frac{1}{\varepsilon(\mathbf{x})}\nabla\times\nabla\times\mathbf{F}(\mathbf{x})\right]\mathbf{G}(\mathbf{x})dx = \int \mathbf{F}(\mathbf{x})\left[\nabla\times\nabla\times\mathbf{G}(\mathbf{x})\right]dx = \int \varepsilon(\mathbf{x})\mathbf{F}(\mathbf{x})\left[\frac{1}{\varepsilon(\mathbf{x})}\nabla\times\nabla\times\mathbf{G}(\mathbf{x})\right]dx = (\mathbf{F}, \hat{\Theta}\mathbf{G})_\varepsilon$. The justification is very similar to the proof that Maxwell's operator is Hermitian in closed systems.

2.2 The laser equations

Next, let us introduce the semi-classical laser equations. Most generally, a laser consists of light which interacts with a gain medium (e.g. excited atoms) inside a resonator. The light is described by the *classical* Maxwell's equations from the previous section. The gain medium, in the simplest description of a "two-level" medium,[†] is described by the *quantum* Bloch equations. Together, these form the Maxwell–Bloch equations [55]:

$$\nabla \times \nabla \times \mathbf{E} + \varepsilon_{\mathrm{c}} \ddot{\mathbf{E}} = -4\pi \ddot{\mathbf{P}}, \tag{2.20}$$

$$\dot{\mathbf{P}} = -i(\omega_{\mathrm{a}} - i\gamma_{\perp})\mathbf{P} - \frac{i\gamma_{\perp}}{4\pi}\mathbf{E}D, \tag{2.21}$$

$$\dot{D} = -\gamma_{\parallel}\left[D_{\mathrm{p}} - D + 2\pi i(\mathbf{E}\cdot\mathbf{P}^{*} - \mathbf{E}^{*}\cdot\mathbf{P})\right]. \tag{2.22}$$

Here, $\mathbf{P}$ is the atomic polarization field, related to the atomic two-level density matrix, ρ, via $\mathbf{P} = Ng\rho_{12}$ [53], where N is the total number of atoms and g is the atomic dipole moment. D is the population inversion (i.e., the difference between number of atoms in the excited and ground states), defined as $D = N(\rho_{22} - \rho_{11})$. The atomic resonance frequency ω_a is the difference between the two energy levels ($\hbar\omega_a = E_2 - E_1$). $\gamma_{\perp}$ and $\gamma_{\parallel}$ are the atomic and inversion relaxation rates respectively. The term D_p represents an external energy source that inverts the population of the atoms, henceforth called "the pump." The last terms in the atomic equations [Eqs. (2.21) and (2.22)] couple the atoms nonlinearly to the electromagnetic field $\mathbf{E}$. In Eq. (2.20), ε_{c} is the (linear) "passive permittivity," which represents the permittivity of the unpumped medium [in contrast to the effective (nonlinear) permittivity, which includes the gain]. The field,

[†]The atoms or molecules in the gain medium have multiple levels, but stimulated emission into the laser field is produced only by relaxation between two specific levels.

polarization and inversion are measured in their natural units: $e_c = p_c = \hbar\sqrt{\gamma_\parallel\gamma_\perp}/(2g)$ and $d_c = \hbar\gamma_\perp/(4\pi g^2)$ respectively [56].

2.2.1 Multimode steady-state lasers

The Maxwell–Bloch equations are difficult to solve in general: They involve three time- and spatially dependent fields and include multiple timescales [18] (ω_a, $\gamma_\parallel$, and $\gamma_\perp$). Traditional laser theories proceed by making a series of simplifying assumptions about the field distribution and cavity geometry, which they use in order to reduce Eqs. (2.20)–(2.22) to a set of ordinary differential equations, commonly called *rate equations* [53]. As discussed in Ch. 1, these assumptions are invalid in nanophotonics and, therefore, modern theories try to avoid them. In 2006, Tureci *et al.* introduced a new powerful approach—the "steady-state *ab-initio* laser theory" (SALT) [56]—which allows to solve the Maxwell–Bloch equations very generally and efficiently.

SALT reduces the Maxwell–Bloch equations to a single nonlinear eigenvalue problem for the electromagnetic field, assuming only that the laser field oscillates at a steady-state superposition of a finite set of modes and that the population inversion, D, is stationary. The first assumption amounts to expressing the electromagnetic field, $\mathbf{E}(\mathbf{x}, t)$, as:

$$\mathbf{E}(\mathbf{x}, t) = \sum_\mu \mathbf{E}_\mu(\mathbf{x}) a_\mu e^{-i\omega_\mu t}, \tag{2.23}$$

where a_μ are the steady-state modal amplitudes, $\mathbf{E}_\mu(\mathbf{x})$ are the field distributions (also called mode profiles), and ω_μ are the lasing frequencies. Using this expansion and a similar expansion for the polarization field, one finds that the lasing modes are real-

frequency outgoing-wave solutions of the nonlinear eigenvalue problem:

$$\left[\nabla \times \nabla \times -\omega_\mu^2 \left(\varepsilon_{\rm c} + \frac{\gamma_\perp}{\omega_\mu - \omega_{\rm a} + i\gamma_\perp} D\right)\right] \mathbf{E}_\mu(\mathbf{x}) = 0. \tag{2.24}$$

where D, the steady-state inversion, is a nonlinear function given by

$$D = \frac{D_{\rm p}}{1 + \sum_\sigma \frac{\gamma_\perp^2}{(\omega_\sigma - \omega_{\rm a})^2 + \gamma_\perp^2} |a_\sigma|^2 |\mathbf{E}_\sigma|^2}. \tag{2.25}$$

The term in round brackets in Eq. (3.50) is the effective permittivity, which contains the passive component, ε_c, and the effective pumped component. At small pump values, ($D_p < D_{\rm th}$), the resonant frequencies are complex with a finite lifetime given by $\mathrm{Im}\,[\omega_\mu]$. As the pump reaches a critical value of $D_{\rm th}$, the stimulated emission rate ("the gain") compensates for cavity losses in one of the modes, and the corresponding eigenfrequency hits the real axis ($\mathrm{Im}\,[\omega_\mu] = 0$). The system begins oscillating without decay, that is, it begins to lase. This point is called the laser threshold. As the pump increases further, additional modes may begin to lase.

2.3 The fluctuation–dissipation theorem

The SALT equations determine all the steady-state properties of microlasers, including resonant frequencies, mode profiles, and thresholds. However, in this thesis, we are not interested in the steady state but rather in the noise spectrum and, in particular, in fundamental quantum noise from spontaneous emission. In our work, we employ thermodynamic tools to determine the noise properties. This idea was developed by Landau and Lifshitz in their groundbreaking work on radiation noise [60], but it was only recently realized that such methods can produce efficient numerical algorithms [66] (when

combined with various linear-algebra tricks). This understanding has revolutionized the field of radiation noise in nanophotonics. For example, Casimir forces, which arise from vacuum electromagnetic fluctuations, were predicted as early as 1948 [67], but for nearly 50 years, could only be computed for extremely simple highly idealized structures like infinite parallel plates. With the new thermodynamic numerical approach, it became possible to handle structures of arbitrary complexity revealing that the forces can depend strongly on the shapes and compositions of the objects and can behave very differently from the monotonic attractive force first predicted by Casimir [68]. Similar achievements have been made in the field of radiative heat transfer and thermophotovoltaic devices [69] (e.g., in the design of efficient solar cells). Given this progress, the time was ripe to apply similar ideas to the problem of laser noise.

The most basic picture of radiation noise is the Rytov's *semiclassical* model [59]: Stochastic radiation is produced by fluctuating currents ($\mathbf{J}$), which appear as a random force ($\mathbf{F}_\mathrm{S}$) in Maxwell's equations:

$$\nabla \times \nabla \times \mathbf{E} + \varepsilon_\mathrm{c}\, \ddot{\mathbf{E}} = -4\pi \ddot{\mathbf{P}} + \mathbf{F}_\mathrm{S}, \tag{2.26}$$

with $\mathbf{F}_\mathrm{S} = 4\pi \frac{\partial \mathbf{J}}{\partial t}$. The currents are sources in the *classical* Maxwell equations, while their correlations are determined by the *quantum* fluctuation–dissipation theorem (FDT) [70], which relates the noise spectrum (the fluctuations) to the imaginary part of the permittivity (the dissipation) in systems at *thermal equilibrium* (at temperature T):

$$\left\langle \widehat{\mathbf{F}}_\mathrm{S}(\mathbf{x},\omega) \widehat{\mathbf{F}}_\mathrm{S}^*(\mathbf{x}',\omega') \right\rangle = 2\hbar\omega^4 \mathrm{Im}\, \varepsilon(\mathbf{x},\omega) \coth\left(\frac{\hbar\omega}{2T}\right) \delta(\mathbf{x}-\mathbf{x}')\delta(\omega-\omega'). \tag{2.27}$$

A more detailed picture of laser noise includes fluctuations not only in Maxwell's equa-

tion [Eq. (2.20)], but also in the polarization and inversion equations [Eqs. (2.21) and (2.22)] [71]. In Sec. 4.4, we prove however that our approach is equivalent, given that the correlations of the noise are computed correctly.

Thermodynamic treatment of lasers requires some justification. In a laser, an external pump constantly supplies energy to the system and maintains a *spatially varying* atomic population inversion. Theories of laser noise are typically based on the assumption that the atoms reach *local equilibrium* with the laser field [72], which means that spatial variations are so slow that, at any point, one can define local thermodynamic variables, which are related via thermodynamic relations. The local ground- and excited-state populations in the laser, $N_1(\mathbf{x})$ and $N_2(\mathbf{x})$ respectively, are related to the local temperature, $T(\mathbf{x})$, via [73]

$$\frac{N_1(\mathbf{x})}{N_2(\mathbf{x})} = e^{-\hbar\omega_a/k_B T(\mathbf{x})}. \tag{2.28}$$

In regions where the gain medium is pumped sufficiently to invert the population, $T(\mathbf{x})$ is negative; in regions where the pump is too weak to invert, $T(\mathbf{x})$ will be positive; and in unpumped regions, $T(\mathbf{x})$ will simply reduce to the equilibrium temperature of the surrounding environment.[§] Traditionally, it is assumed that in the absence of any thermodynamics instabilities, the electromagnetic fluctuations also satisfy the hypothesis of local equilibrium. This approximation is implicit in previous laser-noise theories, and we adopt this ansatz in this thesis as well. However, a more careful analysis in fluid dynamics [74] reveals that the assumption of local equilibrium is only valid for the thermodynamic properties themselves, but not for the correlations among these proper-

[§]In negative-temperature regions, the inversion produces gain and, consequently, the imaginary part of the permittivity is negative as well. Therefore, the right-hand side of Eq. (2.27) is always positive.

ties. Specifically, it was shown for the Rayleigh-Benard problem—a fluid with positive thermal expansion coefficient, confined between two horizontal parallel plates, which are maintained at two different temperatures—that the fluctuations in the presence of a nonzero temperature gradient, ∇T, are enhanced by a factor proportional to $(\nabla T)^2$. It would be interesting to compute the correction to the FDT in application to laser noise and, more generally, in radiation noise, but we leave that for future work.

2.4 Exceptional points

The second part of the thesis is about coalescence of resonances in non-Hermitian systems. If a system depends on some parameter (p):

$$\hat{\Theta}(p)\mathbf{E} = \left(\tfrac{\omega}{c}\right)^2 \mathbf{E}, \tag{2.29}$$

the value (p_0) at which the coalescence occurs is called an exceptional point (EP) [33]. In contrast to ordinary degeneracies, where only the eigenfrequencies merge ($\omega_1^2, \ldots, \omega_m^2 \xrightarrow[p\to p_0]{} \omega_0^2$), at an EP, also the eigenvectors merge ($\mathbf{E}_1, \ldots, \mathbf{E}_m \xrightarrow[p\to p_0]{} \mathbf{E}_0$). The case of two merging resonances is demonstrated in Fig. 2.2 (borrowed from [38]).

Since multiple eigenvectors merge at the EP, the operator $\hat{\Theta}$ does not have a complete basis of eigenvectors. This is most easily understood if we think of $\hat{\Theta}$ as a matrix [e.g., obtained when discretizing space using the finite-difference frequency-domain (FDFD) method]. If the matrix size is $N \times N$ and m eigenvectors merge at an EP, there remain only $N - m$ independent eigenvectors and the matrix is called defective. One can complete the set of eigenvectors at the EP into a basis of space by introducing "Jordan vectors". At a second-order EP (which forms from the coalescence of two resonances),

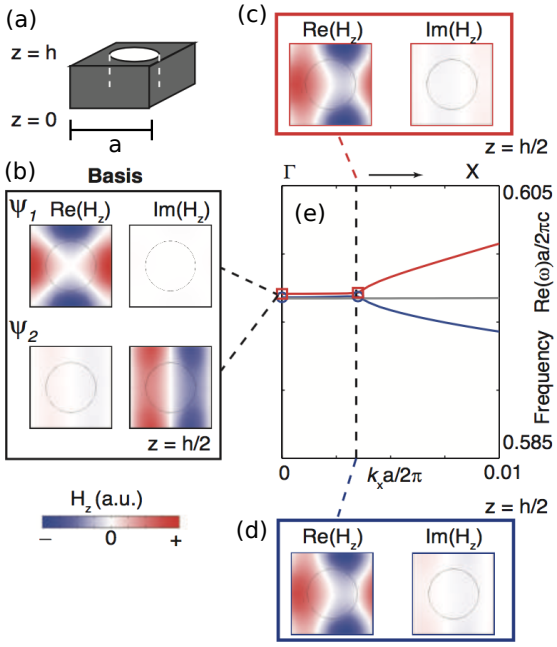

Figure 2.2: Exceptional points in a periodically patterned Si_3N_4 slab. (This image is borrowed from [38].) A unit cell of the periodic slab is shown in (a). The resonances are Bloch states, which depend on the Bloch vector, $\mathbf{k}$ [23]. An EP forms as the Bloch vector reaches a critical value of $k_{\mathrm{EP}}a/2\pi = 0.0035$, where a is the periodicity lengthscale, defined in (a). Away from EP, Maxwell's operator has a complete basis of eigenvectors (b). At the EP, two eigenmodes merge into a single degenerate mode (c,d). Although the dispersion curve (e) seems to imply that the modes are degenerate for all $0 < k_x < k_{\mathrm{EP}}$, this is not the case. Only the real part of the eigenfrequency is shown, but the decay rates of the modes are different for all $k \neq k_{\mathrm{EP}}$.

the Jordan vector is defined via the chain relations [34]:

$$\begin{aligned} \hat{\Theta}(p_0)\mathbf{E}_0^R &= \left(\tfrac{\omega_0}{c}\right)^2 \mathbf{E}_0^R, \\ \hat{\Theta}(p_0)\mathbf{J}_0^R &= \left(\tfrac{\omega_0}{c}\right)^2 \mathbf{J}_0^R + \mathbf{E}_0^R, \end{aligned} \tag{2.30}$$

with similar expressions for the left eigenvector $\mathbf{E}_0^L$ and Jordan vector $\mathbf{J}_0^L$. If the vectors $\mathbf{E}_0^R$ and $\mathbf{J}_0^R$ satisfy Eq. (2.30), then so do $\alpha\mathbf{E}_0^R$ and $\alpha(\mathbf{J}_0^R + \beta\mathbf{E}_0^R)$. In order to uniquely define the chain vectors, we need to specify two normalization conditions [e.g.,

$(\mathbf{E}_0^L, \mathbf{J}_0^R)_\varepsilon = 1$ and $(\mathbf{J}_0^L, \mathbf{J}_0^R)_\varepsilon = 0$]. More generally, when m resonances merge, one needs to introduce m Jordan vectors in order to have a complete basis.[†] In Ch. 8, we use this generalization study spontaneous emission at third-order EPs.

A unique property of EPs is "self-orthogonality" of the degenerate mode [33]:

$$(\mathbf{E}_0^L, \mathbf{E}_0^R)_\varepsilon = 0, \tag{2.31}$$

which follows from the biorthogonality relation [Eq. (2.16)]. The vanishing of the inner product is the source for the special emission properties at EPs: Traditional spontaneous-emission formulas (based on non-degenerate perturbation theory) are inversely proportional to the norm $[(\mathbf{E}_n^L, \mathbf{E}_n^R)_\varepsilon]$, which diverges at the EP. In Ch. 7, we resolve this problem by using a corrected perturbation theory near the EP.

[†]A formal definition is as follows. Let $\mathbf{x}_m = \mathbf{E}_0$ be an mth-order degenerate eigenvector of $\hat{\Theta}$, with eigenvalue $\lambda = \left(\frac{\omega_0}{c}\right)^2$. The Jordan chain generated by $\mathbf{x}_m$ is the set of vectors $\{\mathbf{x}_m, \mathbf{x}_{m-1}, \ldots, \mathbf{x}_1\}$ given by $\mathbf{x}_j = (\hat{\Theta} - \lambda I)\mathbf{x}_{j+1}$, with $j = 1, 2, \ldots, m-1$.[34]

Part I

The Microlaser Noise Spectrum

Chapter 3

Microcavity laser linewidth theory

This chapter presents a formula for the laser linewidth [Eq. (3.3)], which is accurate for multimode lasers with microstructured cavities. Our theory includes all previously known effects, and reduces to the traditional formula in the appropriate limits. This work was motivated by recent advances in laser theory: an elegant formulation of the steady-state laser equations (SALT) [56] and efficient numerical tools that solve the new equations [18]. The central idea is to combine SALT, which describes the steady-state (noise-free) properties of the laser, with the fluctuation–dissipation theorem [58], which relates the noise spectrum to the steady-state Green's function, in order to obtain the linewidth. The work was done in collaboration with Doug Stone from Yale and Alex Cerjan, who was his PhD student at the time. The results were published in [16].

3.1 Introduction

The fundamental limit on the linewidth of a laser is a foundational question in laser theory [75, 53, 11, 76, 77]. It arises from quantum and thermal fluctuations [78, 5], and depends on many parameters of the laser (materials, geometry, losses, pumping, etc.); it remains an open problem to obtain a fully general linewidth theory. In this chapter, we present a multimode laser-linewidth theory for arbitrary cavity structures and ge-

ometries that contains nearly all previously known effects [13, 79, 80, 14, 81] and also finds new nonlinear and multimode corrections. The theory is quantitative and makes no significant approximations; it simplifies, in the appropriate limits, to the Schawlow–Townes formula Eq. (3.2) with the well-known corrections. It also demonstrates the interconnected behavior of these corrections [82, 83], which are usually treated as independent. Most previous laser-linewidth theories have employed simple models for calculating the lasing modes (e.g., making the paraxial approximation). Such simplifications, though appropriate for many macroscopic lasers, are inadequate for describing complex microcavity lasers such as 3d nanophotonic structures or random lasers with inhomogeneities on the wavelength scale [84, 85, 86, 87]. We base our theory on the recent steady-state ab-initio laser theory (SALT) [56, 57], which allows us to efficiently solve the semi-classical laser equations in the absence of noise for arbitrary structures [18]. We treat the noise as a small perturbation to the SALT solutions, allowing us to obtain the linewidths *analytically* in terms of simple integrals over the steady-state lasing modes. Our SALT-based theory is *ab initio* in the sense that it produces a quantitatively accurate formula for the linewidths, with no free parameters, including the full spatial degrees of freedom of the system. Hence, we will refer to this approach as noisy steady-state *ab-initio* laser theory (N-SALT).

Our derivation (Secs. III–V) begins with the Maxwell–Bloch equations (details in Sec. 3.9), which couple the full-vector Maxwell equations to an atomic gain medium [55], combined with random currents (in Sec. 3.4) whose statistics are described by the fluctuation–dissipation theorem (FDT) [58, 59, 88, 89, 70]. In the presence of these random currents, we show that the amplitudes of the lasing modes evolve according to a set of coupled ordinary differential equations (ODEs), which have been called "oscillator models" [21, 90] or "temporal coupled-mode theory" (TCMT) [91, 92, 93, 94, 95] in

similar contexts. In their most general form, our N-SALT TCMT equations (Sec. 3.3) have the form of oscillator equations with a *non-instantaneous* nonlinear term that stabilizes the mode amplitudes around their steady-state values. The non-instantaneous nonlinearity arises since the atomic populations respond with a time delay to field fluctuations; this corresponds to the typical case of "class B" lasers [96, 97, 98], in which the population dynamics cannot be adiabatically eliminated. We are able to show analytically that the resulting linewidths of the lasing peaks are identical to the results one obtains for a simplified model with instantaneous nonlinearity [21, 90], which describes the (less common) case of "class A" lasers, in which the population dynamics are adiabatically eliminated. As expected, however, in certain parameter regimes the full non-instantaneous model can exhibit side peaks alongside the main lasing peaks [99], arising from relaxation oscillations (Sec. 3.5.3).

By solving the N-SALT TCMT equations, we obtain a simple closed-form matrix expression for the linewidths and multimode phase correlations (Sec. 3.5), generalizing earlier two-mode results that used phenomenological models [100]. This gives a multimode "Schawlow–Townes" relation (Sec. 3.6.C), where the linewidth of each lasing mode is proportional to a sum of inverse output powers of the neighboring lasing modes. The theory is valid well above threshold, and whenever a new mode turns on, this inverse-power relation produces a divergence due to the failure of the linearization approximation near threshold. However, we show that this divergence is spurious and can be avoided by solving the nonlinear N-SALT TCMT equations numerically [101]. (Our formalism can be extended to treat the near-threshold regime analytically by including noise from sub-threshold modes, as discussed in Sec. 3.6.B and in Sec. 3.8.) Sec. 3.6 and Sec. 3.7 also present several other model calculations that illustrate the differences between N-SALT and previous linewidth theories. Finally, in Sec. 3.8, we

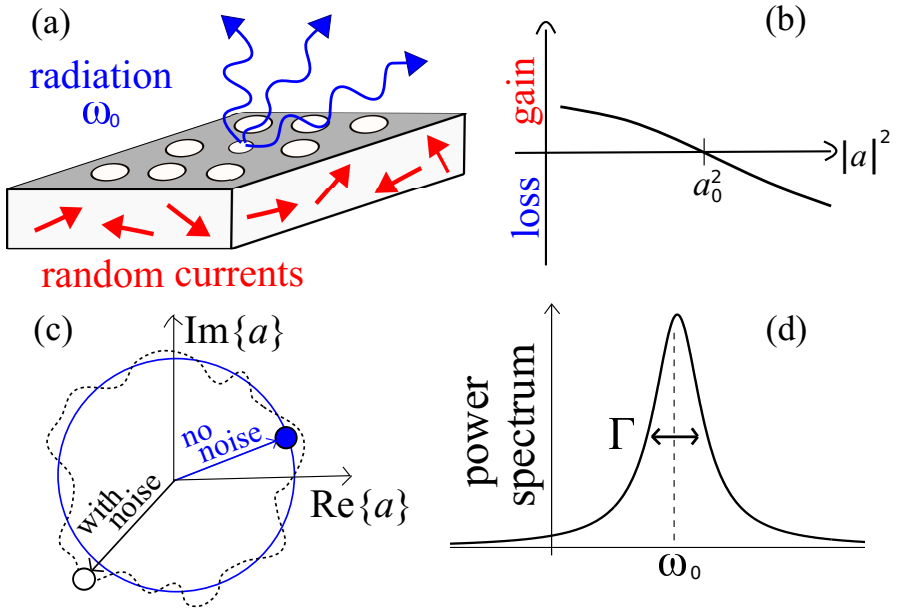

Figure 3.1: (Color online) Schematics illustrating linewidth physics. (a) Photonic-crystal (PhC) laser cavity [94] emitting radiation from the lasing mode at frequency ω_0, perturbed by random currents. (b) The amplitude is stabilized around a_0^2. Below (above) a_0^2, the medium provides light amplification (attenuation). (c) Phasor diagram for the complex field amplitude: a circular oscillation (with $|a| = a_0$) for the noise-free mode and a perturbed path for noise-driven mode. Noise drives small amplitude fluctuations and possibly large phase drifts. (d) The lineshape is a Lorentzian $\sim \Gamma/[(\omega - \omega_0)^2 + (\frac{1}{2}\Gamma)^2]$, centered around ω_0 with width Γ.

discuss some potential additional corrections that will be addressed in future work. In a second manuscript [102], we also compare the theory against full time-dependent integration of the stochastic Maxwell–Bloch equations and find excellent quantitative agreement of the major results presented here.

Laser dynamics are surveyed in many sources [75, 53, 11, 76, 77], but it is useful to review here a simple physical picture of linewidth physics. A resonant cavity [e.g., light bouncing between two mirrors or a photonic-crystal (PhC) microcavity as in Fig. 3.1(a)] traps light for a long time in some volume, and lasing occurs when a gain medium is "pumped" to a population "inversion" of excited states to the point (*threshold*) where

gain balances loss. [Of course, this simple picture is modified once additional modes reach threshold, or for lasers (such as random lasers [103, 104]) in which the passive cavity possesses no strong resonances; all of these complexities are handled by SALT [56, 57] and hence are incorporated into our approach.] For simplicity, consider here a laser operating in the single-mode regime. Above threshold, the gain depends nonlinearly on the mode amplitude $|a|^2$, as sketched in Fig. 3.1(b): increasing the field intensity decreases the gain due to depletion of the excited states until it reaches a stable steady-state amplitude a_0^2. (This gain-saturation effect is called "spatial hole-burning" [76] since it can be spatially inhomogeneous.) In the absence of noise, this results in a stable sinusoidal oscillation with an infinitesimal linewidth, but the presence of noise, which can be modeled by random current fluctuations $\mathbf{J}$ [90, 105, 80], perturbs the mode as depicted in Fig. 3.1(c), resulting in a finite linewidth. There are various sources of noise in real lasers, but spontaneous emission sets a fundamental lower limit on the linewidth [76]; here we will include only spontaneous emission and thermal noise. In particular, although the amplitude is stabilized around a_0^2 by the nonlinear gain, the phase ϕ of the mode drifts according to a random walk (a Brownian/Wiener phase) with variance $\langle \phi^2 \rangle \approx \Gamma\, t$, and the Fourier transform of a Wiener phase yields a Lorentzian lineshape [Fig. 3.1(d)] with full width at half maximum (FWHM) Γ [21]. The goal of linewidth theory is to derive Γ, ideally given only the thermodynamic FDT description of the current fluctuations and the Maxwell–Bloch physics of the laser cavity.

The most basic approximation for the linewidth (sufficiently far above threshold), usually referred to as the Schawlow-Townes (ST) formula [78, 5], takes the form

$$\Gamma = \frac{\hbar \omega_0 \gamma_0^2}{2P}, \tag{3.1}$$

where P is the output power of the laser, γ_0 is the passive cavity resonance width, and ω_0 is the laser frequency, often approximated to be equal to the real part of the passive-cavity resonance pole at $\omega_* = \omega_0 - i\gamma_0/2$. (A slightly more accurate approximation for the laser frequency takes into account the small line-pulling of the laser frequency towards the atomic transition frequency [106].) The inverse-power dependence causes the famous line-narrowing of a laser above threshold.

Over the decades, a number of now-standard corrections to this formula were found [11, 76, 77], leading to the modified ST formula:

$$\Gamma = \frac{\hbar\omega_0{\gamma_0}^2}{2P} \cdot n_{\mathrm{sp}} \cdot \left| \frac{\int_{\mathrm{C}} dx\, |\mathbf{E}_{\mathrm{c}}|^2}{\int_{\mathrm{C}} dx\, \mathbf{E}_{\mathrm{c}}^2} \right|^2 \cdot \left(\frac{\gamma_\perp}{\gamma_\perp + \frac{\gamma_0}{2}} \right)^2 \cdot \left(1 + \alpha_0^2\right). \tag{3.2}$$

First, the gain medium can be thought of, in many respects, as a system at negative temperature T [107], with the limit of complete inversion of the two lasing levels corresponding to $T \to 0^-$. When only partial inversion is present, the linewidth is enhanced by a factor of $n_{\mathrm{sp}} \equiv \frac{N_2}{N_2 - N_1}$ [108, 109], where N_2 and N_1 are the *spatially averaged* populations in the upper and lower states of the lasing transition. We refer to this correction as the incomplete-inversion factor (also known as "the spontaneous emission factor"). Second, due to the openness of the laser system, the modes are not power-orthogonal and the noise power which goes into each lasing mode is enhanced [110]; this correction is known as the Petermann factor, and it becomes significant in low-Q laser systems, where it is not a good approximation to treat the lasing mode $\mathbf{E}_{\mathrm{c}}$ as purely real. ($Q \equiv \omega_0/\gamma_0$ is a dimensionless passive-cavity lifetime defined in units of the optical period [94].) Note that $\mathbf{E}_{\mathrm{c}}$ is the passive-cavity mode [in contrast to SALT solutions, which are the modes of the full non-linear equations, introduced in Eq. (3.6)].

$\int_C dx$ denotes integration over the cavity region. Third, for low-Q laser cavities, it is possible that the gain linewidth $\gamma_\perp$ can be on the order of or smaller than the passive cavity resonance width γ_0, causing significant dispersion effects as the gain is increased to threshold [79]. This correction is commonly called the "bad-cavity" factor [111, 80]. Unlike the other corrections mentioned above, the bad-cavity factor decreases the laser linewidth. However, very few lasers systems are in the parameter regime where this effect is significant [112]. Finally, amplitude fluctuations in the laser field couple to the phase dynamics, leading to a correction known as the "α factor". For atomic gain media, this effect was identified by Lax [79] in the 1960's, and for this case it is typically a small correction. For bulk semiconductor gain media the effect is large, and typically dominates the broadening due to direct phase fluctuations [113, 114, 115]; in this context it is known as the "Henry α factor" [14].

Previous linewidth derivations have taken a number of different approaches, making severe approximations compared to the solution of the full three-dimensional space-dependent Maxwell–Bloch equations in the presence of noise. Generally speaking, linewidth theories can be classified into two categories. The first class includes methods which solve Maxwell's equations with a phenomenological model for the gain medium and account for noise spatial and spectral correlations by using the FDT [90, 105, 80]. Typically, these methods do not handle nonlinear spatial hole-burning above threshold or multimode effects. These methods, commonly used in the semiconductor laser literature, resulted in linewidth formulas which included the Petermann [110], bad-cavity [53, 80], incomplete-inversion [90], and α factors [14]. Most notably, an early work by Arnaud [10] derived a single-mode linewidth formula without making any simplifying assumptions about the field patterns, handling anisotropic, inhomogeneous, and dispersive media. However, this theory was only applied to very simple, effectively one-

dimensional, homogeneous systems, and it was missing hole-burning effects and the α factor.

The second class of linewidth theories consists of scattering-matrix methods [116, 117, 82, 83], which can treat arbitrary geometries without phenomenological parameters and take into account the effects of spatial hole-burning. S-matrix theories only have access to the input and output fields and, therefore, can only treat the noise in a spatially averaged manner and are not able to obtain the α factor rigorously. However, they obtain all of the other corrections to the single-mode linewidth. In particular, the recent S-matrix approach by Chong *et al.* [82, 83] takes advantage, as we do, of the *ab-initio* computational approach of SALT, and hence has the potential to treat arbitrary geometries and spatial hole-burning effects. (We reduce our results to the most recent scattering-matrix linewidth formula [83] in Sec. 3.12.) Note that in practice, S-matrix methods require a substantial independent calculation beyond SALT to extract the linewidths, whereas our approach obtains the linewidths immediately from SALT calculations (or any other method to obtain the steady-state lasing modes) by simple integrals over the fields.

Our derivation of N-SALT, being based on the SALT solutions, has a similar regime of validity. For *single-mode lasing*, SALT and N-SALT are essentially exact, relying only on the rotating-wave approximation and on the laser being sufficiently far above threshold. For multimode lasing, those theories require two additional dynamical constraints [56, 57]: the rates associated with population dynamics must be small compared to both the dephasing rate of the polarization and the lasing mode spacing (roughly, the free spectral range). The former constraint is satisfied in all solid-state lasers, whereas the latter requires a sufficiently small laser cavity. The actual size depends both on details of the cavity and of the gain medium used, but the appropriate limit is realized in

many complex lasers of interest. When these frequency scales are not well-separated, the level populations are not quasi-stationary, and multimode SALT will initially lose accuracy and eventually fail completely (since multimode lasing becomes unstable [118]). Moreover, while the average (SALT) behavior is unaffected by non-lasing poles, they do affect the noise properties, and N-SALT in its current form only accounts for a finite number of poles in the Green's function (Sec. 3.9.2). [We only include lasing poles (i.e., poles on the real axis), but extension to include non-lasing poles, which determine the amplified spontaneous emission (ASE) [101, 119], will be straightforward (Sec. 3.8)]. As noted above, the linewidth formula additionally assumes that the laser is operating far enough above threshold that amplitude fluctuations are small compared to the steady state amplitudes (i.e., $|a(t)| \approx a_0$ in the notation of Sec. 3.5). Hence, our formula does not describe the linewidth near the lasing thresholds. Our perturbation approach takes into account only the lowest-order correction to the complex modal amplitude $a(t)$ and neglects higher-order corrections to the frequency ω_0 and spatial pattern $\mathbf{E}_0(\mathbf{x})$ [see Eq. Eq. (3.7)]. Moreover, we neglect non-Lorentzian corrections to the lineshape [120, 121, 122, 123, 124] (Sec. 3.4). In the following section we present our generalized linewidth formula in the single-mode regime Eq. (3.3) and compare it with traditional linewidth theories.

3.2 The N-SALT linewidth formula

Our main result is a multimode linewidth formula which generalizes Eq. (3.2). In the multimode case, the result takes the form of a covariance matrix for the phases of the various modes, which is presented in Eqs. (3.36) and (3.37) of Sec. 3.5. In the single-

mode case, the N-SALT linewidth formula takes the simple form:

$$\Gamma = \frac{\hbar\omega_0\widetilde{\gamma}_0^2}{2P} \cdot \widetilde{n}_{\rm sp} \cdot \widetilde{K} \cdot \widetilde{B} \cdot (1+\widetilde{\alpha}^2). \tag{3.3}$$

The modified correction factors (marked by tildes) are defined in Table. 3.1. As can be seen from the table, those factors generalize the traditional factors by taking into account both spatial inhomogeneity and nonlinearity. Since the generalized factors depend on the SALT permittivity ε, mode profile $\mathbf{E}_0(\mathbf{x})$, and frequency ω_0, one can no longer regard the effects of cavity-openness, nonlinearity, and dispersion as separate multiplicative effects. In this sense, our formula demonstrates the intermingled nature of the linewidth correction factors, as previously introduced in [82, 83], but here demonstrated in a new level of generality. We denote by $\int dx$ integration over all space, for any number of spatial dimensions. We use the shorthand notation for vector products $|\mathbf{E}_0|^2 = \mathbf{E}_0 \cdot \mathbf{E}_0^*$ and $\mathbf{E}_0^2 = \mathbf{E}_0 \cdot \mathbf{E}_0$, where the latter unconjugated inner product appears naturally because of the biorthogonality relation for lossy complex-symmetric systems [33, 125]. $\mathrm{Im}\,\varepsilon(\mathbf{x})$ denotes the imaginary part of the nonlinear steady-state permittivity Eq. (3.5), which is negative/positive in gain/loss regions. The output power P is related to the SALT solutions by invoking Poynting's theorem, which one can use to show that $P \propto \int_{\rm P} dx\,[-\mathrm{Im}\,\varepsilon(\mathbf{x})]|\mathbf{E}_0(\mathbf{x})|^2$. We use $\int_{\rm P} dx$ to denote some volume which contains the gain medium. The choice of the volume is somewhat arbitrary; e.g., integrating over the cavity region corresponds to the output power at the cavity boundary [90]. Note, however, that this arbitrariness in the choice of the volume is not a general feature of our formula. After substituting the relevant expressions from Table. 3.1 into Eq. (3.3), the integrals which contain $\int_{\rm P} dx$ cancel, resulting in an expression for the linewidth only in terms of integrals over the entire space. The effective inverse temperature $\beta(\mathbf{x})$

is determined by the inhomogeneous steady-state atomic populations $N_1(\mathbf{x})$ and $N_2(\mathbf{x})$, and is defined as [73, 126, 127]

$$\beta(\mathbf{x}) \equiv \frac{1}{\hbar\omega_0} \ln\left(\frac{N_1(\mathbf{x})}{N_2(\mathbf{x})}\right). \tag{3.4}$$

In regions where the gain medium is pumped sufficiently to invert the population, $\beta(\mathbf{x})$ is negative; in regions where the pump is too weak to invert, $\beta(\mathbf{x})$ will be positive [and still given by Eq. (3.4)]; and in unpumped regions, Eq. Eq. (3.4) will simply reduce to the equilibrium temperature of the surrounding environment $(k_B T)^{-1}$. The quantities $N_1(\mathbf{x})$ and $N_2(\mathbf{x})$ are an output of the SALT solution in the absence of noise. The spatially dependent expression inside the square brackets in the definition of $\widetilde{n}_{\mathrm{sp}}$ in Table. 3.1 generalizes the spatially averaged incomplete-inversion factor $\frac{N_2}{N_2-N_1}$. That can be seen by noting that $\frac{1}{2}\coth(\frac{\hbar\omega\beta}{2}) - \frac{1}{2} = (\exp[\hbar\omega\beta] - 1)^{-1} \equiv n_{\mathrm{B}}$, where n_{B} is the usual Bose–Einstein distribution function [128, 129]. (For gain media, it is sometimes convenient to introduce the positive spontaneous-emission factor $n_{\mathrm{sp}} = -n_{\mathrm{B}}$ [72]. Note that this definition ensures that the generalized incomplete-inversion factor is always positive.) The $\frac{1}{2}$ factor subtracted from the hyperbolic cotangent was discussed in [72], and we give a simple classical explanation for it in Sec. 3.13. If standard absorbing layers are used to implement outgoing boundary conditions in the SALT solver [18] and the temperature of the ambient medium is assigned to these layers, then the N-SALT formula includes the effect of incoming thermal radiation. A generalized Petermann factor which formally resembles $\widetilde{K}$ appeared in previous work by Schomerus [117] (in his expression for the Petermann factor for TM modes in two-dimensional dielectric resonators). However, the earlier formula is expressed in terms of passive resonance scalar fields, whereas our correction contains 3d nonlinear SALT solutions. Finally, $\widetilde{\alpha}$ is

Definition	Symbol	Traditional	Generalized
cavity decay rate	$\widetilde{\gamma}_0$	γ_0	$\left\vert \frac{\int dx\, (\omega_0 \mathrm{Im}\, \varepsilon) {\mathbf{E}_0}^2}{\int dx\, \varepsilon\, {\mathbf{E}_0}^2} \right\vert$
incomplete inversion	$\widetilde{n}_{\mathrm{sp}}$	$\frac{N_2}{N_2 - N_1}$	$\frac{\int dx \left[\frac{1}{2} \coth(\frac{\hbar\omega\beta}{2}) - \frac{1}{2} \right] \mathrm{Im}\varepsilon \vert \mathbf{E}_0 \vert^2}{\int_{\mathrm{P}} dx\, \mathrm{Im}\, \varepsilon\, \vert \mathbf{E}_0 \vert^2}$
Petermann	$\widetilde{K}$	$\left\vert \frac{\int_{\mathrm{C}} dx\, \vert \mathbf{E}_{\mathrm{c}} \vert^2}{\int_{\mathrm{C}} dx\, \mathbf{E}_{\mathrm{c}}^2} \right\vert^2$	$\left\vert \frac{\int_{\mathrm{P}} dx\, \mathrm{Im}\, \varepsilon\, \vert \mathbf{E}_0 \vert^2}{\int dx\, \mathrm{Im}\, \varepsilon\, {\mathbf{E}_0}^2} \right\vert^2$
bad cavity	$\widetilde{B}$	$\left(\frac{\gamma_\perp}{\gamma_\perp + \frac{\gamma_0}{2}} \right)^2$	$\left\vert \frac{\int dx\, \varepsilon\, \mathbf{E}_0^2}{\int dx\, \mathbf{E}_0^2 (\varepsilon + \frac{\omega_0}{2} \frac{\partial \varepsilon}{\partial \omega_0})} \right\vert^2$
amplitude-phase coupling	$\widetilde{\alpha}$	$\frac{\omega_{\mathrm{a}} - \omega_0}{\gamma_\perp}$	$\frac{\mathrm{Im}\, C}{\mathrm{Re}\, C}$
nonlinear coupling	C		$\frac{-i \frac{\omega_0}{2} \int dx \frac{\partial \varepsilon}{\partial \vert a \vert^2} \mathbf{E}_0^2}{\int dx \left(\varepsilon + \frac{\omega_0}{2} \frac{\partial \varepsilon}{\partial \omega_0} \right) \mathbf{E}_0^2}$

Table 3.1: Traditional and new linewidth correction factors for the single-mode linewidth formulas Eqs. (3.2) and (3.3).

a generalized α factor, defined explicitly in Sec. 3.5 Eq. (3.30). For atomic gain media, the traditional factor is expressed in terms of the atomic transition frequency ω_{a} and decay rate of the atomic polarization $\gamma_\perp$. In the current work we will only evaluate the atomic case, although the general expression in terms of the non-linear coupling C should also apply to the semiconductor case.

The N-SALT formula Eq. (3.3) reduces to the traditional formula Eq. (3.2) in some limiting cases. Let us consider, for simplicity, a 1d Fabry-Pérot laser cavity of length L surrounded by air (i.e., $\mathrm{Im}\, \varepsilon = 0$ outside the cavity region). Let us assume also that the laser is operating not too far above the threshold and is uniformly pumped, hence $\mathrm{Im}\, \varepsilon$ and β are nearly constant inside the cavity. In this limit, all the integrals in Table. 3.1 can be approximated by reducing the integration limits to the cavity region; terms which contain integration over the imaginary part of the permittivity are non-zero only within the cavity region (e.g., $\int dx\, \mathrm{Im}\, \varepsilon |\mathbf{E}_0|^2$ becomes $\mathrm{Im}\, \varepsilon \int_{\mathrm{C}} dx\, |\mathbf{E}_0|^2$); while terms

of the form $\int dx\, \varepsilon\, \mathbf{E}_0^2$ can be written as the sum of the cavity contribution $\varepsilon \int_{\mathrm{C}} dx\, \mathbf{E}_0^2$ and the surrounding medium contribution $\int_{\mathrm{out}} dx\, \mathbf{E}_0^2$, where the latter is negligible for $L\omega_0 \gg 1$, as shown in Sec. 3.12 and in [83] (here and throughout the chapter, we are setting $c = 1$). Using this approximation, it is immediately apparent from Table. 3.1 that the incomplete-inversion factor reduces to the traditional expression. The generalized Petermann factor reduces to the traditional factor in the limit of a high-Q cavity, where the threshold lasing state $\mathbf{E}(\mathbf{x})$ is approximately the same as the passive resonance state $\mathbf{E}_{\mathrm{c}}(\mathbf{x})$. In order to simplify the remaining terms, recall that the lasing threshold is reached when gain in the system compensates for the loss. For weak losses (small $\mathrm{Im}\,\varepsilon/\varepsilon$) that can be treated by perturbation theory, the threshold condition is $\gamma_0 = \frac{\omega_0 \mathrm{Im}\,\varepsilon}{\varepsilon}$ [53] and, therefore, the generalized decay rate reduces to γ_0 (one can thereby see that the Schawlow–Townes formula Eq. (3.2) neglects nonlinear corrections to γ_0, as was also shown in [82]). Next, let us discuss the generalized bad-cavity factor, which simplifies to $\left(1 + \frac{\omega_0}{2\varepsilon}\frac{\partial \varepsilon}{\partial \omega_0}\right)^{-2}$ after reducing the integration limits. In order to show that it agrees with the traditional factor, we need to show that $\frac{\omega_0}{2\varepsilon}\frac{\partial \varepsilon}{\partial \omega_0} \approx \frac{\gamma_0}{2\gamma_\perp}$. The steady-state effective permittivity, as used in SALT theory (Sec. 3.9.1), is

$$\varepsilon(\mathbf{x}) = \varepsilon_{\mathrm{c}}(\mathbf{x}) + \frac{\gamma_\perp D(\mathbf{x})}{\omega_0 - \omega_{\mathrm{a}} + i\gamma_\perp}, \tag{3.5}$$

where ε_{c} is the passive permittivity and the second term is the active nonlinear permittivity due to the gain medium. The population inversion $D(\mathbf{x}) = N_2(\mathbf{x}) - N_1(\mathbf{x})$ is generally spatially varying above threshold due to spatial hole-burning. Since we assume here that we are close to threshold and that the pumping is uniform, the inversion is also uniform in space and near its threshold value. If one assumes, additionally, that the detuning of the lasing frequency from atomic resonance is small ($|\omega_0 - \omega_{\mathrm{a}}| \ll \gamma_\perp$),

one obtains $\frac{\partial\varepsilon}{\partial\omega_0} \approx \frac{\mathrm{Im}\,\varepsilon}{\gamma_\perp}$. Finally, we show in Sec. 3.6.A that our $\widetilde{\alpha}$ reduces to the known α_0 in homogeneous low-loss cavities, so that all factors of the corrected ST formula are recovered in this limit. (Note that line-pulling effects which may modify the lasing frequency ω_0 are handled by SALT.)

In the next section, we present the TCMT equations which are used in this chapter to derive the N-SALT linewidth formula Eq. (3.3), but which may also be used to extract more information on laser dynamics away from steady state.

3.3 The N-SALT TCMT equations

In the absence of noise, the electric field of a laser operating in the multimode regime is given by the real part of $\mathbf{E}_0(\mathbf{x}, t)$, where

$$\mathbf{E}_0(\mathbf{x}, t) = \sum_\mu \mathbf{E}_\mu(\mathbf{x}) a_{\mu 0} e^{-i\omega_\mu t}, \tag{3.6}$$

and the laser has zero linewidth. (This assumes, of course, that there exists a steady-state multimode solution of the nonlinear semi-classical lasing equations [56, 57].) The modes $\mathbf{E}_\mu(\mathbf{x})$ and frequencies ω_μ can be calculated using SALT, which solves the semi-classical Maxwell-Bloch equations in the absence of noise. (SALT has been generalized to include multi-level atoms [130], multiple lasing transitions, and gain diffusion [131]; any of these cases can thus be treated by N-SALT with minor modifications, but we focus on the two-level case here.) The linewidth can now be calculated by adding Langevin noise, as described below.

In the presence of a weak noise source, the electric field can be written as a superposition of the steady-state lasing modes with time-dependent amplitudes $a_\mu(t)$ which

fluctuate around $a_{\mu 0}$:

$$\mathbf{E}(\mathbf{x},t) = \sum_{\mu} \mathbf{E}_{\mu}(\mathbf{x}) a_{\mu}(t) e^{-i\omega_{\mu} t}. \tag{3.7}$$

In principle, the sum in Eq. (3.7) should also include the non-lasing modes since the set of lasing modes by itself does not form a complete basis for the fields. Non-lasing modes contribute to amplified spontaneous emission (ASE), which has a significant effect on the spectrum near and below the lasing thresholds [101, 119] and will be treated in future work.

In Sec. 3.9, we derive the N-SALT TCMT equations of motion for $a_{\mu}(t)$ starting with the full vectorial Maxwell-Bloch equations. We show that the noise-driven field obeys an effective nonlinear equation which, in the frequency domain, takes the form

$$\left[\nabla \times \nabla \times -\omega^2 \varepsilon(\omega, a)\right] \widehat{\mathbf{E}}(\mathbf{x},\omega) = \widehat{\mathbf{F}}_{\mathrm{S}}(\mathbf{x},\omega), \tag{3.8}$$

where the carets denote Fourier transforms [e.g., $\mathbf{E}(\mathbf{x},t) \equiv \int_0^{\infty} d\omega\, e^{-i\omega t} \widehat{\mathbf{E}}(\mathbf{x},\omega)$]. Spontaneous emission is included via the stochastic noise term $\widehat{\mathbf{F}}_{\mathrm{S}}(\mathbf{x},\omega)$ (quantified in Sec. 3.4), and the effective permittivity $\varepsilon(\omega, a)$ (derived in Sec. 3.9.2) is given by

$$\varepsilon(\omega, a)\widehat{\mathbf{E}}(\mathbf{x},\omega) = \textstyle\sum_{\mu} \left[\varepsilon_{\mathrm{c}} \widehat{a}_{\mu} + \frac{\gamma_{\perp}}{\omega - \omega_{\mathrm{a}} + i\gamma_{\perp}} \widehat{D} * \widehat{a}_{\mu}\right] \mathbf{E}_{\mu}(\mathbf{x}), \tag{3.9}$$

where the asterisk denotes a convolution. The second argument of $\varepsilon(\omega, a)$ denotes the implicit dependence of ε on the modal amplitudes a_{μ} through the inversion $\widehat{D}$. The effective permittivity Eq. (3.9) can be decomposed into a steady-state-amplitude dispersive term and a nonlinear non-dispersive term (similar in spirit to [132]). The key point here is that, to lowest order, there are two corrections to the permittivity in the presence of noise: the *dispersive correction* due to any shift in frequency at the

unperturbed amplitudes $a_{\mu 0}$, and the *nonlinear correction* due to any shift in amplitude at the unperturbed frequency. (Shifts in frequency are small because only frequency components within the mode linewidths matter, while shifts in amplitude are small because of the stabilizing effect of gain feedback.) The coupling between these two perturbations is higher order and is hence dropped, which greatly simplifies the analysis.

Substituting the permittivity expansion (derived explicitly in Sec. 3.9.3) into Maxwell's equation Eq. (3.8), we find that the noise-driven field obeys the linearized equation

$$\left[\nabla \times \nabla \times -\omega^2 \varepsilon(\omega, a_0)\right] \widehat{\mathbf{E}}(\mathbf{x}, \omega) = \widehat{\mathbf{F}}_{\mathrm{NL}}(\mathbf{x}, \omega) + \widehat{\mathbf{F}}_{\mathrm{S}}(\mathbf{x}, \omega), \tag{3.10}$$

i.e., the dispersive permittivity which appears on the left-hand side of Eq. (3.10) is evaluated at the steady-state amplitude a_0. The nonlinear non-dispersive term $\widehat{\mathbf{F}}_{\mathrm{NL}}$ [defined explicitly in Eq. (3.67)], which corresponds to amplitude fluctuations at the unperturbed frequency, appears as a restoring force on the right-hand side. The noise-driven field $\widehat{\mathbf{E}}(\mathbf{x}, \omega)$ is found in Sec. 3.9.4 by convolving the linearized Green's function with the source terms $\widehat{\mathbf{F}}_{\mathrm{NL}}$ and $\widehat{\mathbf{F}}_S$. Finally, the N-SALT TCMT equations are obtained by transforming the noise-driven field back into the time domain.

3.3.1 Time-delayed multimode model

We find that, in the most general case, the TCMT equations take the form

$$\dot{a}_\mu = \sum_\nu \int dx\, c_{\mu\nu}(\mathbf{x}) \times \left[\gamma(\mathbf{x}) \int^t dt' e^{-\gamma(\mathbf{x})(t-t')} \left(a_{\nu 0}^2 - |a_\nu(t')|^2\right)\right] a_\mu + f_\mu. \tag{3.11}$$

Comparing Eq. (3.11) and Eq. (3.10), one can see that the first term on the right-hand side of Eq. (3.11) is related to the nonlinear restoring force $\widehat{\mathbf{F}}_{\mathrm{NL}}$, and the Langevin noise

$f_\mu(t)$ is associated with $\widehat{\mathbf{F}}_S$.

The nonlinear coupling coefficients $c_{\mu\nu}(\mathbf{x})$ [derived in Eq. (3.77)] correspond to local changes in the nonlinear permittivity with respect to intensity changes in each of the modes

$$c_{\mu\nu} = \frac{-i\omega_\mu^2 \frac{\partial\varepsilon(\omega_\mu)}{\partial|a_\nu|^2}\mathbf{E}_\mu^2}{\int dx(\omega_\mu^2\varepsilon)'_\mu \mathbf{E}_\mu^2}, \tag{3.12}$$

where we have introduced a shorthand notation for the derivative in the denominator $(\omega_\mu^2\varepsilon)'_\mu \equiv \frac{\partial}{\partial\omega}\omega^2\varepsilon\big|_{\omega_\mu}$. This modal coupling in the fluctuation dynamics comes about because of saturation of the gain: a fluctuation in mode μ affects the amplitudes of all the other modes ν.

The N-SALT TCMT equations are nonlocal in time because the atomic populations are not in general able to follow the field fluctuations instantaneously and, instead, respond with a time delay determined by the local atomic decay rate $\gamma(\mathbf{x})$, given by

$$\gamma(\mathbf{x}) = \gamma_\parallel \left(1 + \sum_\nu \frac{\gamma_\perp^2}{(\omega_\nu - \omega_\mathrm{a})^2 + \gamma_\perp^2} |a_{\nu 0}|^2 |\mathbf{E}_\nu|^2\right). \tag{3.13}$$

The second term in Eq. (3.13) is precisely the local enhancement of the atomic decay rate due to stimulated emission in the presence of the lasing fields. (A simplified *spatially averaged* enhancement of the atomic decay rate was previously discussed in [99].)

The Langevin force f_μ is the projection of the spontaneously emitted field onto the corresponding mode $\mathbf{E}_\mu$ [90]. Defining $\mathbf{F}_\mu(t) \equiv \mathbf{F}_\mathrm{S} e^{i\omega_\mu t}$, the Langevin force f_μ is

$$f_\mu(t) = \frac{i\int dx \mathbf{E}_\mu \cdot \mathbf{F}_\mu(t)}{\int dx(\omega_\mu^2\varepsilon)'_\mu \mathbf{E}_\mu^2}. \tag{3.14}$$

The full N-SALT TCMT equations Eq. (3.11) describe the most typical situation in

laser dynamics of a "class B" laser [96, 97, 98], in which the polarization of the gain medium can be adiabatically eliminated but the population dynamics is relatively slow and cannot be so eliminated. However, much of the basic linewidth physics can be extracted from the limit when the population dynamics is also adiabatically eliminable, which describes "class A" lasers. Since the mathematical analysis is simpler in this limit, we will begin the spectral analysis in Sec. 3.5 with the latter model. We discuss this limit, which we refer to as the "instantaneous model," in the following section.

3.3.2 Instantaneous single-mode model

When the population relaxation rate $\gamma(\mathbf{x})$ is (everywhere) large compared to the dynamical scales determining $a_\mu(t)$, the exponential terms in Eq. (3.11) act like δ functions. After the spatial integration, and specializing in this section to the single-mode case, we obtain the simple nonlinear oscillator model driven by a weak Langevin force $f(t)$:

$$\dot{a} = C\left(a_0^2 - |a|^2\right) a + f, \tag{3.15}$$

where $C = \int dx\, c(\mathbf{x})$ is the integrated nonlinear coupling. This instantaneous nonlinear oscillator model was previously introduced by Lax [21, 79], and has been used extensively in linewidth theories [53]. The N-SALT approach enables computing the model's parameters *ab initio*, taking full account of the spatial hole-burning term and the vectorial nature of the fields [including multimode effects, when generalizing Eq. (3.15) to the multimode regime]. Also, our approach shows that this well-known model can be explicitly derived from the more general (non-instantaneous) model, presented in the previous section. Above the lasing threshold, $a_0 > 0$ and $\mathrm{Re}[C] > 0$, and the system undergoes self-sustained oscillations with a stable steady state at $|a| = a_0$, as demon-

strated in Fig. 3.1(b). In fact, near threshold one can show that Re[C] is approximately the threshold gain, which balances the cavity loss κ. Hence the dynamical scale of $a(t)$ is of order κ, which must then be much smaller than $\gamma(\mathbf{x})$ for the instantaneous model to hold; this is the standard dynamical condition for class A lasers [96, 97, 98].

The nonlinear term in Eq. (3.15) and the multimode counterpart in Eq. (3.12) are derived rigorously in Sec. 3.9, but we can motivate the resulting expressions using simple physical arguments. The nonlinear term can be viewed as a shift in the oscillation frequency, i.e., $-i\Delta\omega = C(a_0^2 - |a|^2)$. Using first-order perturbation theory [133], the frequency shift due to a change in dielectric permittivity $\Delta\varepsilon$ is given by

$$\Delta\omega = -\omega_0^2 \frac{\int dx\, \Delta\varepsilon\, \mathbf{E}_0^2}{\int dx (\omega_0^2\varepsilon)_0' \mathbf{E}_0^2}. \tag{3.16}$$

Plugging in the differential of the permittivity due to small changes in the squared mode amplitude, $\Delta\varepsilon \approx \frac{\partial\varepsilon}{\partial|a|^2}(|a|^2 - a_0^2)$, we find that the coupling coefficient in the instantaneous model is

$$C = \frac{-i\omega_0^2 \int dx \frac{\partial\varepsilon}{\partial|a|^2}\mathbf{E}_0^2}{\int dx (\omega_0^2\varepsilon)_0' \mathbf{E}_0^2}. \tag{3.17}$$

This is the single-mode version of Eq. (3.12) integrated over space due to rapid relaxation. As we will see, this simple result, combined with the spectrum of the Langevin noise (section IV), is all that is needed to derive the single-mode linewidth formula Eq. (3.3) (see Section V), and the multimode generalization also follows straightforwardly. Hence, after analyzing the noise spectrum, we will first derive the linewidth within the instantaneous model before moving on to the more complicated case of the full N-SALT TCMT equations. The latter will show that the basic linewidth formula is

unchanged from that of the instantaneous model except for the addition of side peaks due to the relaxation oscillations present in class B lasers.

3.4 The autocorrelation function of the Langevin force

In this section, we express the autocorrelation function of the Langevin force f_μ

$$\left\langle f_\mu(t) f_\nu^*(t') \right\rangle = R_\mu \delta_{\mu\nu} \delta(t - t') \tag{3.18}$$

in terms of the autocorrelation function of the noise source $\mathbf{F}_\mu$. It is well known that quantum and thermal fluctuations can be modeled as zero-mean random variables, defined by their correlation functions [89, 70]. This Rytov picture [59] is essentially a consequence of the central-limit theorem (CLT) [134, 135], which holds since the classical forcing $\mathbf{F}_\mathrm{S}$ is the sum of a large number of randomly emitted photons. The autocorrelation function of $\mathbf{F}_\mathrm{S}$ can be found by invoking the fluctuation–dissipation theorem (FDT), as explained below.

The probability distributions of the pumped medium and the electromagnetic field obey Boltzmann statistics, with an effective local temperature β defined in terms of the atomic inversion [107] (see definition in Sec. 3.2). Under the typical conditions of local thermal equilibrium [58, 59, 88, 89, 70], dissipation by optical absorption must be balanced by spontaneous emission from current fluctuations $\mathbf{J}(\mathbf{x}, t)$. One can then apply the FDT for the Fourier-transformed forcing $\widehat{\mathbf{F}}_\mathrm{S}(\mathbf{x}, \omega) = -4\pi\, i\omega \widehat{\mathbf{J}}(\mathbf{x}, \omega)$ [136]:

$$\left\langle \widehat{\mathbf{F}}_\mathrm{S}(\mathbf{x}, \omega) \widehat{\mathbf{F}}_\mathrm{S}^*(\mathbf{x}', \omega') \right\rangle = 2\hbar\omega^4 \mathrm{Im}\, \varepsilon(\mathbf{x}, \omega) \coth\left(\frac{\hbar\omega\beta(\mathbf{x})}{2}\right) \delta(\mathbf{x} - \mathbf{x}')\delta(\omega - \omega'). \tag{3.19}$$

Using this result, we calculate the autocorrelation of the Langevin force $\widehat{f_\mu}$ [i.e., the

Fourier transform of Eq. (3.14), defined as $\widehat{f}_\mu(\omega) \equiv \frac{1}{2\pi}\int_0^\infty dt\, e^{i\omega t} f_\mu(t)]$ and we obtain

$$\left\langle \widehat{f}_\mu(\omega)\widehat{f}^*_\nu(\omega')\right\rangle = \widehat{R}_\mu(\omega)\delta(\omega-\omega')\delta_{\mu\nu}, \tag{3.20}$$

where the frequency-domain autocorrelation coefficient is

$$\widehat{R}_\mu(\omega) = 4\hbar\omega^4 \frac{\int dx\, |\mathbf{E}_\mu|^2 \mathrm{Im}\,\varepsilon(\omega)\left[\frac{1}{2}\coth\left(\frac{\hbar\omega\beta}{2}\right)-\frac{1}{2}\right]}{\left|\int dx\, \mathbf{E}_\mu^2(\omega_\mu^2\varepsilon)'_\mu\right|^2}. \tag{3.21}$$

The $\frac{1}{2}$ factor subtracted from the hyperbolic cotangent is explained in Sec. 3.13 and in [72].

The time-domain diffusion coefficient R_μ can be found directly from Eq. (3.21) taking the inverse Fourier transform. For the common case of a small linewidth, $\mathrm{Im}\,\varepsilon(\omega)$ and $\coth\left(\frac{\hbar\omega\beta}{2}\right)$ are nearly constant for frequencies within the linewidth. [This means, essentially, that the Langevin force $f_\mu(t)$ can be treated as white noise]. Consequently, one can approximate the diffusion coefficient in Eq. (3.21) by its value at ω_μ. With this simplification, the time-domain diffusion coefficient in Eq. (3.18) is conveniently given by $R_\mu = 2\pi\widehat{R}_\mu(\omega_\mu)$ [90].

More generally, however, including this frequency dependence corresponds to temporally correlated fluctuations, leading to non-Lorentzian corrections to the laser lineshape [120, 121, 122, 123, 124]. These "memory effects" can be addressed using our approach (as discussed in Sec. 3.8) and we plan to include them in future work.

3.5 The laser spectrum

In this section, we calculate the laser spectrum using the N-SALT TCMT equations Eqs. (3.11) and (3.15) and the noise autocorrelation function Eqs. (3.20) and (3.21). We begin by showing that the phase of the lasing mode undergoes simple Brownian motion; consequently, the laser spectrum is a Lorentzian, with a width given by the phase-diffusion coefficient. In Sec. 3.5.1, we calculate the phase-diffusion coefficient (hence the linewidth) for the instantaneous model Eq. (3.15) and in Sec. 3.5.2, we outline the analysis for the time-delayed model Eq. (3.11), leaving the details of the derivation to Sec. 3.10. More accurately, the spectrum of the time-delayed model consists of a central Lorentzian peak at the lasing resonance frequency and additional side peaks due to relaxation oscillations, which are present in class B lasers. The latter side peaks are the subject of Sec. 3.5.3.

3.5.1 Instantaneous single-mode model

The complex mode amplitude $a(t)$ can be written in polar form as

$$a(t) = [a_0 + \delta(t)]\, e^{i\phi(t)}. \tag{3.22}$$

a_0 is the steady-state amplitude, while δ and ϕ are *real* amplitude and phase fluctuations. Substituting the modal expansion Eq. (3.22) in Eq. (3.15), defining

$$\begin{aligned} A &\equiv 2a_0^2 \mathrm{Re}\, C \\ B &\equiv 2a_0^2 \mathrm{Im}\, C, \end{aligned} \tag{3.23}$$

and keeping terms to first order in δ/a_0, we obtain

$$\dot{\delta} = -A\delta + f_{\mathrm{R}}, \tag{3.24}$$

$$a_0\dot{\phi} = -B\delta + f_{\mathrm{I}}, \tag{3.25}$$

where $f_{\mathrm{R}} \equiv \mathrm{Re}\{f\}$ and $f_{\mathrm{I}} \equiv \mathrm{Im}\{f\}$. We check the approximation of $|\delta| \ll a_0$ *a posteriori* and we find that it generally holds (as was also shown in [101]), except near threshold ($a_0 \to 0$), which is a case we discuss in Sec. 3.6.C.

When the nonlinear coupling coefficient is real ($B = 0$), it is evident from Eq. (3.25) that the phase undergoes simple Brownian motion (i.e., it is a Wiener process) and hence the phase variance increases linearly in time. An oscillator with Brownian phase noise has a Lorentzian spectrum [137], and one can reproduce that result briefly as follows. The laser spectrum $S_{\mathrm{a}}(\omega)$ is given by the Fourier transform of the autocorrelation function of $a(t)$:

$$\langle a(t)a^*(0)\rangle \approx a_0^2 \left\langle e^{-i(\phi(t)-\phi(0))}\right\rangle = a_0^2 e^{-\frac{1}{2}\left\langle(\phi(t)-\phi(0))^2\right\rangle}. \tag{3.26}$$

For a Wiener phase, whose variance is $\left\langle(\phi(t)-\phi(0))^2\right\rangle = \Gamma|t|$, the Fourier transform of Eq. (3.26) is a Lorentzian whose central-peak width is Γ [21]. In passing from the first to second step in Eq. (3.26), one neglects direct amplitude-fluctuation contributions (which are decoupled from the phase) as these only introduce broad-spectrum background noise, but do not affect the linewidth of the laser peak (we return to this point in Sec. 3.5.3). In passing from the second to the third step, one assumes that the phase is a Gaussian normal variable, which is justified as a consequence of the CLT.

It is well known that also in the general case of $B \neq 0$, the phase is a Wiener

process, with a modified diffusion coefficient [14]. In order to calculate the phase variance explicitly, we solve Eqs. (3.24) and (3.25) and obtain

$$\delta(t) = \int^t e^{-A(t-t')} f_{\mathrm{R}}(t')dt', \tag{3.27}$$

$$a_0\phi(t) = -B\int^t \delta(t')dt' + \int^t f_{\mathrm{I}}(t')dt'. \tag{3.28}$$

Substituting Eq. (3.27) into Eq. (3.28), using the autocorrelation function of f Eq. (3.21), and performing the integration, one obtains that the phase variance in the long-time limit is $\left\langle(\phi(t)-\phi(0))^2\right\rangle = \frac{R}{2a_0^2}\left(1+\left(\frac{B}{A}\right)^2\right)|t|$ (where terms growing more slowly than $|t|$ were neglected, as explained in greater detail in Sec. 3.10). Therefore, the linewidth is

$$\Gamma = \frac{R}{2a_0^2}(1+\widetilde{\alpha}^2), \tag{3.29}$$

where we have defined the generalized α factor:

$$\widetilde{\alpha} = \frac{B}{A} = \frac{\operatorname{Im} C}{\operatorname{Re} C}, \tag{3.30}$$

with the nonlinear coefficient C defined in Eq. (3.17). Substituting the autocorrelation function Eq. (3.21) in Eq. (3.29) and using Poynting's theorem to relate a_0^2 to the output power $P = \frac{\omega_0 a_0^2}{2\pi}\int_{\mathrm{P}} dx\,(-\operatorname{Im}\varepsilon(\mathbf{x}))|\mathbf{E}_0(\mathbf{x})|^2$ [138], we obtain the single-mode linewidth formula Eq. (3.3). From Eq. (3.29), it is evident that the Schawlow–Townes, Petermann, bad-cavity and incomplete-inversion factors are all included in the term $\frac{R}{2a_0^2}$, and generally cannot be separated into the traditional factors of Eq. (3.2) [83].

When the nonlinear coupling coefficient is complex (i.e., when $B \neq 0$), the resonance peak is not only broadened but is also shifted [14]. The shift in center frequency is

found by keeping second-order terms in δ/a_0 and calculating the average phase drift:

$$\delta\omega = \langle\dot{\phi}\rangle = -\frac{RB}{4a_0^2 A}. \tag{3.31}$$

An identical formula was derived in [90] in a phenomenological instantaneous model.

Fig. 3.2 shows the spectrum of the instantaneous model, which is obtained by numerically solving Eq. (3.15) using a stochastic Euler scheme [139]. Introducing the notation $\mathcal{F}(a) \equiv C(a_0^2 - |a|^2)a$ and discretizing time as $a(n\Delta t) \approx a_n$, the Euler update equation for the n-th step is

$$a_n = a_{n-1} + \mathcal{F}\left(a_{n-1}\right)\Delta t + \sqrt{R\,\Delta t}\,\zeta, \tag{3.32}$$

where ζ is a gaussian random variable of mean 0 and variance 1, i.e., $\zeta \in N(0,1)$. [For the data presented inFig. 3.2, Δt was decreased until the simulation results converged. In later sections (Fig. 3.3), we implemented a fourth-order Runge–Kutta method in order to achieve convergence]. The simulated spectra (noisy colorful curves) match the predicted Lorentzian lineshapes (solid black curves), which are calculated using Eqs. (3.29) and (3.31). As $\widetilde{\alpha}$ increases, the linewidths are broadened and the center frequencies are shifted.

3.5.2 Time-delayed multimode model

We now turn to the laser spectrum produced by the time-delayed model, where the nonlinearity is dependent on the modal amplitudes at previous times. Although we calculate the linewidth of the full time-delayed N-SALT TCMT equations Eq. (3.11) in Sec. 3.10, we begin this section by considering the simplified case of a spatially homogeneous medium $\gamma(\mathbf{x}) \approx \gamma_0$ (this is a good approximation for a uniformly pumped

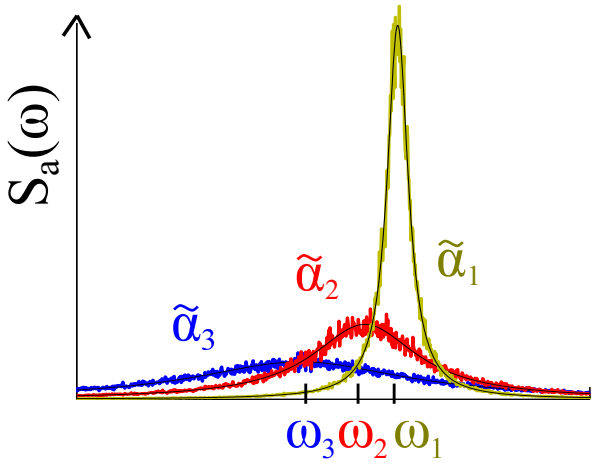

Figure 3.2: (Color online) Simulated spectrum $S_{\rm a}(\omega)$ of the instantaneous model Eq. (3.15) with $\mathrm{Re}\, C = 10$, noise autocorrelation coefficient $R = 0.1$ and three values of $\widetilde{\alpha}$: 10 (blue), 5 (red), 1 (yellow) ($C, R, S_{\rm a}$, and ω are given in arbitrary frequency units). The noisy signal is the simulation result and the black curves are Lorentzian lineshapes with widths Γ and center frequency shifts given by Eqs. (3.29) and (3.31).

class B laser operating near threshold). In this case, the single-mode time-delayed model takes the form

$$\dot{a} = C\left(\gamma_0 \int^t dt' e^{-\gamma_0(t-t')}(a_0^2 - |a(t')|^2)\right) a + f, \tag{3.33}$$

where $C = \int dx\, c(\mathbf{x})$ is the integrated nonlinear coupling and $c(\mathbf{x})$ is defined in Eq. (3.12). This integro-differential equation can be turned into a first-order ODE by using the modal expansion from Sec. 3.5.1: $a = (a_0 + \delta)e^{i\phi}$, keeping terms to first order in δ/a_0, and introducing the variable

$$\xi(t) = \gamma_0 \int^t dt' e^{-\gamma_0(t-t')}\delta(t'). \tag{3.34}$$

Then, Eqs. (3.33) and (3.34) can be recast in the form $\dot{\mathbf{v}} = \mathbb{K}\mathbf{v} + \mathbf{f}$, where $\mathbf{v} = \{\delta, a_0\phi, \xi\}$.

However, most generally, the spatial dependence of $\gamma(\mathbf{x})$ cannot be neglected. The time-averaged deviation $\xi(\mathbf{x}, t)$ is therefore spatially dependent, and one obtains an infinite-dimensional problem. To simplify the algebra, we discretize space [e.g., discretizing Eq. (3.11) into a Riemann sum over sub-volumes V_k] and recover the continuum limit at the end. This yields the discrete-space multimode model:

$$\dot{a}_\mu = \sum_{\nu k} C^k_{\mu\nu} \left(\gamma_k \int^t dt' e^{-\gamma_k (t-t')} (a^2_{\nu 0} - |a_\nu(t')|^2) \right) a_\mu + f_\mu, \tag{3.35}$$

where the discretized nonlinear coupling coefficients are $C^k_{\mu\nu} = \int_{V_k} dx\, c_{\mu\nu}(\mathbf{x})$ (so that $C_{\mu\nu} = \sum_k C^k_{\mu\nu}$), γ_k is the relaxation rate at the k'th spatial point and $a_{\nu 0}$ is the steady-state amplitude of mode ν.

In Sec. 3.10, we study the statistical properties of the solutions to Eq. (3.35). We introduce the the M-dimensional vectors whose entries are $\Phi_\mu \equiv a_{\mu 0}\phi_\mu$ (where M is the number of active lasing modes) and we calculate the covariance matrix $\langle \Phi_\mu(t)\Phi_\nu(0)\rangle$. We find that the result is independent of the relaxation rates γ_k or the discretization scheme:

$$\left\langle \mathbf{\Phi}(t)\mathbf{\Phi}^{\,T}(0) \right\rangle = \left(\frac{\mathbb{R}}{2} + \mathbb{B}\mathbb{A}^{-1} \frac{\mathbb{R}}{2} \left(\mathbb{B}\mathbb{A}^{-1}\right)^T \right) |t|. \tag{3.36}$$

The matrices $\mathbb{A}$ and $\mathbb{B}$ correspond to the real and imaginary parts of the coupling matrices, with entries $A_{\mu\nu} = 2a_{\mu 0}a_{\nu 0}\mathrm{Re}[C_{\mu\nu}]$ and $B_{\mu\nu} = 2a_{\mu 0}a_{\nu 0}\mathrm{Im}[C_{\mu\nu}]$. $\mathbb{R}$ is the autocorrelation function of the Langevin force vector $\mathbf{f}$ [defined in Eq. (3.21)]. The diagonal of this matrix, divided by $|t|$ and by the squared modal amplitude, gives the generalized linewidths

$$\Gamma_\mu = \frac{1}{2a^2_{\mu 0}} \left(R_{\mu\mu} + \left[\mathbb{B}\mathbb{A}^{-1}\mathbb{R} \left(\mathbb{B}\mathbb{A}^{-1}\right)^T \right]_{\mu\mu} \right). \tag{3.37}$$

Therefore, the generalized α factor (which is responsible for linewidth enhancement due to coupling of amplitude and phase fluctuations) is given by

$$\widetilde{\alpha}_{\mu} \equiv \frac{1}{R_{\mu\mu}} \left[\mathbb{B}\mathbb{A}^{-1}\mathbb{R} \left(\mathbb{B}\mathbb{A}^{-1} \right)^{T} \right]_{\mu\mu}. \tag{3.38}$$

In the single-mode case ($M = 1$), this matrix formula reduces to the single-mode linewidth of the instantaneous-model: $\frac{R}{2a_0^2}(1+\left(\frac{B}{A}\right)^2)$ [Eqs. (3.29) and (3.30) in Sec. 3.5.1].

The linewidth in the time-delayed (class B) model is precisely the same (neglecting side peaks) as in the instantaneous (class A) model. While this result was derived for single-mode class B semiconductor lasers using a phenomenological rate-equation framework [99], we prove that this is generally the case in the multimode inhomogeneous regime. Naively, one might expect to obtain different linewidths due to the longer time over which the fluctuations can grow. However, in Sec. 3.10 we obtain a linewidth expression which is independent of the relaxation-oscillation dynamics, which demonstrates that there is a cancellation of two competing processes: as $\gamma_{\|}$ decreases, amplitude fluctuations grow, but they are also averaged over longer periods of time so that their effect is smaller.

Fig. 3.3 presents the simulated spectrum of the time-delayed model in the homogeneous-γ limit, which is obtained by numerically integrating Eq. (3.33) (by applying a stochastic Euler scheme, as in Fig. 3.2). The width of the central peak of the spectrum matches our prediction Eq. (3.29), independent of the value of γ_0. At intermediate relaxation rates, we also observe side peaks in the spectrum due to amplitude relaxation oscillations (RO), in addition to the central peak.

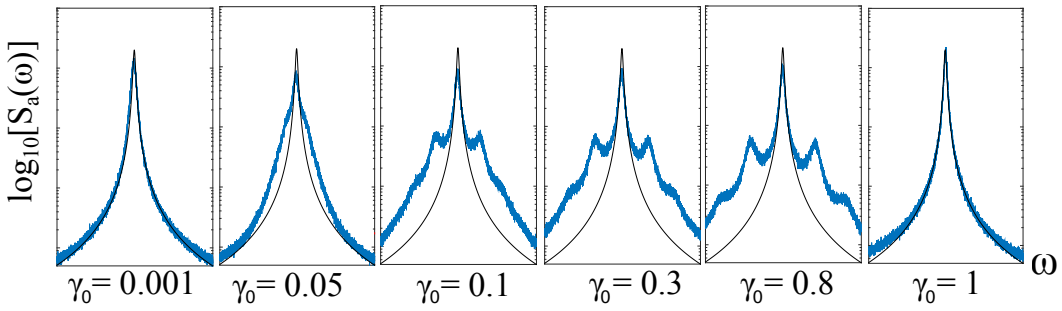

Figure 3.3: (Color online) Simulated spectrum of the time-delayed model Eq. (3.33) with $\mathrm{Re}\, C = 10$ and $R = 0.1$ (in arbitrary frequency units) at six values of γ_0 (using a base 10 logarithmic scale for the y axis). The noisy signal is the simulation result and the black curves are Lorentzian lineshapes with widths given by Eq. (3.29).

3.5.3 Side peaks in the time-delayed model

In class B lasers, amplitude fluctuations relax to steady state via relaxation oscillations [106] and, consequently, give rise to side peaks in the spectrum, in analogy with amplitude modulation of harmonic signals. Mathematically, the oscillation arises from the second-order ODE generated by coupling of the $\dot{\delta}$ and $\dot{\xi}$ equations Eqs. (3.33) and (3.34), producing the coupled amplitude/gain oscillations. Using the same methods that we applied to calculate the linewidth of the central resonance peak Eq. (3.37), we also calculated the full side-peak spectrum in the multimode regime. Our formula is derived under the fairly general assumption that the central resonance peaks are narrower than the side peaks, which is the relevant regime for many lasers [99]. Although the derivation uses the same techniques as in Sec. 3.10, it is fairly involved and will be provided in Ch. 5; we only summarize here.

As was shown in Sec. 3.3, far above threshold, the atomic relaxation rate Eq. (3.13) is enhanced and can even be dominated by the electromagnetic field. This modified relaxation rate, and in particular its spatial dependence due to hole-burning effects, has

important implications on the RO spectrum which, to our knowledge, have not been treated before. For simplicity, we focus here on the case of $\alpha = 0$. (Note that α factor effects on the RO spectrum have been observed and analyzed using a phenomenological *homogeneous* time-delayed model in [99].)

In order to see how one can obtain a closed-form expression for the RO spectrum, recall that when calculating the spectrum of the central resonance peak in Sec. 3.5.1, we neglected direct amplitude-fluctuation contributions in Eq. (3.26), i.e., in passing from the first to second step, we omitted a term of the form

$$\langle \delta(t)\delta(0)\rangle \cdot \left\langle e^{-i(\phi(t)-\phi(0))} \right\rangle . \tag{3.39}$$

Adding this term in Eq. (3.26), one finds that the full spectrum consists of an additional term, which is given by the convolution of the real-amplitude fluctuation spectrum $\langle \delta(t)\delta(0)\rangle$ and the spectrum of the central resonance peak. In the instantaneous model, the amplitude autocorrelation function $\langle \delta(t)\delta(0)\rangle$ decays exponentially in time [see Eq. (3.27)] and the omitted term results in near-constant background noise. However, in the time-delayed model, this neglected term is responsible for the RO side peaks.

For simplicity, consider first a model which can be solved straightforwardly; the single-mode homogeneous-γ time-delayed model [i.e., $\gamma(\mathbf{x}) \approx \gamma_0$ and $\int dx\, c(\mathbf{x}) = C$ as in Eq. (3.33)], which describes uniformly pumped single-mode lasers near threshold. Following the discussion in Sec. 3.5.2, we can rewrite Eqs. (3.33) and (3.34) as a set of linear equations and solve for $\delta(t)$, obtaining

$$\delta(t) = \int dt' e^{-\frac{\gamma_0}{2}(t-t')} \times \left[\cosh\left(\frac{\Delta}{2}(t-t')\right) + \frac{\gamma}{\Delta}\sinh\left(\frac{\Delta}{2}(t-t')\right)\right] f_{\mathrm{R}}(t'), \tag{3.40}$$

where $\Delta \equiv \sqrt{\gamma_0^2 - 4A\gamma_0}$. In the limit of well-resolved side peaks (e.g., $\frac{R}{a_0^2} \ll \gamma_0 \ll A$), the amplitude autocorrelation function is approximately

$$\langle \delta(t)\delta(0)\rangle \approx \frac{R}{2}\left[\frac{\sin\sqrt{\gamma_0 A}\,t}{\sqrt{\gamma_0 A}} + \frac{\cos\sqrt{\gamma_0 A}\,t}{\gamma_0}\right] \times e^{-\frac{\gamma_0 t}{2}}. \tag{3.41}$$

Thus, additional peaks in the spectrum arise at frequencies $\omega_{\mathrm{RO}} = \omega_0 \pm \sqrt{A\gamma_0}$ with widths γ_0. In the high-Q limit near threshold, A is proportional to the cavity decay rate κ, giving the expected behavior for the RO frequency. The side-peak amplitudes $\frac{R}{4}\left[\frac{1}{\sqrt{\gamma_0 A}} + \frac{1}{\gamma_0}\right]$ diverge in the limit of $\gamma_0 \to 0$ (that is, when amplitude fluctuations are not small compared to the steady-state mode amplitude), but this is also the regime in which our analysis of the spectrum (Sec. 3.5.1 and Sec. 3.5.2) breaks down. The inset in Fig. 3.4b shows the simulated spectrum of the homogeneous time-delayed model Eq. (3.33) (the same data was also shown in Fig. 3.3, but we include here the theoretical formula for the side-peak spectrum). The exact numerical solution of Eq. (3.33) (blue curve) reproduces the analytic spectrum prediction of Eq. (3.42) (red curve).

In the limits of extremely small/large relaxation rates γ_0 (compared to A), the side peaks disappear. In the former limit, they merge with the central resonance peak and in the latter case, they merge with the background noise. This behavior can be explained by inspection of the $\dot{\delta}$ and $\dot{\xi}$ equations Eqs. (3.33) and (3.34) in the appropriate limits. When the relaxation rate is very large, the time-delayed model reduces to the instantaneous model, which represents the case where the atomic population follows the field adiabatically. In the opposite limit of extremely small relaxation, the field follows the atomic population adiabatically. In other words, a clear separation of atomic and optical time scales will result in the absence of RO side peaks.

In the most general spatially inhomogeneous time-delayed model, the full spectrum

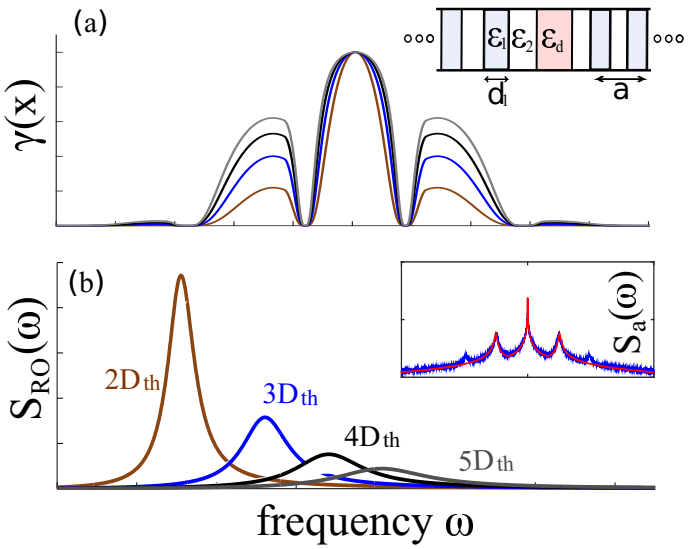

Figure 3.4: (Color online) Dressed decay rate and the RO spectrum based on SALT solutions of a 1d PhC laser. Inset: a quarter-wave PhC (period $a = 1$ mm and alternating layers with permittivities $\varepsilon_1 = 16 + 0.1i$ and $\varepsilon_2 = 2 + 0.1i$ and thicknesses $d_1 = \frac{a\sqrt{\varepsilon_2}}{\sqrt{\varepsilon_1}+\sqrt{\varepsilon_2}}$ and $d_2 = a - d_1$). The center region has permittivity $\varepsilon_{\rm d} = 3 + 0.1i$ and contains gain atoms with bandwidth $\gamma_\perp = 3$ mm^{-1} and resonance frequency $\omega_{\rm a} = 25$ mm^{-1}. (a) Dressed decay $\gamma(\mathbf{x})$ evaluated using Eq. (3.13) at five pump values ($2D_{\rm th}$ brown, $3D_{\rm th}$ blue, $4D_{\rm th}$ black, and $5D_{\rm th}$ gray). (b) Side-peak spectrum $S_{\rm RO}(\omega)$ evaluated using Eq. (3.42) for the five pump values of (a). Inset: full simulated spectrum $S_{\rm a}(\omega)$ on a semi-log scale (of base 10) of the homogeneous time-delayed model Eq. (3.33) with $\gamma_0 = 0.09, A = 10, B = 0, R = 0.01$ (in arbitrary frequency units). The noisy signal is the simulation result and the red curve is the theoretical lineshape Eq. (3.42).

takes the simple form

$$S_{\mathrm{a}}(\omega)=\frac{\Gamma}{\omega^2+\left(\frac{\Gamma}{2}\right)^2}+\frac{\Gamma}{\omega^2\left[1-\int dx\frac{A(\mathbf{x})\gamma(\mathbf{x})}{\omega^2+(\frac{\Gamma}{2}+\gamma(\mathbf{x}))^2}\right]^2+\left[\int dx\frac{A(\mathbf{x})\gamma(\mathbf{x})\left(\gamma(\mathbf{x})+\frac{\Gamma}{2}\right)}{\omega^2+\left(\gamma(\mathbf{x})+\frac{\Gamma}{2}\right)^2}\right]^2} \tag{3.42}$$

where $A(\mathbf{x})$ is the real part of the local nonlinear coupling [defined in Eq. (3.23)], $\gamma(\mathbf{x})$ is the effective decay rate, and Γ is the central peak linewidth. (This formula is valid when the central resonance peak is narrower than the side peaks $\Gamma \ll \gamma_{\parallel}$.) Like our linewidth formula, this formula is easy to evaluate via spatial integrals of the SALT solutions.

While the homogeneous time-delayed model near threshold agrees with standard results on relaxation oscillations [99], the full model above threshold, combined with SALT, is able to include effects not contained in other treatments. As the pump is increased far above threshold, the effects of stimulated emission strongly increase the atomic relaxation rate, and spatial hole burning causes that rate $\gamma(\mathbf{x})$ to vary substantially in space [see Eq. (3.13)]. These two effects cause both a shift and a broadening of the side peaks compared to the near-threshold result. Fig. 3.4 shows the dressed decay rate $\gamma(\mathbf{x})$ and the side-peak spectrum $S_{\mathrm{RO}}(\omega)$ [as given by the second term of Eq. (3.42)], based on a SALT calculation of a one-dimensional photonic crystal (PhC) laser, at four different pump values well above threshold. [The pump value is controlled via the parameter D_{p} in Eq. (3.47), and we denote the threshold value of D_{p} by D_{th}.] This type of cavity (depicted in the inset of Fig. 3.4a) supports a single mode at the simulated parameter regime, which is localized near the defect region. (Further discussion of this structure is given in Sec. 3.6.1 below.) As can be seen from Fig. 3.4a, the decay rate $\gamma(\mathbf{x})$ is enhanced at high intensity regions (i.e., near the defect), and it increases

further as the pump increases. Fig. 3.4b demonstrates the shifting and broadening of the side peaks.

3.6 The generalized α factor

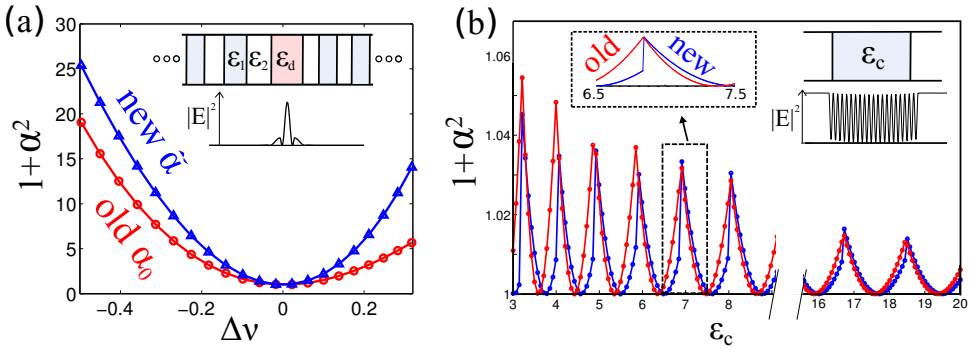

Figure 3.5: (Color online) (a) The generalized (blue) and traditional (red) α factors of a PhC laser vs. relative detuning $\Delta\nu \equiv \frac{\omega_0-\omega_a}{\omega_0}$. Upper inset: quarter-wave PhC geometry (see caption of Fig. 3.4). The gain parameters are $\gamma_\perp = 3$ mm^{-1} and a varying ω_a. Lower inset: intensity distribution of the lasing mode. (b) α factor for an open cavity laser vs. passive permittivity ε_c. Blue (red): generalized (traditional) α factor. Upper inset: dielectric slab, of permittivity ε_c, bounded by air on both sides, containing gain atoms with $\omega_a = 15$ mm^{-1}, $\gamma_\perp = 3$ mm^{-1}. Lower inset: intensity distribution of the lasing mode. Leftmost inset: enlarged segment of the main plot, around $\varepsilon_c = 7$.

Our TCMT derivation of the linewidth formula yields a generalized α factor Eq. (3.38) which depends on the eigenmodes $\mathbf{E}_\mu(\mathbf{x})$ and eigenfrequencies ω_μ of the full nonlinear SALT equations. This is an advance over previous linewidth formulas; the *ab-initio* scattering-matrix linewidth formulas did not obtain an α factor [82, 83], whereas other traditional laser theories that derived α factors could not handle the full nonlinear equations [111]. Therefore, in the following section, we focus on the generalized α factor. We compare the generalized and traditional factors in Sec. 3.6.1, and then we evaluate these factors in the single-mode (Sec. 3.6.2) and multimode (Sec. 3.6.3) regimes.

3.6.1 Comparison with traditional α factor

Linewidth broadening due to amplitude–phase coupling (that is, the α factor linewidth enhancement) was first studied in the 1960s by Lax in the context of single-mode detuned gas lasers [79]. The Lax α factor is $1+\alpha_0^2$, where α_0 is the normalized detuning of the lasing frequency from the atomic resonance, i.e., $\alpha_0 = \frac{\omega_0-\omega_a}{\gamma_\perp}$, which is equal to the ratio of the real part of the gain permittivity to its imaginary part, or equivalently the ratio $\frac{\mathrm{Re}\,\Delta n_g}{\mathrm{Im}\,\Delta n_g}$, where Δn_g is the refractive index change due to fluctuations in the gain. Two decades later, Henry derived an amplitude–phase coupling enhancement factor of the same general type in semiconductor lasers [14], $\alpha_0 = \frac{\mathrm{Re}\,\Delta n_g}{\mathrm{Im}\,\Delta n_g}$, but in the latter case these refractive-index changes arise from carrier-density fluctuations and take a different form. Here, we are considering atomic gain media, so our α factor generalizes the Lax form.

The difference between our single-mode generalized α factor Eq. (3.30) and that of Lax arises because we take into account spatial variation in the gain permittivity due to spatial hole-burning and also the non-Hermitian (complex) nature of the lasing mode. Hence we expect our factor to reduce to the Lax factor in some limits. For instance, consider the situation that was discussed in the last paragraph of Sec. 3.2 of a low-loss 1d Fabry-Pérot cavity laser, operating near threshold. In this case, the nonlinear coupling coefficient is approximately $C \approx \frac{-i\omega_0}{2\varepsilon}\frac{\int \frac{\partial\varepsilon}{\partial|a|^2}\mathbf{E}_0^2}{\int \mathbf{E}_0^2}$, and one can show that the generalized α factor is $\widetilde{\alpha} = \frac{\mathrm{Im}\,C}{\mathrm{Re}\,C} \approx \frac{\mathrm{Re}\,\Delta\varepsilon}{\mathrm{Im}\,\Delta\varepsilon}$ (the last approximation is valid since in essentially all realistic cavities, the modes can be chosen to be predominantly real, i.e., have small imaginary parts).

In many cases, however, our $\widetilde{\alpha}$ deviates from the traditional factor α_0. An obvious example is when the lasing frequency precisely coincides with the atomic resonance

frequency. In this case, the traditional factor vanishes, but $\widetilde{\alpha}$ does not necessarily vanish. In the next section, we calculate and discuss the characteristic properties of the generalized α factor for two 1d laser structures.

3.6.2 Generalized single-mode α factor

In this section, we evaluate the differences between the generalized and traditional α factors in 1d model systems. We solve the full nonlinear SALT equations using our recent finite-difference frequency-domain (FDFD) SALT solver [18].

The generalized factor $\widetilde{\alpha}$ can deviate significantly from the traditional factor α_0 when the latter is large (a similar argument was made in [105]). To see this, let us write the nonlinear coupling coefficient qualitatively as $C \propto (1+i\alpha_0)(1+i\beta)$, where the term $1+i\alpha_0$ is associated with the atomic lineshape $\frac{\gamma_\perp}{\omega_0-\omega_a+i\gamma_\perp}$, and the term $1+i\beta$ is a complex factor due to the remaining integral factors (we refer to the latter term as the *modal contribution* to the α factor). Typically $\beta \ll 1$ and, consequently, the generalized factor is approximately $\widetilde{\alpha} \approx \alpha_0 + \beta(1+\alpha_0^2)$, so the difference between the generalized and traditional factors grows quadratically with α_0.

To verify this argument, we study a model system in which the magnitude of α_0 can be controlled. Consider a quarter-wave dielectric photonic crystal (PhC), with a defect at the center of the structure (the geometry is depicted in the upper inset of Fig. 3.5a, similar to the structure that was studied in Fig. 3.4). Adding enough layers of the periodic structure on each side of the defect to mimic an infinite structure, one finds that the system has a localized mode in the vicinity of the defect (lower inset), whose resonance frequency is fixed to a real value within the energy gap [94]. To study finite-threshold lasers, we introduce gain and some passive loss (i.e., a positive

imaginary permittivity term, which pushes the resonance poles away from the real axis in the complex plane). Since the resonance frequency of the defect mode is fixed by the geometry, by varying the resonance frequency of the gain, we control the detuning of the lasing mode from the atomic resonance, thus controlling the size of α_0. As demonstrated in the figure, the deviation $|\widetilde{\alpha} - \alpha_0|$ grows as the detuning $\Delta\nu \equiv \frac{\omega_0 - \omega_a}{\omega_0}$ increases.

The openness of the cavity also results in an enhancement of the α factor; the more open it is, the larger is the necessary imaginary part of the lasing mode, which causes a deviation from the standard formula. In order to test this prediction, we evaluate the generalized α factor for an open-cavity laser (Fig. 3.5b), where we can control the radiative loss rate through the cavity walls and, consequently, this part of the modal contribution to $\widetilde{\alpha}$. We consider a cavity which consists of a dielectric slab (with permittivity ε_c) surrounded by air on both sides, with gain spread homogeneously inside the slab (upper rightmost inset). The reflectivity of the cavity walls is determined by the difference in cavity and air permittivities $\Delta\varepsilon = \varepsilon_c - \varepsilon_0$. For relatively small dielectric mismatch, the cavity is relatively low-Q and our α factor differs significantly from the Lax factor. As $\Delta\varepsilon$ increases and the cavity Q increases, the generalized α factor converges to the original factor, so that the red and blue curves in the figure overlap.

Unlike a photonic-crystal defect-mode cavity where there is a finite bandwidth of confinement [94], this dielectric cavity has an infinite number of possible lasing resonances and thus when we sweep $\Delta\varepsilon$, the α factor peaks periodically. This is because the free spectral range of the cavity is $\Delta\omega \approx \frac{2\pi}{\sqrt{\varepsilon_c}L}$ [140] and, therefore, changing ε_c corresponds to shifting the passive resonances and, consequently, the lasing modes. Every time a lasing mode crosses an atomic resonance, α_0 vanishes and correspondingly $\widetilde{\alpha}$ becomes very small. The traditional factor is maximized when the atomic resonance is equidistant from two passive modes. The peak value is proportional to the free spectral range

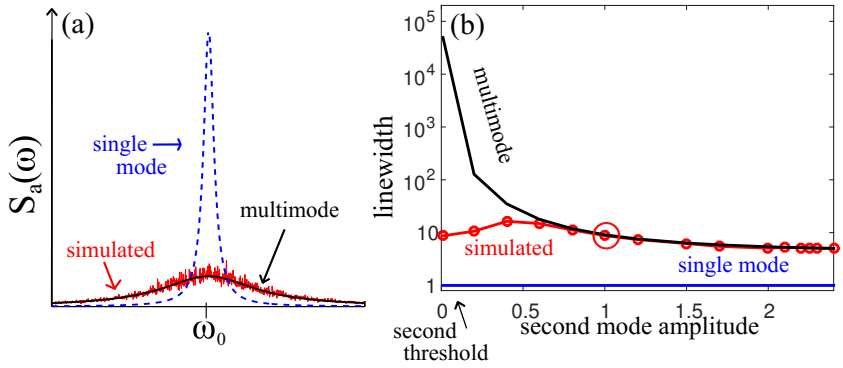

Figure 3.6: (Color online) (a) Spectrum near a resonance peak in the presence of an additional mode. Numerical simulations of Eq. (3.15) (red curve) and analytic single-mode (blue) and multimode (black) formulas. The simulation parameters are chosen so that there are two lasing modes with the same steady-state amplitudes $a_{k0} = 1$ and diffusion coefficients $R_{kk} = 0.05$, and with substantial cross correlations: $C_{kk} = 5, C_{kl} = 4 + 4i, k \neq l$ (in arbitrary frequency units). (b) Linewidth of central resonance peak vs. output power in the neighboring mode [$a_{10} = 1$ and $a_{20} \in (0, 3)$]. Simulated spectrum (red) and analytic single-mode and multimode formulas (blue and black curves). The point $a_{10} = a_{20} = 1$ is encircled, and corresponds to the parameter values of Fig. 3.6a.

and, therefore, we find that it is proportional to $1/\sqrt{\varepsilon_c}$. This type of effect may not have been observed previously because in macroscopic cavities, the cavity resonances are very dense on the scale of the gain bandwidth, so the lasing mode can never be substantially detuned. However, in microcavities with large free spectral range, this could be an important effect. Another intriguing property of the generalized α factor is that it varies discontinuously at the peaks (as is shown more clearly in the upper left-most inset). The traditional factor α_0 depends only on the mode detuning from resonance, so it approaches the same value on different sides of the peak. In contrast, the generalized factor $\widetilde{\alpha}$ depends on the mode profile $\mathbf{E}_\mu$, which differs between the two interchanging laser modes on different sides of the peak, producing the observed asymmetry.

3.6.3 Generalized multimode α factor

Our *multimode* linewidth formula includes linewidth corrections from neighboring modes, which enter through the generalized α factor (since phase fluctuations in each of the modes couple to amplitude fluctuations in all other modes due to saturation of the gain). According to the traditional ST formula Eq. (3.2), when phase cross-correlations between different modes are neglected, each resonance-peak width is inversely proportional to the corresponding modal output power. We find that when phase cross-correlations are included, the linewidth of each mode is a sum of inverse output powers of all the other modes—a type of multimode Schawlow–Townes relation. To see how this comes about, recall that the generalized α factor, as given by Eq. (3.38), is proportional to $\left[\mathbb{B}\mathbb{A}^{-1}\,\mathbb{R}\,\left(\mathbb{B}\mathbb{A}^{-1}\right)^{T}\right]_{ii}$. We show in Sec. 3.11 that individual factors in the product scale as $[\mathbb{B}\mathbb{A}^{-1}]_{ij} \propto \frac{a_{i0}}{a_{j0}}$, where a_{j0} is the steady-state amplitude of the j'th mode. Therefore, the multimode α factor is proportional to the sum: $a_{i0}^2 \sum_j \frac{(\text{const})\times R_{jj}}{a_{j0}^2}$, i.e., a sum over terms which scale as inverse output powers.

In the two-mode case, the linewidth formula for a lasing mode in the presence of a neighboring mode is given explicitly by

$$\Gamma_1 = \frac{R_{11}}{2a_{10}^2} + \frac{R_{11}}{2a_{10}^2}\left[\frac{C_{11}^{\mathrm{I}}C_{22}^{\mathrm{R}} - C_{21}^{\mathrm{I}}C_{21}^{\mathrm{R}}}{C_{11}^{\mathrm{R}}C_{22}^{\mathrm{R}} - C_{12}^{\mathrm{R}}C_{21}^{\mathrm{R}}}\right]^2 + \frac{R_{22}}{2a_{20}^2}\left[\frac{C_{11}^{\mathrm{R}}C_{12}^{\mathrm{I}} - C_{11}^{\mathrm{I}}C_{12}^{\mathrm{R}}}{C_{11}^{\mathrm{R}}C_{22}^{\mathrm{R}} - C_{12}^{\mathrm{R}}C_{21}^{\mathrm{R}}}\right]^2, \tag{3.43}$$

where $C_{ij}^{\mathrm{R}} \equiv \mathrm{Re}\, C_{ij}$ and $C_{ij}^{\mathrm{I}} \equiv \mathrm{Im}\, C_{ij}$. (A similar expression was derived in [100], by using a phenomenological version of the two-mode TCMT equations.) As predicted by the multimode ST relation, the last term in Eq. (3.43) is inversely proportional to the output power of the second mode a_{20}^2. This term becomes significant when the power in the first mode greatly exceeds the power in the second mode (i.e., when

$P_1 \gg P_2$), correcting the unrealistic Schawlow–Townes prediction that the linewidth vanishes when $P_1 \to \infty$; a similar argument was made in [100]. Fig. 3.6a presents the spectrum of a two-mode instantaneous model Eq. (3.15) in the parameter regime where cross-correlations between the two modes are significant. The linewidth of the simulated spectrum (red curve) is in complete agreement with the generalized formula Eq. (3.43) (black curve), but deviates substantially from the single-mode formula Eq. (3.29) (blue curve). In order to reach the regime where this deviation is substantial, in practice, one needs to design a cavity in which the two lasing modes have comparable amplitudes and detunings from the atomic resonance frequency.

Eq. Eq. (3.43) predicts an unphysical divergence near the second threshold, i.e., when $a_{20} \to 0$ (see black curve in Fig. 3.6b). In retrospect, this singularity is to be expected, since the assumptions of our derivation break down in this limit. (Note that an equivalent divergence was present in [100].) In calculating the phase variance, we assumed that amplitude fluctuations in all modes were small compared to the steady-state amplitudes ($\delta_{\mathrm{I}} \ll a_{i0}$), and this assumption is no longer valid near threshold. The N-SALT TCMT equations Eq. (3.11) are still valid, however—it is only their analytical solution for $\left\langle \mathbf{\Phi}\mathbf{\Phi}^T \right\rangle$ that is problematic. Therefore, we study the threshold regime numerically, via stochastic simulations of the N-SALT TCMT equations. As shown in Fig. 3.6b, the simulated linewidth of the first mode approaches a finite value near the second threshold (red curve), and this value is significantly larger than the linewidth prediction one obtains when neglecting the second mode (blue curve). Even at the threshold, noise in the second mode mixes with the first mode through off-diagonal nonlinear coupling terms, thus increasing the linewidth.

Linewidth enhancement at the thresholds of neighboring lasing-modes suggests that the linewidth must also be enhanced *below* the modal thresholds [in the regime where

radiation from non-lasing modes is incoherent, commonly called amplified spontaneous emission (ASE)]. We believe that this phenomenon could be explored using a future generalization of our formalism, with some modifications (extending earlier work [101, 21] on linewidth enhancement from ASE).

3.7 Full-vector 3d example

In order to illustrate the full generality of our approach, we apply it in this section to study a three-dimensional photonic-crystal (PhC) laser. The steady-state properties of this system (i.e., the lasing threshold and mode characteristics) were previously explored in [18]. We use those solutions here to calculate the laser linewidth [using Eq. (3.3)], and we compare the relative contributions of the various correction factors.

The simulated PhC consists of a dielectric slab patterned by a hexagonal lattice of air holes (Fig. 3.7a). A defect is introduced by decreasing the radii of seven holes at the center of the structure [141], giving rise to a doubly-degenerate mode which is situated at the defect (spatially) and in the bandgap of the lattice (spectrally). We select the TE-like mode out of the degenerate pair by imposing even and odd reflection symmetry at $x = 0$ and $y = 0$ respectively, as well as an even reflection symmetry at $z = 0$. Staying close to a potential experimental realization, we choose the pump profile to be uniform inside the high-index dielectric near the defect region, and zero elsewhere. We solve the SALT equations using our scalable FDFD solver, and track the evolution of the first lasing mode upon increasing the pump strength from zero to five times the first-threshold value.

Typically, realistic laser structures do not use 2-level gain media, but employ a more complex optical scheme which involves multiple levels and transitions in order to achieve

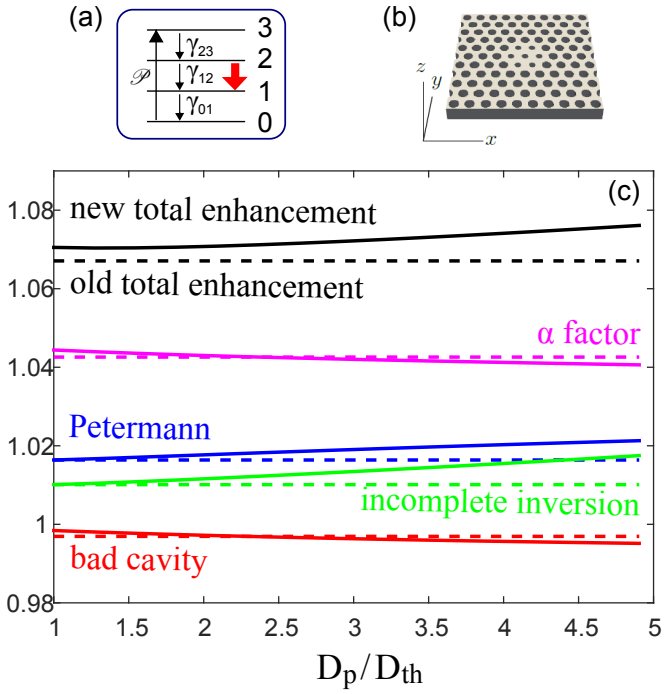

Figure 3.7: (Color online) Linewidth correction factors for a 3d PhC laser. (a) The PhC consists of a hexagonal lattice of air holes (with period $a = 1$ mm and radius 0.3 mm) in a dielectric medium with index $n = \sqrt{\varepsilon_c} = 3.4$. The slab has a thickness of 0.5 mm, with air above and below, terminated by PML absorbers. A cavity is formed by seven holes of radius of 0.2 mm. The pump is non-zero in the hexagonal region for height 2mm in the z-direction. (Borrowed from [18].) (b) Schematics of a 4-level gain medium. Levels $|1\rangle$ and $|2\rangle$ form the lasing transition, with resonance frequency $\omega_a = 1.5$ mm^{-1} and polarization decay $\gamma_\perp = 2.0$ mm^{-1}. The population decay rates are $\gamma_{01}/\gamma_{12} = \gamma_{23}/\gamma_{12} = 10^2$ and $\gamma_{12}/\gamma_\perp = 10^{-2}$. The pump rate $\mathscr{P}$ is varied in the range $\mathscr{P}/\gamma_{12} = 0.4 \ldots 2.2$. (c) Traditional (dashed) and generalized (solid) correction factors, as defined in Table. 3.1. The total correction is defined as the product of the (traditional and generalized) Petermann, α, bad-cavity, and incomplete-inversion factors. The x axis is the D_p/D_{th}, where D_p is the SALT effective pump parameter (see text) and D_{th} is the effective threshold pump.

significant inversion and depletion of the ground-state population. In this section, we apply our formalism to a 4-level gain medium (Fig. 3.7b), using a generalization of SALT [130], which finds the stationary multimode lasing properties of an N-level gain medium. As shown in [130], an N-level system can be mapped into an effective 2-level system, which obeys the (2-level) SALT equations with renormalized pump ($D_{\rm p}$) and atomic relaxation rates ($\gamma_{\parallel}$). Consequently, the linewidth of a 4-level laser will given by our generalized formula Eq. (3.3) with the appropriately renormalized coefficients. By choosing the decay rate between the lasing transition levels (γ_{12} in Fig. 3.7b) to be much smaller than the decay rates into the upper (γ_{23}) and out of the lower (γ_{01}) states, we can achieve substantial inversion and ground-state depletion. Consequently, the incomplete-inversion factor is approximately $n_{\rm sp} \approx 1$, close to typical measured values [108].

Fig. 3.7c presents the traditional and new correction factors (dashed and solid lines respectively), as defined in Table. 3.1. We find that those factors are relatively small for this system and, consequently, the deviations between the new and traditional factors are small. A small Petermann factor arises since the first lasing mode has a relatively high quality factor (i.e., the cold-cavity resonance pole is at $\omega_0 = 1.725 - 0.00512i$ mm^{-1} with a quality factor of $Q \approx 700$, in agreement with experimental realization [141]). Moreover, the cold-cavity resonance lies well within the gain bandwidth, resulting in small α and bad-cavity corrections. The generalized factor $\widetilde{\alpha}$ (solid purple line) is obtained from from Eqs. (3.17) and (3.30). Deviations of $\widetilde{\alpha}$ from the traditional factor $\alpha_0 \equiv \frac{|\omega_0 - \omega_{\rm a}|}{\gamma_\perp}$ (dashed purple line) are due to modal contributions to the α factor (see Sec. 3.6.2). The generalized Petermann factor (full blue curve) is compared against the traditional factor (dashed blue line), which is expressed in terms of the SALT mode (instead of the passive cavity mode). The cavity region is taken to be the entire high-

index medium. (Note the the generalized and traditional factors agree at threshold). Both the Petermann and α factors increase the linewidth. However, the generalized and traditional bad-cavity factors (full and dashed red curves respectively) lead to linewidth reduction.

Last, we evaluate the incomplete-inversion factor $\widetilde{n}_{\rm sp}$. The inversion $D(x)$ is found from the SALT solutions of the effective 2-level system. The excited state population $N_2(x)$ can be derived straightforwardly, using the results of [130] as follows. Assuming that the populations in the non-lasing levels $|0\rangle$ and $|3\rangle$ are at steady-state, one can express those populations in terms of the populations in the lasing transition $|1\rangle$ and $|2\rangle$. Then, by invoking the density conservation condition, $\sum_i N_{\rm I} = n$, where n is the atom number density and $N_{\rm I}$ are the individual level populations, one finds that the population in $|2\rangle$ is given by

$$N_2 = \frac{n + \tau D}{1 + \tau}, \tag{3.44}$$

where $\tau \equiv 1 + \frac{2\gamma_{01}}{\gamma_{23}} + \frac{\gamma_{01}}{\mathscr{P}}$. Having obtained expressions for D and for N_2, we have all that is needed to calculate the incomplete-inversion factor $\widetilde{n}_{\rm sp}$. We define the "linear incomplete-inversion factor" ($n_{\rm sp}$ dashed green line) as the ratio $\frac{N_2(D_{\rm p})}{D_{\rm p}}$, [i.e., both the excited-state population Eq. (3.44) and the inversion are evaluated at $D = D_{\rm p}$, neglecting hole-burning effects]. The "nonlinear incomplete-inversion factor" ($\widetilde{n}_{\rm sp}$ solid green line) is defined in Table. 3.1. The nonlinear factor $\widetilde{n}_{\rm sp}$ coincides with the linear factor $n_{\rm sp}$ at threshold, but exceeds the traditional factor at higher pumps. We also plot the total linewidth correction, which is defined as the product of the (traditional and new) Petermann, α, bad-cavity, and incomplete-inversion factors.

3.8 Concluding Remarks

We presented a generalized multimode linewidth formula, obtained from the N-SALT TCMT equations for the lasing mode amplitudes, which we derived starting from the Maxwell–Bloch equations and using the fluctuation–dissipation theorem to determine the statistical properties of the noise. Our generalized linewidth formula Eq. (3.3) reduces to the traditional formula Eq. (3.2) for low-loss cavities and simple lasing structures, but deviates significantly from the traditional theories for high-loss wavelength-scale laser cavities. By basing our derivation on the SALT steady-state lasing modes, it is possible to apply our formula to cavities of arbitrarily complex geometry (e.g., photonic crystal or microdisk lasers [84, 85, 86, 87]) and arbitrary openness (e.g. random lasers [104]). Also, since SALT includes to high accuracy the effects of spatial hole-burning, our formula includes both gain saturation and the spatial variation of the gain permittivity well above threshold, plus all effects due to modal couplings. From a computational point of view it is important to point out that our formula is analytical and can be evaluated immediately from the output of a numerical SALT calculation without any significant computational effort. A manuscript describing a brute-force numerical validation of our theory against numerical solution of the Maxwell–Bloch equations is currently being prepared [102]. Given only the laser geometry, the pumping profile, and characteristic properties of the gain (i.e., its resonance frequency ω_a and decay rate $\gamma_\perp$), our formula enables linewidth calculation, including a generalized α-factor and accounting for temperature variations, at a level of generality that was not possible before. This generality is most important, of course, in cases where the new result is substantially different than previous theories, and it would be interesting to study laser cavities in which the discrepancy is as large as possible.

One such case is that of lasers which contain exceptional points (EPs) in their spectrum, which are points of degeneracy where two (or more) eigenfrequencies and eigenfunctions coalesce [142, 33]. EPs in laser systems have been explored recently, both theoretically [143] and experimentally [144]. At the EP, the modes become self-orthogonal and that causes the denominator of Eq. (3.3) to vanish and is already known to greatly enhance the Petermann factor [42]. Since a similar denominator appears in the integrals defining our generalized α factor Eqs. (3.12) and (3.30), we expect that our $\widetilde{\alpha}$ will differ substantially from previous results near an EP (and similarly for the inhomogeneous-temperature correction).

An important and exciting addition to the theory would be a treatment of amplified spontaneous emission (ASE) from modes below threshold; we believe this can be achieved by deriving TCMT equations for below-threshold (passive) modes, in which there is no steady-state oscillation (generalizing previous ASE work which used simplified models [21, 101]). Incorporating the ASE contribution to the spectrum will allow us to follow the noise through the lasing thresholds, correcting the unphysical divergence which was discussed in Sec. 3.6.2. More importantly, treating below threshold ASE should allow an ab-initio theory of LEDs in arbitrary cavities

Future work could also incorporate several additional corrections that were not treated in this chapter. Our derivation applies to isotropic materials described by a scalar permittivity ε, but extension to anisotropic permittivity $\hat{\varepsilon}$, magnetic permeability ($\hat{\mu}$), and even bianisotropic materials would be very straightforward (e.g., for an anisotropic $\hat{\varepsilon}$, the only change is that $\varepsilon\mathbf{E}^2$ factors and similar are replaced by $\mathbf{E}\cdot(\hat{\varepsilon}\mathbf{E})$ etcetera, as in [10]). As discussed in Sec. 3.5.3, we are also able to exploit our framework to analytically solve for the relaxation-oscillation side-peak spectra (see Ch. 5). We believe it will be possible to extend our formalism to handle non-Lorentzian lineshapes arising from frequency de-

pendence (correlations) in the noise within the laser linewidth [120, 121, 122, 123, 124], as also discussed in Sec. 3.4. Instead of treating the noise spectrum $S_{\mathbf{F}}(\omega)$ as a constant $S_{\mathbf{F}}(\omega_\mu)$, one needs to include a first-order correction , e.g., by Taylor expanding $S_{\mathbf{F}}(\omega)$ around ω_μ; it might be convenient to fit $S_{\mathbf{F}}(\omega)$ to a Lorentzian matching the amplitude and slope at ω_μ, since the Fourier transform of a Lorentzian is an exponential that should be easy to integrate. Finally, as noted above, although our derivation was for the two-level Maxwell–Bloch equations, a similar approach should apply to more complex gain media (including multi-level atoms [130], multiple lasing transitions, and gain diffusion [131].) The N-SALT linewidth theory can be generalized to account for these laser models following along the lines of our approach here.

3.9 Appendix A: Derivation of the oscillator equations

In this appendix, we derive the TCMT equations for the lasing mode amplitudes. Our starting point is the Maxwell–Bloch equations [53, 55], which describe the dynamics of the electromagnetic field in a resonator interacting with a two-level gain medium:

$$\nabla \times \nabla \times \mathbf{E} + \varepsilon_{\mathrm{c}}\, \ddot{\mathbf{E}} = -4\pi \ddot{\mathbf{P}} + \mathbf{F}_{\mathrm{S}}, \tag{3.45}$$

$$\dot{\mathbf{P}} = -i(\omega_{\mathrm{a}} - i\gamma_\perp)\mathbf{P} - \frac{i\gamma_\perp}{4\pi}\mathbf{E}D, \tag{3.46}$$

$$\dot{D} = -\gamma_\parallel \left[D_{\mathrm{p}} - D + 2\pi i(\mathbf{E}\cdot\mathbf{P}^* - \mathbf{E}^*\cdot\mathbf{P})\right], \tag{3.47}$$

where $\mathbf{E}$ is the electromagnetic field, while $\mathbf{P}$ and D are the atomic polarization and population inversion. (From here on, for brevity, we refer to D as the "inversion.") ω_{a} is the atomic resonance frequency, and $\gamma_\perp$ and $\gamma_\parallel$ are the population and inversion relaxation rates. D_{p} is the external pump, which determines the steady-state inversion, and

ε_c is the passive dielectric permittivity. The field, polarization and inversion are measured in their natural units: $e_c = p_c = \hbar\sqrt{\gamma_\parallel \gamma_\perp}/(2g)$ and $d_c = \hbar\gamma_\perp/(4\pi g^2)$ respectively, where g is the atomic dipole matrix element [56, 57, 18]. We introduce spontaneous emission noise by including a random source term $\mathbf{F}_\mathrm{S} = 4\pi\frac{\partial \mathbf{J}}{\partial t}$ in Eq. (3.45), written in the frequency domain as

$$\widehat{\mathbf{F}}_\mathrm{S}(\mathbf{x},\omega) = -i4\pi\omega\widehat{\mathbf{J}}(\mathbf{x},\omega), \tag{3.48}$$

where $\widehat{\mathbf{J}}(\mathbf{x},\omega)$ is a random fluctuating current, and the correlations of $\widehat{\mathbf{F}}_\mathrm{S}(\mathbf{x},\omega)$ are given by the FDT.

Steady-state ab-initio laser theory (SALT) handles the noise-free regime of the Maxwell–Bloch equations (i.e., $\widehat{\mathbf{F}}_\mathrm{S} = 0$) and reduces this set of coupled equations to a frequency-domain nonlinear generalized eigenvalue problem for the electric field $\widehat{\mathbf{E}}$ (as reviewed in Sec. 1.1). When noise is introduced ($\widehat{\mathbf{F}}_\mathrm{S} \neq 0$), the cavity field is perturbed from steady-state and the nonlinear permittivity is modified (Sec. 1.2). This gives rise to a restoring force (denoted $\widehat{\mathbf{F}}_\mathrm{NL}$), which we calculate in Sec. 1.3. The noise-driven field $\widehat{\mathbf{E}}$ is then found by integrating the Green's function (derived in Sec. 1.4) over the noise terms $\widehat{\mathbf{F}}_S$ and $\widehat{\mathbf{F}}_\mathrm{NL}$. Finally, the TCMT equations are obtained by transforming back into the time domain (Sec. 1.5).

3.9.1 Review of SALT

We begin by reviewing the steady-state theory. In the SALT approach, the steady-state electromagnetic field is expressed as a superposition of a finite number of lasing modes:

$$\mathbf{E}_0(\mathbf{x},t) = \sum_\mu \mathbf{E}_\mu(\mathbf{x}) a_{\mu 0} e^{-i\omega_\mu t}, \tag{3.49}$$

where $\mathbf{E}_0(\mathbf{x}, t)$ denotes the steady-state field and $a_{\mu 0}$ are the steady-state modal amplitudes. The lasing modes $\mathbf{E}_\mu(\mathbf{x})$ are real frequency solutions of the nonlinear eigenvalue problem

$$\left[\nabla \times \nabla \times -\omega_\mu^2 \widehat{\varepsilon}_0(\omega_\mu, a_0)\right] \mathbf{E}_\mu(\mathbf{x}) = 0, \tag{3.50}$$

with outgoing boundary conditions. The effective permittivity has a linear (passive) term ε_{c} and a nonlinear (**E**-dependent) gain term:

$$\widehat{\varepsilon}_0(\omega, a_0) = \varepsilon_{\mathrm{c}} + \frac{\gamma_\perp}{\omega - \omega_{\mathrm{a}} + i\gamma_\perp} D_0(a_0). \tag{3.51}$$

The steady-state inversion $D_0(a_0)$ [which is a notation shortcut for $D_0(\{\mathbf{E}_\mu\}, \{\omega_\mu\}, \{a_{\mu 0}\})$] is given by

$$D_0(a_0) = \frac{D_{\mathrm{p}}}{1 + \sum_\mu \frac{\gamma_\perp^2}{(\omega_\mu - \omega_{\mathrm{a}})^2 + \gamma_\perp^2} |a_{\mu 0}|^2 |\mathbf{E}_\mu|^2}. \tag{3.52}$$

To avoid possible confusion, note that in previous SALT works, the steady-state inversion was denoted by D and D_0 was the external pump parameter, whereas in this work, D_0 is the steady-state inversion and D_{p} is the external pump parameter.

3.9.2 Noise-driven Maxwell-Bloch equations

In the presence of a small noise source, the electric field and polarization can be written as superpositions of the steady-state lasing modes with time-dependent amplitudes $a_\mu(t)$

and $b_\mu(t)$:

$$\mathbf{E}(\mathbf{x},t) = \sum_\mu \mathbf{E}_\mu(\mathbf{x}) a_\mu(t) e^{-i\omega_\mu t}$$
$$\mathbf{P}(\mathbf{x},t) = \sum_\mu \mathbf{P}_\mu(\mathbf{x}) b_\mu(t) e^{-i\omega_\mu t}. \tag{3.53}$$

Substituting the perturbation ansatz Eq. (5.2) into the polarization equation Eq. (3.46), we obtain

$$(\dot{b}_\mu + i\omega_\mu b_\mu)\mathbf{P}_\mu = -i(\omega_\mathrm{a} - i\gamma_\perp) b_\mu \mathbf{P}_\mu - \frac{i\gamma_\perp a_\mu}{4\pi}\mathbf{E}_\mu D. \tag{3.54}$$

Taking the Fourier transform and rearranging terms, we find

$$\widetilde{B}_\mu \mathbf{P}_\mu = \frac{1}{4\pi}\frac{\gamma_\perp}{\omega - \omega_\mathrm{a} + i\gamma_\perp}\widehat{a}_\mu * \widehat{D}\mathbf{E}_\mu, \tag{3.55}$$

where we have introduced the shifted frequency $\omega \equiv \omega_\mu + \Omega$ and the Fourier-domain envelopes $\widehat{a}_\mu(\Omega) = \widehat{a}_\mu(\omega - \omega_\mu)$, $\widetilde{B}_\mu(\Omega)$ and $\widehat{D}(\Omega)$. The asterisk * denotes a convolution.

Next, consider Eq. Eq. (3.45) in the frequency domain

$$\nabla \times \nabla \times \widehat{\mathbf{E}} - \omega^2 \varepsilon_\mathrm{c} \left(\widehat{\mathbf{E}} + 4\pi\widehat{\mathbf{P}}\right) = \widehat{\mathbf{F}}_\mathrm{S}. \tag{3.56}$$

When the spacing between adjacent lasing modes is much larger than their linewidths, a noise source with frequency $\omega \approx \omega_\mu$ excites only the mode $\mathbf{E}_\mu(\mathbf{x})$. Equivalently, the Green's function can be approximated by the contribution of the single pole at ω_μ. (Note that we require only that the peaks in the laser spectrum above threshold are non-overlapping; we do not require isolated resonances in the passive cavity spectrum.) Therefore, at frequencies $\omega \approx \omega_\mu$, we can substitute Eq. (3.55) into Eq. (3.56) and

obtain an effective equation for the noise-driven field $\widehat{\mathbf{E}}_\mu(\mathbf{x},\omega)$:

$$\left[\nabla\times\nabla\times-\omega^2\varepsilon(\omega,a)\right]\widehat{\mathbf{E}}_\mu(\mathbf{x},\omega)=\widehat{\mathbf{F}}_{\mathrm{S}}(\mathbf{x},\omega), \tag{3.57}$$

where the effective permittivity $\varepsilon(\omega,a)$ is given by

$$\varepsilon(\omega,a)\widehat{\mathbf{E}}_\mu(\mathbf{x},\omega)=\left[\varepsilon_{\mathrm{c}}\widehat{a}_\mu+\frac{\gamma_\perp}{\omega-\omega_{\mathrm{a}}+i\gamma_\perp}\widehat{D}*\widehat{a}_\mu\right]\mathbf{E}_\mu(\mathbf{x}). \tag{3.58}$$

The second variable of $\varepsilon(\omega,a)$ denotes the implicit dependence of ε on the modal amplitudes a_μ through the Fourier transform of the inversion $\widehat{D}$. We calculate $\widehat{D}$ explicitly in the next section.

3.9.3 The nonlinear force term

The noise source $\widehat{\mathbf{F}}_{\mathrm{S}}$ perturbs the modal amplitudes a_ν from steady state, causing a change in the atomic inversion D. We neglect dispersion corrections to D (which amounts to setting $\dot{b}_\mu=0$ in Eq. (3.54) [98]) as these corrections do not affect the linewidth formula to leading order in the noise [see discussion following Eq. (3.9) in the main text]. From Eq. (3.47) and Eq. (3.54), we obtain

$$\dot{D}=-\gamma_\parallel\left[D-D_{\mathrm{p}}+\textstyle\sum_\nu\frac{\gamma_\perp^2}{(\omega_\nu-\omega_{\mathrm{a}})^2+\gamma_\perp^2}\,|a_\nu|^2D\,|\mathbf{E}_\nu|^2\right]. \tag{3.59}$$

In order to solve Eq. (3.59), we linearize the time dependent products $|a_\nu|^2D$ in the sum around the steady state $|a_\nu|^2D\approx a_{\nu0}^2D_0+D_0(|a_\nu|^2-a_{\nu0}^2)+a_0^2(D-D_0)$, where D_0 is the steady state (SALT) inversion Eq. (3.52). To simplify the notation, we define the

local decay rate

$$\gamma(\mathbf{x}) \equiv \gamma_{\parallel}\left(1+\sum_{\nu}\frac{\gamma_{\perp}^{2}}{(\omega_{\nu}-\omega_{\mathrm{a}})^{2}+\gamma_{\perp}^{2}}\,|a_{\nu 0}|^{2}|\mathbf{E}_{\nu}|^{2}\right). \tag{3.60}$$

The second term in Eq. (3.60) gives precisely the increased atomic decay rate due to stimulated emission. Using the definitions above , Eq. (3.59) becomes

$$\dot{D} = -\gamma(\mathbf{x})(D-D_{0}) - \gamma_{\parallel}D_{0}\cdot\sum_{\nu}\frac{\gamma_{\perp}^{2}}{(\omega_{\nu}-\omega_{\mathrm{a}})^{2}+\gamma_{\perp}^{2}}\,|\mathbf{E}_{\nu}|^{2}(|a_{\nu}|^{2}-|a_{\nu 0}|^{2}), \tag{3.61}$$

which we can integrate, and obtain

$$D = D_{0}+\sum_{\nu}D_{0}\left(\frac{\gamma_{\perp}^{2}}{(\omega_{\nu}-\omega_{\mathrm{a}})^{2}+\gamma_{\perp}^{2}}|\mathbf{E}_{\nu}|^{2}\right)\times\gamma_{\parallel}\int^{t}dt' e^{-\gamma(\mathbf{x})(t-t')}(|a_{\nu 0}|^{2}-|a_{\nu}(t')|^{2}). \tag{3.62}$$

Having derived an explicit expression for $D(t)$, we substitute its Fourier transform $\widehat{D}$ into the effective permittivity Eq. (3.58) and obtain

$$\varepsilon(\omega,a)\widehat{\mathbf{E}}_{\mu} \approx \varepsilon(\omega,a_{0})\widehat{\mathbf{E}}_{\mu}+\sum_{\nu}\chi_{\nu}(\omega,a_{0})\widehat{\Delta a_{\nu}}*\widehat{\mathbf{E}}_{\mu}, \tag{3.63}$$

where $\varepsilon(\omega,a_{0})$ is the steady-state SALT permittivity which was defined in Eq. (3.51), $\chi_{\nu}(\omega,a_{0})$ is the permittivity differential due to deviation in the modal amplitude a_{ν} [which we denote by "$\frac{\partial\varepsilon}{\partial|a|^{2}}$" in the text, e.g., in Eq. (3.12)]:

$$\chi_{\nu} \equiv \frac{\gamma_{\perp}}{\omega-\omega_{\mathrm{a}}+i\gamma_{\perp}}D_{0}\left(\frac{\gamma_{\perp}^{2}}{(\omega_{\nu}-\omega_{\mathrm{a}})^{2}+\gamma_{\perp}^{2}}|\mathbf{E}_{\nu}|^{2}\right)\frac{\gamma_{\parallel}}{\gamma(\mathbf{x})}, \tag{3.64}$$

and $\widehat{\Delta a_{\nu}}$ is the Fourier transform of the time-averaged modal deviation from steady

state

$$\Delta a_\nu = \gamma(\mathbf{x}) \int^t dt' e^{-\gamma(\mathbf{x})(t-t')}(|a_{\nu 0}|^2 - |a_\nu(t')|^2). \tag{3.65}$$

Substituting the permittivity expansion Eq. (3.63) into Maxwell's equation Eq. (3.57), we obtain

$$\left[\nabla \times \nabla \times -\omega^2 \varepsilon(\omega, a_0)\right] \widehat{\mathbf{E}}_\mu(\mathbf{x}, \omega) = \widehat{\mathbf{F}}_{\mathrm{NL}}(\mathbf{x}, \omega) + \widehat{\mathbf{F}}_{\mathrm{S}}(\mathbf{x}, \omega), \tag{3.66}$$

where the nonlinear restoring force is

$$\widehat{\mathbf{F}}_{\mathrm{NL}}(\mathbf{x}, \omega) = \omega^2 \sum_\nu \chi_\nu(\omega, a_0) \widehat{\Delta a_\nu} * \widehat{\mathbf{E}}_\mu(\mathbf{x}, \omega). \tag{3.67}$$

The left-hand side of Eq. (3.66) is just the linearized steady-state equation Eq. (3.50), and the nonlinear correction to the effective permittivity due to the noise $\widehat{\mathbf{F}}_{\mathrm{S}}$ appears as an additional source term $\widehat{\mathbf{F}}_{\mathrm{NL}}$. As noted above, the noise-driven field $\widehat{\mathbf{E}}_\mu$ is found by integrating the Green's function of the steady-state equation Eq. (3.50) over the noise terms $\widehat{\mathbf{F}}_{\mathrm{NL}}$ and $\widehat{\mathbf{F}}_S$. In the following section we derive an approximate formula for the Green's function.

3.9.4 The linearized Green's function

The single-pole approximation of the Green's function is valid for frequencies near the resonances $\omega \approx \omega_\mu$ as long as the spectrum consists of non-overlapping resonance peaks, i.e., when the spacing between resonant modes exceeds the modal linewidths. First, let us rewrite the left-hand side of Eq. (3.50) as an operator $\mathcal{L}_\omega$ acting on the field $\mathbf{E}(\mathbf{x}, \omega)$:

$$\mathcal{L}_\omega \mathbf{E}(\mathbf{x}, \omega) \equiv \left(\nabla \times \nabla \times -\omega^2 \widehat{\varepsilon}_0(\omega, a_0)\right) \mathbf{E}(\mathbf{x}, \omega). \tag{3.68}$$

Next, we choose a complete set (see below) of eigenfunctions $\mathbf{E}_n(\mathbf{x},\omega)$ and eigenvalues $\lambda_n(\omega)$ of the operator $\mathcal{L}_\omega$:

$$\mathcal{L}_\omega \mathbf{E}_n(\mathbf{x},\omega) = \lambda_n(\omega)\mathbf{E}_n(\mathbf{x},\omega). \tag{3.69}$$

We define the inner product of two vector fields, $\mathbf{A}(\mathbf{x})$ and $\mathbf{B}(\mathbf{x})$, as $(A,B) \equiv \int dx\ \mathbf{A}(\mathbf{x})\cdot \mathbf{B}(\mathbf{x})$. The operator $\mathcal{L}_\omega$ is complex symmetric under this inner product, i.e., $(A,\mathcal{L}_\omega B) = (\mathcal{L}_\omega A, B)$ [94, 33]. Therefore, we use unconjugated inner products throughout the derivation. In order to treat the set $\{\mathbf{E}_n\}$ as a discrete (countable) basis, a convenient theoretical trick is to place the system in a box with absorbing boundary layers in which the absorption turns on more and more gradually. This procedure also gives the states $\mathbf{E}_n$ finite norms (E_n, E_n). Because the operator is non-Hermitian, completeness of the basis can break down at an "exceptional point" [142, 33], but exceptional points are not generically present—they must be forced by careful tuning of parameters. Therefore, we assume completeness in this manuscript and will treat the influence of exceptional points (self-orthogonal modes) as a limiting case in future work, as discussed in Sec. 3.8.

Let $G(\omega,\mathbf{x},\mathbf{x}')$ be the Green's function of the operator $\mathcal{L}_\omega$, defined via $\mathcal{L}_\omega G(\omega,\mathbf{x},\mathbf{x}') = \delta(\mathbf{x}-\mathbf{x}')$ [145]. Given the complete set of eigenfunctions and eigenvalues $\{\mathbf{E}_n,\lambda_n\}$, the Green's function can be expressed as the sum [145]

$$G(\omega,\mathbf{x},\mathbf{x}') = \sum_n \frac{\mathbf{E}_n(\mathbf{x})\mathbf{E}_n^T(\mathbf{x}')}{\lambda_n(\omega)\cdot\int dx\ \mathbf{E}_n^2(\mathbf{x})}. \tag{3.70}$$

Each lasing mode is associated with an eigenvalue $\lambda_\mu(\omega)$ of $\mathcal{L}_\omega$, which has a zero at a real frequency $\omega = \omega_\mu$. Consequently, $G(\omega,\mathbf{x},\mathbf{x}')$ has a pole at ω_μ and at frequencies

near ω_μ, it is dominated by a single term in the sum. Expanding $\lambda_\mu(\omega)$ around the pole $\lambda_\mu(\omega) \approx (\omega - \omega_\mu)\lambda'_\mu$ (where $\lambda'_\mu \equiv \frac{\partial\lambda}{\partial\omega}\big|_{\omega_\mu}$), we obtain

$$G_{\mu\mu}(\omega, \mathbf{x}, \mathbf{x}') \approx \frac{\mathbf{E}_\mu(\mathbf{x})\mathbf{E}_\mu^T(\mathbf{x}')}{(\omega - \omega_\mu)\lambda'_\mu \cdot \int dx\ \mathbf{E}_\mu^2(\mathbf{x})}. \tag{3.71}$$

In order to evaluate λ'_μ, let us rewrite $\mathcal{L}_\omega$ as $\mathcal{L}_\omega \approx \mathcal{L}_{\omega_\mu} + V(\omega)$, where $\mathcal{L}_{\omega_\mu} \equiv \nabla \times \nabla \times -\omega_\mu^2 \widehat{\varepsilon}_0(\omega_\mu)$ and $V(\omega) \equiv -\left[\omega^2 \widehat{\varepsilon}_0(\omega)\right]'_\mu (\omega - \omega_\mu)$. According to the Hellmann–Feynman theorem, the derivative of the eigenvalue $\lambda_\mu(\omega)$ with respect to ω is given by

$$\lambda'_\mu = \frac{\int dx\ \mathbf{E}_\mu^2(\mathbf{x})\left[-\omega^2 \widehat{\varepsilon}_0(\omega)\right]'_\mu}{\int dx\ \mathbf{E}_\mu^2(\mathbf{x})}, \tag{3.72}$$

and substituting Eq. (3.72) in Eq. (3.71), we find that for frequencies near the resonances $\omega \approx \omega_\mu$, the Green's function is approximately

$$G_{\mu\mu}(\mathbf{x}, \mathbf{x}', \omega) \approx \frac{\mathbf{E}_\mu(\mathbf{x})\mathbf{E}_\mu^T(\mathbf{x}')}{(\omega_\mu - \omega)\int dx\ \mathbf{E}_\mu^2(\mathbf{x})\left[\omega^2 \widehat{\varepsilon}_0(\omega)\right]'_\mu}. \tag{3.73}$$

3.9.5 The oscillator equations

Having derived an expression for the Green's function, the noise-driven field can be found by integrating the Green's function over the source terms $\widehat{\mathbf{F}}_{\mathrm{NL}}(\mathbf{x}', \omega)$ and $\widehat{\mathbf{F}}_{\mathrm{S}}(\mathbf{x}', \omega)$:

$$\widehat{\mathbf{E}}_\mu(\mathbf{x}, \omega) = \sum_\nu \omega_\mu^2 \int dx' G(\mathbf{x}, \mathbf{x}', \omega)\chi_\nu(\omega_\mu, a_0)\widehat{\Delta a_\nu} * \widehat{\mathbf{E}}_\mu + \int dx' G(\mathbf{x}, \mathbf{x}', \omega)\widehat{\mathbf{F}}_{\mathrm{S}}. \tag{3.74}$$

In the first term on the right-hand side, we approximate $\omega \approx \omega_\mu$ because the correction term is $\mathcal{O}\left[(\omega-\omega_\mu)\cdot\widehat{\Delta a}\right]$, which is second order in the noise. Substituting the single-pole approximation Eq. (3.73) in Eq. (3.74) yields

$$\mathbf{E}_\mu \widehat{a}_\mu = \sum_\nu \frac{\omega_\mu^2}{(\omega-\omega_\mu)} \frac{\mathbf{E}_\mu \int dx\, \chi_\nu(\omega_\mu, a_0)\mathbf{E}_\mu^2}{\int dx\, \mathbf{E}_\mu^2(\mathbf{x})\left[\omega^2\widehat{\varepsilon}_0(\omega)\right]'_\mu} \widehat{\Delta a_\nu} * \widehat{a}_\mu + \frac{\mathbf{E}_\mu}{\omega-\omega_\mu} \frac{\int dx\, \widehat{\mathbf{F}}_{\mathrm{S}}(\mathbf{x}',\omega)\mathbf{E}_\mu}{\int dx\, \mathbf{E}_\mu^2(\mathbf{x})\left[\omega^2\widehat{\varepsilon}_0(\omega)\right]'_\mu}. \tag{3.75}$$

Finally, multiplying both side by $\omega-\omega_\mu$ and taking the inverse Fourier transform, we arrive at the N-SALT TCMT equations, which govern the evolution of the modal amplitudes a_μ:

$$\dot{a}_\mu = \sum_\nu \int dx c_{\mu\nu}(\mathbf{x})\gamma(x) \int^t dt' e^{-\gamma(\mathbf{x})(t-t')}(|a_{\nu 0}|^2 - |a_\nu(t')|^2)a_\mu + f_\mu(t). \tag{3.76}$$

The nonlinear coupling coefficient is

$$c_{\mu\nu}(\mathbf{x}) \equiv -i\omega_\mu^2 \frac{\chi_\nu(\omega_\mu, a_0)\mathbf{E}_\mu^2}{\int dx\, \mathbf{E}_\mu^2(\mathbf{x})\left[\omega^2\widehat{\varepsilon}_0(\omega)\right]'_\mu}, \tag{3.77}$$

and the Langevin force is

$$f_\mu(t) \equiv i \frac{\int [\mathbf{F}_{\mathrm{S}}(\mathbf{x}',t)e^{-i\omega_\mu t}]\mathbf{E}_\mu}{\int dx\, \mathbf{E}_\mu^2(\mathbf{x})\left[\omega^2\widehat{\varepsilon}_0(\omega)\right]'_\mu}. \tag{3.78}$$

3.10 Appendix B: Derivation of the multimode linewidth

In this section, we calculate the laser linewidth for the multimode time-delayed model by generalizing the solution strategy of Sec. 3.5 in the text. We begin our analysis

with the discretized time-delayed N-SALT TCMT equation Eq. (3.35) (repeated here for convenience):

$$\dot{a}_\mu = \sum_{\nu k} C^k_{\mu\nu} \left[\gamma_k \int^t dt' e^{-\gamma_k (t-t')} (|a_\nu(t')|^2 - |a_{\nu 0}|^2) \right] a_\mu + f_\mu. \tag{3.79}$$

Following the approach of Sec. 3.5.1, we linearize Eq. (3.79) by expanding the mode amplitudes a_μ around their steady-state values: $a_\mu = (a_{\mu 0} + \delta_\mu) e^{i\phi_\mu}$ (where $\delta_\mu \ll a_{\mu 0}$), and we omit the terms $\mathcal{O}(\delta_\mu^2)$. Then, we introduce additional variables ξ^k_μ

$$\xi^k_\mu = \gamma_k \int^t dt' e^{-\gamma_k (t-t')} \delta_\mu(t'), \tag{3.80}$$

where ξ^k_μ is the time-averaged amplitude deviation of mode $\mu = 1 \dots M$ from steady state at the spatial point $k = 1 \dots N$. Having introduced the auxiliary variables ξ^k_μ, the set of integro-differential equations Eq. (3.79) turns into a linear system of ODEs, which we solve by applying several linear-algebraic transformations to obtain a compact expression for the covariance matrix, as described in detail below.

Introducing the vector $\Phi_\mu \equiv a_{\mu 0} \phi_\mu$, the linear system of ODEs is conveniently written as

$$\dot{\delta}_\mu = -\sum_{\nu k} (2 a_{\mu 0} a_{\nu 0} \mathrm{Re}[C^k_{\mu\nu}]) \xi^k_\nu + f^{\mathrm{R}}_\mu, \tag{3.81}$$

$$\dot{\Phi}_\mu = -\sum_{\nu k} (2 a_{\mu 0} a_{\nu 0} \mathrm{Im}[C^k_{\mu\nu}]) \xi^k_\nu + f^{\mathrm{I}}_\mu \tag{3.82}$$

$$\dot{\xi}^k_\mu = -\gamma_k \xi^k_\mu + \gamma_k \delta_\mu. \tag{3.83}$$

To simplify the notation further, we introduce the $M \times M$ matrices $\mathbb{A}^k$ and $\mathbb{B}^k$ ($k =$

$1 \ldots N$), with entries

$$A^k_{\mu\nu} = 2a_{\mu 0}a_{\nu 0}\mathrm{Re}[C^k_{\mu\nu}]) \tag{3.84}$$

$$B^k_{\mu\nu} = 2a_{\mu 0}a_{\nu 0}\mathrm{Im}[C^k_{\mu\nu}]), \tag{3.85}$$

and we rearrange the set of equations Eqs. (3.81)–(3.83) in a matrix form [compare with Eqs. (3.24) and (3.25)]:

$$\frac{d}{dt}\boldsymbol{\delta} = -\sum_k \mathbb{A}_k \boldsymbol{\xi}^{\,k} + \mathbf{f}^{\,\mathrm{R}}, \tag{3.86}$$

$$\frac{d}{dt}\boldsymbol{\Phi} = -\sum_k \mathbb{B}_k \boldsymbol{\xi}^{\,k} + \mathbf{f}^{\,\mathrm{I}}, \tag{3.87}$$

$$\frac{d}{dt}\boldsymbol{\xi}^{\,k} = -\gamma_k \boldsymbol{\xi}^{\,k} + \gamma_k \boldsymbol{\delta}. \tag{3.88}$$

The autocorrelation matrix of the phase vector $\boldsymbol{\Phi}$, which we calculate in this section, is determined by the autocorrelation matrix of the Langevin force

$$\left\langle \mathbf{f}(t)\mathbf{f}^{*T}(t') \right\rangle = \mathbb{R}\delta(t-t'). \tag{3.89}$$

In order to compute $\left\langle \boldsymbol{\Phi}\boldsymbol{\Phi}^T \right\rangle$, we solve Eq. (3.87) by straightforward integration. We find that the phase covariance matrix is a sum of a "pure" phase-diffusion term, proportional to $\frac{\mathbb{R}}{2}$, and an amplitude–phase coupling term, proportional to $\mathcal{J}$:

$$\left\langle \boldsymbol{\Phi}(t)\boldsymbol{\Phi}^{\,T}(0) \right\rangle = \left(\frac{\mathbb{R}}{2} + \mathcal{J} \right) |t|, \tag{3.90}$$

where we have the introduced the shorthand notation

$$\mathcal{J} \equiv \frac{1}{|t|} \sum_{kl} \mathbb{B}_k \iint dt' ds' \left\langle \xi_k(t') \xi_l^T(s') \right\rangle \mathbb{B}_l^T \tag{3.91}$$

for the second term, which is responsible for the generalized α factor.

In the remainder of this section, we calculate $\mathcal{J}$. First, we solve the set of ODEs for $\boldsymbol{\xi}^k$ and $\boldsymbol{\delta}$ Eqs. (3.86) and (3.88), and then we substitute the solution for $\boldsymbol{\delta}$ into Eq. (3.91) and evaluate the integrals. To this end, we begin by rewriting the equations for $\boldsymbol{\xi}^k$ and $\boldsymbol{\delta}$ more compactly. We define the $[(N+1)\cdot M] \times 1$ vectors $\mathbf{x}$ and $\mathbf{F}$ and the $[(N+1)\cdot M] \times [(N+1)\cdot M]$ matrix $\mathbb{K}$:

$$\mathbf{x} = \begin{pmatrix} \boldsymbol{\delta} \\ \boldsymbol{\xi}^1 \\ \vdots \\ \boldsymbol{\xi}^N \end{pmatrix} \quad , \quad \mathbf{F} = \begin{pmatrix} \mathbf{f}^{\mathrm{R}} \\ \mathbf{0} \\ \vdots \\ \mathbf{0} \end{pmatrix} \quad , \quad \mathbb{K} = \begin{pmatrix} 0 & \mathbb{A}_1 & \mathbb{A}_2 & \dots & \mathbb{A}_N \\ \mathbb{A}_1 & -\mathbb{A}_1 & 0 & \dots & 0 \\ \mathbb{A}_2 & 0 & -\mathbb{A}_2 & & 0 \\ \vdots & \vdots & 0 & \ddots & 0 \\ \mathbb{A}_N & 0 & \dots & 0 & -\mathbb{A}_N \end{pmatrix}, \tag{3.92}$$

where $\mathbb{A}_k$ are block-diagonal $M \times M$ matrices with γ_k on the diagonal entries, and the zeros in the definition of $\mathbb{K}$ are block $M \times M$ zero matrices. Using these definitions, the equations for $\boldsymbol{\xi}^k$ and $\boldsymbol{\delta}$ Eqs. (3.86) and (3.88) can be conveniently written as

$$\frac{d}{dt}\mathbf{x} = -\mathbb{K}\mathbf{x} + \mathbf{F}. \tag{3.93}$$

The solution of Eq. (3.93) is

$$x_m(t) = \int^t dt' \sum_\rho \left[e^{-\mathbb{K}(t-t')}\right]_{m\rho} F_\rho(t') \tag{3.94}$$

and, in particular, the solution for ξ_μ^k is

$$\xi_\mu^k = \int^t dt' \sum_{s=1}^{M} \left[e^{-\mathbb{K}(t-t')}\right]_{Mk+\mu,s} f_{\rm S}^{\rm R}(t'). \tag{3.95}$$

For ease of notation, let us denote the $(k+1)^{\rm st}$ $M \times M$ block in the first column of the matrix $e^{-\mathbb{K}(t-t')}$ by the shorthand notation $[e^{-\mathbb{K}(t-t')}]_{k+1,1}$, so that $\boldsymbol{\xi}_k = \int_0^t dt' [e^{-\mathbb{K}(t-t')}]_{k+1,1} \mathbf{f}^{\rm R}(t')$. Substituting the expression for $\boldsymbol{\xi}_k$ into $\mathcal{J}$ and using the autocorrelation function of the Langevin force Eq. (3.89), we obtain

$$\mathcal{J} = \frac{1}{|t|} \sum_{k\ell} \mathbb{B}_k \iiint dt' dt'' ds' \left[e^{-\mathbb{K}(t'-t'')}\right]_{k+1,1} \times \frac{\mathbb{R}}{2} \left[e^{-\mathbb{K}^T(s'-t'')}\right]_{\ell+1,1} \mathbb{B}_\ell^T. \tag{3.96}$$

We proceed (not shown) by diagonalizing the matrix $\mathbb{K}$ and evaluating the integrals in Eq. (3.96). (The intermediate steps depend on the eigenvalues of $\mathbb{K}$ and the matrix of eigenvectors, but the final result can be expressed in terms of the matrix inverse $\mathbb{K}^{-1}$). In the long-time limit, we keep the leading order term (which grows linearly in time) and we obtain

$$\mathcal{J} = \left(\sum_k \mathbb{B}_k \left[\mathbb{K}\right]^{-1}_{k+1,1}\right) \frac{\mathbb{R}}{2} \left(\sum_\ell (\mathbb{B}_\ell \left[\mathbb{K}\right]^{-1}_{\ell+1,1})^T\right). \tag{3.97}$$

In order to complete the derivation of the linewidth formula, we use the following identity:

$$\left[\mathbb{K}\right]^{-1}_{k+1,1} = \left(\sum_j \mathbb{A}_j\right)^{-1}, \tag{3.98}$$

which we prove below. Noting that $A_{\mu\nu} = \sum_k A^k_{\mu\nu}$ and $B_{\mu\nu} = \sum_k B^k_{\mu\nu}$ and using the identity Eq. (3.98), we find that Eq. (3.97) reduces to

$$\mathcal{J} = \mathbb{B}\mathbb{A}^{-1} \frac{\mathbb{R}}{2} \left(\mathbb{B}\mathbb{A}^{-1}\right)^T, \tag{3.99}$$

which completes the derivation of the linewidth formula in the most general time-delayed model. In particular, and somewhat remarkably, the γ terms completely cancel in the computation of the first column of the matrix inverse, and drop out of the final result.

Proof of the identity Eq. (3.98): We use Schur complement [146] for the lower-left corner of a matrix inverse:

$$\begin{pmatrix} \mathbb{A} & \mathbb{B} \\ \mathbb{C} & \mathbb{D} \end{pmatrix}^{-1} = \begin{pmatrix} * & * \\ -\mathbb{D}^{-1}\mathbb{C}(\mathbb{A} - \mathbb{B}\mathbb{D}^{-1}\mathbb{C})^{-1} & * \end{pmatrix},$$

($\mathbb{A}$ and $\mathbb{D}$ need to be square matrices). Decomposing the matrix $\mathbb{K}$ into the blocks

$$\mathbb{A} = \begin{pmatrix} 0 \end{pmatrix} \quad , \quad \mathbb{B} = \begin{pmatrix} \mathbb{A}_1 & \mathbb{A}_2 & \dots & \mathbb{A}_N \end{pmatrix} \quad ,$$

$$\mathbb{C} = \begin{pmatrix} \mathbb{A}_1 \\ \mathbb{A}_2 \\ \vdots \\ \mathbb{A}_N \end{pmatrix} \quad , \quad \mathbb{D} = \begin{pmatrix} -\mathbb{A}_1 & 0 & \dots & 0 \\ 0 & -\mathbb{A}_2 & & 0 \\ \vdots & 0 & \ddots & 0 \\ 0 & \dots & 0 & -\mathbb{A}_N \end{pmatrix},$$

we can calculate the lower-left corner of $[\mathbb{K}]^{-1}_{k+1,1}$:

$$-\mathbb{D}^{-1}\mathbb{C}(\mathbb{A}-\mathbb{B}\mathbb{D}^{-1}\mathbb{C})^{-1} = (\mathbb{D}^{-1}\mathbb{C})[\mathbb{B}(\mathbb{D}^{-1}\mathbb{C})]^{-1} =$$

$$-\begin{pmatrix}1\\1\\\vdots\\1\end{pmatrix}\left[\begin{pmatrix}\mathbb{A}_1 & \mathbb{A}_2 & \dots & \mathbb{A}_N\end{pmatrix}\begin{pmatrix}1\\1\\\vdots\\1\end{pmatrix}\right]^{-1} = -\begin{pmatrix}1\\1\\\vdots\\1\end{pmatrix}\left[\sum_{\mathrm{I}}\mathbb{A}_{\mathrm{I}}\right]^{-1}. \tag{3.100}$$

Therefore, we obtain $[\mathbb{K}]^{-1}_{k+1,1} = \left(\sum_j \mathbb{A}_j\right)^{-1}$.

3.11 Appendix C: Proof of the lemma: $\left[\mathbb{B}\mathbb{A}^{-1}\right]_{ij} \propto \frac{a_{i0}}{a_{j0}}$

In Sec. 3.6.2, we present a multimode Schawlow–Townes relation, which states that the linewidths are proportional to a sum of inverse output powers of all the other modes. This result arises from a lemma which we prove here. We use the standard matrix-inverse formula [147]

$$\mathbb{A}^{-1} = \frac{1}{\det\mathbb{A}}\,\mathrm{adj}\mathbb{A}, \tag{3.101}$$

where the adjugate matrix is defined as

$$\mathrm{adj}\mathbb{A} = \left((-1)^{i+j}M_{ij}\right)^T. \tag{3.102}$$

$\mathbb{M}$ is the cofactor matrix, i.e. the matrix whose (i,j) entry is the determinant of the (i,j) minor of $\mathbb{A}$ (which is the matrix obtained from $\mathbb{A}$ by deleting the i'th row and the

j'th column). From the definition of $\mathbb{A}$ (i.e., $A_{ij} \equiv \mathrm{Re}[C_{ij}]a_{i0}a_{j0}$), it follows that

$$M_{ij} = \left(\prod_{k \neq i,j} a_{k0}^2 \right) a_{i0} a_{j0} Q_{ij}. \tag{3.103}$$

where Q_{ij} (and later Q) denote constants that may depend on i and j, but are independent of the modal amplitudes. Note also that

$$\det \mathbb{A} = \prod_k a_{k0}^2 \cdot Q. \tag{3.104}$$

Using Eqs. (3.101)–(3.104), we obtain

$$A_{ij}^{-1} = \frac{1}{a_{i0}a_{j0}} \cdot Q_{ij}. \tag{3.105}$$

Therefore, one can easily see that the lemma follows, since $[\mathbb{B}\mathbb{A}^{-1}]_{ij} \propto \sum_k a_{i0}a_{k0} \cdot \frac{1}{a_{k0}a_{j0}} \propto \frac{a_{i0}}{a_{j0}}$.

3.12 Appendix D: Scattering-matrix linewidth theory

In a recent scattering-matrix based linewidth theory [83], Pillay *et al.* obtain a formula for the linewidth of a one-dimensional laser system, expressed in terms of integrals over the modes which solve the nonlinear SALT equations. In this appendix, we prove that their formula (which applies to 1d systems) is equivalent to our linewidth formula Eq. (3.3) (except that their formula gives a spatially averaged incomplete-inversion factor and omits the α factor).

In the scattering-matrix approach, the lasing modes are described as purely outgoing

wave functions ψ_0, which satisfy the nonlinear SALT equation

$$\nabla \times \nabla \times \psi_0(x) - \omega_0^2 \varepsilon(x, \omega_0)\psi_0(x) = 0, \tag{3.106}$$

and can be expressed as a superposition of outgoing channel modes $\mathbf{u}_\mu$ outside of the laser region

$$\psi_0(x) = \sum_k b_k \mathbf{u}_k(x, \omega_0) \qquad \text{for r} \notin C. \tag{3.107}$$

C denotes the scattering region (i.e., $\varepsilon = 1$ for $x \notin C$). Note that $\psi_0(x)$ is precisely the same the mode $\mathbf{E}_0(\mathbf{x})$ (which was used in Sec. 3.2) inside the cavity region.] The outgoing mode-amplitudes $\mathbf{b}$ are normalized to the value of ψ_0 at the cavity boundary ($x = L$)

$$\mathbf{b}^T \mathbf{b} = \psi_0^2(L). \tag{3.108}$$

The apparent difference between our formula and the linewidth formula in [83] is that the integral term in the denominator of our linewidth formulaEq. (3.3) is replaced by a sum of two terms in the scattering-matrix approach

$$\int_{\substack{\text{all} \\ \text{space}}} dx \left[\varepsilon\omega_0 + \frac{\omega_0^2}{2}\frac{d\varepsilon}{d\omega_0}\right]\psi_0^2 \longrightarrow \frac{i\mathbf{b}^T\mathbf{b}}{2} + \int_{\text{C}} dx \left[\varepsilon\omega_0 + \frac{\omega_0^2}{2}\frac{d\varepsilon}{d\omega_0}\right]\psi_0^2. \tag{3.109}$$

In order for the two formulas to agree, we need to show that

$$\omega_0 \int_L^\infty dx \psi_0^2(x) = \frac{i\mathbf{b}^T\mathbf{b}}{2} \tag{3.110}$$

(where we have used the fact that $\varepsilon = 1$ outside the cavity region). We show that

the latter condition Eq. (3.110) holds for any solution ψ_0 of Eq. (3.106) which satisfies outgoing boundary conditions. One way to impose outgoing boundary conditions is to invoke the limiting-absorption principle (i.e., add loss to eliminate incoming waves from infinity and take the limit of infinitesimal absorption at the end of the calculation [148, 28]). Formally, we define the integral on the left-hand side of Eq. (3.110) as

$$\int_L^\infty dx\psi_0^2(x) \equiv \lim_{s\to 0^+} \int_L^\infty dx e^{-sx}\psi_0^2(x). \tag{3.111}$$

By substituting $\psi_0(x) = e^{ik_0 x}$ into Eq. (3.111) and taking the limit of $s \to 0^+$, we obtain $\int_L^\infty dx\psi_0^2(x) = \frac{i}{2k}e^{2ik_0 L} = \frac{i}{2k}\mathbf{b}^T\mathbf{b}$, and since $\omega_0 = ck_0$ this finishes the proof of Eq. (3.108) (with the units convention of $c = 1$).

3.13 Appendix E: Zero-point fluctuation cancellation

The hyperbolic cotangent factor in the FDT Eq. (3.19) arises as a sum of a Bose–Einstein distribution and a $1/2$ factor stemming from quantum zero-point (ZP) fluctuations [128, 129], and this is why it does not vanish in the limit of zero temperature ($\beta \to \infty$). However, it turns out that contribution of this ZP term cancels in the linewidth formula, as was shown by Henry and Kazarinov [72] from a quantum-operator viewpoint, and it is convenient to explicitly subtract the ZP term from the hyperbolic cotangent as in Eq. (3.3) and Eq. (3.21). Here, we provide a purely classical explanation for why this cancellation occurs, and why it is important to perform the explicit subtraction in order to eliminate a subtlety arising from the definition of outgoing boundary conditions.

The FDT has a hyperbolic cotangent factor, and when we apply the FDT to find the $\langle f_\mu f_\nu^* \rangle$ correlation function in Sec IV, the same hyperbolic cotangent factor arises in the

R integral, appearing in the form

$$\int dx|\mathbf{E}_\mu|^2 \mathrm{Im}\,\varepsilon_0(\omega_\mu) \cdot \frac{1}{2}\coth\left(\frac{\hbar\omega_\mu\beta}{2}\right)$$
$$= \int dx|\mathbf{E}_\mu|^2 \mathrm{Im}\,\varepsilon_0(\omega_\mu)\left[\left(\frac{1}{2}\coth\frac{\hbar\omega_\mu\beta}{2} - \frac{1}{2}\right) + \frac{1}{2}\right] \tag{3.112}$$

for a lasing mode μ, where we have trivially added and subtracted the ZP $1/2$ factor from coth. Now, we wish to analyze the final $1/2$ term, which is the integral $\frac{1}{2}\int dx|\mathbf{E}_\mu|^2 \mathrm{Im}\,\varepsilon_0(\omega_\mu)$. Before we treat outgoing boundary conditions, let us consider the simpler case of a laser surrounded by an explicit absorbing medium, as in [72]. (This is also the situation in more recent computational models, for which one uses a finite spatial domain surrounded by absorbing layers [18].) For any steady-state lasing mode (real ω_μ), the net gain + loss is zero, but $\frac{1}{2}\int dx|\mathbf{E}_\mu|^2 \mathrm{Im}\,\varepsilon_0(\omega_\mu)$ is proportional to the net power absorbed or gained by the electric field [3] and hence this integral is *zero*. Therefore, in such a case, whether or not we include the $1/2$ factor is irrelevant, because the $\pm 1/2$ terms integrate to zero.

However, a subtlety arises in this integral in the common case where the laser is surrounded by an infinite zero-temperature ($\beta = \infty$) lossless medium with outgoing radiation boundary conditions. Outgoing boundary conditions can be defined mathematically by the limiting absorption principle [148, 28]: one takes the lossless medium to be the limit of a lossy medium as the losses go to zero from above, which can be expressed by writing ε as $\varepsilon + i0^+$. Just as in appendix D, the correct approach is to take the lossless limit *after* solving the problem, i.e. the 0^+ limit is taken *outside* of the integral. Before we take this limit, it makes no difference whether the $1/2$ factor is included, just as above: it integrates to zero. However, after we take the lossless limit, there is no explicit absorbing region ($\mathrm{Im}\,\varepsilon > 0$) in the integral (the absorption

has been "moved to infinity" in some sense), so if we perform the coth integral without subtracting $1/2$ then we would obtain an incorrect contribution from the ZP fluctuations in the gain medium (which should have been canceled). Instead, if we integrate against $1/2 \coth -1/2$, the result is correct without requiring any explicit contribution from the absorbing boundary conditions.

Note that if the laser is surrounded by an infinite lossless medium at a *positive* temperature, then there is a nonzero contribution of incoming thermal radiation to the linewidth [53, 11]. This can be included in one of two ways. In practice, we typical solve the SALT equations in a finite computational box with an explicit absorbing region, in which case no modification to our linewidth formula is required: one simply assigns the ambient temperature to the absorbing region. If, on the other hand, the outgoing boundary conditions are imposed in some other way (e.g. semi-analytically as in earlier SALT work [56, 149, 104, 57]), then an explicit source term must be added to account for incoming thermal radiation, as in previous works [150].

Chapter 4

Verification of the microcavity laser linewidth theory

The previous chapter presented a theory for the linewidth of micro-structured lasers. Here we review subsequent work, lead by Alex Cerjan and Douglas Stone at Yale University, which validates our linewidth formula using brute-force simulations of the stochastic Maxwell–Bloch equations.[§] The chapter focuses on three results that we worked on collaboratively: Comparison between our linewidth formula and previous results (Sec. 4.2), verification of the sidepeak spectrum[†] (Sec. 4.3), and a justification for modeling radiation noise by a random current in Maxwell's equations (Sec. 4.4).

4.1 Introduction

Since the topic of linewidth theory was surveyed in great detail in the introduction of the previous chapter, we review here only the necessary background on the numerical techniques that we use. We refer to our linewidth theory from Ch. 3 as N-SALT (SALT plus noise). We believe that the N-SALT linewidth formula quantitatively predicts

[§]The results of this work were published in [17].

[†]Here we treat only a laser in which fluctuations in the field intensity are decoupled from phase fluctuations, i.e., the α factor [defined in Eq. (3.30)] vanishes. The more general case is treated in Ch. 5

the laser linewidth (far above threshold) including all corrections in an appropriately generalized form, and in that sense represents completely the effects of spontaneous emission on the laser linewidth. We test this hypothesis in the current work by direct integration of the laser equations with noise. In the single-mode regime, the N-SALT linewidth formula [Eq. (3.3)] can be rewritten as

$$\delta\omega_{\mathrm{N-SALT}} = \frac{\hbar\omega_0}{2P}\frac{\omega_0^2\left(\int \mathrm{Im}[\varepsilon(\mathbf{x},\omega_0)]|\boldsymbol{\psi_0}(\mathbf{x})|^2 dx\right)\left(\int \mathrm{Im}[\varepsilon(\mathbf{x},\omega_0)]\frac{N_2(\mathbf{x})}{D(\mathbf{x})}|\boldsymbol{\psi}_0(\mathbf{x})|^2 dx\right)}{\left|\int \boldsymbol{\psi}_0^2(\mathbf{x})\left(\varepsilon(\mathbf{x},\omega_0)+\frac{\omega_0}{2}\frac{d\varepsilon}{d\omega}\right)dx\right|^2}(1+\tilde{\alpha}^2) \qquad (4.1)$$

where $\boldsymbol{\psi}_0(\mathbf{x})$ is the the semiclassical lasing field inside of the cavity found from the steady-state *ab-initio* laser theory (SALT), normalized such that $\int dx\, \boldsymbol{\psi}_0^2 = 1$, and the integral is over the cavity region. $\varepsilon(\mathbf{x})$ is the total dielectric function of the passive cavity plus gain medium, assumed here to be homogeneously broadened two-level atoms, and $N_2(\mathbf{x})$ and $D(\mathbf{x})$ are the number of excited atoms and the atomic inversion respectively (generalization to multi-level, multi-transition atoms is straightforward within SALT and N-SALT, see [130]). $\tilde{\alpha}$ is the generalized α factor, which can be calculated analytically from knowledge of $\boldsymbol{\psi}_0(\mathbf{x})$ and $\varepsilon(\mathbf{x})$. This formula is derived under the conditions that $\delta\omega_{\mathrm{N-SALT}} \ll \gamma_{\parallel}, \Delta$. This equation reduces to the separable corrections discussed above in the appropriate limits [82], but shows that in general the incomplete inversion, Petermann, and bad-cavity linewidth corrections cannot be considered independent from each other or separate from the cavity decay rate.

Here, we test the predictions of the N-SALT linewidth formula against the Schawlow-Townes linewidth formula, including all the relevant corrections by directly integrating the laser equations using the Finite Difference Time Domain (FDTD) method, including the quantum fluctuations using the method proposed by Drummond and Raymer [151], and employing the timestepping method proposed by Bidégaray [152]. Many previous

numerical studies of spontaneous emission in laser cavities have implemented the noise based on knowledge of the lasing mode structure [153, 154]. However, these studies did not have access to the above-threshold lasingmode profiles, which can differ significantly from the passive cavity modes used e.g. in calculating the traditional Petermann factor. In our approach we will not make a particular modal ansatz. Hofmann and Hess derived FDTD-based noisy lasing equations similar to ours for applications to semiconductors, but the analysis made further assumptions not valid above the lasing threshold [155]. The effects of fluctuations in the electromagnetic fields due to thermal noise has also been previously studied using the FDTD algorithm [156, 150]; these effects are necessary to include when studying the noise properties of masers or other long wavelength lasers, but can be safely neglected at optical frequencies, where the spontaneous emission events being considered here dominate the noise of the laser. The approach used in this chapter is similar to that used by Andreasen et al. [71, 157], both in the equations used and in the analytic method to extract the signal's linewidth. More recently FDTD simulations of a noisy gain medium inside nanoplasmonic metamaterials have been performed to understand the interesting properties of these structures both below and above the lasing threshold [158, 159]. However unlike those earlier studies we will analyze the linewidth far above threshold where it can be compared quantitatively to previously proposed formulas. To our knowledge this is the first study of this type. To this end, we will be considering relatively simple and small laser cavities, allowing us to achieve the spectral resolution necessary to resolve the narrow laser linewidths far above the lasing threshold. Furthermore, despite the generality of Eq. (4.1), for computational reasons we will restrict our attention to atomic gain media, which have small α factors. Further effects of the α factor, such as the linewidth sideband asymmetry observed by Vahala et al. [19], are treated in Ch. 5.

4.2 Verification of the single-mode N-SALT formula

To test the predictions of the N-SALT linewidth, Eq. (4.1), against the Schawlow-Townes linewidth [5], we first study the simple one-dimensional, single-sided dielectric slab cavity, $n = 3$. Here, we use the "fully-corrected" form of the Schawlow-Townes linewidth as the point of comparison, which includes the Petermann factor, bad-cavity correction, and Henry α factor, and is given by,

$$\delta\omega_{\mathrm{ST}}^{(\mathrm{corr})} = \frac{\hbar\omega_0\gamma_c^2}{2P}\left(\frac{\bar{N}_2}{\bar{D}}\right)\left|\frac{\int|\boldsymbol{\phi}_0(\mathbf{x})|^2dx}{\int\boldsymbol{\phi}_0(\mathbf{x})^2dx}\right|^2\left|\frac{1}{1+\frac{\omega_0}{2\varepsilon}\frac{\partial\varepsilon}{\partial\omega}}\right|^2(1+\alpha^2), \tag{4.2}$$

where $\boldsymbol{\phi}_0(\mathbf{x})$ is the passive cavity resonance corresponding to the lasing mode, the spatial average of the inversion and occupation of the upper lasing state is denoted as $\bar{D} = \int dx\, D(\mathbf{x})$, the spatially averaged inversion is used to calculate the bad-cavity factor, and α is the Henry a factor. The first term in parentheses of Eq. (4.2) corresponds to the cavity-averaged incomplete inversion factor and the second corresponds to the Petermann factor [13]. The quantities $\boldsymbol{\psi}_0(\mathbf{x}), \boldsymbol{\phi}_0(\mathbf{x}), D(\mathbf{x})$, and $\varepsilon(\mathbf{x})$ are calculated using SALT, while the FDTD simulations are run for enough time steps to average together at least six resulting spectra using Bartlett's method. For the chosen parameters, the cold-cavity decay rate is on the order of the relaxation rate of the inversion, placing it on the border between Class A and Class B lasers [160], close enough to the former that no relaxation oscillation side-peaks are seen in the resulting spectra.

As can be seen in the left panel of Fig. 4.1, excellent quantitative agreement is seen between the N-SALT prediction (green line) and the linewidths measured through direct integration of the noisy Maxwell-Bloch equations (magenta triangles), while both results differ from the corrected Schawlow-Townes theory (blue line). This discrepancy is shown

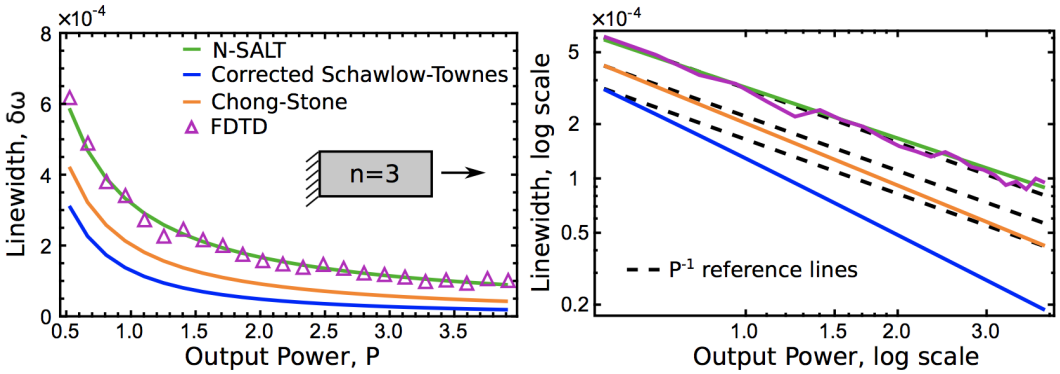

Figure 4.1: Fig. 2. (Left panel) Plot showing the linewidth predictions given by the N-SALT given in Eq. (4.1) (green), corrected Schawlow-Townes theory given in Eq. (4.2) (blue), integral form of the Chong-Stone linewidth formula given in Eq. (4.3) (orange), and FDTD simulations (magenta) for a uniformly pumped, dielectric slab cavity with $n = 3$, $\omega_a = 42.4$, $\gamma_\perp = 0.5$, $\gamma_\parallel = 0.01$, $\theta = 2 \times 10^{-9}$, and $N_A = 10^{10}$. All of the linewidth formulas are evaluated using the spatially dependent integral definition of the power given by Eq. (4.6). (Right panel) Plot of the same data shown on a log-log scale, with reference lines for strict inverse power dependence, P^{-1}, provided for comparison (black dashed). Schematic inset shows the cavity geometry. The rates and frequency are given in units of c/L, the number of atoms in the cavity is given in terms of the SALT units of $4\pi\theta^2/(\hbar\gamma_\perp)$, and the output power is given in the SALT units of $4\theta^2/(\hbar^2\gamma_\parallel\gamma_\perp)$.

to be more than a simple scaling factor in the right panel of Fig. 4.1, where the same data is plotted on a log-log scale, and it can be seen that the power law narrowing of the linewidth with respect to the output power differs between the N-SALT and corrected Schawlow-Townes linewidth predictions. Somewhat surprisingly only the N-SALT and FDTD results are very close to P^{-1} (black dashed lines), the others show a measurably faster narrowing.

To understand the source of this discrepancy, we also plot the Chong–Stone linewidth [82],

calculated using its integral form [83],

$$\delta\omega_{\mathrm{CS}} = \frac{\hbar\omega_0}{2P}\left(\frac{\bar{N}_2}{D}\right)\frac{\left(\omega_0\int \mathrm{Im}[\varepsilon(\mathbf{x},\omega_0)]|\boldsymbol{\psi}_0(\mathbf{x})|^2 dx\right)^2}{\left|\int \boldsymbol{\psi}_0^2(\mathbf{x})\left(\varepsilon+\frac{\omega_0}{2}\frac{d\varepsilon}{d\omega}\right)dx\right|^2}(1+\alpha^2), \tag{4.3}$$

where we have neglected the vanishingly small boundary term (discussed in Sec. 3.12). The Chong-Stone linewidth formula is derived through considering the behavior of the SALT-based scattering matrix of the cavity, and thus is able to account correctly for all effects stemming from the cavity; it gives the proper cavity decay rate above threshold, and the same Petermann factor, and bad-cavity correction as N-SALT. However, it does not provide an accurate treatment of the fluctuations inside the gain medium, particularly amplitude fluctuations, and thus is unable to find the α factor and finds an inaccurate, cavity-averaged incomplete inversion factor similar to conventional theories. For the dielectric slab cavity studied here, the detuning of the lasing mode from the atomic transition is very small, such that $\alpha \ll 1$. Thus the significant discrepancy between the N-SALT and FDTD results and the Chong-Stone prediction indicates that the largest source of discrepancy lies in the treatment of the incomplete inversion factor. The ratio of the N-SALT and Chong-Stone linewidth predictions in the limit that $\tilde{\alpha} = \alpha = 0$ can be written as

$$\frac{\delta\omega_{\mathrm{CS}}}{\delta\omega_{\mathrm{N-SALT}}} = \frac{\frac{\bar{N}_2}{D}\int D(\mathbf{x})|\boldsymbol{\psi}_0(\mathbf{x})|^2 dx}{\int N_2(\mathbf{x})|\boldsymbol{\psi}_0(\mathbf{x})|^2 dx}, \tag{4.4}$$

However, for the two-level atomic gain media simulated here, the number of atoms in the excited atomic level is nearly constant $N_2 \approx N_1 \approx N/2$, allowing for this ratio to be

expressed as

$$\frac{\delta\omega_{\mathrm{CS}}}{\delta\omega_{\mathrm{N-SALT}}} = \frac{\int D(\mathbf{x})|\boldsymbol{\psi}_0(\mathbf{x})|^2 dx}{\int |\boldsymbol{\psi}_0(\mathbf{x})|^2 dx \int D(\mathbf{x}) dx}, \tag{4.5}$$

In absolute terms, the fluctuations in N_2, N_1, and D are all of the same magnitude, but as $D(\mathbf{x}) = N_2(\mathbf{x}) - N_1(\mathbf{x}) \ll N_2$, its spatial variation is much larger on a relative scale and cannot be neglected, leading to a significant discrepancy between the N-SALT/FDTD and Chong-Stone linewidth predictions. Note that the approximation of spatial invariance of the occupation of the upper lasing level does not necessarily hold when considering more realistic gain media, with more than two levels, and is a result of the well known difficulty in pumping a two-level medium past the transparency point to achieve lasing. However the residual discrepancy between Chong-Stone and the corrected ST prediction indicates that the incomplete inversion factor only accounts for roughly half the discrepancy, and the remainder (Petermann and bad cavity effects) would be present in lasers with more than two levels. We note that it is important in these comparisons to calculate the output power from its fundamental definition via Poynting's theorem [3],

$$P = \frac{\omega_0}{2\pi} \int \mathrm{Im}[-\varepsilon(\mathbf{x})]|\mathbf{E}_0(\mathbf{x})|^2 dx \tag{4.6}$$

where this equation is given in Gaussian units, $\mathbf{E}_0(\mathbf{x}) = \sqrt{I}\boldsymbol{\psi}_0(\mathbf{x})$ is the unnormalized lasing mode, and I is the mode intensity.

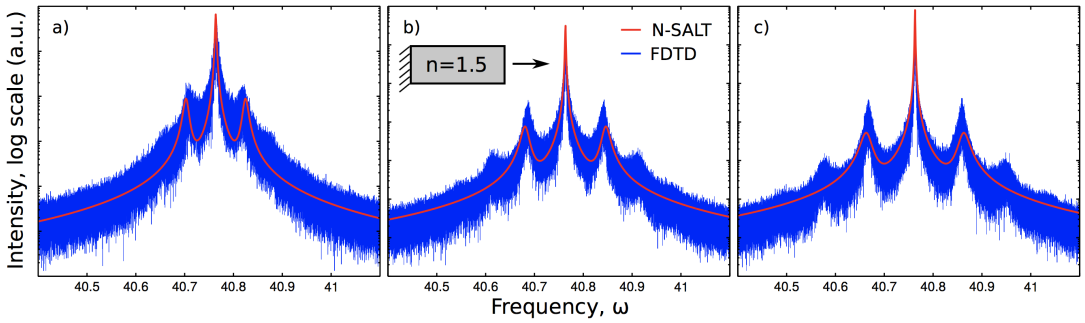

Figure 4.2: Plots showing a comparison between the N-SALT prediction (red) and FDTD simulations (blue) of the optical intensity spectrum for increasing values of the pump, D_0, for a single-sided, dielectric slab cavity with $n = 1.5$, $\omega_a = 40.7$, $\gamma_\perp = 1$, $\gamma_\parallel = 0.0025$, $\theta = 6 \times 10^{-10}$, and $N_A = 10^{10}$. (a) $D_0 = 0.18$, (b) $D_0 = 0.28$, (c) $D_0 = 0.38$. As can be seen, increasing the pump value increases the rate of stimulated emission, increasing $\gamma(\mathbf{x})$, Eq. (4.7), resulting in increasing separation between the relaxation oscillation side peaks and the central lasing frequency. In all three panels of Fig. 5, the central frequency, ω_0, chosen to evaluate Eq. (4.9) is the central frequency found by the FDTD simulations. Intensity is plotted on a log scale in arbitrary units, rates are given in units of c/L, and the inversion and total number of atoms are given in SALT units of $4\pi\theta^2/\hbar\gamma_\perp$.

4.3 Relaxation oscillation sidebands

In Class B lasers, fluctuations in the amplitude of the electric field undergo relaxation oscillations while decaying to the steady-state. These relaxation oscillations give rise to side-peaks in the spectrum of the output intensity and in this section we will demonstrate that the N-SALT is able to correctly reproduce the location and size of these side-peaks. It has been known for many decades that the relaxation oscillation frequency increases as the laser is pumped further above threshold [96], but previous studies did not take into account the spatial variation in the gain saturation, which was shown to play an important role in quantitatively predicting the laser linewidth. Using the spatial lasing mode profiles and inversion calculated using SALT, N-SALT demonstrates that the

output optical intensity spectrum is dependent upon the total local decay rate,

$$\gamma(\mathbf{x}) = \gamma_{\parallel}\left(1 + \frac{\gamma_{\perp}^2}{(\omega_0 - \omega_a)^2 + \gamma_{\perp}^2}|\mathbf{E}_{\mathrm{SALT}}(\mathbf{x})|^2\right), \tag{4.7}$$

which contains contributions from both the non-radiative decay rate of the inversion, $\gamma_{\parallel}$, as well as the local rate of stimulated emission given by the second term in Eq. (4.7). N-SALT yields two main results for the effects of relaxation oscillations on the linewidth. First, that relaxation oscillation side peaks will appear for cavities whose parameters satisfy the inequality $\delta\omega_{\mathrm{N-SALT}} \ll \gamma_{\parallel} \ll \int dx\, A(\mathbf{x})$, in which

$$A(\mathbf{x}) = 2I\mathrm{Re}\left[\frac{i\omega_0 \boldsymbol{\psi}_0^2(\mathbf{x})\frac{\partial\varepsilon}{\partial I}}{2\int \boldsymbol{\psi}_0^2(\mathbf{x})\left(\varepsilon + \frac{\omega_0}{2}\frac{\partial\varepsilon}{\partial\omega}\right)dx}\right], \tag{4.8}$$

where I is the intensity of the electric field, as defined above. Second, N-SALT gives an explicit form for the output optical intensity spectrum in the presence of relaxation oscillations (with $\alpha = 0$):

$$S_{\mathrm{N-SALT}}(\omega) = \frac{\delta\omega_{\mathrm{N-SALT}}}{\omega^2 + \left(\frac{\delta\omega_{\mathrm{N-SALT}}}{2}\right)^2} + \frac{\delta\omega_{\mathrm{N-SALT}}}{\omega^2(1 - R(\omega))^2 + \tilde{R}(\omega)^2}, \tag{4.9}$$

$$R(\omega) = \int \frac{A(\mathbf{x})\gamma(\mathbf{x})}{\omega^2 + \left(\frac{\delta\omega_{\mathrm{N-SALT}}}{2} + \gamma(\mathbf{x})\right)^2}dx, \tag{4.10}$$

$$\tilde{R}(\omega) = \int \frac{A(\mathbf{x})\gamma(\mathbf{x})\left(\frac{\delta\omega_{\mathrm{N-SALT}}}{2} + \gamma(\mathbf{x})\right)}{\omega^2 + \left(\frac{\delta\omega_{\mathrm{N-SALT}}}{2} + \gamma(\mathbf{x})\right)^2}dx. \tag{4.11}$$

The second term in Eq. (4.9) describes the side peaks due to relaxation oscillations. In Fig. 4.2 we show the output optical intensity spectrum of a dielectric slab cavity pumped above the first lasing threshold, in the parameter regime where side peaks are

expected. Each of the plots shows a comparison between the N-SALT prediction (red line) and the FDTD simulations (blue line) for increasing values of the pump, (a) to (c). As can be seen in all three plots, excellent quantitative agreement is seen between the simulated spectrum and the N-SALT prediction. To reiterate, N-SALT has no free parameters, so the agreement seen here is a demonstration of a first principles test of N-SALT. As can be see in the FDTD simulations, there are additional peaks in the spectrum at a distance of twice the relaxation oscillation frequency from the central peak. In principle N-SALT can be used to predict these additional side-peaks as well. Finally, relaxation oscillations are proportional to the square root of the decay rate of the cavity, $\omega_{\mathrm{RO}} \sim \sqrt{(1)\int dx\, \gamma(\mathbf{x})}$, thus we expect for the side peaks seen in the spectrum to move away from the central peak as the rate of stimulated emission increases due to an increasing pump. As the pump is increased from Fig. 4.2(a) to Fig. 4.2(c) we observe exactly this behavior in both the FDTD simulations and N-SALT results, verifying this prediction. Finally, we note that due to the use of an atomic gain medium with a small a factor in these simulations, the sideband asymmetry observed by Vahala *et al.* [19] cannot be resolved here.

4.4 Microscopic and macroscopic noise equivalence

There are two different ways of incorporating the effects of spontaneous emission on the electric field inside of the laser cavity, either by using the fluctuation-dissipation theorem alongside the wave equation, or by including spontaneous emission in the atomic degrees of freedom, which are coupled non-linearly to the wave equation. In this section we will explicitly demonstrate the equivalence of these two methods, which we term the macroscopic and microscopic perspectives respectively, as the derivation of the N-SALT

linewidth equation uses the former method, while the Langevin equations augmenting the FDTD simulations use the latter. This section also serves as a proof that despite the non-equilibrium nature of the laser, with power flowing in and light flowing out, the system does reach a point of stability wherein the fluctuations of the electric field can be appropriately treated with the fluctuation-dissipation theorem.

The derivation of the N-SALT equation incorporates all of the noise due to the quantum fluctuations in the gain medium directly into the wave equation as

$$[\nabla \times \nabla \times -\omega^2 \varepsilon(\omega, \mathbf{E}_0)]\mathbf{E} = \omega^2(\varepsilon(\omega, \mathbf{E}) - \varepsilon(\omega, \mathbf{E}_0))\mathbf{E} + \mathbf{F}_{\mathrm{S}} \tag{4.12}$$

where $\varepsilon(\omega, \mathbf{E})$ is the full dielectric function of the cavity and gain medium, $\varepsilon(\omega, \mathbf{E}_0)$ is the non-linear saturated dielectric function of the cavity evaluated using the semiclassical lasing mode $\mathbf{E}_0(x) = \sqrt{I}\boldsymbol{\psi}_0(x)$, where I is the lasing mode intensity, and $\mathbf{F}_S$ is a random noise source corresponding to the spontaneous emission from the gain medium. The first term on the right hand side of Eq. (4.12) corresponds to the effective source due to fluctuations in the field leading to fluctuations in the saturation of the gain medium, while the second term corresponds to spontaneous emission contributing directly to noise in the electric field. The inclusion of the full space-dependent non-linearity of the active cavity dielectric function above threshold in the noise term is a key feature distinguishing N-SALT from previous linewidth theories. The autocorrelation of the random noise source is assumed to be given directly by the fluctuation–dissipation theorem [70],

$$\left\langle \mathbf{F}_{\mathrm{S}}^{\dagger}(\mathbf{x}, \omega)\mathbf{F}_{\mathrm{S}}(\mathbf{x}', \omega') \right\rangle = 2\hbar\omega^4 \mathrm{Im}[\varepsilon(\omega, \mathbf{E}_0)] \coth\left(\frac{\hbar\omega\beta(\mathbf{x})}{2}\right) \delta(\mathbf{x} - \mathbf{x}')\delta(\omega - \omega') \tag{4.13}$$

where $\beta(x) = (1/\hbar\omega_0)\ln(N_1(\mathbf{x})/N_2(\mathbf{x}))$ is the effective (negative) inverse temperature of

the inverted gain medium, with N_1 and N_2 are the number of atoms in the ground and excited atomic levels respectively. (Note that $\mathrm{Im}[\varepsilon(\omega, \mathbf{E}_0)] < 0$ in the inverted state, so that the correlation remains positive).

In this treatment of the noise in the laser field due to spontaneous emission, the atomic degrees of freedom have been completely integrated out, and the fluctuation–dissipation theorem has been invoked from a macroscopic perspective, relating the autocorrelation of the noise source to the imaginary part of the material response function and a temperature dependent term. The hyperbolic cotangent factor arises as a sum of a Bose-Einstein distribution and a factor of 1/2 from the quantum zero-point fluctuations, which is why the auto-correlation does not vanish in the zero temperature limit ($\beta \to \infty$). However, it was shown by Henry and Kazarinov that the contributions from the zero-point fluctuations cancel in the linewidth formula [72] (a simpler, semiclassical proof of this is in Sec. 3.13), and as such it is convenient to explicitly subtract this contribution, allowing for the effective temperature of the gain medium to be determined by relative occupations of the atomic levels comprising the lasing transition,

$$\frac{1}{2}\coth\left[\frac{\hbar\omega\beta(\mathbf{x})}{2} - 1\right] = -\frac{N_2(\mathbf{x})}{D(\mathbf{x})} \tag{4.14}$$

where $D(\mathbf{x}) = N_2(\mathbf{x}) - N_1(\mathbf{x})$ is the number of inverted atoms. Thus, for the laser systems considered here, Eq. (4.13) can be written as

$$\left\langle \mathbf{F}_{\mathrm{S}}^{\dagger}(\mathbf{x}, \omega)\mathbf{F}_{\mathrm{S}}(\mathbf{x}', \omega')\right\rangle = 4\hbar\omega^4 \mathrm{Im}[\varepsilon(\omega, \mathbf{E}_0)]\coth\left[\frac{1}{2}\frac{\hbar\omega\beta(\mathbf{x})}{2} - \frac{1}{2}\right]\delta(\mathbf{x} - \mathbf{x}')\delta(\omega - \omega') \tag{4.15}$$

In contrast to this macroscopic picture, many traditional theories of the noise due to spontaneous emission from the gain media begin by treating the Langevin forces on the

quantum operators of individual gain atoms and building up an understanding of the total noise this generates in the electric field, a more microscopic viewpoint [79]. We will demonstrate the equivalence of these two methods by deriving the total Langevin force on the polarization from the microscopic perspective. For a two-level atomic gain medium, the evolution equation for the off-diagonal matrix element of the αth atom, $\rho_{21}^{(\alpha)}$, including the Langevin force, $\Gamma_{(\rho)}^{(\alpha)}(t)$, is given by,

$$\partial_t \rho_{21}^{(\alpha)}(t) = -(\gamma_\perp + i\omega_a)\rho_{21}^{(\alpha)}(t) + \frac{id^{(\alpha)}}{\hbar}\boldsymbol{\theta}\cdot\mathbf{E}(\mathbf{x}^{(\alpha)},t) + \Gamma_{(\rho)}^{(\alpha)}(t) \tag{4.16}$$

in which ω_a is the atomic transition frequency, $\gamma_\perp$ is the dephasing rate, and $\boldsymbol{\theta}$ is the dipole coupling matrix element. Furthermore, the evolution of the inversion for that atom, $d^{(\alpha)}$, including the Langevin force, $\Gamma_{(d)}^{(\alpha)}(t)$, is given by

$$\partial_t d^{(\alpha)} = \gamma_\parallel(d_0^{(\alpha)} - d^{(\alpha)}) + \frac{2}{i\hbar}\boldsymbol{\theta}\cdot\mathbf{E}(\mathbf{x}^{(\alpha)},t)(\rho_{21}^{(\alpha)}(t)^* - \rho_{21}^{(\alpha)}(t)) + \Gamma_{(d)}^{(\alpha)}(t) \tag{4.17}$$

where $d_0^{(\alpha)}$ is the inversion of the αth atom in the absence of any electric field. Finally, the wave equation for the electric field can be written in this context by explicitly including the coupling between the field and each individual gain atom [see Eqs. (5.48) and (5.55) in [11]],

$$[\nabla\times\nabla\times - \omega_0^2\varepsilon_c]\mathbf{E}(\mathbf{x},\omega) = 4\pi\omega_0^2\boldsymbol{\theta}\sum_\alpha \delta(\mathbf{x}-\mathbf{x}^{(\alpha)})\rho_{21}^{(\alpha)} \tag{4.18}$$

in which we have approximated that the electric field is oscillating at frequencies close to the semiclassical lasing frequency, ω_0, and retained only the positive frequency components for both the electric field and atomic polarization. Our aim is to determine the form of the effective total Langevin force on the electric field by solving Eqs. (4.16) and

(4.17) for the polarization and inversion, insert these expressions into the wave equation, and collect the resulting Langevin force terms.

To leading order, ρ_{21} will oscillate at the lasing frequency, ω_0, and if we approximate this as its only frequency component, we can solve for

$$\rho_{21}^{(\alpha)} = \frac{-d^{(\alpha)}}{\hbar(\omega_0 - \omega_a + i\gamma_\perp)}\boldsymbol{\theta}\cdot\tilde{\mathbf{E}}(\mathbf{x}^{(\alpha)},\omega) + \frac{ie^{i\omega_0 t}}{\omega_0 - \omega_a + i\gamma_\perp}\Gamma_{(\rho)}^{(\alpha)} \tag{4.19}$$

where the electric field is assumed to be a constant over the volume of the atom at $\mathbf{x}^\alpha$. The fluctuation dissipation theorem states that the strength of the fluctuations is proportional to the strength of the dissipative terms. Thus, for the Class A and B lasers considered here, $\gamma_\parallel \ll \gamma_\perp$, so $\Gamma_{(d)}^{(\alpha)}(t) \ll \Gamma_{(\rho)}^{(\alpha)}(t)$, and we can safely ignore the fluctuations in the atomic inversion. Thus, we can insert Eq. (4.19) into Eq. (4.18),

$$\begin{aligned}[\nabla\times\nabla\times - \omega_0^2\varepsilon_c]\mathbf{E}(\mathbf{x},\omega) = 4\pi\omega_0^2\boldsymbol{\theta}\sum_\alpha \delta(\mathbf{x}-\mathbf{x}^{(\alpha)}) \\ \times\left[\frac{-d^{(\alpha)}}{\hbar(\omega_0-\omega_a+i\gamma_\perp)}\boldsymbol{\theta}\cdot\tilde{\mathbf{E}}(\mathbf{x}^{(\alpha)},\omega) + \frac{ie^{i\omega_0 t}}{\omega_0-\omega_a+i\gamma_\perp}\Gamma_{(\rho)}^{(\alpha)}\right]\end{aligned} \tag{4.20}$$

Equation (4.20) allows for the identification of the spontaneous noise in the polarization, $\mathbf{P}_N$, using Eq. (4.12) and noting that $\mathbf{F}_S = -4\pi\omega^2\mathbf{P}_N$, as

$$\mathbf{P}_{\mathrm{N}}(\mathbf{x},\omega) = \sum_\alpha \delta(\mathbf{x}-\mathbf{x}^{(\alpha)})\frac{i\boldsymbol{\theta}e^{i\omega_0 t}}{\omega_0-\omega_a+i\gamma_\perp}\Gamma_{(\rho)}^{(\alpha)} \tag{4.21}$$

We can now directly calculate the correlation function of the spontaneous noise in the

polarization using the correlation of the atomic Langevin force [11],

$$\left\langle \Gamma_{(\rho)}^{(\alpha)}(t)\Gamma_{(\rho)}^{(\beta)\dagger}(t')\right\rangle = \left[\gamma_{\perp}(1+\langle d^{(\alpha)}\rangle) + \tfrac{\gamma_{\parallel}}{2}(d_0^{(\alpha)} - \langle d^{(\alpha)}\rangle)\right]\delta_{\alpha\beta}\delta(t-t') \tag{4.22}$$

in which each atom is taken to only be in equilibrium with its reservoir [53]. Note that the only place the non-equilibrium nature of the reservoir comes in is via the term $\left\langle d^{(\alpha)}\right\rangle = \rho_{22}^{(\alpha)} - \rho_{11}^{(\alpha)}$. Since no higher moments or correlations enter the calculation, it is safe to define an effective temperature for the system which can be negative via this relation and apply the fluctuation–dissipation theorem. Note also that $\left\langle d^{(\alpha)}\right\rangle$ contains the non-linear effect of gain saturation and spectral hole burning when calculated by the FDTD method given below.

By assuming that the inversion is relatively stationary, we can identify the same frequency auto-correlation of the noise as [89]

$$\left\langle \Gamma_{(\rho)}^{(\alpha)}(\omega)\Gamma_{(\rho)}^{(\beta)\dagger}(\omega')\right\rangle = \gamma_{\perp}(1+\langle d^{(\alpha)}\rangle)\delta_{\alpha\beta} \tag{4.23}$$

in which we have again dropped the noise source proportional to $\gamma_{\parallel}$, to be consistent with the approximation neglecting fluctuations in the inversion made above. This allows us to solve for

$$\left\langle \mathbf{P}_{\mathrm{N}}^{\dagger}(\mathbf{x},\omega)\mathbf{P}_{\mathrm{N}}(\mathbf{x}',\omega')\right\rangle = \frac{2\boldsymbol{\theta}^2\gamma_{\perp}}{(\omega_0-\omega_a)^2+\gamma_{\perp}^2}N_2(\mathbf{x})\delta(\mathbf{x}-\mathbf{x}') \tag{4.24}$$

where the number of atoms in the upper lasing state, $N_2(\mathbf{x})$ has been identified using,

$$N_2(\mathbf{x},\omega) = \frac{1}{2}\sum_{\alpha}\delta(\mathbf{x}-\mathbf{x}^{(\alpha)})(1+\langle d^{(\alpha)}\rangle) \tag{4.25}$$

Upon substitution of the imaginary part of the dielectric function,

$$\mathrm{Im}[\varepsilon] = -\frac{4\pi\boldsymbol{\theta}^2}{\hbar}\frac{\gamma_\perp D(\mathbf{x})}{(\omega-\omega_a)^2+\gamma_\perp^2} \tag{4.26}$$

we can identify the same frequency auto-correlation of the noise source $\mathbf{F}_S$ as

$$\left\langle \mathbf{F}_{\mathrm{S}}^{\dagger}(\mathbf{x},\omega)\mathbf{F}_{\mathrm{S}}(\mathbf{x}',\omega)\right\rangle = 8\pi\hbar\omega^4\mathrm{Im}[\varepsilon(\omega,\mathbf{E}_0)]\frac{N_2(\mathbf{x})}{D(\mathbf{x})}\delta(\mathbf{x}-\mathbf{x}') \tag{4.27}$$

Finally, noting that the different frequency auto-correlation function can be found as [89],

$$\left\langle \mathbf{F}_{\mathrm{S}}^{\dagger}(\mathbf{x},\omega)\mathbf{F}_{\mathrm{S}}(\mathbf{x}',\omega')\right\rangle = \frac{1}{2\pi}\left\langle \mathbf{F}_{\mathrm{S}}^{\dagger}(\mathbf{x},\omega)\mathbf{F}_{\mathrm{S}}(\mathbf{x}',\omega)\right\rangle \delta(\omega-\omega') \tag{4.28}$$

and using the definition of the temperature factor given in Eq. (4.14), we recover the expected auto-correlation of the random noise source given in Eq. (4.15).With this, we have verified that the microscopic and macroscopic methods of treating the fluctuations in the gain medium produce identical results, which allows us to use a microscopic model of the gain medium in our FDTD simulations to test the predictions of the N-SALT theory.

4.5 Summary

In this work we have performed a first principles test of the N-SALT linewidth results presented in the previous chapter. To do this, we used the FDTD algorithm to simulate the Maxwell-Bloch equations coupled to a set of Langevin noise equations, thus including the effects of spontaneous emission. We found excellent quantitative agreement between

the N-SALT linewidth predictions and the FDTD simulations, while finding substantial deviations from the 'fully corrected' Schawlow-Townes theory, demonstrating that the intertwining of the cavity decay rate, Petermann factor, incomplete inversion factor, bad-cavity correction and Henry α factor in the N-SALT linewidth formula is necessary and correct. This comparison was first done in a parameter range in which the relaxation oscillations were weak (near the Class A boundary). Through comparison with the Chong and Stone linewidth theory [82], we demonstrated that for the small, $20\lambda_a \sim L$, cavities studied here, much but not all of the improved agreement found by N-SALT is due to the proper treatment of the incomplete inversion factor. Next, we successfully demonstrated that N-SALT gives the correct output optical intensity spectrum including relaxation oscillations for Class B lasers, and correctly reproduces the side-peaks due to relaxation oscillations. This set of simulations also verified that the side-peaks shift away from the center of the spectrum as the pump on the gain medium is increased.We then studied the different predictions for the linewidth enhancement due to the coupling between intensity and phase fluctuations, the α factor, and demonstrated that the N-SALT form of the α factor yields quantitative agreement with the FDTD simulations, while previous forms of the α factor are shown to disagree. This set of simulations is particularly remarkable, because in the absence of the N-SALT prediction for $\tilde{\alpha}$, one might conclude that the FDTD simulations do not correctly capture the effects of the α factor. Instead, it is clear that the FDTD algorithm used does contain all of the relevant physics, and that there can be a significant difference between the various forms of the α factor. Finally, we demonstrated that the N-SALT theory correctly predicts the linewidth for multiple active lasing modes.

Chapter 5

Relaxation oscillation spectrum in microcavity lasers

In the first two chapters we derived a new formula for the laser linewidth [Eq. (3.3)]. In addition, we presented (without proving) a formula for the sidebands that may occur due to relaxation oscillations in lasers with a zero α factor [Eq. (3.42)]. Due to the length of the derivations and discussions, we left the derivation of the sideband formula and its generalization to lasers with nonzero α for this chapter. An accurate sideband formula is useful for measuring the α factor (using the method in Ref. [20]), which is typically the biggest linewidth enhancement factor in semiconductor lasers [12].

5.1 Introduction

The ability to compute the laser spectrum is essential for understanding its coherence properties and performance limitations. While traditional theories are excellent at predicting the spectral properties of macro-scale lasers [19, 20], they fail when applied to microstructured lasers with wavelength-scale inhomogeneities [82], and they also require empirical fit parameters. In recent work [16], we presented a formula for the widths of the lasing resonant peaks (i.e., the central linewidths) which is valid for complex microcav-

ities. In this paper, we apply a similar approach to obtain not only the linewidths, but also the entire laser spectrum, including sidepeaks arising from relaxation oscillations (Fig. 5.1) [106] with no empirical parameters other than the material parameters (refractive index, lasing transition rates/frequency) of the laser cavity. Here and in [17], we verify our formula with brute-force simulations of the stochastic Maxwell–Bloch equations (Fig. 5.4) demonstrating the generality of our formulation, which assumes only the existence of a multimode steady-state laser field and a stationary population inversion of the gain medium. Our approach uses the recent steady-state *ab-initio* laser theory (SALT) [56], which enables computing the laser modes and frequencies in the steady state, while taking into account inhomogeneity in the modes and pump and treating the nonlinear gain nonperturbatively. Our single-mode spectral formula [Eq. (5.3)] agrees with earlier theories in the appropriate limits (reducing to the result of [20] in the limit of constant atomic-relaxation rates and to [16] when phase and intensity fluctuations of the field are decoupled) and deviates quantitatively for lasers with wavelength-scale inhomogeneity (Fig. 5.2). We predict several new spectral effects, such as smearing of the sidepeaks due to gain saturation (Fig. 5.2b), new multimode sidepeaks due to amplitude modulation of the relaxation-oscillation (RO) signal in the multimode regime (Fig. 5.2c), and three generalized intensity–phase coupling constants (i.e., α factors, Fig. 5.3a).

The nonlinear interaction between the laser field and gain medium stabilizes the laser intensity and atomic inversion at a steady state [11]. Spontaneous emission and other noise produce perturbations from steady state [54, 161] which relax via oscillations when the relaxation rates of the gain and light are comparable (a regime sometimes called "type-B lasers" [106]). Early work by Yariv *et al.* [19, 162] attributed the sidepeaks in the noise spectrum of single-mode semiconductor lasers to RO dynamics. They

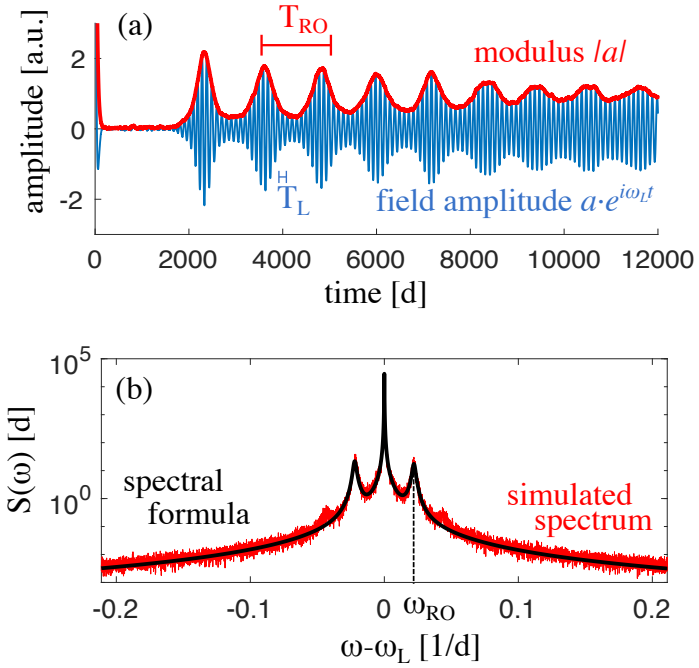

Figure 5.1: (a) The laser-field amplitude, $ae^{i\omega_L t}$, and modulus, $|a|$. a is obtained from Eq. (5.1) with initial state $a(0) = 5$, steady state $a_0 = 1$, noise intensity $R = 1.44 \cdot 10^{-4}$, constant relaxation $\gamma(x) = 0.0025$, and nonlinear coupling $\int dx\, c(x) = 0.19 + 1.18i$. The field amplitude oscillates at frequency $\omega_L = \frac{2\pi}{T_L}$ while the modulus undergoes relaxation oscillations with frequency $\omega_{\mathrm{RO}} = \frac{2\pi}{T_{\mathrm{RO}}}$. (b) The spectrum, obtained by computing the periodogram of Eq. (5.1) (red) and by evaluating the spectral formula (black) [Eq. (5.3)].

presented a theory for the spectrum of macrocavity lasers (without wavelength-scale inhomogenieties), which they verified experimentally using buried optical waveguide (BOG) GaAlAs laser. They also observed an asymmetry between the amplitudes of the high- and low-frequency sidepeaks, which they attributed to the coupling of phase and amplitude fluctuations of the laser field (the dimensionless coupling strength is the α factor [113, 114]). Later, van Exter *et al.* [20] derived a simple closed-form expression

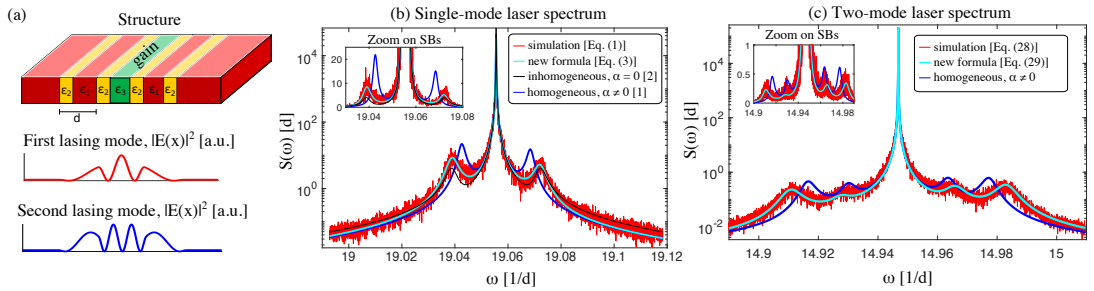

Figure 5.2: (a) Top: Schematics of the geometry. Stacked layers with permittivities $\varepsilon_1 = 1, \varepsilon_2 = 16, \varepsilon_3 = 7$, and thicknesses $d_1 = d_3 = 0.2a, d_2 = \frac{\sqrt{\varepsilon_1}a}{\sqrt{\varepsilon_1}+\sqrt{\varepsilon_2}} = 0.8a$, where a is the unit cell size. Gain is added in the three central layers with resonance frequency $\omega_a = 18$ and bandwidth $\gamma_\perp = 1$ in (b) and $\omega_a = 17$, $\gamma_\perp = 2$ in (b). (All frequencies are in units of $1/a$) . Bottom: Intensity profiles of the first and second lasing modes (with threshold frequencies $\omega_1 = 19.05$ and $\omega_2 = 14.95$ respectively). (b) Spectrum of a single-mode laser, on a log-linear scale. The stochastic equations [Eq. (5.1)] are solved by employing Euler's method, and then computing the periodogram of the signal by ensemble averaging its FFT. We compare the resulting spectrum (red) with our single-mode formula [Eq. (5.3)] (cyan) and earlier results: [20] (black) which neglected $\alpha-$factor corrections and [16] (blue) which neglected inhomogeniety and nonlinearity of the modes and gain. Inset: Magnification of the sidepeaks, plotted on a linear scale, which shows the asymmetry of the peaks. (c) Spectrum of a multimode laser. We compare the numerical solution of the stochastic equations [Eq. (5.28)] (red) with our multimode formula [Eq. (5.29)] (cyan). Additionally, we plot the homogeneous limit of our formula (black) . Inset: Zoom on the sidepeaks.

for the single-mode macrocavity laser spectrum, $S(\omega)$. They showed that the ratio of low- and high-frequency sidepeak amplitudes is $\frac{S(\omega_L-\Omega)}{S(\omega_L+\Omega)} = 1 + \frac{8\alpha}{1+\alpha^2}\left(\frac{\Gamma}{\Omega}\right)$, where ω_L is the laser frequency, Ω is the RO frequency, and Γ is the RO relaxation rate. This result implied that the asymmetry is most pronounced for lasers with $\alpha \approx 1$ and that, since α is positive in typical semiconductor lasers, the low-frequency sidepeaks are stronger than the high-frequency ones. These early works [162, 20] are adequate for single-mode macroscale lasers, but are not accurate for lasers with wavelength-scale inhomogeneities, do not include nonlinear corrections to the mode profiles and relaxation rates, and do

not analyze multimode effects on the sideband spectrum. Our new formulas [Eqs. (5.3) and (5.29)] correct those features.

The starting point of our derivation (here and in Ch. 3) is the Maxwell–Bloch equations, which we solve in the absence of noise using SALT. For simplicity, we begin by discussing the single-mode regime (Sec. 5.2, Sec. 5.4, and Sec. 5.5) and present the general multimode formulation in Sec. 5.6 and in Sec. 5.10. Once noise is included, the actual lasing solutions will be perturbed from the SALT modes. We represent this effect by writing the lasing electric field as a product of the mode profile, a rapid oscillating term, and a slowly varying amplitude [56]: $\mathbf{E}(x,t) = \mathbf{E}_0(x)a(t)e^{i\omega_L t}$. By performing perturbation theory around the SALT solutions, one can show that the mode amplitude $a(t)$ satisfies the stochastic integro-differential oscillator equation:

$$\dot{a} = \int dx\, c(x)\gamma(x) \int^t dt' e^{-\gamma(x)(t-t')} \left(a_0^2 - |a(t')|^2\right) a + f, \tag{5.1}$$

where the nonlinear coefficient $c(x)$, dressed decay rate $\gamma(x)$, steady-state amplitude a_0, and Langevin force f are expressed in terms of SALT solutions (the explicit expressions were derived in Ch. 3). One realization of this stochastic process, $a(t)$, is shown in Fig. 5.1a.

According to the Wiener–Khintchine theorem [163], the power spectrum of the field is given by the Fourier transform of the autocorrelation $\langle a(t)a^*(0)\rangle$ [where angle brackets denote an ensemble average over realizations of Eq. (5.1)]. In order to compute the spectrum, it is convenient to rewrite the complex mode amplitude a as [21]:

$$a(t) = a_0 e^{-u(t)+i\phi(t)}, \tag{5.2}$$

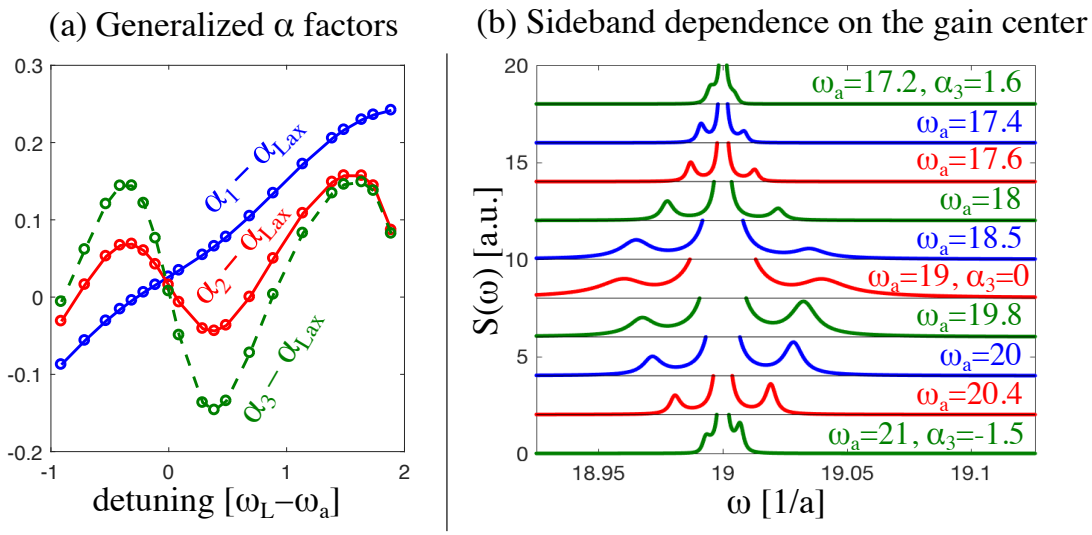

Figure 5.3: (a) Deviation of the generalized α factors (defined in the text) from the traditional factor ($\alpha_{\mathrm{Lax}} \approx \frac{\omega_a - \omega_L}{\gamma_\perp}$ [79]) for the structure from Fig. 5.2a. The relaxation rates of the inversion and polarization are $\gamma_\parallel = 0.006$ and $\gamma_\perp = 1$ respectively. The unsaturated inversion is $D_0 = 0.095$. Each detuning produces a different threshold and output power. (b) Sideband spectrum. By detuning the gain center in the range $\omega_a = 17.2 \ldots 21$, we control the α factors. The sideband asymmetry is reversed when α_3 flips sign. We chose $\gamma_\parallel = 0.02$, $\gamma_\perp = 1$ and $D_0 = 0.095$. Each curve has a different different output power. The y-axis is shifted for representation reasons.

where the phase drift $d\phi(t)/dt$ and intensity $u(t)$ can be treated as Gaussian random variables [164]. Using Eq. (5.2) when evaluating the autocorrelation $\langle a(t)a^*(0)\rangle$ enables us to employ standard results on log-normal distributions and to express the autocorrelation in terms of second moments of $u(t)$ and $\phi(t)$ [165] (Sec. 5.4). We substitute Eq. (5.2) into Eq. (5.1) and linearize the equations assuming that, on average, the intensity fluctuations are small ($\langle |u(t)| \rangle \ll a_0$) since they are suppressed by the nonlinear gain (Sec. 5.5). Then, by solving the linear equations, we obtain explicit expressions for the second moments. The intensity and phase evolve on different time scales: a slow phase drift, which produces the central linewidth, and fast intensity RO, which give rise to sidepeaks. The central linewidth was already calculated in Ch. 3 and is

essentially the phase diffusion coefficient with the α-factor correction. Most generally, the RO dynamics produce an infinite series of decreasing-amplitude sidepeaks and, in most cases, only the first-order sidepeaks are strong enough to be observed. Here we compute only the first-order sidepeaks, but our formulation can also lead to formulas for the higher-order sidepeaks, as outlined in [162]. In Sec. 5.6, we generalize our analysis to the multimode regime. The multimode amplitudes obey a set of coupled stochastic integro-differential equations [Eq. (5.28)], which we linearize by writing each modal amplitude in the form of Eq. (5.2). We find that in the presence of M lasing modes, each resonance peak has $2M$ RO sidepeaks. In contrast to the single-mode higher-order sidepeaks mentioned above, which have exponentially decreasing intensities, the extra peaks we predict in the multimode case are of comparable amplitude (Fig. 5.2c). Even though our derivation requires many pages of algebra, we compare the final result to numerical solution of the oscillator equations [Eqs. (5.1) and (5.28)] and the results match perfectly (Fig. 5.2). Additionally, we verify our theory by directly simulating the stochastic Maxwell–Bloch equations (Fig. 5.4).

5.2 Single-mode formula

Before going through the details of the derivation (in Sec. 5.5), we begin by summarizing our results: the new formula, its validation, and its consequences. We obtain the following result for the spectrum (central peak and first sidebands) of a single-mode

laser:

$$S(\omega) = \frac{\Gamma_0(\alpha_1^2+1)}{(\omega-\omega_L)^2+[\frac{\Gamma_0}{2}(\alpha_1^2+1)]^2}\left(1-\frac{\Gamma_0(\alpha_2^2+1)}{4\Gamma}\right)+$$
$$\frac{\Gamma_0(\alpha_2^2+1)/4}{\Gamma_{\text{eff}}^2+(\omega-\omega_L+\Omega)^2}\left(1+\frac{4\alpha_3}{\alpha_2^2+1}\cdot\frac{\Gamma}{\Omega}+\frac{3\alpha_2^2-1}{\alpha_2^2+1}\cdot\frac{\omega-\omega_L+\Omega}{\Omega}\right)+$$
$$\frac{\Gamma_0(\alpha_2^2+1)/4}{\Gamma_{\text{eff}}^2+(\omega-\omega_L-\Omega)^2}\left(1-\frac{4\alpha_3}{\alpha_2^2+1}\cdot\frac{\Gamma}{\Omega}-\frac{3\alpha_2^2-1}{\alpha_2^2+1}\cdot\frac{\omega-\omega_L-\Omega}{\Omega}\right). \tag{5.3}$$

In the following sections, we express all the parameters in Eq. (5.3) in terms of the coefficients from Eq. (5.1): the Langevin force f, nonlinear coefficients $c(x)$, and dressed decay rate $\gamma(x)$. As such, their evaluation requires no additional free parameters besides those appearing in the Maxwell–Bloch equations: the gain center frequency (ω_a), the relaxation rates of polarization ($\gamma_\perp$) and inversion ($\gamma_\parallel$), and the unsaturated inversion (D_0); Given the Maxwell–Bloch parameters and the laser geometry, one can solve the SALT equations numerically [56] and use Ref. [16] to compute $c(x)$, $\gamma(x)$, and f.

The first term in Eq. (5.3) corresponds to the central Lorentzian peak while the second and third terms are the high- and low-frequency RO sidepeaks. The linewidth of the central peak is $\Gamma_0 = R/a_0^2$, where R is the Langevin noise amplitude, $\langle f(t)f^*(t')\rangle = R\delta(t-t')$, which we computed in Ch. 3 from the fluctuation–dissipation theorem [70] (see Ch. 3). The RO sidepeak frequency and linewidth are $\Omega \approx \pm\left[2a_0^2\int dx\,\mathrm{Re}\,c(x)\gamma(x)\right]^{1/2}$ and $\Gamma_{\text{eff}} \equiv \Gamma_0(\alpha_1^2+1)+\Gamma$ respectively, where $\Gamma \approx \int dx\gamma(x)/2$ is the RO relaxation rate. Since some of the noise power goes into the sidepeaks, the amplitude of the central peak is reduced by a factor of $1-\frac{\Gamma_0}{4\Gamma}(1+\alpha_2^2)$, where the generalized α factor, α_2, Eq. (5.3) is valid when $\Gamma \ll \Omega$ and the sidepeaks do not overlap with the central peak. Eq. (5.3) is formally similar to the result of Ref. [20] but we obtain three kinds of generalized α factors ($\alpha_1, \alpha_2, \alpha_3$ defined below) and derive all the coefficients directly from the Maxwell–Bloch equations, whereas the parameters (Γ_0, Γ, Ω, and α) in Ref. [20] were

expressed in terms of many additional empirical parameters (such as the mode volume, confinement factor, cold-cavity decay rate, effective differential gain, gain saturation coefficient, etc.) and, quantitatively, were only obtained by empirical fits. In Fig. 5.2b, we compare our spectral formula Eq. (5.3) with the numerical solution of Eq. (5.1) and previous theories. The coefficients in Eqs. (5.1) and (5.3) are evaluated for the single-mode one-dimensional complex-cavity laser described in Fig. 5.2a. The numerical spectrum is obtained by time-stepping Eq. (5.1) using a standard Euler scheme and computing the periodogram of the signal by ensemble averaging the FFT of the mode intensity $|a|^2$. Our new formula (cyan) matches the numerical spectrum (red), correcting the shortcoming of theories that did not treat the spatial dependence of the nonlinear coefficient [20] (blue) or the α factor [16] (black). More details on the numerical solution are given in Sec. 5.3.

We find three kinds of generalized amplitude–phase coupling constants: $\alpha_1 = \frac{\int \mathrm{Im}\,[c(x)]}{\int \mathrm{Re}\,[c(x)]}$, $\alpha_2 = \frac{\int \gamma(x)\mathrm{Im}\,[c(x)]}{\int \gamma(x)\mathrm{Re}\,[c(x)]}$, and $\alpha_3 = \frac{\int \gamma(x)^2\mathrm{Im}\,[c(x)]}{\int \gamma(x) \int \gamma(x)\mathrm{Re}\,[c(x)]}$. The generalized α factors deviate from the traditional factor for large α [16] and when $c(x)$ and $\gamma(x)$ vary strongly in space, as demonstrated in Fig. 5.3a. The traditional α factor was first introduced by Lax in the context of single-mode detuned gas lasers [79]. He showed that the amplitude–phase coupling constant is equal to the normalized detuning of the lasing frequency from the atomic resonance, i.e., $\alpha_0 = \frac{\omega_0 - \omega_\mathrm{a}}{\gamma_\perp}$ (which is equal to the ratio of the real and imaginary parts of a refractive index change due to fluctuations in the gain). Later on, the α factor turned out to be a dominant linewidth enhancement factor in semiconductor lasers [14]. In contrast to the Lax factor, which can be either negative or positive depending on the sign of the detuning, the α factor in semiconductor lasers (which arises from refractive-index changes due to carrier-density fluctuations) is typically positive. From Eq. (5.3), it is evident that when α_3 is positive, the low-frequency sidepeaks are stronger than the

high frequency sidepeaks. However, more generally, the asymmetry can change sign, as we show in Fig. 5.3b.

When correctly accounting for gain saturation, one finds that the atomic relaxation rate is enhanced by the presence of the field [as derived in Ch. 3, Eq. (3.13)]. Since the laser-mode profile is spatially varying, the "dressed" relaxation rate $\gamma(x)$ is spatially varying as well [16], in contrast to the bare relaxation rate in Ref. [162] or the constant dressed relaxation rate in Ref. [20], which was obtained from a zero-dimensional model. It is important to note that very close to threshold, the enhancement is small and previous theories are valid. The signature of spatially varying relaxation on the spectrum is smearing of the sidepeaks. The smearing is evident in Figs. 2b–c, where we compare the predictions of our spectral formulas (blue) to a homogeneous model, which corresponds to replacing the dressed decay rate $\gamma(x)$ by the constant (unsaturated) decay $\gamma_{\parallel}$ when evaluating Eqs. (5.3) and (5.29).

5.3 Numerical verification

We verify our single-mode and multimode spectral formulas by comparing the analytical results [Eq. (5.3) and Eq. (5.29)] with brute-force simulations of the stochastic oscillator equations [Eq. (5.1) and Eq. (5.28)]. We study a numerical example where the α factor can be easily tuned: a periodic array of dielectric layers, with gain medium in the three central layers (Fig. 5.1a). We choose the parameters of the structure so that it has a bandgap with two localized modes in the gap (the parameters are given in the figure caption). Using the rule of thumb for low-loss resonators, that α is proportional to the detuning of the gain resonance from the cavity resonance, we can tune α by varying the resonance frequency of the gain. We employ a finte-difference frequency domain

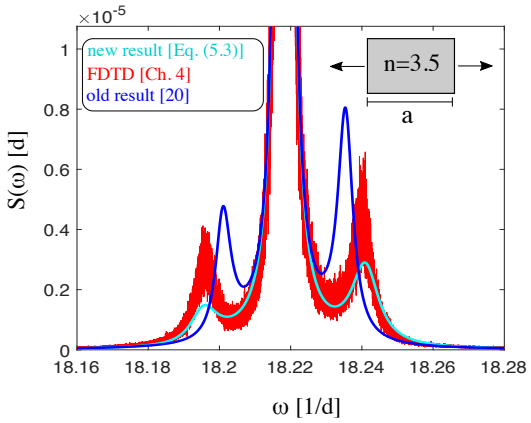

Figure 5.4: Spectrum of a Fabry-Perot laser as predicted by our single mode formula [Eq. (5.3)], FDTD simulations including Langevin noise terms (Ch. 4), and previous theories [20]. The Fabry-Perot laser has an index of n=3.5 and is open on both ends, while the atomic gain medium it contains has a central frequency of $\omega_a = 18.3$, dephasing rate $\gamma_\perp = 0.05$, inversion relaxation rate $\gamma_\parallel = 0.005$, atomic dipole strength $\theta = 2 \times 10^{-9}$, density $N_0 = 10^{10}$, and is pumped to an equilibrium inversion density of $D_0 = 1.34$. Here, the rates are given in units of c/a (a is defined in the inset), while the densities are given in SALT units [56].

(FDFD) [166] approach to discretize the SALT equations on a grid with 180 pixels and solve the resulting equations using the numerical algorithm from [18]. Using the SALT solution, we evaluate the coefficients of the oscillator equations [Eqs. (5.1) and (5.28)] and the spectral formulas [Eqs. (5.3) and (5.29)]. These results are shown in Fig. 5.2 and Fig. 5.3.

We also compare our analytical results against a first-principles simulation based on the finite-difference time-domain method (FDTD) (Fig. 5.4). In these simulations, the electric field is coupled to a set of auxiliary equations which represent the evolution of the inversion and polarization of the atomic degrees of freedom, which are augmented with Langevin force terms (as in Ch. 4). These simulations automatically include the effects of dispersion, radiative losses at the cavity boundary, and the non-linear coupling between the amplitude and phase fluctuations. As such, these simulations represent a

complete test of our theory. In order to demonstrate the new features of our spectral formula we study a Fabry-Perot cavity in which the polarization dephasing rate is much smaller than the free spectral range of the cavity, $\gamma_\perp \ll \Delta\omega$, enabling us to significantly detune the central frequency of the gain medium from the cavity resonance so as to achieve a moderate α factor. As can be seen in Fig. 5.4, semi-quantitative agreement is seen between the analytic theory [Eq. (5.3)] and the noisy FDTD simulations. In particular, although the exact strength of the sidebands is slightly underestimated, their spectral location is predicted nearly exactly, in contrast to previous theories.

5.4 The autocorrelation function

Assuming that $\phi(t)$ and $u(t)$ are Gaussian variables and using standard results on log-normal distributions, one finds that the average autocorrelation of the field is [20, 165]

$$\frac{\langle a(t+t')a^*(t')\rangle}{\langle |a(t')|^2\rangle} = e^{-\frac{1}{2}\left\{\langle[\phi(t+t')-\phi(t')]^2\rangle - \langle[u(t+t')+u(t')]^2\rangle + 4\langle[u(t')]^2\rangle\right\}} \times e^{-i\langle[u(t+t')+u(t')][\phi(t+t')-\phi(t')]\rangle} \tag{5.4}$$

By substituting the ansatz Eq. (5.2) into the oscillator equation Eq. (5.1), we find that the autocorrelations have the form[§]

$$\begin{aligned}
\left\langle[\phi(t+t')-\phi(t')]^2\right\rangle &= a_1 t + a_2(1-e^{-\Gamma t}\cos\Omega t) + a_3 e^{-\Gamma t}\sin\Omega t \\
\left\langle[u(t+t')+u(t')]^2\right\rangle &= a_4(1+e^{-\Gamma t}\cos\Omega t) + a_5 e^{-\Gamma t}\sin\Omega t \\
\left\langle[u(t+t')+u(t')][\phi(t+t')-\phi(t')]\right\rangle &= a_6 + a_7 e^{-\Gamma t}\cos\Omega t + a_8 e^{-\Gamma t}\sin\Omega t.
\end{aligned} \tag{5.5}$$

[§]Note that $\left\langle[u(t+t')+u(t')]^2\right\rangle - 4\left\langle[u(t')]^2\right\rangle = -a_4(1-e^{-\Gamma t}\cos\Omega t) + a_5 e^{-\Gamma t}\sin\Omega t$.

We prove this result in Sec. 5.5 and the coefficients a_i are given in Eq. (5.17), Eq. (5.21), and Eq. (5.27). When the RO sidepeaks are spectrally separated from the central peak, the autocorrelation [Eq. (5.4)] can be simplified. (Mathematically, this is valid when $|a_i| \ll |a_1| \, \forall i = 2 \ldots 8$, which can be interpreted as strong phase diffusion since a_1 is essentially the diffusion coefficient). In this regime, we find

$$\frac{\langle a(t+t')a^*(t')\rangle}{\langle |a(t')|^2\rangle} =$$
$$\begin{cases} e^{-\frac{a_1|t|}{2}}\left(1-\frac{a_2+a_4+2ia_6}{2}\right)+e^{-\Gamma_{\text{eff}}|t|}\left[\cos\Omega|t|\left(\frac{a_2+a_4-2ia_7}{2}\right)+\sin\Omega|t|\left(\frac{a_5-a_3-2ia_8}{2}\right)\right] \\ \qquad\qquad\qquad\qquad\qquad\qquad\qquad\qquad\qquad\qquad \text{if } t>0 \\ e^{-\frac{a_1|t|}{2}}\left(1-\frac{a_2+a_4-2ia_6}{2}\right)+\left[e^{-\Gamma_{\text{eff}}|t|}\cos\Omega|t|\left(\frac{a_2+a_4+2ia_7}{2}\right)+\sin\Omega|t|\left(\frac{a_5-a_3+2ia_8}{2}\right)\right] \\ \qquad\qquad\qquad\qquad\qquad\qquad\qquad\qquad\qquad\qquad \text{otherwise} \end{cases}$$

where $\Gamma_{\text{eff}} \equiv \frac{a_1}{2} + \Gamma$.

The spectrum is then found by taking the Fourier transform of Eq. (5.5), and we obtain:[†]

$$S(\omega) = \frac{a_1}{\omega^2+(a_1/2)^2}\left(1-\frac{a_2+a_4+2a_6}{2}\right)+\frac{\Gamma_{\text{eff}}}{(\omega+\Omega)^2+\Gamma_{\text{eff}}^2}\left[\left(\frac{a_2+a_4+2a_8}{2}\right)+\frac{\Omega+\omega}{\Gamma_{\text{eff}}}\left(\frac{a_5-a_3+2a_7}{2}\right)\right]+$$
$$\frac{\Gamma_{\text{eff}}}{(\omega-\Omega)^2+\Gamma_{\text{eff}}^2}\left[\left(\frac{a_2+a_4-2a_8}{2}\right)-\frac{\Omega-\omega}{\Gamma_{\text{eff}}}\left(\frac{a_5-a_3-2a_7}{2}\right)\right]. \tag{5.6}$$

In the next section, we derive the autocorrelation functions [Eq. (5.5)].

[†]Some Fourier transforms are given in Sec. 5.8.

5.5 Obtaining second-order moments

In this section, we obtain expressions for the phase and intensity correlations. Substituting the ansatz [Eq. (5.2)] into the oscillator equation [Eq. (5.1)] and assuming small intensity fluctuations, one finds the linearized equations:

$$\begin{aligned}
\dot{\phi} &= \int dx\, B(x)\xi(x) + f_I/a_0 \\
\dot{u} &= -\int dx\, A(x)\xi(x) + f_R/a_0 \\
\dot{\xi}(x) &= -\gamma(x)\xi(x) + \gamma(x)u
\end{aligned} \tag{5.7}$$

where we introduced the auxiliary variable $\xi(x) \equiv \int^t dt' e^{-\gamma(x)(t-t')}u(t')$ to turn the integro-differential equation into a set of ordinary differential equations. We define $A(x) \equiv 2a_0^2 \operatorname{Re} c(x)$, $B(x) \equiv 2a_0^2 \operatorname{Im} c(x)$, $f_R = \operatorname{Re}(e^{-i\phi}f)$ and $f_I = \operatorname{Im}(e^{-i\phi}f)$. It is convenient to solve these linear equations in the frequency domain. The Fourier transform of Eq. (5.7) is:

$$\begin{aligned}
i\omega\tilde{\phi} &= \int dx\, B(x)\tilde{\xi}(x) + \tilde{f}_I/a_0 \\
i\omega\tilde{u} &= -\int dx\, A(x)\tilde{\xi}(x) + \tilde{f}_R/a_0 \\
i\omega\tilde{\xi}(x) &= -\gamma(x)\tilde{\xi}(x) + \gamma(x)\tilde{u}
\end{aligned} \tag{5.8}$$

which we solve and obtain

$$\begin{aligned}
\tilde{u} &= \frac{1}{i\omega + \int dx \frac{A(x)\gamma(x)}{\gamma(x)+i\omega}} \cdot \frac{\tilde{f}_R}{a_0} \\
\tilde{\xi}(x) &= \frac{\gamma(x)}{\gamma(x)+i\omega} \cdot \frac{1}{i\omega + \int dx \frac{A(x)\gamma(x)}{\gamma(x)+i\omega}} \cdot \frac{\tilde{f}_R}{a_0} \\
\tilde{\phi} &= \frac{\int dx B(x)\tilde{\xi}(x)}{i\omega} + \frac{\tilde{f}_I}{i\omega a_0}.
\end{aligned} \tag{5.9}$$

By inspection of Eq. (5.9), the functions $\tilde{u}, \tilde{\xi}$, and $\tilde{\phi}$ have poles at $\omega = 0$ and additional complex frequencies. The poles in the upper-half of the complex frequency plane give rise to the spectral peaks.

5.5.1 The phase variance

The phase variance is related to the Fourier transform of the phase via:[§] [167]

$$\left\langle [\phi(t+t') - \phi(t')]^2 \right\rangle = \mathrm{Re}\left[\frac{1}{\pi} \int_{-\infty}^{\infty} d\omega \left\langle |\tilde{\phi}(\omega)|^2 \right\rangle (1 - e^{i\omega t}) \right]. \tag{5.10}$$

In order to compute Eq. (5.10), we use Eq. (5.9) to write

$$\left\langle |\tilde{\phi}(\omega)|^2 \right\rangle = \frac{R}{\omega^2 a_0^2} + \frac{\int\int dx\, dx'\, B(x)B(x')\left\langle \tilde{\xi}(x)\tilde{\xi}^*(x') \right\rangle}{\omega^2}. \tag{5.11}$$

Substitution of Eq. (5.11) into Eq. (5.10) yields two improper integrals, which can be evaluated using the Cauchy residue theorem, with knowledge of the location of the poles.

[§]This relation is derived by substituting the Fourier transform of the phase difference, $\phi(t+t') - \phi(t') = \frac{1}{\sqrt{2\pi}} \int d\omega\, \tilde{\phi}(\omega)\, e^{i\omega t'}(e^{i\omega t} - 1)$, into the phase variance, $\left\langle [\phi(t+t') - \phi(t')]^2 \right\rangle$, and then simplifying the resulting expression: $\frac{1}{2\pi} \int\int d\omega\, d\omega' \left\langle \tilde{\phi}(\omega)\tilde{\phi}^*(\omega') \right\rangle e^{i(\omega-\omega')t'}(e^{i\omega t} - 1)(e^{-i\omega' t} - 1) = \frac{1}{2\pi} \int d\omega \left\langle |\tilde{\phi}(\omega)|^2 \right\rangle (2 - e^{i\omega t} - e^{-i\omega t})$.

The first term in Eq. (5.11) has a pole at $\omega = 0$ and gives rise to a linear diffusion term in the phase variance. That can be seen by calculating the improper integral:

$$\int_{-\infty}^{\infty} \frac{d\omega\,(1-e^{i\omega t})}{\omega^2} = \lim_{\beta\to 0} \oint \frac{dz\,(1-e^{izt})}{(z+i\beta)(z-i\beta)} = 2\pi i \frac{1-e^{-\beta t}}{2i\beta} = \pi t \tag{5.12}$$

The second term in Eq. (5.11) has one pole at $\omega = 0$, which is responsible for the α-factor broadening of the central peak, and two additional poles in the upper-half of the complex plane, which produce the RO sidepeaks. In order to show this, we prove in Sec. 5.9 that $\tilde{\xi}(x)$ can be written as

$$\tilde{\xi}(x) = \frac{\gamma(x)}{\gamma(x)+i\omega} \cdot \frac{\left[\int dx\, Q_x(\omega)\right]^{-1}}{(\omega-\omega_+)(\omega-\omega_-)} \cdot \frac{\tilde{f}_R}{a_0}, \tag{5.13}$$

where $Q_x(\omega) \equiv [\gamma(x) + i\omega]^{-1}$. We find two poles at $\omega_\pm = \pm\Omega + i\Gamma$, where $\Omega \approx [\int dx A(x)\gamma(x) - (\int dx\, \frac{\gamma(x)}{2})^2]^{1/2}$ and $\Gamma \approx \int dx\, \frac{\gamma(x)}{2}$. Substitution of Eq. (5.13) into Eqs. (5.10) and (5.11) yields the improper integral:

$$\begin{aligned} &\int_{-\infty}^{\infty} d\omega \left\langle \tilde{\xi}(x)\tilde{\xi}(x')^* \right\rangle \frac{1-e^{i\omega t}}{\omega^2} = \\ &\int_{-\infty}^{\infty} \frac{d\omega\,\gamma(x)\gamma(x')R}{[i\omega+\gamma(x)][-i\omega+\gamma(x')]} \frac{\left|[\int dx\, Q_x(\omega)\,]\right|^{-2}}{|(\omega-\omega_+)(\omega-\omega_-)|^2} \frac{1-e^{i\omega t}}{\omega^2} \equiv \mathcal{J}_0 + \mathcal{J}_\pm \end{aligned} \tag{5.14}$$

where $\mathcal{J}_0$ and $\mathcal{J}_\pm$ are the terms associated with the poles at 0 and $\omega_\pm$ correspondingly. $\mathcal{J}_0$ is most easily computed by noting that $\tilde{\xi}(0) = \frac{f_R}{Aa_0^2}$ where $A = \int dx\, A(x)$ [as can be seen from Eq. (5.9)]. Therefore,

$$\mathcal{J}_0 = \frac{2\pi R t}{A^2}. \tag{5.15}$$

We compute $\mathcal{J}_\pm$ in the limit of resolved sidepeaks ($\Gamma \ll \Omega$), and find[†]:

$$\mathcal{J}_\pm = \left[\frac{2\pi i\gamma(x)\gamma(x')R(1-e^{i\omega_+ t})}{(\omega_+-\omega_-)(\omega_+-\omega_+^*)(\omega_+-\omega_-^*)\omega_+^2} + \frac{2\pi i\gamma(x)\gamma(x')R(1-e^{i\omega_- t})}{(\omega_--\omega_+)(\omega_--\omega_+^*)(\omega_--\omega_-^*)\omega_-^2}\right] = \frac{\pi\gamma(x)\gamma(x')R}{4\Omega\Gamma}\left[\frac{1-e^{i\omega_+ t}}{(\Omega+i\Gamma)^3} + \frac{1-e^{i\omega_- t}}{(\Omega-i\Gamma)^3}\right] \tag{5.16}$$

Substituting Eqs. (5.11)–(5.16) into Eq. (5.10), we obtain the phase variance:

$$\left\langle[\phi(t+t')-\phi(t')]^2\right\rangle = \frac{R}{a_0^2}\left(1+\alpha_1^2\right)t + \frac{R\alpha_2^2}{2a_0^2\Gamma}(1-e^{-\Gamma t}\cos\Omega t) - \frac{3R\alpha_2^2}{2a_0^2\Omega}e^{-\Gamma t}\sin\Omega t \tag{5.17}$$

where we introduced the generalized α-factors: $\alpha = \frac{\int dx\, B(x)}{\int dx\, A(x)}$ and $\alpha_2 = \frac{\int dx\, B(x)\gamma(x)}{\int dx\, A(x)\gamma(x)}$. Comparing Eq. (5.17) with Eq. (5.5), we find that $a_1 = \frac{R}{a_0^2}\left(1+\alpha^2\right)$, $a_2 = \frac{R\alpha_2^2}{2a_0^2\Gamma}$, and $a_3 = -\frac{3R\alpha_2^2}{2a_0^2\Omega}$.

5.5.2 Intensity autocorrelation

Similar to the derivation of Eq. (5.10), one can show that the intensity autocorrelation is related to the Fourier transform of the intensity via

$$\left\langle[u(t+t')+u(t')]^2\right\rangle = \mathrm{Re}\left[\frac{1}{\pi}\int_{-\infty}^{\infty} d\omega\left\langle|\tilde{u}(\omega)|^2\right\rangle(1+e^{i\omega t})\right]. \tag{5.18}$$

Using the results of Sec. 5.9, $\tilde{u}$ can be written as

$$\tilde{u} = \frac{\left[\int dx\, Q_x(\omega)\right]^{-1}}{(\omega-\omega_+)(\omega-\omega_-)}\cdot\frac{\tilde{f}_R}{a_0}. \tag{5.19}$$

[†]We derive Eq. (5.16) by considering the regime of resolved sidepeaks, where $Q_x(\omega_\pm) = -\frac{1}{\gamma(x)+i\omega_\pm} \approx \frac{i}{\omega_\pm}$. That enables to simplify the residues since $\frac{\gamma(x)\gamma(x')[|\int dx\, Q_x(\omega_\pm)|]^{-2}}{[i\omega_\pm+\gamma(x)][-i\omega_\pm+\gamma(x')]} \approx \gamma(x)\gamma(x')$.

Substitution of Eq. (5.19) into Eq. (5.18) yields an improper integral that we calculate using Cauchy's residue theorem. The integrand has two poles at $\omega_\pm$. In the limit of resolved sidepeaks, we approximate $Q_x(\omega_\pm) \approx \frac{i}{\omega_\pm}$ and find:

$$\int_{-\infty}^{\infty} d\omega \frac{\left|\int dx\, Q_x(\omega)\right|^{-2}(1+e^{i\omega t})}{|(\omega-\omega_+)(\omega-\omega_-)|^2} \approx \frac{2\pi i\omega_+^2(1+e^{i\omega_+ t})}{(\omega_+-\omega_-)(\omega_+-\omega_+^*)(\omega_+-\omega_-^*)} + \frac{2\pi i\omega_-^2(1+e^{i\omega_- t})}{(\omega_--\omega_+)(\omega_--\omega_+^*)(\omega_--\omega_-^*)} = \frac{\pi}{4\Omega\Gamma}\left[\frac{\omega_+^2(1+e^{i\omega_+ t})}{\Omega+i\Gamma} + \frac{\omega_-^2(1+e^{i\omega_- t})}{\Omega-i\Gamma}\right] \tag{5.20}$$

Finally, in the limit of $\Omega \gg \Gamma$, the intensity autocorrelation is

$$\left\langle [u(t+t') + u(t')]^2 \right\rangle = \frac{R}{2\Gamma a_0^2}(1 + \cos\Omega t e^{-\Gamma t}) + \frac{R}{2\Omega a_0^2}\sin\Omega t e^{-\Gamma t} \tag{5.21}$$

Comparing Eq. (5.21) with Eq. (5.5), we find that $a_4 = \frac{R}{2\Gamma a_0^2}$ and $a_5 = \frac{R}{2\Omega a_0^2}$.

5.5.3 The cross term

Similar to the previous sections, one can relate the time averaged cross term to the Fourier transforms of $\tilde{u}$ and $\tilde{\phi}$ via

$$\left\langle [\phi(t+t') - \phi(t')][u(t+t') + u(t')] \right\rangle = \frac{i}{\pi}\int_{-\infty}^{\infty} d\omega\, \sin\omega t \left\langle \tilde{u}^*\tilde{\phi} \right\rangle. \tag{5.22}$$

As in the previous sections, the integrand in Eq. (5.22) has three poles, at $0, \omega_+$ and ω_-. We evaluate the improper integral using Cauchy's theorem, which can be easily applied after rewriting $\tilde{u}$ and $\tilde{\phi}$ using the results of Sec. 5.9:

$$\left\langle \tilde{u}^*\tilde{\phi} \right\rangle = \frac{R}{a_0^2}\int dx\, \frac{B(x)\gamma(x)}{\gamma(x)^2+\omega^2} \cdot \frac{(\frac{\gamma_k}{i\omega} - 1)\left|\int dx\, Q_x(\omega)\right|^{-2}}{|(\omega-\omega_+)(\omega-\omega_-)|^2}. \tag{5.23}$$

When substituting this result into Eq. (5.22), only the odd part of $\left\langle \tilde{u}^* \tilde{\phi} \right\rangle$ contributes to the integral since $\sin \omega t$ is an odd function in ω [which is obtained by replacing the $(\frac{\gamma_k}{i\omega} - 1)$ in the numerator of the integrand by $\frac{\gamma_k}{i\omega}$]. Therefore, Eq. (5.22) reduces to $\frac{1}{\pi} \int_{-\infty}^{\infty} d\omega \, e^{i\omega t} \left\langle \tilde{u}^* \tilde{\phi} \right\rangle_{\text{odd}}$. We find

$$\begin{aligned} &\left\langle [\phi(t+t') - \phi(t')][u(t+t') + u(t')] \right\rangle = \\ &\frac{R}{\pi a_0^2 i} \int dx \, B(x) \int_{-\infty}^{\infty} d\omega \frac{e^{i\omega t}}{\omega} \frac{\gamma(x)^2}{\gamma(x)^2 + \omega^2} \frac{|\int dx \, Q_x(\omega)|^{-2}}{|(\omega - \omega_+)(\omega - \omega_-)|^2} \\ &\qquad\qquad \equiv \mathcal{I}_0 + \mathcal{I}_\pm \end{aligned} \tag{5.24}$$

where $\mathcal{I}_0$ and $\mathcal{I}_\pm$ denote the contributions from the poles at 0 and $\omega_\pm$ correspondingly. The contribution of the pole at 0 is most easily computed bu returning to the solutions of $\tilde{\phi}$ and $\tilde{u}$ [Eq. (5.9)]. We find that[§]

$$\mathcal{I}_0 = \frac{RB}{a_0^2 A^2} \frac{1}{\pi i} \int_{-\infty}^{\infty} d\omega \frac{e^{i\omega t}}{\omega} = \frac{R}{a_0^2} \frac{B}{A^2} \tag{5.25}$$

where we defined $B \equiv \int dx \, B(x)$. We compute $\mathcal{I}_\pm$ by using the approximation $Q_x(\omega_\pm) \approx \frac{i}{\omega_\pm}$, which is valid in the regime of resolved sidepeaks. Therefore, we obtain:

$$\begin{aligned} \mathcal{I}_\pm \approx \frac{\int dx \, B(x) \gamma(x)^2 R}{\pi i a_0^2} \cdot \left(\frac{2\pi i \, e^{i\omega_+ t}}{\omega_+ (\omega_+ - \omega_-)(\omega_+ - \omega_+^*)(\omega_+ - \omega_-^*)} + \frac{2\pi i \, e^{i\omega_- t}}{\omega_- (\omega_- - \omega_+)(\omega_- - \omega_-^*)(\omega_- - \omega_+^*)} \right) = \\ \frac{\int dx \, B(x) \gamma(x)^2 R}{4 i \Gamma \Omega a_0^2} \left(\frac{e^{i\omega_+ t}}{(\Omega + i\Gamma)^2} - \frac{e^{i\omega_- t}}{(\Omega - i\Gamma)^2} \right) \end{aligned} \tag{5.26}$$

[§]Use $\int_{-\infty}^{\infty} d\omega \frac{e^{i\omega t}}{\omega} = \lim_{\alpha \to 0} \int_{-\infty}^{\infty} d\omega \frac{e^{i\omega t}}{\omega + i\alpha} = \pi i$.

Substituting Eqs. (5.23)–(5.26) into Eq. (5.22), we find that the cross-term is

$$\left\langle [\phi(t+t') - \phi(t')][u(t+t') + u(t')] \right\rangle = \frac{R\alpha}{a_0^2 A} + \frac{R\alpha_3}{a_0^2 \Omega} \left(-\frac{2\Gamma}{\Omega} \cos \Omega t \, e^{-\Gamma t} + \sin \Omega t \, e^{-\Gamma t} \right) \tag{5.27}$$

where $\alpha_3 = \frac{\int dx \, B(x)\gamma(x)^2}{2\Gamma \int dx \, A(x)\gamma(x)}$. By comparing Eq. (5.27) with Eq. (5.5), we find that $a_6 = \frac{R\alpha}{a_0^2 A}, a_7 = \frac{2\Gamma R \alpha_3}{a_0^2 \Omega^2}$, and $a_8 = \frac{R\alpha_3}{a_0^2 \Omega}$. This completes our derivation of the single-mode formula [Eq. (5.3)].

5.6 Multimode lasers

In Sec. 5.10, we generalize the analysis of the previous section to the multimode regime. The mode amplitudes (a_μ) in a multimode laser evolve according to a set of coupled nonlinear oscillator equations [16]:

$$\dot{a}_\mu = \sum_\nu \int dx \, c_{\mu\nu}(x) \left[\gamma(x) \int^t dt' e^{-\gamma(x)(t-t')} \left(a_{\nu 0}^2 - |a_\nu(t')|^2 \right) \right] a_\mu + f_\mu \tag{5.28}$$

where $\mu, \nu = 1 \ldots M$, for M lasing modes. We find that the multimode spectrum is given by

$$\begin{aligned} S_{\mu\nu}(\omega) = {} & \frac{\Gamma_{\mu\nu}}{\omega^2 + (\Gamma_{\mu\nu}/2)^2} \left(1 - \frac{\sum_\sigma [\mathbb{S}^\sigma_{\mu\nu} + \mathbb{U}^\sigma_{\mu\nu}]}{2} \right) + \\ & \sum_\sigma \frac{\Gamma_{\text{eff}}^{\mu\nu\sigma}}{(\omega + \Omega_\sigma)^2 + (\Gamma_{\text{eff}}^{\mu\nu\sigma})^2} \left[\left(\frac{\mathbb{S}^\sigma_{\mu\nu} + \mathbb{U}^\sigma_{\mu\nu} + 2\mathbb{Y}^\sigma_{\mu\nu}}{2} \right) + \frac{\Omega_\sigma + \omega}{\Gamma_{\text{eff}}} \left(\frac{\mathbb{V}^\sigma_{\mu\nu} - \mathbb{T}^\sigma_{\mu\nu}}{2} \right) \right] \\ & + \sum_\sigma \frac{\Gamma_{\text{eff}}^{\mu\nu\sigma}}{(\omega - \Omega_\sigma)^2 + (\Gamma_{\text{eff}}^{\mu\nu\sigma})^2} \left[\left(\frac{\mathbb{S}^\sigma_{\mu\nu} + \mathbb{U}^\sigma_{\mu\nu} - 2\mathbb{Y}^\sigma_{\mu\nu}}{2} \right) - \frac{\Omega_\sigma - \omega}{\Gamma_{\text{eff}}} \left(\frac{\mathbb{V}^\sigma_{\mu\nu} - \mathbb{T}^\sigma_{\mu\nu}}{2} \right) \right] \end{aligned} \tag{5.29}$$

where $\Gamma_{\mu\nu} \equiv \frac{2\mathbb{R}_{\mu\nu}}{a_{\mu 0} a_{\nu 0}} + \frac{2(\mathbb{B}\mathbb{A}^{-1}\mathbb{R}\mathbb{A}^{\dagger -1}\mathbb{B}^\dagger)_{\mu\nu}}{a_{\mu 0} a_{\nu 0}}$ are the central linewidths and $\Gamma_{\text{eff}}^{\mu\nu\sigma} \equiv \frac{\Gamma_{\mu\nu}}{2} + \Gamma_\sigma$ are the linewidths of the sidepeaks. $\mathbb{R}$ is the matrix of correlations of noise terms in

each of the modes. $\mathbb{A}$ and $\mathbb{B}$ are matrices whose entries are $A_{\mu\nu} = 2a_{\mu 0}a_{\nu 0}\mathrm{Re}[\int dx\, c_{\mu\nu}(x)]$ and $B_{\mu\nu} = 2a_{\mu 0}a_{\nu 0}\mathrm{Im}[\int dx\, c_{\mu\nu}(x)]$ respectively. The frequencies Ω_σ and linewidths Γ_σ are the real and imaginary parts of the eigenvalues of the matrix $\sqrt{\gamma\mathbb{A}} + i\gamma\mathbb{I}$, where $\sigma = 1 \ldots M$. The matrices $\mathbb{S}^\sigma, \mathbb{T}^\sigma, \mathbb{U}^\sigma, \mathbb{V}^\sigma, \mathbb{X}^\sigma$ and $\mathbb{Y}^\sigma$ are defined in the appendix, along with the derivation.

5.7 Discussion

In this chapter, we used the *ab-initio* theory of radiation noise in lasers from Ch. 3, and presented formulas for the relaxation-oscillation sidepeaks in single- and multimode micro-structured lasers. Since our formulation relies on the methods from Ch. 3, it a similar validity regime, with an additional assumption that the RO relaxation rate (Γ) is faster than the phase diffusion rate, which is the regime when the RO sidepeaks do not overlap with the central peak [$\Gamma_0 = \frac{R}{a_0^2}(1+\alpha_1^2)$]. The effects that are not covered by our linewidth formula are also not treated by our RO sidepeak formula. For example, we assume that spontaneous emission noise is small, and that the laser is operating far enough above threshold. The threshold regime is treated in the next chapter. Our single-mode result [Eq. (5.3)] implies that the spectrum consists of a central peaks at the lasing frequency and two sidepeaks. If we kept higher orders in the small parameter, Γ/Γ_0, our formulation could produce closed-form expressions for higher-order sidepeaks. A similar approach was explored in[162]. However, the amount of noise in subsequent sidepeaks is exponentially decreasing and, therefore, they are almost always negligible.

The ability to compute the RO spectrum while taking full account of spatial variations of the field patterns is a powerful new tool, which may have applications in other fields were ROs have been observed, such as neural gamma-oscillations in the brain [168],

noise-driven synchronization in predator-prey models [169], models for explaining the seismic cycle of earthquake recurrence [170] and more. We discuss these examples in greater detail in Ch. 9.

5.8 Appendix A: List of Fourier transforms

In our derivations, we use the Fourier transforms:

$$\int_{-\infty}^{\infty} dt\, e^{-i\omega t} e^{-\gamma|t|} = \tfrac{2\gamma}{\omega^2+\gamma^2}$$
$$\int_{-\infty}^{\infty} dt\, e^{-i\omega t} e^{-\gamma|t|} \cos\Omega|t| = \tfrac{\gamma}{(\Omega+\omega)^2+\gamma^2} + \tfrac{\gamma}{(\Omega-\omega)^2+\gamma^2}$$
$$\int_{-\infty}^{\infty} dt\, e^{-i\omega t} e^{-\gamma|t|} \sin\Omega|t| = \tfrac{\Omega+\omega}{(\Omega+\omega)^2+\gamma^2} + \tfrac{\Omega-\omega}{(\Omega-\omega)^2+\gamma^2}$$
$$\int_{-\infty}^{\infty} dt\, \mathrm{sign}(t) e^{-i\omega t} e^{-\gamma|t|} \sin\Omega|t| = \tfrac{\gamma/i}{(\Omega+\omega)^2+\gamma^2} - \tfrac{\gamma/i}{(\Omega-\omega)^2+\gamma^2}$$
$$\int_{-\infty}^{\infty} dt\, \mathrm{sign}(t) e^{-i\omega t} e^{-\gamma|t|} \cos\Omega|t| = \tfrac{(\Omega+\omega)/i}{(\Omega+\omega)^2+\gamma^2} + \tfrac{(\Omega-\omega)/i}{(\Omega-\omega)^2+\gamma^2}$$

5.9 Appendix B: Derivation details of Eq. (5.13)

In order to prove Eq. (5.13), we perform several algebraic manipulations. First, we write the denominator of Eq. (5.9) as:

$$i\omega + \int dx\, \tfrac{A(x)\gamma(x)}{\gamma(x)+i\omega} \int dx\, Q_x(\omega)\{A(x)\gamma(x) + i\omega[\gamma(x)+i\omega]\}. \tag{5.30}$$

where $Q_x(\omega) \equiv [\gamma(x)+i\omega]^{-1}$. Then, we use the quadratic formula to rewrite the expression in square brackets as:

$$A(x)\gamma(x) + i\omega[\gamma(x)+i\omega] = [\omega-\omega_+(x)][\omega-\omega_-(x)], \tag{5.31}$$

with $\omega_{\pm}(x) \equiv \pm\sqrt{A(x)\gamma(x) - \frac{\gamma(x)^2}{4}} + i\frac{\gamma(x)}{2}$. Next, we collect powers of ω and obtain:

$$\int dx\, Q_x[\omega - \omega_+(x)][\omega - \omega_-(x)] =$$
$$\int dx\, Q_x(\omega)\left[\omega^2 - \omega\frac{\int dx\, Q_\mu(\omega)[\omega_+(x)+\omega_-(x)]}{\int dx\, Q_x(\omega)} + \frac{\int dx\, Q_x(\omega)\omega_+(x)\omega_-(x)}{\int dx\, Q_x(\omega)}\right] =$$
$$\int dx\, Q_x(\omega) \times [\omega - z_+(\omega)][\omega - z_-(\omega)]. \tag{5.32}$$

with

$$z_{\pm}(\omega) = \frac{-\int dx Q_x(\omega)[\omega_+(x)+\omega_-(x)]}{2\int Q_x(\omega)} \pm \left[\left(\frac{\int Q_x(\omega)[\omega_+(x)+\omega_-(x)]}{2\int Q_x(\omega)}\right)^2 - \frac{\int dx Q_x(\omega)\omega_+(x)\omega_-(x)}{\int dx Q_x(\omega)}\right]^{1/2}. \tag{5.33}$$

We need to find the zeros of Eq. (5.32), since only those contribute to the spectrum. A numerical solution can be easily obtained with Newton's method. However, we proceed by approximating $Q_x(\omega) = dx/(i\omega + \gamma_x)$ to simplify the algebra. In the limit of resolved sidepeaks ($A \gg \gamma_x$ for all x), the RO frequencies are much greater than γ_x and therefore, at the RO frequencies $Q_x(\omega) \approx dx/i\omega$. We obtain a zeroth order approximation to the RO frequencies:

$$z_{\pm}^0 \approx \pm\sqrt{\int dx A(x)\gamma(x) - \left(\int dx \frac{\gamma(x)}{2}\right)^2} + i\int dx \frac{\gamma(x)}{2}. \tag{5.34}$$

In our calculations, we improved the accuracy of the results by taking the first order approximation and setting

$$\omega_{\pm} \approx z_{\pm}(z_{\pm}^0) \tag{5.35}$$

5.10 Appendix C: Derivation of the multimode formula

In this appendix we compute the sideband spectrum for a laser operating in a multimode regime. We showed in previous work that the mode amplitudes in this regime obey coupled nonlinear oscillator equations:

$$\dot{a}_\mu = \sum_{\nu k} C^k_{\mu\nu} \left[\gamma_k \int^t dt' e^{-\gamma_k (t-t')} \left(a^2_{\nu 0} - |a_\nu(t')|^2 \right) \right] a_\mu + f_\mu \tag{5.36}$$

Here we consider the case of M lasing modes and we discretize space into N regions (e.g., employing a finite-difference approach), which becomes exact in the limit of $N \to \infty$. In order to compute the spectrum, we use the following ansatz for the modal amplitudes $a_\mu = a_{\mu 0} e^{-u_\mu + i\phi_\mu}$ and we linearize the equations around steady state, assuming small intensity fluctuations ($u_\mu \ll a_{\mu 0}$). We obtain

$$\begin{aligned} \dot{u}_\mu &= -\sum_{\nu k} A^k_{\mu\nu} \xi^k_\nu + f^R_\mu \\ \dot{\phi}_\mu &= \sum_{\nu k} B^k_{\mu\nu} \xi^k_\nu + f^I_\mu \\ \dot{\xi}^k_\mu &= -\gamma_k \xi^k_\mu + \gamma_k u_\mu \end{aligned} \tag{5.37}$$

where $\xi^k_\mu = \gamma_k \int^t dt' e^{-\gamma_k (t-t')} u_\mu(t')$, $A^k_{\mu\nu} \equiv 2a^2_{\nu 0} \mathrm{Re}[C^k_{\mu\nu}]$ and $B^k_{\mu\nu} \equiv 2a^2_{\nu 0} \mathrm{Re}[C^k_{\mu\nu}]$. Similar to the single-mode case, we take the Fourier-transform of Eq. (5.37) and we solve the equations. We first solve the set of equations for u and ξ_k using matrix manipulations, and then use the results to compute ϕ. First, we write the equations for u_μ and ξ^k_μ in matrix form:

$$\mathbf{x} = [i\omega \mathbb{I} + \mathbf{K}]^{-1} \mathbf{f} \tag{5.38}$$

where:

$$\mathbf{K} = \begin{pmatrix} 0 & \mathbb{A}_1 & \dots & \mathbb{A}_N \\ -\Lambda_1 & \Lambda_1 & & \\ \vdots & & \ddots & \\ -\Lambda_N & & & \Lambda_N \end{pmatrix} \quad \mathbf{x} = \begin{pmatrix} \mathbf{u} \\ \boldsymbol{\xi}^1 \\ \vdots \\ \boldsymbol{\xi}^N \end{pmatrix} \quad \mathbf{f} = \begin{pmatrix} \mathbf{f}_R \\ 0 \\ \vdots \\ 0 \end{pmatrix}. \tag{5.39}$$

$\mathbf{u}$ is the vector whose entries are u_μ and similarly $\mathbf{f}_R$ and $\boldsymbol{\xi}^k$ for $k = 1 \dots N$. Λ_k are diagonal matrices with γ_k on the diagonal. In order to solve Eq. (5.38) and find $\mathbf{u}$ and $\boldsymbol{\xi}_k$, we need to invert the matrix

$$i\omega\mathbb{I} + \mathbf{K} = \begin{pmatrix} A_\omega & B \\ C & D_\omega \end{pmatrix} \tag{5.40}$$

Here

$$\begin{aligned} A_\omega &= \mathbb{I}\omega & B &= \begin{pmatrix} \mathbb{A}_1 & \dots & \mathbb{A}_N \end{pmatrix} \\ C &= \begin{pmatrix} -\Lambda_1 \\ \vdots \\ -\Lambda_N \end{pmatrix} & D_\omega &= \begin{pmatrix} \Lambda_1 + i\omega\mathbb{I} & & \\ & \ddots & \\ & & \Lambda_N + i\omega\mathbb{I} \end{pmatrix} \end{aligned} \tag{5.41}$$

Using Schur's complement, the matrix inverse is

$$[i\omega\mathbb{I} + \mathbf{K}]^{-1} = \begin{pmatrix} (A_\omega - BD_\omega^{-1}C)^{-1} & -(A_\omega - BD_\omega^{-1}C)^{-1}BD_\omega^{-1} \\ -D_\omega^{-1}C(A_\omega - BD_\omega^{-1}C)^{-1} & D_\omega^{-1} + D_\omega^{-1}C(A_\omega - BD_\omega^{-1}C)^{-1}BD_\omega^{-1} \end{pmatrix} \tag{5.42}$$

Therefore, we obtain

$$\mathbf{u} = (A_\omega - BD_\omega^{-1}C)^{-1}\frac{\mathbf{f}_R}{a_0} = \left(i\omega\mathbb{I} + \sum_\mu \mathbb{A}_\mu \frac{\Lambda_\mu}{\Lambda_\mu + i\omega\mathbb{I}}\right)^{-1}\frac{\mathbf{f}_R}{a_0}$$
$$\boldsymbol{\xi}^k = -\left[D_\omega^{-1}C(A_\omega - BD_\omega^{-1}C)^{-1}\right]_k \frac{\mathbf{f}^R}{a_0} = \frac{\Lambda_k}{\Lambda_k + i\omega\mathbb{I}}\cdot\left(i\omega\mathbb{I} + \sum_\mu \mathbb{A}_\mu \frac{\Lambda_\mu}{\Lambda_\mu + i\omega\mathbb{I}}\right)^{-1}\cdot\frac{\mathbf{f}^R}{a_0} \tag{5.43}$$

Similar to the single-mode case, we now show that the matrix $\left(i\omega\mathbb{I} + \sum_\mu \mathbb{A}_\mu \frac{\Lambda_\mu}{\Lambda_\mu + i\omega\mathbb{I}}\right)$ has $2M$ zeros in the upper-half of the complex plane, where M is the number of lasing modes. These zeros give rise to $2M$ RO sidepeaks *around each lasing frequency.*

In order to find the location of the poles, we rewrite the denominator of $\tilde{\xi}_k$ Eq. (5.9) as a second-order polynomial (with zeros at $\omega_\pm$) times a function, $\sum_\mu Q_\mu(\omega)$, which has no zeros in the upper-half plane:

$$i\omega\mathbb{I} + \sum_\mu \mathbb{A}_\mu \frac{\Lambda_\mu}{\Lambda_\mu + i\omega\mathbb{I}} = \left(-\sum_\mu \mathbb{Q}_\mu\right)(\omega - \mathbb{M}_1)(\omega - \mathbb{M}_2) \tag{5.44}$$

where we introduced the definitions $\mathbb{Q}_\mu(\omega) \equiv (\Lambda_\mu + i\omega)^{-1}$ and $\mathbb{M}_{1,2} \equiv \pm\sqrt{\frac{\sum_\mu N\mathbb{Q}_\mu\mathbb{A}_\mu\Lambda_\mu}{\sum_\mu \mathbb{Q}_\mu} - \left(\frac{\sum_\mu \mathbb{Q}_\mu\Lambda_\mu}{\sum_\mu 2\mathbb{Q}_\mu}\right)^2} + i\frac{\sum_\mu \mathbb{Q}_\mu\Lambda_\mu}{\sum_\mu 2\mathbb{Q}_\mu}$. (Note that the square root of a diagonalizable matrix $\mathbb{M} = \mathbb{V}\mathbb{D}\mathbb{V}^{-1}$ is $\sqrt{\mathbb{M}} = \mathbb{V}\sqrt{\mathbb{D}}\mathbb{V}^{-1}$.) In order to show Eq. (5.44), we perform several algebraic manipulations. First, we write $i\omega\mathbb{I} + \sum_\mu \mathbb{A}_\mu \frac{\Lambda_\mu}{\Lambda_\mu + i\omega\mathbb{I}}$ as $\sum_\mu \mathbb{Q}_\mu[N\mathbb{A}_\mu\Lambda_\mu + i\omega(\Lambda_\mu + i\omega\mathbb{I})] = (\sum_\mu \mathbb{Q}_\mu)(-\omega^2 + i\omega\frac{\sum_\mu \mathbb{Q}_\mu\Lambda_\mu}{\sum_\mu \mathbb{Q}_\mu} + \frac{\sum_\mu N\mathbb{Q}_\mu\mathbb{A}_\mu\Lambda_\mu}{\sum_\mu \mathbb{Q}_\mu})$, where in the last equality, we collected powers of ω. Then, since the matrices Λ_μ and $\mathbb{Q}_\mu$ are proportional to unity and therefore commute with any matrix, we can use the quadratic formula for matrices and rewrite this expression in the form of Eq. (5.44).

5.10.1 The phase variance

Similar to the single-mode case, we compute the phase variance using the average of the Fourier transforms $\left\langle \tilde{\phi}_\mu \tilde{\phi}_\nu^* \right\rangle$. The result contains a linear diffusion term coming from the pole of $\left\langle \tilde{\phi}_\mu \tilde{\phi}_\nu^* \right\rangle$ at $\omega = 0$ and additional terms due to relaxation oscillations. We denote these terms by $\mathcal{J}_0$ and $\mathcal{J}_\pm$ correspondingly:

$$\langle \Delta\phi_\mu(t)\Delta\phi_\nu(t)\rangle = \mathrm{Re}\left[\frac{1}{\pi}\int_{-\infty}^{\infty} d\omega \left\langle \tilde{\phi}_\mu \tilde{\phi}_\nu^* \right\rangle [1 - e^{i\omega t}]\right] \equiv \mathcal{J}_0 + \mathcal{J}_\pm \tag{5.45}$$

The quantity $\left\langle \tilde{\phi}_\mu \tilde{\phi}_\nu^* \right\rangle$ can be found using the results from the previous section:

$$\begin{aligned} \boldsymbol{\phi} &= \frac{\sum_k \mathbb{B}_k \boldsymbol{\xi}^k}{i\omega} + \frac{\mathbf{f}_I}{i\omega} \\ \boldsymbol{\xi}^k &= \frac{\Lambda_k}{\Lambda_k + i\omega\mathbb{I}} \cdot \left[\left(-\sum_\mu \mathbb{Q}_\mu\right)(\omega - \mathbb{M}_1)(\omega - \mathbb{M}_2)\right]^{-1} \cdot \frac{\mathbf{f}^R}{a_0}. \end{aligned} \tag{5.46}$$

We obtain

$$\langle \tilde{\phi}_\mu \tilde{\phi}_\nu^* \rangle = \left[\sum_{mn} \frac{\Lambda_m}{\Lambda_m + i\omega\mathbb{I}} \frac{\Lambda_n}{\Lambda_n - i\omega\mathbb{I}} \left|\sum_\ell \mathbb{Q}_\ell\right|^{-2} \frac{\mathbb{B}_m(\omega - \mathbb{M}_1)^{-1}(\omega - \mathbb{M}_2)^{-1}\mathbb{R}(\omega + \mathbb{M}_2^\dagger)^{-1}(\omega + \mathbb{M}_1^\dagger)^{-1}\mathbb{B}_n^\dagger}{a_0^2\omega^2} + \frac{\mathbb{R}}{a_0^2\omega^2}\right]_{\mu\nu} \tag{5.47}$$

Substituting Eq. (5.47) into Eq. (5.46) and applying Cauchy's theorem, we find that the pole at $\omega = 0$ gives

$$\mathcal{J}_0 = \left(\frac{[\mathbb{B}\mathbb{A}^{-1}\mathbb{R}\mathbb{A}^{\dagger -1}\mathbb{B}^\dagger]_{\mu\nu}}{a_0^2} + \frac{\mathbb{R}_{\mu\nu}}{a_0^2}\right) 2t \tag{5.48}$$

where we first used the definition of the matrices $\mathbb{M}_{1,2}$ and $\mathbb{Q}_\mu$ to write $(\mathbb{M}_1)^{-1}(\mathbb{M}_2)^{-1}\mathbb{R}(\mathbb{M}_2^\dagger)^{-1}(\mathbb{M}_1^\dagger)^{-1} = \left|\sum_\ell \mathbb{Q}_\ell(0)\right|^2 \mathbb{A}^{-1}\mathbb{R}\mathbb{A}^{\dagger -1}$ and then introduced the spatially

integrated matrices: $\mathbb{A} \equiv \sum_n \mathbb{A}_n$ and $\mathbb{B} \equiv \sum_n \mathbb{B}_n$.

In order to compute $\mathcal{J}_1$, we introduce the eigenvalue decomposition of $\mathbb{M}_1$ and $\mathbb{M}_2$:

$$(\omega - \mathbb{M}_k)^{-1} = \sum_m \frac{\mathbb{P}_{km}}{\omega - \omega_{km}} \tag{5.49}$$

where $i\omega_\sigma$ are the eigenvalues of $\mathbb{M}_\sigma$ and $\mathbb{P}_\sigma$ are projection operators onto the corresponding eigenspaces. The real and imaginary parts of ω_σ determine the frequencies and widths of the RO side peaks. Substituting Eq. (5.49) into Eq. (5.47) and performing the contour integration, we obtain

$$\mathcal{J}_1 = \sum_{\substack{pq \\ \sigma\ell mn}} \mathrm{Re}\left\{ \frac{(2i\Lambda_p \mathbb{B}_p \mathbb{P}_{1\sigma} \mathbb{P}_{2\ell} \mathbb{R} \mathbb{P}^\dagger_{2m} \mathbb{P}^\dagger_{1n} \mathbb{B}^\dagger_q \Lambda_q)_{\mu\nu}}{a_0^2} \right.$$
$$\left. \left(\frac{1-e^{i\omega_{1\sigma}t}}{\omega_\sigma^2(\omega_{1\sigma}-\omega_{2\ell})(\omega_{1\sigma}-\omega^*_{1m})(\omega_{1\sigma}-\omega^*_{2n})} + \frac{1-e^{i\omega_{2\ell}t}}{\omega_\ell^2(\omega_{2\ell}-\omega_{1\sigma})(\omega_{2\ell}-\omega^*_{1m})(\omega_{2\ell}-\omega^*_{2n})} \right) \right\}, \tag{5.50}$$

which can be conveniently written as

$$\mathcal{J}_1 = \sum_\sigma \left[\mathbb{S}^\sigma_{\mu\nu}(1 - e^{-\Gamma_\sigma t}\cos\Omega_\sigma t) + \mathbb{T}^\sigma_{\mu\nu} e^{-\Gamma_\sigma t}\sin\Omega_\sigma t \right] \tag{5.51}$$

where we introduced

$$\mathbb{S}^\sigma_{\mu\nu} \equiv \mathrm{Re}\left\{ \sum_{\ell mnpq} \frac{(2i\Lambda_p \mathbb{B}_p \mathbb{P}_{1\sigma} \mathbb{P}_{2n} \mathbb{R} \mathbb{P}^\dagger_{2\ell} \mathbb{P}^\dagger_{1m} \mathbb{B}^\dagger_q \Lambda_q)_{\mu\nu}}{a_0^2 \omega_{1\sigma}^2 (\omega_{1\sigma}-\omega_{2n})(\omega_{1\sigma}-\omega^*_{1\ell})(\omega_{1\sigma}-\omega^*_{2m})} + \frac{(2i\Lambda_p \mathbb{B}_p \mathbb{P}_{1n} \mathbb{P}_{2\sigma} \mathbb{R} \mathbb{P}^\dagger_{2\ell} \mathbb{P}^\dagger_{1m} \mathbb{B}^\dagger_q \Lambda_q)_{\mu\nu}}{a_0^2 \omega_{2\sigma}^2 (\omega_{2\sigma}-\omega_{1n})(\omega_{2\sigma}-\omega^*_{1\ell})(\omega_{2\sigma}-\omega^*_{2m})} \right\}$$
$$\mathbb{T}^\sigma_{\mu\nu} \equiv -\mathrm{Im}\left\{ \sum_{\ell mnpq} \frac{(2i\Lambda_p \mathbb{B}_p \mathbb{P}_{1\sigma} \mathbb{P}_{2n} \mathbb{R} \mathbb{P}^\dagger_{2\ell} \mathbb{P}^\dagger_{1m} \mathbb{B}^\dagger_q \Lambda_q)_{\mu\nu}}{a_0^2 \omega_{1\sigma}^2 (\omega_{1\sigma}-\omega_{2n})(\omega_{1\sigma}-\omega^*_{1\ell})(\omega_{1\sigma}-\omega^*_{2m})} - \frac{(2i\Lambda_p \mathbb{B}_p \mathbb{P}_{1n} \mathbb{P}_{2\sigma} \mathbb{R} \mathbb{P}^\dagger_{2\ell} \mathbb{P}^\dagger_{1m} \mathbb{B}^\dagger_q \Lambda_q)_{\mu\nu}}{a_0^2 \omega_{2\sigma}^2 (\omega_{2\sigma}-\omega_{1n})(\omega_{2\sigma}-\omega^*_{1\ell})(\omega_{2\sigma}-\omega^*_{2m})} \right\} \tag{5.52}$$

Indeed, we find that $\left\langle \tilde{\phi}_\mu \tilde{\phi}^*_\nu \right\rangle$ is of the form Eq. (5.6) with $a_1 = 2\left(\frac{[\mathbb{B}\mathbb{A}^{-1}\mathbb{R}\mathbb{A}^{\dagger -1}\mathbb{B}^\dagger]_{\mu\nu}}{a_0^2} + \frac{\mathbb{R}_{\mu\nu}}{a_0^2} \right)$,

$a_{2\sigma} = \mathbb{S}^{\sigma}_{\mu\nu}$ and $a_{3\sigma} = \mathbb{T}^{\sigma}_{\mu\nu}$.

5.10.2 The intensity autocorrelation

As in the single-mode case, we need to compute

$$\left\langle [u_\mu(t+t') + u_\mu(t')][u_\nu(t+t') + u_\nu(t')] \right\rangle = \pi^{-1}\mathrm{Re}\int_{-\infty}^{\infty} d\omega \, \langle \tilde{u}_\mu \tilde{u}^*_\nu \rangle \, (1 + e^{i\omega t}) \tag{5.53}$$

Using the results of Sec. 5.10.1, we have:

$$\mathbf{u} = \left(-\sum\nolimits_\mu \mathbb{Q}_\mu \right)^{-1} (\omega - \mathbb{M}_1)^{-1} (\omega - \mathbb{M}_2)^{-1} \frac{\mathbf{f}_R}{a_0}. \tag{5.54}$$

and therefore the average of the Fourier transformed intensity fluctuations is

$$\begin{aligned} \langle \tilde{u}_\mu \tilde{u}^*_\nu \rangle = \frac{\left[(\omega - \mathbb{M}_1)^{-1} (\omega - \mathbb{M}_2)^{-1} \mathbb{R} (\omega + \mathbb{M}_2^\dagger)^{-1} (\omega + \mathbb{M}_1^\dagger)^{-1} \right]_{\mu\nu}}{a_0^2 \left| \sum_\ell \mathbb{Q}_\ell \right|^2} = \\ \frac{1}{a_0^2 \left| \sum_\ell \mathbb{Q}_\ell \right|^2} \sum_{\mu\nu\sigma\tau} \frac{\left[\mathbb{P}_{1\mu} \mathbb{P}_{2\nu} \mathbb{R} \mathbb{P}^\dagger_{2\sigma} \mathbb{P}^\dagger_{1\tau} \right]_{\mu\nu}}{(\omega - \omega_{1\mu})(\omega - \omega_{2\nu})(\omega - \omega^*_{1\sigma})(\omega - \omega^*_{2\tau})} \end{aligned} \tag{5.55}$$

Next, we perform the integration using Cauchy's theorem and obtain

$$\begin{aligned} \frac{1}{\pi} \int_{-\infty}^{\infty} d\omega \, \langle \tilde{u}_\mu \tilde{u}^*_\nu \rangle \, [1 + e^{i\omega t}] = \mathrm{Re} \left\{ \sum_{\sigma n \ell m} \frac{\left[2i \mathbb{P}_{1\sigma} \mathbb{P}_{2n} \mathbb{R} \mathbb{P}^\dagger_{2\ell} \mathbb{P}^\dagger_{1m} \right]_{\mu\nu}}{a_0^2} \right. \\ \left. \left(\frac{(1 + e^{i\omega_{1\sigma} t}) \omega_\sigma^2}{(\omega_{1\sigma} - \omega_{2n})(\omega_{1\sigma} - \omega^*_{1\ell})(\omega_{1\sigma} - \omega^*_{2m})} + \frac{(1 + e^{i\omega_{2n} t}) \omega_n^2}{(\omega_{2n} - \omega_{1\sigma})(\omega_{2n} - \omega^*_{1\ell})(\omega_{2n} - \omega^*_{2m})} \right) \right\} \end{aligned} \tag{5.56}$$

Once again, we rewrite the result in compact form as

$$\begin{aligned}&\left\langle [u_\mu(t+t')+u_\mu(t')][u_\nu(t+t')+u_\nu(t')]\right\rangle = \\ &\sum_\sigma \left[\mathbb{U}^\sigma_{\mu\nu}(1+e^{-\Gamma_\sigma t}\cos\Omega_\sigma t)+\mathbb{V}^\sigma_{\mu\nu}e^{-\Gamma_\sigma t}\sin\Omega_\sigma t\right],\end{aligned} \tag{5.57}$$

where we introduced the matrices

$$\begin{aligned}\mathbb{U}^\sigma_{\mu\nu} &\equiv \mathrm{Re}\left\{\sum_{\ell mn}\frac{\left[2i\omega^2_{1\sigma}\mathbb{P}_{1\sigma}\mathbb{P}_{2n}\mathbb{R}\mathbb{P}^\dagger_{2\ell}\mathbb{P}^\dagger_{1m}\right]_{\mu\nu}}{a_0^2(\omega_{1\sigma}-\omega_{2n})(\omega_{1\sigma}-\omega^*_{1\ell})(\omega_{1\sigma}-\omega^*_{2m})}+\frac{\left[2i\omega^2_{2\sigma}\mathbb{P}_{1n}\mathbb{P}_{2\sigma}\mathbb{R}\mathbb{P}^\dagger_{2\ell}\mathbb{P}^\dagger_{1m}\right]_{\mu\nu}}{a_0^2(\omega_{2\sigma}-\omega_{1n})(\omega_{2\sigma}-\omega^*_{1\ell})(\omega_{2\sigma}-\omega^*_{2m})}\right\} \\ \mathbb{V}^\sigma_{\mu\nu} &\equiv -\mathrm{Im}\left\{\sum_{\ell mn}\frac{\left[2i\omega^2_{1\sigma}\mathbb{P}_{1\sigma}\mathbb{P}_{2n}\mathbb{R}\mathbb{P}^\dagger_{2\ell}\mathbb{P}^\dagger_{1m}\right]_{\mu\nu}}{a_0^2(\omega_{1\sigma}-\omega_{2n})(\omega_{1\sigma}-\omega^*_{1\ell})(\omega_{1\sigma}-\omega^*_{2m})}-\frac{\left[2i\omega^2_{2\sigma}\mathbb{P}_{1n}\mathbb{P}_{2\sigma}\mathbb{R}\mathbb{P}^\dagger_{2\ell}\mathbb{P}^\dagger_{1m}\right]_{\mu\nu}}{a_0^2(\omega_{2\sigma}-\omega_{1n})(\omega_{2\sigma}-\omega^*_{1\ell})(\omega_{2\sigma}-\omega^*_{2m})}\right\}.\end{aligned} \tag{5.58}$$

The intensity correlations are of the form Eq. (5.6), with $a_{4\sigma}=\mathbb{U}^\sigma_{\mu\nu}$ and $a_{5\sigma}=\mathbb{V}^\sigma_{\mu\nu}$.

5.10.3 The cross term

Similar to the previous sections, we need to compute

$$\left\langle [\phi_\mu(t+t')-\phi_\mu(t')][u_\nu(t+t')+u_\nu(t')]\right\rangle = \frac{1}{\pi}\int_{-\infty}^{\infty}d\omega\, e^{i\omega t}\left\langle \tilde{\phi}\,\tilde{u}^*\right\rangle_o \tag{5.59}$$

Use the expressions from the previous section:

$$\begin{aligned}\mathbf{u} &= \left(-\textstyle\sum_\ell \mathbb{Q}_\ell\right)^{-1}(\omega-\mathbb{M}_1)^{-1}(\omega-\mathbb{M}_2)^{-1}\frac{\mathbf{f}_R}{a_0} \\ \boldsymbol{\phi} &= \sum_k \mathbb{B}_k\frac{\Lambda_k}{\Lambda_k+i\omega}\left(-\textstyle\sum_\ell \mathbb{Q}_\ell\right)^{-1}\frac{(\omega-\mathbb{M}_1)^{-1}(\omega-\mathbb{M}_2)^{-1}\mathbf{f}_R}{i\omega a_0}+\frac{\mathbf{f}_I}{i\omega a_0},\end{aligned} \tag{5.60}$$

we find that the average of the Fourier transformed phase and intensity fluctuations is

$$\left\langle \tilde{\phi}_\mu \tilde{u}_\nu^* \right\rangle_o = \left[\sum_k \frac{\gamma_k}{\gamma_k + i\omega} \frac{\left[\mathbb{B}_k (\omega - \mathbb{M}_1)^{-1} (\omega - \mathbb{M}_2)^{-1} \mathbb{R} (\omega - \mathbb{M}_2^\dagger)^{-1} (\omega - \mathbb{M}_1^\dagger)^{-1} \right]_{\mu\nu}}{i\omega a_0^2 \left| \sum_\ell \mathbb{Q}_\ell \right|^2} \right]_o = \sum_k \frac{\gamma_k}{\gamma_k^2 + \omega^2} \frac{\gamma_k}{i\omega} \frac{\left[\mathbb{B}_k (\omega - \mathbb{M}_1)^{-1} (\omega - \mathbb{M}_2)^{-1} \mathbb{R} (\omega - \mathbb{M}_2^\dagger)^{-1} (\omega - \mathbb{M}_1^\dagger)^{-1} \right]_{\mu\nu}}{a_0^2 \left| \sum_\ell \mathbb{Q}_\ell \right|^2} \tag{5.61}$$

Substituting the latter expression into Eq. (5.59) we find[†]

$$\frac{1}{\pi} \int_{-\infty}^{\infty} d\omega \, e^{i\omega t} \left\langle \tilde{\phi}_\mu \tilde{u}_\nu^* \right\rangle = \frac{\left[2\mathbb{B}\mathbb{A}^{-1} \mathbb{R} (\mathbb{A}^\dagger)^{-1} \right]_{\mu\nu}}{a_0^2} + \sum_{\sigma n \ell m k} \frac{\left[(2\Lambda_k^2 \mathbb{B}_k) \mathbb{P}_{1\sigma} \mathbb{P}_{2n} \mathbb{R} \mathbb{P}_{2\ell}^\dagger \mathbb{P}_{1m}^\dagger \right]_{\mu\nu}}{a_0^2} \left(\frac{e^{i\omega_{1\sigma} t}}{\omega_{1\sigma} (\omega_{1\sigma} - \omega_{2n}) (\omega_{1\sigma} - \omega_{1\ell}^*) (\omega_{1\sigma} - \omega_{2m}^*)} + \frac{e^{i\omega_{2n} t}}{\omega_{2n} (\omega_{2n} - \omega_{1\sigma}) (\omega_{2n} - \omega_{1\ell}^*) (\omega_{2n} - \omega_{2m}^*)} \right) \tag{5.62}$$

Finally, we rewrite Eq. (5.62) in compact form

$$\left\langle [u_\mu(t + t') + u_\mu(t')][\phi_\nu(t + t') + \phi_\nu(t')] \right\rangle = \frac{\left[2\mathbb{B}\mathbb{A}^{-1} \mathbb{R} \mathbb{A}^{-1} \right]_{\mu\nu}}{a_0^2} + \sum_\sigma \left[\mathbb{X}_{\mu\nu}^\sigma e^{-\Gamma_\sigma t} \cos \Omega_\sigma t + \mathbb{Y}_{\mu\nu}^\sigma e^{-\Gamma_\sigma t} \sin \Omega_\sigma t \right], \tag{5.63}$$

[†]Use $\int_{-\infty}^{\infty} \frac{d\omega (1 - e^{i\omega t})}{\omega^2} = \lim_{\alpha \to 0} \int_{-\infty}^{\infty} \frac{d\omega (1 - e^{i\omega t})}{(\omega + i\alpha)(\omega - i\alpha)} = \lim_{\alpha \to 0} 2\pi i \frac{(1 - e^{-\alpha t})}{2i\alpha} = \pi t$ and $\int_{-\infty}^{\infty} \frac{d\omega e^{i\omega t}}{\omega} = \lim_{\alpha \to 0} \int_{-\infty}^{\infty} \frac{d\omega e^{i\omega t}}{(\omega + i\alpha)} = \lim_{\alpha \to 0} 2\pi i e^{-\alpha t} = 2\pi i$

where we introduced the definitions

$$\mathbb{X}^{\sigma}_{\mu\nu} \equiv \left(\sum_p 2\gamma_p^2 \mathbb{B}_p\right)\left(\sum_{\ell mn} \frac{\left[\mathbb{P}_{1\sigma}\mathbb{P}_{2n}\mathbb{R}\mathbb{P}^{\dagger}_{2\ell}\mathbb{P}^{\dagger}_{1m}\right]_{\mu\nu}}{a_0^2\omega_{1\sigma}(\omega_{1\sigma}-\omega_{2n})(\omega_{1\sigma}-\omega^*_{1\ell})(\omega_{1\sigma}-\omega^*_{2m})} + \frac{\left[\mathbb{P}_{1n}\mathbb{P}_{2\sigma}\mathbb{R}\mathbb{P}^{\dagger}_{2\ell}\mathbb{P}^{\dagger}_{1m}\right]_{\mu\nu}}{a_0^2\omega_{2\sigma}(\omega_{2\sigma}-\omega_{1n})(\omega_{2\sigma}-\omega^*_{1\ell})(\omega_{2\sigma}-\omega^*_{2m})}\right)$$
$$\mathbb{Y}^{\sigma}_{\mu\nu} \equiv i\left(\sum_p 2\gamma_p^2 \mathbb{B}_p\right)\left(\sum_{\ell mn} \frac{\left[\mathbb{P}_{1\sigma}\mathbb{P}_{2n}\mathbb{R}\mathbb{P}^{\dagger}_{2\ell}\mathbb{P}^{\dagger}_{1m}\right]_{\mu\nu}}{a_0^2\omega_{1\sigma}(\omega_{1\sigma}-\omega_{2n})(\omega_{1\sigma}-\omega^*_{1\ell})(\omega_{1\sigma}-\omega^*_{2m})} - \frac{\left[\mathbb{P}_{1n}\mathbb{P}_{2\sigma}\mathbb{R}\mathbb{P}^{\dagger}_{2\ell}\mathbb{P}^{\dagger}_{1m}\right]_{\mu\nu}}{a_0^2\omega_{2\sigma}(\omega_{2\sigma}-\omega_{1n})(\omega_{2\sigma}-\omega^*_{1\ell})(\omega_{2\sigma}-\omega^*_{2m})}\right). \tag{5.64}$$

Indeed, the cross term is of the form of Eq. (5.6) , with $a_{6\sigma} = \frac{\left[2\mathbb{B}\mathbb{A}^{-1}\mathbb{R}\mathbb{A}^{-1}\right]_{\mu\nu}}{a_0^2}$, $a_{7\sigma} = \mathbb{X}^{\sigma}_{\mu\nu}$, and $a_{8\sigma} = \mathbb{Y}^{\sigma}_{\mu\nu}$.

Chapter 6

Microcavity laser linewidth near threshold

Most laser linewidth formulas (including ours) have an apparently puzzling feature: they are derived assuming that the laser operates above threshold, but when extrapolated to the threshold regime, the linewidth blows up. In this chapter, we remedy this problem. By including *amplified spontaneous emission* (ASE) from sub-threshold modes, we obtain generalized oscillator equations, which are valid not only above (as in Ch. 3) but also below and at threshold. We compute the laser linewidth at threshold by brute-force time-stepping of the equations. The numerical computation of the spectrum is similar in spirit to early work by Lax [21], but in contrast to Ref. [21], our oscillator equations are more general and are valid for nanophotonic lasers. Moreover, our formulation easily extends to the second threshold and multimode regimes, which are far less studied. In fact, to the best of our knowledge, only Ref. [100] and Ref. [16] obtained closed-form expressions for the linewidth of a two-mode laser, and both expression diverge at the second threshold. In Sec. 6.3.2, we provide an analytic finite formula for the second-threshold linewidth. Our results apply to microstructured amplifiers and lasers with moderate levels of ASE (leaving the problem of strong ASE to future work).

6.1 Introduction

Amplified spontaneous emission (ASE) is *incoherent light*, produced by spontaneous emission, that has been amplified by stimulated emission in a gain medium [171]. Feedback of the ASE by the laser's optical cavity may produce laser operation if the lasing threshold is reached. In high-power lasers and gain amplifiers, ASE is usually an unwanted effect: the excitation of the gain medium is depleted by incoherent ASE rather than by coherent laser radiation [172]. Therefore, effort has been made to suppress ASE in such devices [173]. However, ASE can also be desirable in applications that require low temporal coherence, such as optical coherence tomography [174]. Other examples of applications of ASE include superluminescent diodes and doped fiber amplifiers [175].

Similar to the problem of the laser noise, a theoretical description of ASE in microstructured devices is complicated, as it involves analyzing a stochastic field that satisfies the Maxwell–Bloch equations [Eqs. (2.20) and (2.22)] below the lasing threshold. An additional complication comes from the fact that ASE can modify the steady-state properties of the laser; Strong ASE can deplete the gain and prevent lasing, so it must be taken into account when computing the lasing threshold and, therefore, cannot be described by steady-state theories, such as SALT. In this chapter, we address the situation where the ASE level is moderate, so that it does not affect (to first order) the lasing steady state properties, like threshold and frequency. We use this approach to obtain a finite field intensity at threshold and correct the apparent divergence of our linewidth formula [Eq. (3.3)]. The case of strong ASE can be analyzed with generalization of our theory, as described in the outlook (Sec. 6.4).

Here, we generalize the theory of microlaser noise from Ch. 3 and include ASE from sub-threshold modes. Similar to our treatment of noise in lasers, we first derive dynam-

ical equations for the lasing- and subthreshold-mode amplitudes and then, calculate the variances and autocorrelation functions of the modal amplitudes, from which we obtain the spectrum below, above and near the thresholds. Note that our oscillator equations [Eq. (6.3)] fail far bellow the threshold (when $2\kappa_\mu \leq \gamma(x)$). However, since modes far below the lasing threhold have negligible contributions to the noise spectrum, this mathematical issue does not pose a real difficulty in applying the theory to realistic spectrum calculations. We leave the far sub-threshold regime to future work. Our results reduce to the results of Lax in Ref. [21] for single-mode lasers in the limit of decoupled phase and intensity fluctuations (i.e., when the α factor vanishes), and deviate from the traditional results for complex-cavity devices and far above threshold. We also use our approach to study the multimode regime, and specifically discuss the linewidth enhancement due to mixing of ASE from subthreshold modes with the lasing mode. Since we focus here on computing only the central linewidths (as in Ch. 3), and not the relaxation oscillation sidepeaks (Ch. 5), we analyze the spectrum using an instantaneous toy model which corresponds to the limit where the population inversion relaxes to steady state instantaneously. This ansatz proved to be accurate in computing the laser linewidth above threshold, and we anticipate that it is also exact near threshold.

Let us first introduce the instantaneous toy model. The cavity field can be expressed as a superposition of lasing and subthreshold modes, $\mathbf{E}(x,t) = \sum_\mu a_\mu(t)\mathbf{E}_\mu(x)e^{i\omega_\mu t}$. The modes $\mathbf{E}_\mu$ are eigenstates of a generalized Maxwell equation with a nonlinear permittivity [Eq. (3.50)] [56]. Lasing modes are real-frequency solutions, while subthreshold modes correspond to complex eigenfrequencies with $\mathrm{Im}[\omega_\mu] < 0$. In the presence of noise, the mode amplitudes a_μ are slowly varying, and their autocorrelation determines the laser spectrum. In the single-mode regime, the instantaneous toy model for the laser

mode amplitude is in the form of the Van der Pol oscillator equation, [21]

$$\dot{a} = C(\rho - |a|^2)a + f, \tag{6.1}$$

with ρ changing sign at threshold. (For simplicity, we drop the subscript μ in the single-mode regime.) Above threshold, the nonlinear interaction between the gain and the laser field stabilizes the mode amplitude at a steady state, a_0, and $\rho = a_0^2 > 0$. The Langevin term f represents spontaneous-emission noise, which drives small perturbations away from the steady state, and the amplitude returns to steady state provided that $\mathrm{Re}[C] > 0$. Below threshold, the mode amplitude is zero on average. Any perturbation relaxes to zero at a rate given by the imaginary part of the complex eigenfrequency, $\kappa \equiv \mathrm{Im}[\omega]$. In the spirit of coupled-mode theory (CMT), the dynamics can be written as

$$\dot{a} = \kappa a - C|a|^2 a + f, \tag{6.2}$$

where the nonlinear and Langevin terms have the same form as above threshold. When C is real, Eq. (6.2) agrees with Eq. (6.1) when introducing $\rho = \frac{\mathrm{Im}[\omega]}{C} < 0$. More generally, when C is complex, Eq. (6.2) can be rewritten as: $\dot{a} = C(\rho - |a|^2)a + i\Delta a + f$, with the order parameter $\rho \equiv \frac{\kappa \mathrm{Re}[C]}{|C|^2}(1+\alpha^2)$, the frequency detuning $\Delta \equiv -\kappa\alpha$, and $\alpha \equiv \frac{\mathrm{Im}[C]}{\mathrm{Re}[C]}$, the usual α factor.

We obtain the toy model [Eq. (6.1)] from the Maxwell–Bloch equations [Eqs. (2.20)–(2.22)], in the limit where atoms respond instantaneously to changes in the field intensity (satisfied in "type-A lasers" [160, 16]). More generally, we find that the dynamical

equations are:

$$\dot{a}_\mu = \kappa_\mu a_\mu + \sum_\nu \int dx\, c_{\mu\nu}(x)\gamma(x) \int^t dt' e^{-\gamma(x)(t-t')+2\kappa_\nu t'} \left(\langle |a_\nu| \rangle^2 - |a_\nu(t')|^2 \right) a_\mu + f_\mu. \tag{6.3}$$

For subthreshold modes, $\kappa_\mu < 0$, whereas for lasing modes, $\kappa_\mu = 0$, and the first term on the right-hand side of Eq. (6.3) vanishes. The sum contains contributions from lasing and subthreshold modes. For lasing modes, $\langle |a_\nu| \rangle^2 = a_{\nu 0}^2 > 0$, and the corresponding terms in the sum represent a nonlinear restoring force. For subthreshold, the mode amplitudes have a zero mean $\langle |a_\nu| \rangle^2 = 0$, but a non-zero variance, which increases the linewidths, as we show below. The nonlinear coupling $[c_{\mu\nu}(x)]$, dressed-decay rate $[\gamma(x)]$, and Langevin force (f_μ) are expressed in terms of integrals over SALT solutions [given in Eq. (3.77), Eq. (3.60), and Eq. (3.78) in Ch. 3]. The derivation of the subthreshold terms is explained in the following section. Note that Eq. (6.3) is only valid close enough to threshold so that $2\kappa_\nu < \gamma(x)$. As discussed above, this mathematical issue is insignificant in practice because only near-threshold modes contribute significantly to the ASE spectrum, and will be addressed elsewhere.

The general oscillator equations [Eq. (6.3)] reduce to the instantaneous toy model [Eq. (6.1)] in the appropriate limits. In the single-mode regime, the atomic relaxation rate below threshold is just the bare rate, $\gamma(x) = \gamma_\parallel$, and the nonlinear gain term reduces to:

$$C_{\mu\mu}\gamma_\parallel \int^t dt' e^{-\gamma_\parallel (t-t')-2\kappa_\mu t'} \left(\langle |a_\mu| \rangle^2 - |a_\mu(t')|^2 \right) a_\mu, \tag{6.4}$$

where $C_{\mu\mu} \equiv \int dx c_{\mu\mu}(x)$. When the relaxation rate, $\gamma_\parallel$, is much greater or much

smaller than the nonlinear restoring rate, $\mathrm{Re}[C_{\mu\mu}]a_{\mu 0}^2$, the time delayed nonlinear term in Eq. (6.4) reduces to an instantaneous term similar to Eq. (6.1). In this regime, Eq. (6.3) agrees with Eq. (6.1) when neglecting the term $e^{-2\kappa_\mu t'}$ in the integrand, which is justified because subthreshold modes contribute to the spectrum only when sufficiently close to threshold, but in this regime $\kappa_\mu \ll \gamma_\parallel$.

6.2 Derivation of the oscillator equations

We begin by reviewing the derivation of the oscillator equations for lasing-mode amplitudes [Eq. (3.11)], and then point out differences in the derivation when treating subthreshold modes. First, consider the steady-state regime (analyzed by SALT [56]). In the absence of noise, Maxwell–Bloch equations can be greatly simplified assuming that the field oscillates at a multimode steady state (an assumption which holds for most microlasers). Writing the field as a superposition of modes, $\mathbf{E}(x,t) = \sum_\mu a_{\mu 0}\mathbf{E}_\mu(x)e^{i\omega_\mu t}$, SALT finds that the lasing modes are solutions of the effective Maxwell's equation, $[\nabla\times\nabla\times -\omega_\mu^2\varepsilon(\omega_\mu)]\mathbf{E}_\mu = 0$, with outgoing boundary conditions. The dispersive nonlinear permittivity is:

$$\varepsilon(\omega) = \varepsilon_c + \frac{\gamma_\perp}{(\omega-\omega_a)+i\gamma_\perp}D \tag{6.5}$$

where D is the population-inversion of the gain medium and ε_c is the "cold cavity" permittivity in the absence of gain. The dispersion has a Lorenzian lineshape, $\Gamma(\omega) \equiv \frac{\gamma_\perp}{(\omega-\omega_a)+i\gamma_\perp}$, centered around the gain center frequency ω_a, with width given by the polarization decay rate $\gamma_\perp$. Next, one can include noise (from spontaneous emission, thermal sources or technical noise) by introducing a fluctuating source term on the right-

hand side of Maxwell's equation, $[\nabla \times \nabla \times -\omega_\mu^2 \varepsilon(\omega_\mu)]\mathbf{E}_\mu = \mathbf{F}_\mu$. The noise perturbs the field, causes fluctuations in the modal amplitudes [16]

$$\mathbf{E}(x,t) = \sum_\mu a_\mu(t)\mathbf{E}_\mu(x)e^{i\omega_\mu t}. \tag{6.6}$$

In the spirit of time-dependent perturbation theory, one can substitute this expansion into the Maxwell–Bloch equations and show that the amplitude perturbations give rise to the nonlinear restoring term in the generalized oscillator equations [Eq. (3.11)].

When including subthreshold modes, there are two key differences. First, the Lorenzian linewidth is reduced by the resonance lifetime

$$\Gamma(\omega_\mu) = \varepsilon_c + \frac{\gamma_\perp}{(\omega_\mu - \omega_a) + i(\gamma_\perp + \kappa_\mu)}D \tag{6.7}$$

The new factor, $\Gamma(\omega_\mu)$, modifies the definition of the nonlinear coefficients , $c_{\mu\nu}(x)$, which correspond to subthreshold modes [see Eq. (3.77)]. At at threshold, κ approaches zero, and we reproduce the nonlinear coefficient from Ch. 3. Since we are interested here in the effects of ASE near threshold, this modification leads only to a small quantitative correction.

Another difference is an increased time delay or, equivalently, a reduced relaxation rate of the nonlinear gain term in Eq. (6.3). [In other words, the effective decay rate of the subthreshold mode μ is modified from $\gamma(x)$ to $\gamma(x) - 2\kappa_\mu$; a description that breaks down when $\gamma(x) = 2\kappa_\mu$.] The source for this modification is as follows. The nonlinear gain term is found by computing changes in the population inversion due to changes in the mode amplitudes. In the Maxwell–Bloch framework, temporal changes of the

inversion are governed by

$$\dot{D} = -\gamma_{\parallel} \left[D_{\mathrm{p}} - D + 2\pi i (\mathbf{E} \cdot \mathbf{P}^* - \mathbf{E}^* \cdot \mathbf{P}) \right], \tag{6.8}$$

where $\gamma_{\parallel}$ is the inversion relaxation rate, D_p represents the pump, and the last term is the nonlinear coupling of the field $\mathbf{E}$ to the atomic inversion D via the polarization field $\mathbf{P}$. Assuming that the field is a superposition of a finite set of lasing modes and resonances, one expands the field $\mathbf{E}$ and polarization $\mathbf{P}$ [see Eq. (6.6) and Eq. (5.2) respectively]. Therefore, the product $\mathrm{Im}[\mathbf{E}^* \cdot \mathbf{P}]$ contains cross-terms from different modes, which oscillate at the beating frequency $\Delta_{\mu\nu} \equiv \omega_\mu - \omega_\nu$. In macrocavity lasers, the mode spacing (free spectral range, $\Delta_{\mu\nu}$) is typically much greater than the atomic decay rates, $\gamma_{\parallel}$ and $\gamma_{\perp}$, and the beating terms can be neglected because the effect of rapid oscillations on the average steady state is negligible. Lasing modes are associated with real frequency solutions ($\mathrm{Im}[\omega_\mu] = 0$) and, therefore, the phases of the self terms, $\propto \mathbf{E}_\mu \cdot \mathbf{P}_\mu^* - \mathbf{E}_\mu^* \cdot \mathbf{P}_\mu$, cancel so the inversion is stationary. However, for non-lasing modes, ω_μ is complex and the self term contains an exponentially decaying factor of $e^{-2\kappa_\mu t}$. Once again, this modification vanishes as a subthreshold mode reaches threshold and κ_μ approaches zero.

6.3 Applications

6.3.1 Single-mode linewidth near the first threshold

In this section, we compute the linewidth of a one-dimensional microcavity laser (shown in the inset of Fig. 6.1). For simplicity, we focus on the case where the nonlinear coefficient [C in Eq. (6.3)] is real, which means that the α factor [defined in Eq. (3.30)] is zero.

In that case, the linewidth above threshold is given by a generalized Schawlow-Townes relation, $\Gamma = \frac{1}{2\langle|a|^2\rangle}$ [Eq. (3.29)]. Well below threshold, the linewidth is $\Gamma = \frac{1}{\langle|a|^2\rangle}$ [53], which can be shown by neglecting the nonlinear term in Eq. (6.1). The linewidth above threshold is smaller by a factor of two, due to suppression of intensity fluctuations by the nonlinear interaction. The threshold regime can only be handled numerically. In Ref. [21], the near-threshold spectrum was computed using the eigenvalues of the associated Fokker–Planck equation, while here, we compute the spectrum by directly time-stepping Eq. (6.3). The advantage of our formulation here is that it is adequate for microstructured lasers.

We verify numerically that the product $\Gamma \cdot \left\langle|a|^2\right\rangle / R$ changes from 1 below to $\frac{1}{2}$ above threshold (Fig. 1). The linewidth Γ is obtained from a numerical fit of the simulated spectrum. The amplitude variance $\left\langle|a|^2\right\rangle$ can be calculated analytically far above and below threshed, but near threshold, we use the interpolation formula [21]: $\left\langle|a|^2\right\rangle = \frac{1}{2}\left(\rho + \sqrt{\rho^2 + \frac{2R}{\mathrm{Re}[C]}}\right)$, where R is the diffusion coefficient of the Langevin term, defined via $\langle f(t) f^*(t')\rangle = R\delta(t-t')$.

6.3.2 Linewidth enhancement near subsequent thresholds

According to the traditional Schawlow–Townes formula, the laser linewidth decreases upon increasing the pump power. However, in Sec. 3.6.3, we saw that when additional modes approach threshold, ASE from those modes can mix with the laser signal and actually increase the linewidth. [This effect is similar in spirit to the linewidth enhancement near the first threshold in lasers with a large α factor [101], defined in Eq. (3.30).] In Ch. 3, we computed the spectrum above the second threshold and extrapolated the results to the threshold region. Here, we handle the threshold regime exactly; we ana-

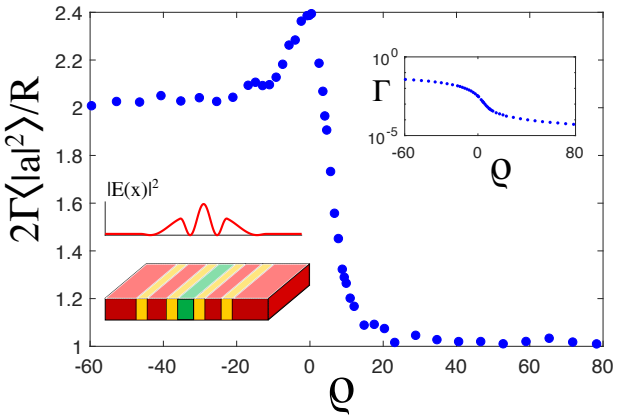

Figure 6.1: The linewidth of a single-mode laser above, below, and near threshold. We compute the linewidth by time-stepping Eq. (6.1) and verify that the product $\frac{2\Gamma\cdot\langle|a|^2\rangle}{R}$ changes from 2 to 1 when crossing threshold. The coefficients of the oscillator equation are computed for the structure shown in the inset—a one-dimensional array of dielectric layers with varying permittivities [$\varepsilon_1 = 1$ (red) and $\varepsilon_2 = 16$ (yellow)] and thicknesses $d_1 = 1$ and d_2 set by the quarter-wave plate condition: $\sqrt{\varepsilon}_1 d_1 = \sqrt{\varepsilon}_2 d_2$. The permittivity of the center layer, $\varepsilon_d = 3$ (green), is chosen to create the localized gap mode (with passive frequency $\omega_c \approx 19.11$) shown at the bottom of the inset. Gain is added in the defect area. We vary ρ (defined in the text) by increasing the pump. The gain center frequency $\omega_a = 19.11$ and linewidth $\gamma_\perp = 1$ are chosen so that the Lax α factor, $\frac{\omega_a - \omega_L}{\gamma_\perp}$, is negligible. The dots are obtained at unsaturated inversion $D_0 = 0 \ldots 0.045$, where the threshold value is $D_{\text{th}} = 0.017$. All parameters are defined in Eq. (6.6) in Ch. 3.

lyze the oscillator equations Eq. (6.3), which are valid throughout the threshold regime, and compute the enhancement analytically.

The oscillator equation of a single-mode laser near the second threshold is

$$\dot{a}_1 = C_{11}(a_{10}^2 - |a_1|^2)a_1 - C_{12}|a_2|^2 a_1 + f_1. \tag{6.9}$$

Assuming that the amplitudes a_1 and a_2 are uncorrelated and evolve on different time scales, we can simplify the second nonlinear term using mean-field approximation: $|a_2|^2 \approx \langle|a_2|^2\rangle_{th}$, where the latter is the variance at the second threshold, computed

below. Defining $\beta \equiv -C_{12}\left\langle |a_2|^2 \right\rangle_{th}$, we obtain the oscillator equation

$$\dot{a}_1 = C_{11}(a_{10}^2 - |a_1|^2)a_1 + \beta a_1 + f_1. \tag{6.10}$$

In order to compute the spectrum, it is convenient to rewrite Eq. (6.10) as

$$\dot{a}_1 = C_{11}(\eta - |a_1|^2)a_1 + i\Delta a_1 + f_1, \tag{6.11}$$

where we introduced two real variables[§]: $\eta \equiv a_{10}^2 + \frac{\mathrm{Re}\,(\beta C_{11}^*)}{|C_{11}|^2} + \frac{\mathrm{Im}\,(\beta C_{11}^*)}{|C_{11}|^2} \cdot \frac{\mathrm{Im}\, C_{11}^*}{\mathrm{Re}\, C_{11}^*}$ and $\Delta \equiv \frac{\mathrm{Im}\,(\beta C_{11}^*)}{\mathrm{Re}\,(C_{11}^*)}$. The presence of ASE from the second mode produces a shift in the mean amplitude and in the oscillation frequency. Using the results of Sec. 6.3.1, we obtain the central result of this section—the linewidth at the second threshold:

$$\Gamma = \frac{R_1}{2\left[a_{10}^2 - \frac{\mathrm{Re}\left(\langle |a_2|^2\rangle_{th} C_{12} C_{11}^*\right)}{|C_{11}|^2} - \frac{\mathrm{Im}\left(\langle |a_2|^2\rangle_{th} C_{12} C_{11}^*\right)}{|C_{11}|^2} \cdot \frac{\mathrm{Im}\, C_{11}^*}{\mathrm{Re}\, C_{11}^*}\right]} \tag{6.12}$$

Typically $\mathrm{Re}[C_{11}^* C_{12}] > 0$ and the denominator is smaller than a_{10}^2, leading to linewidth enhancement. The physical explanation is that intensity in the second mode depletes the gain for the first mode, which causes reduced intensity and enhanced noise.

In order to complete the calculation, we need to compute the second-mode variance at threshold, $\left\langle |a_2|^2 \right\rangle_{th}$. The oscillator equation for the second mode is

$$\dot{a}_2 = C_{21}(\rho_{10} - |a_1|^2)a_2 + C_{22}(p_2 - |a_2|^2)a_2 + f_2, \tag{6.13}$$

[§]The details are as follows. We write $C_{11}(a_{10}^2 - |a_1|^2)a_1 + \beta a_1 = C_{11}\left(a_{10}^2 - |a_1|^2\right)a_1 + C_{11}\frac{\beta C_{11}^*}{|C_{11}|^2}a_1 = C_{11}\left(a_{10}^2 + \frac{\mathrm{Re}[\beta C_{11}^*]}{|C_{11}|^2} - |a_1|^2\right)a_1 + iC_{11}\frac{\mathrm{Im}[\beta C_{11}^*]}{|C_{11}|^2}a_1$ an then introduce two real variables, A and Δ, and require that $iC_{11}\frac{\mathrm{Im}[\beta C_{11}^*]}{|C_{11}|^2} = C_{11}A + i\Delta$. This gives a single complex equations with two unknowns. Finally, $\eta = a_{10}^2 + \frac{\mathrm{Re}\,(\beta C_{11}^*)}{|C_{11}|^2} + A$.

where p_2 in the second parenthesis implies linear decay below and nonlinear restoring force above threshold. Using mean-field approximation for a_1

$$\dot{a}_2 = C_{22}(p_2 - |a_2|^2)a_2 + f_2. \tag{6.14}$$

We use the quasi-linear approximation [x] to estimate the mean variance:

$$\left\langle |a_2|^2 \right\rangle = \frac{1}{2}\left(p_2 + \sqrt{p_2^2 + \frac{2R_2}{\mathrm{Re}[C_{22}]}}\right) \tag{6.15}$$

with $\langle f_2(t) f_2^*(s)\rangle = R_2\delta(t-s)$. At the second threshold, $p_2 = 0$ and the steady-state mean variance at the second threshold is $\left\langle |a_2|^2 \right\rangle_{th} \approx \frac{1}{2}\sqrt{\frac{R_2}{2\mathrm{Re}[C_{22}]}}$.

6.4 Outlook

In this chapter, we incorporated the effect of ASE from subthreshold modes into our microcavity laser-linewidth theory (presented in Ch. 3). We restricted the analysis to "weak ASE" or, more explicitly, to cases where the depletion of the inversion by the ASE field is small enough so that, to first order, it can be neglected when computing the lasing properties. This analysis allowed us to obtain a finite result for the laser linewidth near the first and second thresholds. However, our current analysis does not apply to high-power lasers and high-gain amplifiers, where the ASE field modifies the steady-state lasing properties and, hence, is not captured by SALT.

We anticipate that SALT can be quite easily generalized to incorporate ASE, even at high gain levels. The steady-state field would satisfy a SALT-type nonlinear Maxwell

equation

$$\left[\nabla\times\nabla\times-(\omega_\mu+i\kappa_\mu)^2\left(\varepsilon_c(\mathbf{x})+\frac{\gamma_\perp}{\omega_\mu-\omega_a+i(\gamma_\perp-\kappa_\mu)}D(\mathbf{x})\right)\right]\mathbf{E}_\mu=0, \tag{6.16}$$

with a generalized inversion of the form

$$D(\mathbf{x})=\frac{D_0(\mathbf{x})}{1+\sum_\mu \frac{\gamma_\perp^2}{(\omega_\mu-\omega_a)^2+(\gamma_\perp-\kappa_\mu)^2}\langle|\mathbf{E}_\mu(\mathbf{x})|^2\rangle.} \tag{6.17}$$

In contrast to standard SALT, the steady-state modal intensities $|\mathbf{E}_\mu|^2$ in the denominator should be replaced by the modal mean variances, $\langle|\mathbf{E}_\mu(\mathbf{x})|^2\rangle$, which are finite even for subthreshold modes despite their zero mean [$\langle\mathbf{E}_\mu(\mathbf{x})\rangle=0$]. Similar to our approach in Ch. 3, we can use the fluctuation–dissipation theorem [58, 70] to relate the variance of the field to the linearized Green's function:

$$\langle\mathbf{E}_\mu(\mathbf{x},\omega)\mathbf{E}_\mu^*(\mathbf{x}',\omega')\rangle=-2\hbar\omega^2\mathrm{Im}\,G_{\mu\mu}(\mathbf{x},\mathbf{x},\omega)\coth\left(\frac{\hbar\omega\beta(\mathbf{x})}{2}\right)\delta(\mathbf{x}-\mathbf{x}')\delta(\omega-\omega'). \tag{6.18}$$

The green's function, $G_{\mu\mu}$, may be approximated (in some appropriate limits) by the single-pole approximation via Eq. (3.73) and the inverse temperature, β, is defined in Eq. (3.4). Similar to SALT, this approach produces a nonlinear Maxwell-type equation for the modes, with a generalized nonlinear permittivity which incorporates the effect of ASE of arbitrary intensity.

Part II

Spontaneous Emission at Exceptional Points

Chapter 7

Spontaneous emission at exceptional points

This chapter provides a complete solution to a problem of broad current interest, and which has appeared in multiple recent high-profile publications [38, 176, 177, 178, 179, 180]: understanding light-matter interactions at "exceptional points," where the non-Hermitan eigenvector decomposition breaks down [33].[§] Although there have been several experimental and theoretical papers on this topic, the existing theory is incomplete and often even erroneous, with several authors [42, 48, 49] attributing false significance to the diverging "Petermann" factor at exceptional points ($\widetilde{K}$ in Table 1.1), whereas we prove that the true interaction is always finite and not described by the Petermann factor. Even theoretical descriptions that correctly captured the finite behavior [50] were not general (limited to one dimensional systems or other simplifications). Furthermore, similar problems with exceptional points appear in many other areas of physics [35, 36, 181] and mathematics [46].

[§]The results in this chapter were published in [44].

7.1 Introduction

Electromagnetic resonances enable precise control and enhancement of spontaneous emission and other light–matter interactions. While it is well known that resonances can enhance spontaneous emission rates via the celebrated Purcell effect [29, 182, 183] by confining light to small volumes for long times, recent work [47, 184, 42] suggests that giant enhancements can occur via the less familiar Petermann effect [13, 185, 186, 119, 110]. The Petermann enhancement factor is a measure of non-orthogonality of the modes in non-Hermitian systems and it appears to diverge when two modes coalesce at an *exceptional point* (EP)—an exotic degeneracy in which two modes share the same frequency and mode profile [33, 187]. In recent years, there has been an explosion of interest in EPs due to the many interesting and counter-intuitive phenomena associated with them, e.g., unidirectional reflection and transmission [188, 189, 190], topological mode switching [176, 36, 177], intrinsic single-mode lasing [37, 191], and lasers with unconventional pump dependence [178, 180, 192]. An understanding of spontaneous emission at EPs is essential for their implementation in optical devices, but the existing theory is limited to one-dimensional [50, 193] or discrete oscillator systems [194].

In this chapter, we present a general theory of spontaneous emission near EPs. Our theory extends beyond spontaneous emission to any light–matter interaction described by the local density of states (LDOS) or, more precisely, any situation in which one analyzes the contribution of a given resonance to the emission of a source, such as narrowband thermal emission [195, 196, 197, 198], absorption [199], perfect coherent absorption [200, 201, 202], and nonlinear harmonic generation [203]. Whereas traditional theories of spontaneous emission imply infinite enhancement factors at EPs (since the Petermann factor diverges), we use a modified Jordan-form-based perturbation theory

to derive (finite) bounds on the enhancement at second- and higher-order EP systems. We show that line narrowing leads to a maximum enhancement of 4 in passive systems with second-order EPs and significantly larger enhancements (exceeding 400×) in gain-aided and higher-order EP systems. Our analytical results are presented in Sec. 7.2, where we express the emission rate at an EP in terms of the degenerate mode and its corresponding Jordan vector. This derivation assumes negligible dispersion, but we show in Sec. 7.7 that the effect of dispersion amounts to merely modifying the normalization of the resonant modes, changing the results quantitatively but not qualitatively. Then, in Sec. 7.3, we demonstrate the implications of our theory via a concrete numerical example of coupled plasmonic resonators. Motivated by the fact that an EP is associated with a double pole in the Green's function, we find specific locations where the emission lineshape becomes a squared Lorentzian, with peak amplitude scaling as Q^2, where Q is the resonance quality factor (a dimensionless measure of the resonance lifetime). We show that the enhancement at the EP is thus, potentially, much larger than the Purcell factor, which scales linearly with Q. Then, in Sec. 7.4, we derive bounds on the maximal enhancement at an EP, and we explore these bounds using a periodic system, which allows us to tune gain, loss, and degeneracy independently. Our theory provides a quantitative prescription for achieving large enhancements in practical optical systems, which is applicable to arbitrary geometries and materials and can be implemented with the recent experimental realizations of EPs [38, 191, 37, 190, 35, 178, 176, 36].

Traditional enhancement formulas fail at EPs since they are based on non-degenerate perturbation theory, which is invalid at EPs. Standard perturbation theory relies on Taylor expansions of differentiable functions while, near EPs, eigenvalues change non-analytically in response to small matrix perturbations. Instead, one needs to use a Jordan-form-based perturbative expansion [34, 204]. Although Jordan-vector per-

turbation theory is well known in linear algebra, along with related results on resolvent operators, these algebraic facts have not previously been applied to analyze Purcell/Petermann enhancement or LDOS in a general EP setting. By using such a modified expansion, we obtain a quantitative formula for the LDOS, which is a measure of how much power a dipole source can radiate [28] or, equivalently, a measure of its spontaneous emission rate. Note that similar expansion methods were previously used to evaluate the Green's functions at EPs [205, 65, 206]; however, these works were limited to one-dimensional and paraxial systems, and were not applied to study spontaneous emission. An alternative semi-analytic approach was presented in [50]. In this work, the authors applied a scattering matrix formulation to model a simple one-dimensional system and analyzed its emission properties under $\mathcal{PT}$-symmetry conditions. With proper modifications, such an analysis could be generalized to handle more complicated *one-dimensional* structures (e.g., continuously varying media or complex layered media). However, our general formulas [Eqs. (7.9) and (7.10)] can be directly applied to *any* system with an EP (e.g., three-dimensional photonic or plasmonic structures). Our results demonstrate that the unique spectral properties at EPs are general and do not rely on certain symmetry or dimensionality. Moreover, our theory enables modeling complex experimental apparatuses, performing numerical optimization and design, and deriving bounds on the enhancement, thereby clarifying the usefulness and limitations of EPs for enhancing light matter interactions.

Formally, the Petermann factor is inversely proportional to the "unconjugated norm" of the resonant mode $\int dx\, \varepsilon\, \mathbf{E}_n^2$, where $\mathbf{E}_n$ is the mode profile and ε is the dielectric permittivity (with modifications to this "norm" when treating dispersive media [3].) At an EP, the unconjugated norm vanishes, $\int dx\, \varepsilon\, \mathbf{E}_n^2 = 0$ [187] (a property also called "self-orthogonality" [33]), and the Petermann factor diverges. In fact, the Petermann

factor can *only* diverge at an EP. This is because the Petermann factor is proportional to the sensitivity of an eigenvalue to perturbations [46] (its "condition number"), and that sensitivity can only diverge when two eigenvectors coalesce (i.e., at an EP) by the Bauer–Fike theorem [46]. This implies that our theory is applicable to any system exhibiting a giant Petermann factor. Specifically, in *any* laser and optical parametric oscillator (OPO) system where a giant Petermann factor was identified [207, 48, 49], there must have been a nearby "hidden" EP.

7.2 Local density of states and Green's function expansions

In the following section, we give some background on LDOS calculations in non-degenerate systems, i.e., systems without EPs (Sec. 7.2.1), and then we review perturbation theory for systems with EPs (Sec. 7.2.2). Finally, in Sec. 7.2.3, we present a condensed derivation of our key analytical result—a formula for the LDOS at an EP [Eqs. (7.9) and (7.10)].

7.2.1 LDOS formula for non-degenerate resonances

The spontaneous emission rate of a dipolar emitter, oriented along the direction $\hat{\mathbf{e}}_\mu$, is proportional to the local density of states (LDOS) [208, 209, 210], which can be related to the dyadic Green's function G via [208, 211, 28]

$$\mathrm{LDOS}_\mu(\mathbf{x},\omega) = -\tfrac{2\omega}{\pi}\mathrm{Im}[G_{\mu\mu}(\mathbf{x},\mathbf{x},\omega)]. \tag{7.1}$$

Here, G is defined as the response field to a point source $\mathbf{J} = \delta(\mathbf{x}-\mathbf{x}')\hat{\mathbf{e}}_\mu$ at frequency ω. More generally, currents and fields are related via Maxwell's frequency-domain partial differential equation, $(\nabla \times \nabla \times -\omega^2\varepsilon)\mathbf{E} = i\omega\mathbf{J}$, where ε is the dielectric permittivity of the medium. Throughout the chapter, we use bold letters for vectors, carets for unit vectors, and Greek letters for vector components. Moreover, we set the speed of light to be one ($c = 1$).

Computationally, one can directly invert Maxwell's equations to find G and evaluate Eq. (7.1), but this provides little intuitive understanding. A modal expansion of the Green's function, when applied properly, can be more insightful. Away from an EP, one can use the standard modal expansion formula for non-dispersive media [147]:

$$G_{\mu\mu}(\omega, \mathbf{x}, \mathbf{x}') = \sum_n \frac{E^R_{n\mu}(\mathbf{x})E^L_{n\mu}(\mathbf{x}')}{(\omega^2 - \omega_n^2)(\mathbf{E}^L_n, \mathbf{E}^R_n)}. \tag{7.2}$$

(We review the derivation of this formula for non-dispersive media in Sec. 7.6 and treat dispersion effects in Sec. 7.7). Here, $\mathbf{E}^R_n$ is a solution to the source-free Maxwell's equation with outgoing boundary conditions or, more explicitly, is a right eigenvector of the eigenvalue problem: $\hat{\mathcal{A}}\,\mathbf{E}^R_n = \omega_n^2\mathbf{E}^R_n$ [23] (with $\hat{\mathcal{A}} \equiv \varepsilon^{-1}\nabla \times \nabla\times$). Left modes ($\mathbf{E}^L_n$) are eigenvectors of the transposed operator $\hat{\mathcal{A}}^T \equiv \nabla \times \nabla \times \varepsilon^{-1}$. In reciprocal media $\varepsilon = \varepsilon^T$, and one can easily derive a simple relation between left and right eigenvectors: $\mathbf{E}^L_n = \varepsilon\mathbf{E}^R_n$. Right and left modes which correspond to different eigenvalues are orthogonal under the unconjugated "inner product" $(\mathbf{E}^L_n, \mathbf{E}^R_m) \equiv \int dx\, \mathbf{E}^L_n \cdot \mathbf{E}^R_m = \delta_{m,n}$ [212, 171, 56]. [The convergence of the denominator $(\mathbf{E}^L_n, \mathbf{E}^R_n)$ is proven in Sec. 7.8.] Due to the outgoing boundary condition, the modes solve a non-Hermitian eigenvalue problem whose eigenvalues (ω_n^2) are generally complex, with the imaginary part indicating the decay of modal energy in time (in accordance with our intuition that typical

resonances have finite lifetimes). From Eq. (7.2), it follows that the eigenfrequencies, $\pm\omega_n$, are poles of the Green's function—a key concept in the mathematical analysis of resonances [213]. When considering dispersive media, the denominator in Eq. (7.2) changes to $\int dx \mathbf{E}_n^L(x)[\omega^2\varepsilon(\omega,x) - \omega_n^2\varepsilon(\omega_n,x)]\mathbf{E}_n^R(x)$, as shown in Sec. 7.7.

In many cases of interest, one can get a fairly accurate approximation for the LDOS by including only low-loss resonances in the Green's function expansion [Eq. (7.2)] since only those contribute substantially to the emission spectrum. Under this approximation (i.e., considering only resonances $\omega_n = \Omega_n - i\gamma_n$ which lie close to the real axis in the complex plane, with $\gamma_n \ll \Omega_n$), the spectral lineshape of the LDOS reduces to a sum of Lorentzian functions, weighted by the local field intensity:

$$\mathrm{LDOS}_\mu(\mathbf{x},\omega) \approx \sum_n \frac{1}{\pi}\frac{\gamma_n}{(\omega-\Omega_n)^2+\gamma_n^2}\,\mathrm{Re}\left[\frac{E_{n\mu}^R(\mathbf{x})E_{n\mu}^L(\mathbf{x})}{(\mathbf{E}_n^L,\mathbf{E}_n^R)}\right]. \tag{7.3}$$

Near the resonant frequencies, $\omega \approx \Omega_n$, the peak of the LDOS scales linearly with the resonance quality factor $Q_n \equiv \frac{\Omega_n}{2\gamma_n}$, leading to the celebrated Purcell enhancement factor [29]. On the other hand, the "unconjugated norm," $(\mathbf{E}_n^L, \mathbf{E}_n^R)$, which appears in the denominator of Eq. (7.3) leads to the Petermann enhancement factor, defined as $(\mathbf{E}_n^{R*}, \mathbf{E}_n^R)(\mathbf{E}_n^{L*}, \mathbf{E}_n^L)/\left|(\mathbf{E}_n^L, \mathbf{E}_n^R)\right|^2$ [184]. In non-Hermitian systems, the mode profiles $(\mathbf{E}_n)$ are complex and the Petermann factor is, generally, greater than one. At the extreme case of an EP, the unconjugated norm in the denominator vanishes and the enhancement factor diverges. However, this divergence does not properly describe LDOS or spontaneous emission at EPs since Eq. (7.3) is invalid at the EP. That is because the derivation of Eq. (7.2) assumes that the set of eigenvectors of the operator $\hat{\mathcal{A}}$ spans the Hilbert space, but this assumption breaks down at the EP. In order to complete the set of eigenvectors of $\hat{\mathcal{A}}$ into a basis and obtain a valid expansion for the Green's

function and the LDOS at the EP, we introduce in the following section additional Jordan vectors [46, 34, 214].

7.2.2 Jordan vectors and perturbation theory near EPs

At a (second order) EP, the operator $\hat{\mathcal{A}}_0$ is defective—it does not have a complete basis of eigenvectors and is, therefore, not diagonalizable. However, one can find an eigenvector ($\mathbf{E}_0^R$) and an associated Jordan vector ($\mathbf{J}_0^R$), which satisfy the chain relations [34]:

$$\begin{aligned} \hat{\mathcal{A}}_0 \mathbf{E}_0^R &= \lambda_{\mathrm{EP}} \mathbf{E}_0^R, \\ \hat{\mathcal{A}}_0 \mathbf{J}_0^R &= \lambda_{\mathrm{EP}} \mathbf{J}_0^R + \mathbf{E}_0^R, \end{aligned} \tag{7.4}$$

where $\lambda_{\mathrm{EP}} = \omega_{\mathrm{EP}}^2$ is the degenerate eigenvalue. Equivalent expressions can be written for the left eigenvector $\mathbf{E}_0^L$ and Jordan vector $\mathbf{J}_0^L$. In order to uniquely define the Jordan chain vectors, we need to specify two normalization conditions, which we choose to be $(\mathbf{E}_0^L, \mathbf{J}_0^R) = 1$ and $(\mathbf{J}_0^L, \mathbf{J}_0^R) = 0$.

Near the EP, on can find a pair of nearly degenerate eigenvectors and eigenvalues that satisfy

$$\hat{\mathcal{A}}(p) \mathbf{E}_\pm^R = \lambda_\pm \mathbf{E}_\pm^R, \tag{7.5}$$

where $p \ll 1$ represents a small deviation from the EP. [More explicitly, $\hat{\mathcal{A}}(p) \equiv \frac{1}{\varepsilon(p)} \nabla \times \nabla \times = \hat{\mathcal{A}}_0 + \hat{\mathcal{A}}_1 p + \mathcal{O}(p^2)$, with $\hat{\mathcal{A}}_0$ being defective]. In order to obtain consistent perturbative expansions for $\mathbf{E}_\pm$ and $\lambda_\pm$ near the EP, one can use alternating Puiseux

series [34]:

$$\lambda_\pm = \lambda_0 \pm p^{1/2}\lambda_1 + p\,\lambda_2 \pm p^{3/2}\lambda_3 + \dots$$
$$\mathbf{E}^R_\pm = \mathbf{E}^R_0 \pm p^{1/2}\,\mathbf{E}^R_1 + p\,\mathbf{E}^R_2 \pm p^{3/2}\,\mathbf{E}^R_3 + \dots \tag{7.6}$$

Substituting Eq. (7.6) into Eq. (7.5) and using the additional normalization condition $(\mathbf{J}^L_0, \mathbf{E}^R_\pm) = 1$, one finds that the leading-order terms in the series are

$$\lambda_\pm = \lambda_0 \pm p^{1/2}\Delta + \mathcal{O}(p),$$
$$\mathbf{E}^R_\pm = \mathbf{E}^R_0 \pm p^{1/2}\Delta\,\mathbf{J}^R_0 + \mathcal{O}(p), \tag{7.7}$$

where $\Delta = \sqrt{\frac{(\mathbf{E}^L_0, \hat{\mathcal{A}}_1, \mathbf{E}^R_0)}{(\mathbf{J}^L_0, \mathbf{E}^R_0)}}$ and $(\mathbf{E}^L, \hat{\mathcal{A}}_1, \mathbf{E}^R) \equiv \int \mathbf{E}^L_0 \hat{\mathcal{A}}_1 \mathbf{E}^R_0$. In the next section, we use these results to derive a formula for the LDOS at the EP.

7.2.3 LDOS formula at exceptional points

Near the EP (i.e., for small but non-zero p), one can use the non-degenerate expansion formula Eq. (7.2) to compute G. In order to compute G at the EP, we substitute the perturbative expansions for $\lambda_\pm$ and $\mathbf{E}_\pm$ [Eq. (7.7)] into Eq. (7.2) and take the limit of p going to zero, namely:

$$G^{\mathrm{EP}}_{\mu\mu}(\omega, \mathbf{x}, \mathbf{x}') \approx \lim_{p\to 0}\left[\frac{E^R_{+\mu}(\mathbf{x})E^L_{+\mu}(\mathbf{x}')}{(\lambda-\lambda_+)(\mathbf{E}^L_+, \mathbf{E}^R_+)} + \frac{E^R_{-\mu}(\mathbf{x})E^L_{-\mu}(\mathbf{x}')}{(\lambda-\lambda_-)(\mathbf{E}^L_-, \mathbf{E}^R_-)}\right]. \tag{7.8}$$

The denominators in Eq. (7.8) vanish in the limit of $p \to 0$ since $(\mathbf{E}^L_\pm, \mathbf{E}^R_\pm) = \pm 2\,p^{\frac{1}{2}}\lambda_1 + \mathcal{O}(p)$ [as follows from Eq. (7.6)]. Most importantly, however, the opposite signs of the denominators lead to cancellation of the divergences and a finite value remains, leading

to

$$G^{\mathrm{EP}}_{\mu\mu}(\omega,\mathbf{x},\mathbf{x}') \approx \frac{1}{(\omega^2-\omega^2_{\mathrm{EP}})^2}\frac{E^R_{0\mu}(\mathbf{x})E^L_{0\mu}(\mathbf{x}')}{(\mathbf{E}^L_0,\mathbf{J}^R_0)} + \frac{1}{\omega^2-\omega^2_{\mathrm{EP}}}\frac{E^R_{0\mu}(\mathbf{x})J^L_{0\mu}(\mathbf{x}')+J^R_{0\mu}(\mathbf{x})E^L_{0\mu}(\mathbf{x}')}{(\mathbf{E}^L_0,\mathbf{J}^R_0)}. \qquad (7.9)$$

A formula for the LDOS at the EP is obtained by taking the imaginary part of Eq. (7.9). Considering again low-loss resonances (at which the enhancement is largest), and evaluating the LDOS near the EP frequency ($\omega \approx \omega_{\mathrm{EP}}$), we find

$$\mathrm{LDOS}^{\mathrm{EP}}_{\mu}(\mathbf{x},\omega) \approx$$
$$\frac{\Omega_n}{2\pi}\left(\frac{\gamma_n}{(\omega-\Omega_n)^2+\gamma_n^2}\right)^2 \times \left[\frac{1}{2}\mathrm{Im}\left(\frac{E^R_{0\mu}(\mathbf{x})E^L_{0\mu}(\mathbf{x})}{(\mathbf{E}^0_n,\mathbf{J}^0_n)}\right) - \frac{\omega-\Omega_n}{\gamma_n}\mathrm{Re}\left(\frac{E^R_{0\mu}(\mathbf{x})E^L_{0\mu}(\mathbf{x})}{(\mathbf{E}^0_n,\mathbf{J}^0_n)}\right)\right]. \qquad (7.10)$$

Crucially, Eqs. (7.9) and (7.10) yield finite results at the EP resonance frequency Ω_{EP}. Moreover, a squared Lorentzian prefactor, $\frac{\Omega_n}{2\pi}(\frac{\gamma_n}{(\omega-\Omega_n)^2+\gamma_n^2})^2$, replaces the traditional Lorentzian prefactors near non-degenerate resonances, $\frac{1}{\pi}\frac{\gamma_n}{(\omega-\Omega_n)^2+\gamma_n^2}$ [compare with Eq. (7.3)]. This unique spectral feature follows directly from the existence of a double pole in the modified expansion formula for G [the first term in Eq. (7.9)]. As shown in the following section, a squared Lorentzian lineshape implies a narrower emission peak and greater resonant enhancement in comparison with a non-degenerate resonance at the same complex frequency. The strength of our formulation [Eqs. (7.9) and (7.10)] is that it is applicable to arbitrary structures and can therefore be used to design and optimize complex three-dimensional geometries with EPs. Moreover, it clarifies the conditions under which LDOS enhancement is maximal; essentially, determined by the relative magnitude of the two terms in Eq. (7.9), depending on the location of the emitter.

7.3 Properties of the LDOS at EPs

In this section, we explore the spectral emission properties at EPs [following Eqs. (7.9) and (7.10)] via a numerical model system of coupled plasmonic resonators.

7.3.1 Example: EPs in plasmonic systems

A convenient approach for tailoring the LDOS in practice is by using plasmonic resonances in metallic structures, which can enable ultra-high LDOS enhancements and are widely used in various applications [215]. In this subsection, we numerically explore a system of two plasmonic resonators with approximate parity-time ($\mathcal{PT}$) symmetry. $\mathcal{PT}$ symmetric systems in optics are characterized by having balanced distributions of gain and loss, and are known to possess EPs at critical gain/loss values at which the mode profiles undergo spontaneous symmetry breaking [216]. Our numerical setup is shown on the left-hand side of Fig. 7.1(a). It includes two rods with metallic cores ($\varepsilon = -2.3 + 0.0001i$) and a silica coating ($\varepsilon = 2.1316$) surrounded by air ($\varepsilon = 1$). The dimensions of the structure ($b = 0.643a, t_1 = 0.536a, t_2 = 0.16a$, and $t_3 = 0.268a$) were tuned in order to have two nearly degenerate resonances that are spectrally separated from the neighboring resonances of the structure. We implement outgoing boundary conditions using perfectly matched layers (PML) [28]. In order to preserve the approximate $\mathcal{PT}$ symmetry of the system, gain and loss are added symmetrically to the outer parts of the coating. By brute-force optimization, we find that an EP occurs when the gain/loss value is $|\mathrm{Im}\,\varepsilon| \approx 0.0002551$ and the background permittivity of the upper half of the silica coating is slightly shifted to $\varepsilon \approx 2.129$. The right-hand side of Fig. 7.1(a) depicts the trajectories of the two eigenvalues (red and blue curves) that merge at the

EP (orange dot) upon varying the gain/loss parameter $|\mathrm{Im}\,\varepsilon|$. More details on the numerical optimization procedure are given in Sec. 7.9.

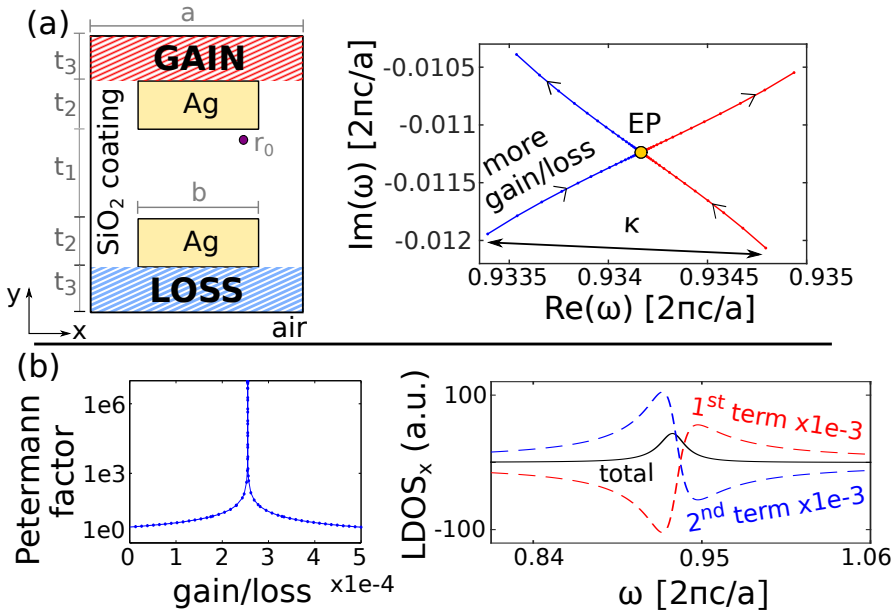

Figure 7.1: Plasmonic system with exceptional points. (a) Left: Two plasmonic resonators with silver cores and a silica coating, with gain and loss (red/blue) added to the outer sides of the coating. Right: Eigenvalue trajectories in the complex plane upon increasing gain/loss. The trajectories merge at the EP (orange dot). (b) The Petermann factor, $(\mathbf{E}_n^{R*}, \mathbf{E}_n^R)(\mathbf{E}_n^{L*}, \mathbf{E}_n^L)/\left|(\mathbf{E}_n^L, \mathbf{E}_n^R)\right|^2$, diverges at the EP (left) while the LDOS_x [evaluated using Eq. (7.2)] remains finite (right), since the giant contributions of the terms in Eq. (7.2) have opposite signs (blue/red curves, scaled by 10^{-3}).

We discretize Maxwell's equations using a finite-difference frequency-domain (FDFD) approach [217] and compute the LDOS by taking imaginary part of the Green's function. The Green's function is found via three methods: (i) directly inverting Maxwell's partial differential equation, (ii) using the non-degenerate expansion formula, Eq. (7.2), which is valid away from the EP, and (iii) using the degenerate formula, Eq. (7.9), at the EP. In principle, one can use the non-degenerate formula, Eq. (7.2), very close to the EP to compute the LDOS, relying on cancellation between the terms to yield a finite

result. However, non-degenerate perturbation theory obfuscates the finite enhancement at the EP, confusing previous estimates of LDOS, whereas our formulation, based on degenerate perturbation theory, naturally captures the finite enhancement.

Our numerical results are shown in Fig. 7.1(b). The plot on the left shows the Petermann factor, which diverges at the EP, while the right-hand side plot shows the finite LDOS. We excite TM modes and, therefore, compute the LDOS for x-polarized modes (denoted by LDOS_x). The red and blue curves show the two terms that contribute to the sum in Eq. (7.2). Upon approaching the EP, the individual contributions to the sum diverge with opposite signs, while their sum (black curve) remains finite. The red and blue curves are scaled by 10^{-3} for ease of presentation.

7.3.2 Simplified model for the LDOS

Although our general formula for the LDOS at the EP can be directly applied to the plasmonic system of Fig. 7.1, it is useful to introduce a simplified model to interpret the results. First, we project Maxwell's operator, $\hat{\mathcal{A}} = \varepsilon^{-1}\nabla\times\nabla\times$, onto the two-dimensional subspace spanned by the nearly degenerate eigenvectors near the EP, thus producing a reduced 2×2 matrix, $\hat{A}$ (which gives a meaningful description of the system as long as the emission spectrum is dominated by the two coalescing resonances). Second, we employ an approach similar in spirit to coupled-mode theory (CMT) [218, 219], which involves expressing the modes of the two-rod system (*the coupled system*) in terms of modes of two reduced systems (*the uncoupled systems*), containing only one or the other rod. Such an approach is valid whenever the rod–rod separation (t_1) in the coupled system is large enough so that the frequency splitting induced by the coupling [κ depicted in Fig. 7.1(a)] is smaller than the uncoupled resonance frequencies. Denoting by U and V

the matrices whose columns are the right and left eigenvectors of the uncoupled system ($\mathbf{E}^R_{1,2}$ and $\mathbf{E}^L_{1,2}$ corresponding to rod 1 and 2 respectively), we find in Sec. 7.10 that the reduced operator is

$$\hat{A} = V^T \hat{\mathcal{A}} U = \begin{pmatrix} [\omega_{\mathrm{EP}} - i\eta]^2 & 2\Omega_{\mathrm{EP}}\kappa \\ 2\Omega_{\mathrm{EP}}\kappa & [\omega_{\mathrm{EP}} + i\eta]^2 \end{pmatrix}. \tag{7.11}$$

Here, $\omega_{\mathrm{EP}} \equiv \Omega_{\mathrm{EP}} - i\gamma$ is the degenerate eigenvalue (Ω_{EP} is the resonant frequency while γ denotes the decay rate), and κ is the near-field coupling between the rods. In general, κ is complex; however, in low-loss systems, κ is almost real and, in the current analysis, we neglect its imaginary part entirely for ease of discussion. Finally, $\eta \approx \frac{\Omega_{\mathrm{EP}}}{2} \frac{\int dx\, \mathbf{E}^L_n (\mathrm{Im}\,\varepsilon/\varepsilon) \mathbf{E}^R_n}{(\mathbf{E}^L_n, \mathbf{E}^R_n)}$ is the imaginary frequency shift induced by the gain and loss ($\mathrm{Im}\,\varepsilon$) in the coating. (This definition of η follows from perturbation theory for small gain/loss [23].) This approach is closely related to the recent 2×2 formalism used in $\mathcal{PT}$-symmetry works [189, 190, 178, 191, 37]. In fact, the formulations are equivalent for low-loss resonances, $\gamma \ll \Omega_{\mathrm{EP}}$, which is the regime considered in this section. We note that the EP occurs at a complex frequency (i.e., below the real axis in the complex plane) due to outgoing boundary conditions.

$\mathbb{1}$

Next, we obtain a simplified formula for the LDOS at the EP. The reduced matrix $\hat{A}$ has an EP at the critical gain/loss value: $\eta = \kappa$. Denoting the defective matrix by $\hat{A}_0$ and the identity operator by $\mathbb{1}$, we can relate the full Green's function at the EP to $\hat{A}_0$ via:

$$G_{\mathrm{EP}}(\mathbf{r}, \mathbf{r}', \omega) \equiv (\hat{\mathcal{A}}_0 - \omega^2 \mathbb{1})^{-1} \approx U(\hat{A}_0 - \omega^2 \mathbb{1})^{-1} V^T. \tag{7.12}$$

A formula for the LDOS is obtained by taking the imaginary part of Eq. (7.12), which allows expressing the LDOS in terms of entries of the 2×2 resolvent operator, $(\hat{A}_0 - \omega^2 \mathbb{1})^{-1}$, weighted by a product of the left and right local fields $\mathbf{E}_n^R \mathbf{E}_m^L$ (with $n, m = 1, 2$ denoting the two resonances of the uncoupled system).

The advantage of this formulation becomes apparent when evaluating the LDOS in close proximity to one of the resonators. For instance, near the gain region [e.g., at $\mathbf{r}_0$ in Fig. 7.1(a)], the lossy mode intensity, $\propto |\mathbf{E}_2^R \mathbf{E}_2^L|$, is negligible, so it follows from Eq. (7.12) that the LDOS is proportional to the first diagonal entry of the resolvent

$$(\hat{A}_0 - \omega^2 \mathbb{1})^{-1}_{[1,1]} = \frac{1}{\omega^2 - \omega_{\mathrm{EP}}^2} + \frac{2\Omega_{\mathrm{EP}}\kappa}{[\omega^2 - \omega_{\mathrm{EP}}^2]^2}. \tag{7.13}$$

Moreover, since we consider low-loss resonances, we can normalize the mode profiles so that they are mainly real ($\mathrm{Re}[\mathbf{E}_1] \approx \mathbf{E}_1$), and we find

$$\mathrm{LDOS}_x(\mathbf{r}_0, \omega) \approx \frac{\mathbf{E}_1^R(\mathbf{r}_0)\mathbf{E}_1^L(\mathbf{r}_0)}{2\Omega_{\mathrm{EP}}} \left[\frac{\gamma}{(\omega - \Omega_{\mathrm{EP}})^2 + \gamma^2} + \frac{\kappa\left[\gamma^2 - (\omega - \Omega_{\mathrm{EP}})^2\right]}{\left[\gamma^2 - (\omega - \Omega_{\mathrm{EP}})^2\right]^2 + \left[2\gamma(\omega - \Omega_{\mathrm{EP}})\right]^2} \right]. \tag{7.14}$$

The inset in Fig. 7.2(b) demonstrates the nearly perfect agreement between this simplified CMT-based LDOS formula (red dashed curve) and brute-force inversion of Maxwell's equation, discretized via FDFD (black curve).

7.3.3 Quadratic scaling and linewidth narrowing

In this subsection, we apply our CMT-based simplified formulas [Eqs. (7.12)–(7.14)] to evaluate the LDOS_x near the upper rod [see Fig. 7.1(a)]. As can be seen from Eq. (7.14),

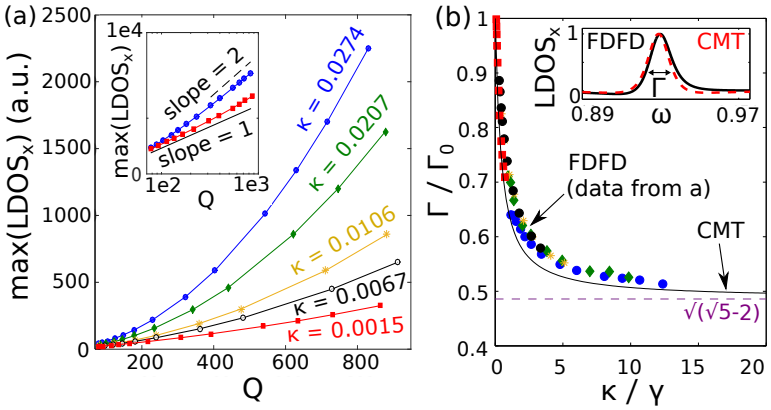

Figure 7.2: Spectral properties of LDOS at EPs. (a) LDOS peak vs. quality factor Q for five coupling values κ, showing quadratic (linear) scaling for large (small) κ values. Q is varied by adding gain to the coating, while κ is varied by changing the rod–rod separation. Inset: Red and blue points from the main plot, on a log-log scale. (b) Normalized linewidth (FWHM) at the EP, Γ/Γ_0, vs. normalized coupling, κ/γ , computed using: 1. FDFD-discretization of Maxwell's equations (dots), and 2. the CMT-based linewidth formula, Eq. (7.16) (black line). The limit as $\kappa/\gamma \to \infty$ is shown in purple (dashed line). ($\Gamma_0 \equiv 2\gamma$ is the FWHM of a Lorentzian curve, see text.) Inset: LDOS$_x$ at the EP, computed via FDFD (black) and via CMT [Eq. (7.14), red dashed line].

the LDOS peak value scales as

$$M_{\mathrm{EP}} \equiv \max_{\omega}\{\mathrm{LDOS}(\mathbf{r}_0,\omega)\} \propto \frac{1}{\gamma} + \frac{\kappa}{\gamma^2}. \tag{7.15}$$

When the resonance-decay rate γ is much smaller than the mode-coupling rate κ, the lineshape approaches a squared Lorentzian curve and M_{EP} scales quadratically with the quality factor $Q \equiv \frac{\Omega_{\mathrm{EP}}}{2\gamma}$ [23]. On the other hand, when $\gamma \gg \kappa$, the LDOS peak scales linearly with Q (similar to isolated resonances, as predicted by Purcell [29]). Figure 7.2(a) demonstrates this key feature. To this end, we computed the LDOS peak, M_{EP}, for several resonance decay rates γ (corresponding to several Q values), varied by introducing homogeneous background gain in the coating. We repeated this procedure

for five rod–rod separations (corresponding to five κ values, ranging from 0.0015 to 0.0274), and verified the scaling laws of Eq. (7.15). The inset in Fig. 7.2(a) presents the blue and red data points from the main plot on a log-log scale, providing additional confirmation for the quadratic scaling at $\gamma \ll \kappa$ (blue) and the linear scaling in the opposite limit of $\gamma \gg \kappa$ (red).

Another consequence of a squared Lorentzian lineshape is a narrower emission peak, compared to that of a standard Lorentzian spectrum. The full-width half maximum (FWHM) of a standard Lorentzian curve, $\frac{1}{\pi}\frac{\gamma_n}{(\omega-\Omega_n)^2+\gamma_n^2}$, is $\Gamma_0 = 2\gamma$ (where $\Omega_0 \pm \Gamma_0/2$ is the frequency at which the Lorentzian drops to half of its maximal value). On the other hand, following Eq. (7.14), the FWHM of the LDOS near an EP with $\mathrm{Im}[\omega_{\mathrm{EP}}] = \gamma$ is

$$\Gamma = \Gamma_0 \sqrt{\frac{\sqrt{\gamma^2 + 2\gamma\kappa + 5\kappa^2} - 2\kappa}{\gamma + \kappa}}. \tag{7.16}$$

As shown in Fig. 7.2(b), the FWHM at the EP is always smaller than Γ_0, approaching a value of $\sqrt{\sqrt{5}-2}\Gamma_0 \approx 0.48\Gamma_0$ in the limit of $\kappa/\gamma \to \infty$. We computed the FWHM directly from the FDFD-discretization of Maxwell's equations (dots) and by using the CMT-based simplified expression, Eq. (7.14) (black solid line), proving very good agreement between the two methods.

7.4 LDOS enhancement at EPs

In the previous section, we showed that a squared Lorentzian lineshape can lead to enhanced emission rates and reduced linewidth. In this section, we quantify the enhancement at the EP and study its bounds. To demonstrate our results, we employ another numerical example: a periodic waveguide (Sec. 7.4.1). This structure allows

us to independently tune gain/loss and degeneracy and, therefore, demonstrate the impacts of the two effects separately. We treat both passive (Sec. 7.4.2) and active (Sec. 7.4.4) systems (i.e., systems without and with gain respectively), and then generalize our results (in Sec. 7.4.3) to higher-order EPs, which form at the coalescence of multiple resonance.

7.4.1 Example: EPs in periodic structures

To demonstrate our results in this section, we numerically explore the periodic structure shown in Fig. 7.3(a). The modes of a periodic system are Bloch wavefunctions of the form $\mathbf{E}(r) = \mathbf{E}_k(r)e^{i\mathbf{k}\cdot\mathbf{r}}$, where $\mathbf{E}_k(r)$ is a periodic function and $\mathbf{k}$ is the wavevector [220]. At each $\mathbf{k}$, the mode $\mathbf{E}_k(r)$ solves an eigenvalue problem of the form [218, 219]: $\hat{\mathcal{A}}(\mathbf{k})\mathbf{E}_{nk} = \omega_{nk}^2\mathbf{E}_{nk}$, where $\hat{\mathcal{A}}(\mathbf{k}) \equiv \varepsilon^{-1}(\nabla + i\mathbf{k}) \times (\nabla + i\mathbf{k})\times$ and n labels the band. The figure of merit for spontaneous emission in periodic structures is the LDOS per wavevector k and field component μ, which is a measure of the power expended by a Bloch-periodic dipole source with a particular k-vector, in the presence of an electromagnetic field polarized along direction μ. We abbreviate it as LDOS_k (also called the mutual density of states [221]). The LDOS_k can be integrated over k to obtain the LDOS from an isolated (non-periodic) point source in the periodic structure [222]. However, the effect of the EP is much clearer in the integrand (LDOS_k) than in the integral (LDOS), and so we focus here on the former for illustration purposes, exploiting the fact that k allows us to control how close we are to an EP without altering losses.

Our example system consists of a waveguide with periodic index modulation along its central axis, $\hat{x}$ [Fig. 7.3(a)]. PML are used to truncate the transverse ($\hat{y}$) direction. The design parameters are: $\varepsilon_1 = 12, \varepsilon_2 = 13.137$, $d = 0.51a$, and $t = 0.25a$. These

parameters were chosen so that the corresponding one-dimensional system (with the same $\varepsilon_1, \varepsilon_2, d$ and infinite thickness, $t \to \infty$) has nearly degenerate second and third frequency bands near $k_x = 0$ [guaranteed by choosing parameters close to the quarter-wave plate condition: $\sqrt{\varepsilon}_1 d = \sqrt{\varepsilon}_2 (a - d)$]. We force an EP for TM-polarized modes (E_z, H_x, H_y) by fine-tuning the wavevector k_x and the permittivity contrast $\delta\varepsilon \equiv \varepsilon_2 - \varepsilon_1$ (see Sec. 7.9, Fig. 7.6). Figure 7.3(a) also depicts the real and imaginary parts of the coalescing eigenvalues (blue and red curves respectively). At $\mathbf{k} = 0$ (also called the Γ point), Maxwell's eigenvalue problem is complex-symmetric and, consequently, the eigenvectors $\mathbf{E}_1^R$ and $\mathbf{E}_2^R$ are orthogonal (see mode profiles in the lower-left corner, having even/odd symmetry when x is flipped to $-x$). At the EP, the eigenmodes $\mathbf{E}_{1,2}^R$ merge into a single degenerate mode $\mathbf{E}_0^R$ (upper-right panel). We also compute the Jordan vector ($\mathbf{J}_0^R$) with our novel iterative method [45], and use it to verify our formula for the LDOS at the EP [Eq. (7.10)].

7.4.2 Passive structures with EPs

Figure 7.3(b) depicts the LDOS_k near the periodic waveguide at several wavevectors ($k_{\text{EP}}, k_1, k_2, k_\infty$ marked on the lower plot). Far from the EP (at k_∞), the LDOS_k is a sum of two non-overlapping Lorentzian curves. As k approaches the EP (e.g., at k_1 and k_2), the resonance peaks begin to overlap and the LDOS_k peaks increase due to the growing Petermann factor. Most importantly, for k values near but not equal to k_{EP}, the traditional modal expansion formula [Eq. (7.2)] approaches the limiting Jordan-form-based formula [Eq. (7.9)]. Physically, this means that structures with nearby EPs can be approximated by truly defective structures, making this analysis useful for experimental systems, which can only be close to but not exactly at an EP due to

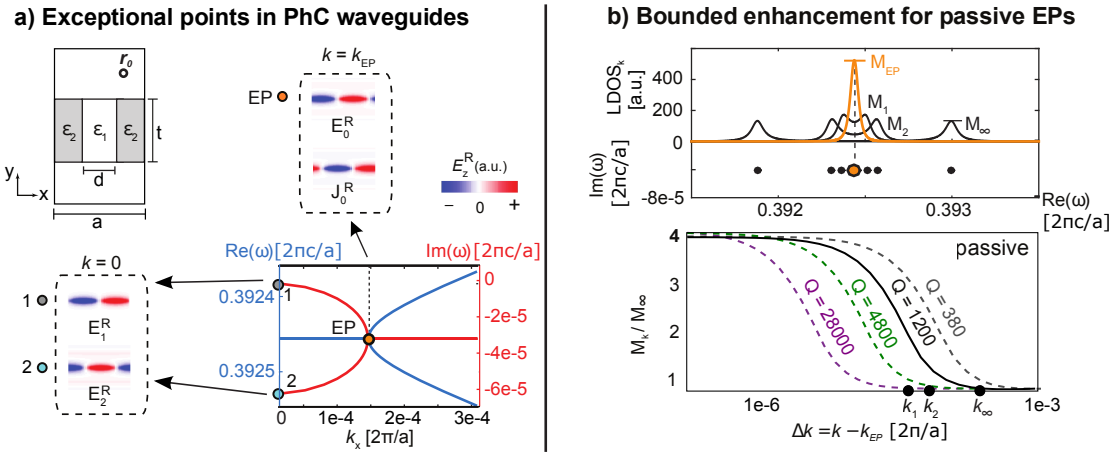

Figure 7.3: Passive periodic waveguides with EPs. (a) Top left: Periodic waveguide with outgoing boundary condition in the transverse direction. Bottom left: Field patterns of TM modes at $k = 0$ (only the real part is shown). Top right: Degenerate mode and Jordan vector at $k_{\rm EP}$. Bottom right: Resonance $[\omega_n(k)]$ vs. k-vector, showing an EP (orange dot) at $k_{\rm EP}a/2\pi \approx 1.46 \times 10^{-4}$. (b) Top plot, positive y-axis: LDOS_k at $\mathbf{r}_0$ for four k-values ($k_{\rm EP}$, k_1, k_2, k_∞, marked on the lower plot). Negative y-axis: Resonances $[\omega_n(k)]$ in the complex plane. Bottom: Normalized LDOS_k peak (M_k/M_∞) vs. deviation from the EP (Δk) for four structures with different Q values, showing 4-fold enhancement at the EP. (M_k is the LDOS peak at k.)

fabrication and calibration imperfections. Computationally, this implies that as long as Maxwell's operator $A(k)$ is not exactly defective, one can use Eq. (7.2) to evaluate the LDOS_k, when properly canceling the divergent terms in the sum.

The lower plot in Fig. 7.3(b) compares the enhancement, M_k/M_∞, for structures with varying quality factors, where we introduce the definitions $M_k \equiv \gamma \cdot \max_\omega[\mathrm{LDOS}_k(\omega)]$ and $M_\infty \equiv \gamma \cdot \max_\omega[\mathrm{LDOS}_\infty(\omega)]$. We change Q by modifying the permittivity contrast $\delta\varepsilon$: Radiation losses decrease with decreasing index contrast of the periodic modulation [223], with the limit of zero contrast corresponding to infinite Q. By plotting the normalized LDOS_k peak (M_k/M_∞) vs. deviation from the EP ($\Delta k \equiv k - k_{\rm EP}$), we find that the enhancement at the EP ($M_{\rm EP}/M_\infty$) is always four-fold, regardless of Q. This follows from a sum rule which states that the spectrally integrated LDOS (and,

therefore, also the LDOS$_k$) is a constant [224]. It implies that the maximum LDOS at an EP [i.e., the peak of a square Lorentzian $\frac{M_{\mathrm{EP}}\gamma^3}{[(\omega-\Omega_{\mathrm{EP}})^2+\gamma^2]^2}$] is four times larger than the maximum LDOS at a non-degenerate resonance [i.e., the peak of a simple Lorentzian $\frac{M_\infty\gamma}{(\omega-\Omega_{\mathrm{EP}})^2+\gamma^2}$].

7.4.3 Passive structures with higher order EPs

Motivated by recent interest in higher-order EPs [225, 226, 227, 179], we generalize our results from the previous section to nth order degeneracies (i.e., EPs that form when n degenerate eigenvectors merge). In this case, we define the enhancement factor as the ratio of the LDOS peak at the EP and at a reference point with n non-degenerate resonances (generalizing our earlier definition for M_{EP}/M_∞). Following the arguments from Sec. 7.3.2, we expect to find a squared Lorentzian emission curve at second-order EPs, a cubic Lorentzian curve at third-order EPs, and a Lorentzian to the nth power, $L_n(\omega) = \frac{M_n\gamma^{2n-1}}{[(\omega-\Omega_{\mathrm{EP}})^2+\gamma^2]^n}$, at nth order EPs. (This is essentially equivalent to a known result on the rate of divergence of the norm of the resolvent matrix as an nth order EP is approached [46].) From the sum rule mentioned above [224], the spectrally integrated LDOS at an nth order EP, $S_n = \int d\omega L_n(\omega) = \frac{M_n\sqrt{\pi}\Gamma[n-\frac{1}{2}]}{\Gamma[n]}$, is equal to the integrated LDOS before the n resonances merge (here, $\Gamma[n]$ is the gamma function). Realizing that the enhancement at the EP is maximal when merging n identical resonances, a bound can be computed by solving $S_n = nS_1$. We find that the enhancement at the EP is at most $M_n/M_1 = \frac{\sqrt{\pi}\Gamma[n+1]}{\Gamma[n-\frac{1}{2}]}$. For example, at third order passive EPs ($n = 3$), the enhancement is at most 8-fold (as some of us recently confirmed in [51]).

These results imply that higher order EPs could potentially provide a new route for achieving order-of-magnitude enhancement of the LDOS and order-of-magnitude nar-

rowing of the emission linewidth (in contrast to traditional methods, which typically aim to maximize the traditional Purcell factor by increasing the quality factor and reducing the mode volume [29]). However, this result does not necessarily mean that higher-order EPs will yield a larger LDOS than the *best* lower-order EP or single resonance. The reason is that the degrees of freedom that one would use to bring n resonances together might otherwise be employed to enhance the Q of an individual resonance. In practice, there will be a tradeoff between the quality of individual resonances and the order of the EP.

7.4.4 Active structures

We show in this section that much greater enhancements can be achieved in active systems, i.e., by introducing gain. Figure 7.4 compares four periodic waveguides with different index contrasts ($\delta\varepsilon$), corresponding to different passive quality factors, Q_p. Gain and loss are added to each of the waveguides in order to force EPs, all of which share the same active quality factor Q_a. The empty (filled) markers in Fig. 7.4(a) are the EP resonances (ω_{EP}) in the complex plane before (after) adding gain/loss. As shown in Fig. 7.4(b), the structure with the smallest passive quality factor Q_p has the largest LDOS_k enhancement at the EP since it requires more gain in order to attain the same Q_a. Structures with smaller initial Q_p values can lead to even greater enhancements, and we present such a case in Sec. 7.11. In principle, the relative enhancement at the EP, $M_{\mathrm{EP}}/M_{\infty}$, is not bounded in this computational model. However, in practice, giant *relative* enhancements do not necessarily imply giant *absolute* LDOS values (since the value of the LDOS at the reference point may be very small). Moreover, when adding enough gain to bring the system to the lasing threshold, stimulated emission eventually

limits line narrowing and LDOS enhancement at the EP.

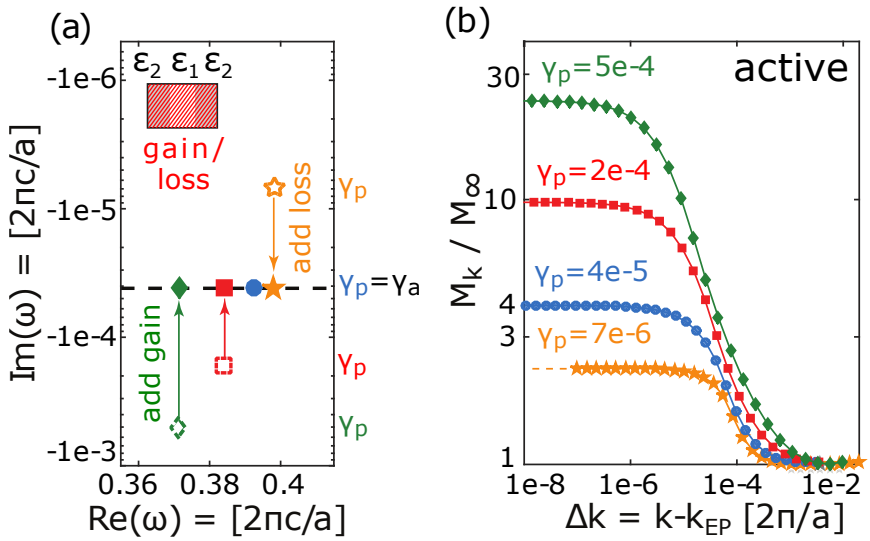

Figure 7.4: LDOS$_k$ enhancement in active structures. (a) Resonances with different passive loss rates $\gamma_{\rm p}$ (hollow symbols) and equal active loss rates γ_a (full symbols). Inset: Structure from Fig. 7.3(a) with gain/loss added to the waveguide. (b) Normalized LDOS$_k$ peak (M_k/M_∞) vs. Δk, evaluated at $\mathbf{r}_0$ [marked in Fig. 7.3(a)], after adding gain/loss. The enhancement at the EP increases with the overall gain.

Similar to the analysis of the plasmonic example in Sec. 7.3, we can introduce a simplified 2×2 model to interpret the results [analogous to Eq. (7.11)]. We project the full Maxwell's operator $\hat{\mathcal{A}}$ onto the subspace spanned by the two modes at $k_x = 0$ [shown in the left-lower corner of Fig. 7.3(a)] and we obtain

$$\hat{A} = \begin{pmatrix} [\Omega_{\rm EP} \pm i\eta]^2 & 2\Omega_{\rm EP} v_g k \\ 2\Omega_{\rm EP} v_g k & [\Omega_{\rm EP} - 2i\gamma_p \pm i\eta]^2 \end{pmatrix}, \tag{7.17}$$

where $v_g \equiv \frac{\partial \omega}{\partial k}\big|_{k=0}$ is the the group velocity (similar to the model used in [38]). Prior to adding gain/loss, an EP occurs when $v_g k = \gamma_p$, and the degenerate frequency is $\omega_{\rm EP} = \Omega_{\rm EP} - i\gamma_p$. After adding gain/loss, $\pm i\eta$, the EP frequency moves vertically in the

complex plane, becoming $\Omega_{\mathrm{EP}} - i\gamma_a$, while the EP condition remains the same: $v_g k = \gamma_p$. In analogy to Eq. (7.15), this model implies that the maximal enhancement at the EP scales as $M_{\mathrm{EP}} \propto \frac{\gamma_p}{\gamma_a^2} + \frac{1}{\gamma_a}$. The quadratic scaling of M_{EP} with Q_a in the limit of $\gamma_a \ll \gamma_p$ is demonstrated in Sec. 7.11 [but this result is essentially another demonstration of the spectral property shown in Fig. 7.2(b)].

7.5 Discussion

The theory presented in this work provides a quantitative prescription for achieving large spontaneous emission rates using EPs, potentially exceeding by orders of magnitude those attained with standard non-degenerate resonances. Such enhancements could be useful for various applications, including fluorescent and Raman sensing [228], high-power low-coherence light sources [174], and sources with tunable coherence [229]. Moreover, by extending the current *linear* theory to account for EPs in nonlinear systems, our approach could be applied to study the properties of lasers at EPs—a topic that has recently drawn great attention in the optics community [178, 191, 37, 230].

Our formulation for the LDOS at the EP [Eqs. (7.9) and (7.10)] establishes that the enhancement generally consists of two terms, one that scales linearly and one that scales quadratically with the quality factor. In Sec. A.2 and Sec. 7.4, we verified this scaling argument via two numerical examples, and we employed simplified 2×2 models to estimate the coefficients of the quadratic terms in the LDOS formula. (In the plasmonic system, we found that the coefficient was the coupling constant κ, while in the periodic example, the coefficient was the passive decay rate γ_p.) More generally, we show in

Sec. 7.12 that for arbitrary low-loss systems, the quadratic coefficient is bounded by

$$\kappa \leq |\omega_{\mathrm{EP}}| \sqrt{\max |\mathrm{Im}\, \varepsilon|}. \tag{7.18}$$

This result provides an easy-to-evaluate upper bound on the maximal enhancement in complicated geometries, depending only on the maximal gain/loss of the constituent materials. More explicitly, in active systems, we find that the maximal enhancement at the EP is bounded by $\frac{M_{\mathrm{EP}}}{M_\infty} = 2(1 + \frac{\kappa}{\mathrm{Im}[\omega_{\mathrm{EP}}]}) \leq 2\left(1 + 2Q|\sqrt{\max |\mathrm{Im}\, \varepsilon|}\right)$. Note that in our plasmonic example, the quadratic coefficient is within 10% of the bound.

Finally, our theory extends beyond spontaneous emission, and can be applied to a broader class of phenomena described by the LDOS. For example, we anticipate similar enhancements in higher-harmonic generation rates in nonlinear media (e.g., Kerr media). In that case, the input lower-harmonic field (multiplied by the nonlinear susceptibility) acts as a source to the higher-harmonic field. To lowest order in the nonlinearity, the converted power is found by convolving the Green's function with the input signal. This is analogous to our formulation of spontaneous emission (which involved convolving a dipole source with the Green's function), and would therefore result in similar enhancements [52]. More generally, a similar treatment could produce enhancements in related quantities at EPs in other areas of physics (e.g., exciton-polariton [35] mechanical systems [36], and also leak-wave antennas both at radio-frequency and visible frequencies [231, 232]). Finally, our theory can be generalized to study scattering and extinction problems. We find, however, that even though EPs can produce special spectral features in scattering cross-sections, they do not give rise to giant scattering enhancements, since the scattered intensity is bounded by the incoming intensity (and the bound of perfect scattering can be easily achieved with a single non-degenerate

resonance [233]).

7.6 Appendix A: Traditional Green's function expansion

In this section we review the derivation of the Eq. (7.2) in the main text. Our derivation is similar to standard methods for *Hermitian* eigenvalue problems [147], with the necessary modifications for treating general *non-Hermitian* systems (most importantly, using the unconjugated "inner product" [33] between left and right eigenmodes).

Given a non-magnetic medium with dielectric permittivity ε, the fields $\mathbf{E}$ and currents $\mathbf{J}$ in the medium are related via Maxwell's frequency-domain partial differential equation:

$$(\hat{\mathcal{A}}_{\mathbf{r}} - \omega^2 \mathbb{1})\mathbf{E}(\mathbf{r}) = i\omega \mathbf{J}(\mathbf{r}). \tag{7.19}$$

where $\hat{\mathcal{A}}_{\mathbf{r}} \equiv \frac{1}{\varepsilon}\nabla_{\mathbf{r}} \times \nabla_{\mathbf{r}} \times$. The response to arbitrary currents can be found by convolving the dyadic Green's function with the current sources: $\mathbf{E}(\mathbf{r}) = \int d\mathbf{r}' \mathbb{G}(\mathbf{r}, \mathbf{r}')\mathbf{J}(\mathbf{r}')$, where $\mathbb{G}$ is defined via:

$$(\hat{\mathcal{A}}_{\mathbf{r}} - \omega^2 \mathbb{1})\mathbb{G}(\mathbf{r}, \mathbf{r}') = -\delta(\mathbf{r} - \mathbf{r}')\mathbb{1}. \tag{7.20}$$

In this section, we expand G in terms of right and left resonant modes ($\mathbf{E}_n^R$ and $\mathbf{E}_n^L$), which are outgoing solutions of the partial differential equations

$$\begin{aligned}(\hat{\mathcal{A}}_{\mathbf{r}} - \omega_n^2 \mathbb{1})\mathbf{E}_n^R(\mathbf{r}) &= 0 \\ (\hat{\mathcal{A}}_{\mathbf{r}}^T - \omega_n^2 \mathbb{1})\mathbf{E}_n^L(\mathbf{r}) &= 0.\end{aligned} \tag{7.21}$$

When the set of eigenvectors of Eq. (7.21) forms a complete basis of the Hilbert space, one can introduce the completeness relation, which consists of expanding the Dirac delta

function as

$$\delta(\mathbf{r}-\mathbf{r}')\mathbb{1} = \sum_n \mathbf{E}_n^R(\mathbf{r}) \otimes \mathbf{E}_n^L(\mathbf{r}'), \tag{7.22}$$

where $\otimes$ is the outer/tensor product $\mathbf{u} \otimes \mathbf{v} = \mathbf{u}\mathbf{v}^T$. The question of completeness of eigenmodes in non-Hermitian open systems has not been proven in general, for arbitrary three-dimensional systems. However, since in this work we always evaluate the Green's function in close proximity to the resonators and at frequencies close to the resonance frequencies, the eigenmodes which overlap spectrally and spatially with the emitter give a good approximation for the LDOS, justifying the use of Eq. (7.22).

Similarly, we wish to find an expansion formula for $\mathbb{G}$ or, more explicitly, find the coefficients $\mathbf{a}_n(\mathbf{r}')$ in the series

$$\mathbb{G}(\mathbf{r},\mathbf{r}') = \sum_n \mathbf{E}_n^R(\mathbf{r}) \otimes \mathbf{a}_n(\mathbf{r}'). \tag{7.23}$$

To this end, we substitute Eq. (7.22) and Eq. (7.23) into Eq. (7.20) and obtain

$$\sum_n \left(\mathcal{A}_\mathbf{r} - \omega^2\right) \mathbf{E}_n^R(\mathbf{r}) \otimes \mathbf{a}_n(\mathbf{r}') = -\sum_n \mathbf{E}_n^R(\mathbf{r}) \otimes \mathbf{E}_n^L(\mathbf{r}'). \tag{7.24}$$

Next, we multiply both sides of the equation by $[\mathbf{E}_m^L(\mathbf{r})]^T$. Using the relation: $[\mathbf{E}_m^L(\mathbf{r})]^T \mathcal{A}_\mathbf{r} = \omega_m^2 [\mathbf{E}_m^L(\mathbf{r})]^T$, integrating over $\mathbf{r}$, and invoking the bi-orthogonality relation for non-Hermitian systems [234]:

$$\int dr\, \mathbf{E}_m^L(\mathbf{r}) \cdot \mathbf{E}_n^R(\mathbf{r}) = \delta_{m,n}, \tag{7.25}$$

we obtain $\mathbf{a}_m(\mathbf{r}') = \frac{\mathbf{E}_m^L(\mathbf{r}')}{\omega^2 - \omega_m^2}$. Finally, substituting this result in Eq. (7.23) we obtain an eigenmode expansion of the dyadic Green's function [which reduces to Eq. (7.2) in the

text]:

$$\mathbb{G}(\mathbf{r},\mathbf{r}',\omega)=\sum_n \frac{1}{\omega^2-\omega_n^2}\frac{\mathbf{E}_n^R(\mathbf{r})\otimes\mathbf{E}_n^L(\mathbf{r}')}{\int dr\,\mathbf{E}_n^R(\mathbf{r})\cdot\mathbf{E}_n^L(\mathbf{r})}. \tag{7.26}$$

The integral in the denominator of Eq. (7.26) is one, but we keep it here for comparison with Eq. (7.2).

Last, we note that in reciprocal media $\varepsilon=\varepsilon^T$, and there exists a simple relation between left and right eigenvectors: $\mathbf{E}_n^L=\varepsilon\mathbf{E}_n^R$. More generally, the left and right eigenvectors of a symmetric generalized eigenvalue problem (EVP): $\mathbb{A}\mathbf{E}_n^R=\lambda_n\mathbb{B}\,\mathbf{E}_n^R, \mathbb{A}^T\mathbf{E}_n^L=\lambda_n\mathbb{B}^T\mathbf{E}_n^L$, with $A=A^T$ and $B=B^T$ are related via $\mathbf{E}_n^L=\mathbb{B}\mathbf{E}_n^R$. To see this, rewrite the EVP for the left vectors as $(\mathbb{B}^{-1}\mathbb{A})^T\mathbf{E}_n^L=\mathbb{A}(\mathbb{B}^{-1}\mathbf{E}_n^L)=\lambda_n\mathbb{B}(\mathbb{B}^{-1}\mathbf{E}_n^L)$ which shows that $\mathbb{B}^{-1}\mathbf{E}_n^L$ is a right eigenvector. Note that this relation holds also with Bloch-periodic boundary conditions (and the surface-term correction found in [235] does not appear in our formulation). Although the matrix $\mathbb{A}$ is no longer symmetric in the k-periodic problem, it satisfies the relation $\mathbb{A}(k)^T=\mathbb{A}(-k)$, and since we are essentially relating k-right eigenvectors to $(-k)$-left eigenvectors, the relation above remains unchanged.

7.7 Appendix B: LDOS formula for dispersive media

In this appendix, we consider the effects of dispersion on the Green's function near and at the EP. In accordance with previous work on quasi-normal modes in dispersive media [236, 237], we find that the Green's function has non-diagonal contributions $\propto\mathbf{E}_{\pm}^L\otimes\mathbf{E}_{\mp}^R$ near the EP. However, exactly at the EP, the Green's function has exactly the same form as the non-dispersive degenerate formula [Eq. (7.9)], with dispersion affecting only the normalization of the degenerate mode ($\mathbf{E}_0$) and Jordan vector ($\mathbf{J}_0$).

In the same spirit as our derivation of the non-dispersive formula, we expand the

Green's function $\mathbb{G}$ in eigenmodes:

$$\mathbb{G}(\mathbf{r}, \mathbf{r}_0, \omega) = \sum_m \mathbf{E}_m^R(\mathbf{r}) \otimes \boldsymbol{\alpha}_m(\omega, \mathbf{r}_0), \tag{7.27}$$

and use simple algebraic manipulations to express the coefficients $\boldsymbol{\alpha}_m$ in terms of the modes. Recall that $\mathbb{G}$ is defined as the solution to the partial differential equation:

$$\left[\nabla \times \nabla \times -\omega^2 \varepsilon(\mathbf{r}, \omega)\right] \mathbb{G}(\mathbf{r}, \mathbf{r}_0, \omega) = -\delta(\mathbf{r} - \mathbf{r}_0)\mathbb{1} \tag{7.28}$$

By multiplying both sides of Eq. (7.28) from the left by $\mathbf{E}_n^L(\mathbf{r})$ and integrating over dr, we obtain

$$\mathbf{E}_n^L(\mathbf{r}_0) = \int dr\, \mathbf{E}_n^L(\mathbf{r}) \left[\omega^2 \varepsilon(\mathbf{r}, \omega) - \omega_n^2 \varepsilon(\mathbf{r}, \omega_n)\right] \mathbb{G}(\mathbf{r}, \mathbf{r}_0, \omega) \tag{7.29}$$

Then, by substituting Eq. (7.27) into Eq. (7.29), we find

$$\mathbf{E}_n^L(\mathbf{r}_0) =$$
$$\sum_m \int dr\, \mathbf{E}_n^L(\mathbf{r})[\omega^2 \varepsilon(\omega) - \omega_n^2 \varepsilon(\omega_n)]\mathbf{E}_m^R(\mathbf{r}) \otimes \boldsymbol{\alpha}_m(\omega, \mathbf{r}_0) \equiv \sum_m (\mathbf{E}_m, \mathbf{E}_n)\boldsymbol{\alpha}_m(\omega, \mathbf{r}_0). \tag{7.30}$$

(Note that this result was also derived in [237] by invoking Lorentz reciprocity.) Since we are interested in emission from emitters in close proximity to the resonators and in frequencies near the resonant frequencies, we may assume that a finite set of N eigenvectors adequately describes the system's response [similar to our assumption in the non-dispersive derivation in Eq. (7.22)]. We introduce the vector $\mathbf{s}(\mathbf{r}) = \{\mathbf{E}_1(\mathbf{r}), \ldots, \mathbf{E}_N(\mathbf{r})\}$ and the matrix $\mathbb{O}_{mn} \equiv (\mathbf{E}_m, \mathbf{E}_n)$, and rewrite Eq. (7.30) as: $\mathbf{s}(\mathbf{r}_0) = \mathbb{O}(\omega)\boldsymbol{\alpha}(\omega, \mathbf{r}_0)$ or equivalently $\boldsymbol{\alpha}(\omega, \mathbf{r}_0) = \mathbb{O}^{-1}(\omega)\mathbf{s}(\mathbf{r}_0)$. With this notation, Eq. (7.27) can be rewritten

as: $\mathbb{G} = \boldsymbol{\alpha}(\omega, \mathbf{r}_0)^T \mathbf{s}(\mathbf{r}) = \mathbf{s}(\mathbf{r}_0)^T (\mathbb{O}^{-1})^T \mathbf{s}(\mathbf{r}_0)$ or

$$\mathbb{G}(\mathbf{r}, \mathbf{r}_0, \omega) = \sum_{nm} (\mathbb{O}^{-1})_{nm} \mathbf{E}_n^R(\mathbf{r}) \otimes \mathbf{E}_m^L(\mathbf{r}_0) \tag{7.31}$$

where

$$\mathbb{O}_{ij} = \int dr\, \mathbf{E}_i^L [\omega^2 \varepsilon(\mathbf{r}, \omega) - \omega_i^2 \varepsilon(\mathbf{r}, \omega_i)] \mathbf{E}_j^R. \tag{7.32}$$

Equation (7.31) and Eq. (7.32) are the main result of this appendix—an eigenmode expansion of the Green's function in the presence of dispersion, generalizing Eq. (7.2) from the main text. In the non-dispersive limit, this expression reproduces our previous result since $\mathbb{O}_{mn} = (\mathbf{E}_m, \mathbf{E}_n) = (\omega^2 - \omega_n^2) \int dr\, \varepsilon\, \mathbf{E}_m^L \cdot \mathbf{E}_n^R = (\omega^2 - \omega_n^2)\delta_{mn}$ and $\mathbb{G} = \sum_n (\omega^2 - \omega_n^2)^{-1} \mathbf{E}_n^R(\mathbf{r}) \otimes \mathbf{E}_n^L(\mathbf{r}_0)$.

Next, let us calculate the limit of Eq. (7.31) when two modes $\mathbf{E}_\pm$ coalesce at an EP. Keeping only the terms corresponding to $\mathbf{E}_\pm$ in Eq. (7.31), expanding both ω and $\omega_\pm$ in Taylor series around ω_0 and introducing the notation:

$$\omega^2 \varepsilon(\omega) - \omega_\pm^2 \varepsilon(\omega_\pm) = (\omega - \omega_\pm) \left. \frac{d(\omega^2 \varepsilon)}{d\omega} \right|_{\omega_0} \equiv (\omega - \omega_\pm)(\omega^2 \varepsilon)_0' \,, \tag{7.33}$$

we find that $\mathbb{O}_{ij} = (\omega - \omega_j) \int dr (\omega^2 \varepsilon)_0' \mathbf{E}_i^L \cdot \mathbf{E}_j^R$, and the matrix inverse is

$$\mathbb{O}^{-1} = \begin{pmatrix} \frac{1}{\omega - \omega_+} \frac{\int (\omega^2 \varepsilon)_0' \mathbf{E}_-^L \cdot \mathbf{E}_-^R}{N} & -\frac{1}{\omega - \omega_+} \frac{\int (\omega^2 \varepsilon)_0' \mathbf{E}_+^L \cdot \mathbf{E}_-^R}{N} \\ -\frac{1}{\omega - \omega_-} \frac{\int (\omega^2 \varepsilon)_0' \mathbf{E}_-^L \cdot \mathbf{E}_+^R}{N} & \frac{1}{\omega - \omega_-} \frac{\int (\omega^2 \varepsilon)_0' \mathbf{E}_+^L \cdot \mathbf{E}_+^R}{N} \end{pmatrix}, \tag{7.34}$$

where $N \equiv \left[\int (\omega^2 \varepsilon)_0' \mathbf{E}_+^L \cdot \mathbf{E}_+^R\right] \left[\int (\omega^2 \varepsilon)_0' \mathbf{E}_-^L \cdot \mathbf{E}_-^R\right] - \left[\int (\omega^2 \varepsilon)_0' \mathbf{E}_+^L \cdot \mathbf{E}_-^R\right] \left[\int (\omega^2 \varepsilon)_0' \mathbf{E}_-^L \cdot \mathbf{E}_+^R\right]$. Substituting Eq. (7.34) into Eq. (7.31), we find that the Green's function near the EP

is

$$\mathbb{G}(\mathbf{r},\mathbf{r}_0,\omega)=\frac{\mathbf{E}_+^R\otimes\mathbf{E}_+^L}{\omega-\omega_+}\frac{\int(\omega^2\varepsilon)_0'\mathbf{E}_-^L\cdot\mathbf{E}_-^R}{N}+\frac{\mathbf{E}_-^R\otimes\mathbf{E}_-^L}{\omega-\omega_-}\frac{\int(\omega^2\varepsilon)_0'\mathbf{E}_+^L\cdot\mathbf{E}_+^R}{N}-\\ \frac{\mathbf{E}_-^R\otimes\mathbf{E}_+^L}{\omega-\omega_+}\frac{\int(\omega^2\varepsilon)_0'\mathbf{E}_+^L\cdot\mathbf{E}_-^R}{N}-\frac{\mathbf{E}_+^R\otimes\mathbf{E}_-^L}{\omega-\omega_-}\frac{\int(\omega^2\varepsilon)_0'\mathbf{E}_-^L\cdot\mathbf{E}_+^R}{N}. \tag{7.35}$$

Last, we want to take the limit of Eq. (7.35) as the two modes $\mathbf{E}_\pm$ approach the EP. We expand $\omega_\pm$ and $\mathbf{E}_\pm$ around the EP using degenerate perturbation theory (using the notation of Sec. 7.2.2):

$$\omega_\pm\approx\omega_0\pm\sqrt{p}\Delta,$$
$$\mathbf{E}_\pm\approx\mathbf{E}_0\pm\sqrt{p}\Delta\,\mathbf{J}_0. \tag{7.36}$$

Generalizing our derivation of the non-dispersive formula, we choose the normalization conditions $\int(\omega^2\varepsilon)_0'\mathbf{E}_0^L\mathbf{J}_0^R=\int(\omega^2\varepsilon)_0'\mathbf{J}_0^L\mathbf{E}_0^R=1$ and $\int(\omega^2\varepsilon)_0'\mathbf{J}_0^L\mathbf{J}_0^R=0$, while the condition $\int(\omega^2\varepsilon)_0'\mathbf{E}_0^L\mathbf{E}_0^R=0$ is automatically satisfied due to self-orhotognality. With this normalization, we can calculate integrals in Eq. (7.35):

$$\int(\omega^2\varepsilon)_0'\mathbf{E}_\pm^L\mathbf{E}_\pm^R=\cancel{\int(\omega^2\varepsilon)_0'\mathbf{E}_0^L\mathbf{E}_0^R}\pm2\sqrt{p}\Delta\int(\omega^2\varepsilon)_0'\mathbf{E}_0^L\mathbf{J}_0^R+p\Delta^2\cancel{\int(\omega^2\varepsilon)_0'\mathbf{J}_0^L\mathbf{J}_0^R}+\mathcal{O}(p^{3/2})$$
$$\int(\omega^2\varepsilon)_0'\mathbf{E}_\pm^L\mathbf{E}_\mp^R=\cancel{\int(\omega^2\varepsilon)_0'\mathbf{E}_0^L\mathbf{E}_0^R}-p\Delta^2\cancel{\int(\omega^2\varepsilon)_0'\mathbf{J}_0^L\mathbf{J}_0^R}+\mathcal{O}(p^{3/2})$$
$$N=-4p\Delta^2\int(\omega^2\varepsilon)_0'\mathbf{E}_0^L\mathbf{J}_0^R+\mathcal{O}(p^{3/2})$$

The first two terms in Eq. (7.35) have the same form as the non-dispersive expansion [Eq. (7.8)]: $\frac{1}{2\Delta\sqrt{p}}\frac{\mathbf{E}_+^R\otimes\mathbf{E}_+^L}{\omega-\omega_+}-\frac{1}{2\Delta\sqrt{p}}\frac{\mathbf{E}_-^R\otimes\mathbf{E}_-^L}{\omega-\omega_-}+\mathcal{O}(p^{3/2})$. Upon approaching the EP, each contributions diverges with an opposite sign, and a finite contribution remains. The

last two terms scale as $\sqrt{p}$ near the EP, and vanish at the EP. Finally, we obtain

$$\mathbb{G}_{\mathrm{EP}}(\mathbf{r},\mathbf{r}_0,\omega)=\frac{\mathbf{E}_0^R(\mathbf{r})\otimes\mathbf{E}_0^L(\mathbf{r}_0)}{(\omega-\omega_0)^2}+\frac{\mathbf{J}_0^R(\mathbf{r})\otimes\mathbf{E}_0^L(\mathbf{r}_0)+\mathbf{E}_0^R(\mathbf{r})\otimes\mathbf{J}_0^L(\mathbf{r}_0)}{\omega-\omega_0}. \tag{7.37}$$

Equation (7.37) implies that the green's function at the EP in dispersive media has the same form as the non-dispersive formula [Eq. (7.9) in the text], but the normalization of the modes changes.

7.8 Appendix C: Convergence of the "unconjugated norm"

In this appendix, we show that when perfectly matched layers (PML) are used to implement outgoing boundary conditions, the "unconjugated norm" of a scattering eigenmode, $\int dx\,\varepsilon(\mathbf{x})\mathbf{E}_n(\mathbf{x})^2$, converges to a finite result as the PML thickness tends to infinity. Scattering eigenmodes are solutions to Maxwell's eigenvalue problem, $\varepsilon^{-1}\nabla\times\nabla\times\mathbf{E}_n=\omega_n^2\mathbf{E}_n$ [23], with outgoing radiation conditions. These solutions (also called "leaky modes" [64]) have complex frequencies ω_n which lie in the lower-half of the complex plane ($\mathrm{Im}[\omega_n]<0$) [238] and, consequently, the modal amplitudes ($|\mathbf{E}_n|$) grow unboundedly at large distances from the structure. Even though the modal amplitude diverges, we show that the unconjugated inner product is finite and independent of the PML parameters, as long as the PML works effectively (i.e., designed so that outgoing waves are attenuated exponentially inside the PML and are not reflected at the air-PML interface.) We provide a simple proof for a one dimensional geometry. An abstract proof for the independence of the unconjugated norm on the PML parameters appeared in [237] (using a generalized definition of the norm, which includes dispersion). An alternative one-dimensional proof was given in [239], where the authors used

analytic continuation of the coordinates, similar to the coordinate stretching method that we use here.

We consider the one-dimensional geometry depicted in Fig. 7.5(a), which consists of a slab of thickness a and refractive index n, embedded in air. (Generalizations to more complex one-dimensional structures straightforwardly follow.) We truncate the computational cell by placing PML at a finite distance from the slab ($|x| = L/2$), and we impose metallic boundary conditions at the cell boundary ($x = \pm\frac{N}{2}$). The PML can be viewed as an analytic continuation of the spatial coordinate into the complex plane [240], $\widetilde{x} = x + if(x)$, where the derivative of f satisfies $\frac{df}{dx} = \frac{\sigma(x)}{\omega}$. (The latter condition guaranties that fields oscillating at different frequencies ω will be attenuated inside the PML at rate that is independent of ω.) For concreteness, we choose: $\sigma(x) = \frac{\sigma_0 x}{d}$, where $d = \frac{N-L}{2}$ is the PML thickness. Consequently, the coordinate stretching transformation inside the PML is

$$\widetilde{x} = x + i\frac{\sigma_0 \left(x - \frac{L}{2}\right)^2}{2\omega d}. \tag{7.38}$$

Scattering solution for this geometry can be written explicitly as

$$E_n = \begin{cases} A_n e^{-i\omega_n x - (\sigma_0/2d)(x+L/2)^2} + B_n e^{i\omega_n x + (\sigma_0/2d)(x+L/2)^2} & -N/2 < x < -L/2 \\ A_n e^{-i\omega_n x} + B_n e^{i\omega_n x} & -L/2 < x < -a/2 \\ e^{-i\omega_n n x} + e^{i\omega_n n x} & -a/2 < x < a/2 \\ A_n e^{i\omega_n x} + B_n e^{-i\omega_n x} & a/2 < x < L/2 \\ A_n e^{i\omega_n x - (\sigma_0/2d)(x-L/2)^2} + B_n e^{-i\omega_n x + (\sigma_0/2d)(x-L/2)^2} & L/2 < x < N/2 \end{cases},$$

where the coefficients A_n, B_n and resonant frequency ω_n are found by requiring continuity of the field (E_n) and its derivative (dE_n/dx) at the interfaces, while imposing the

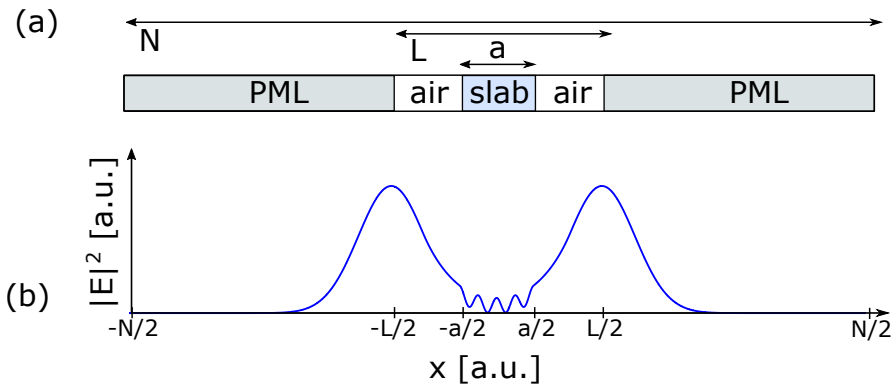

Figure 7.5: Leaky modes in one dimension. (a) A slab in air with PML at the cell boundary. (b) The intensity of the leaky mode increases exponentially in the air region and is attenuated in the PML.

boundary condition: $E_n = 0$ at $\pm N/2$. We obtain

$$A_n = \frac{e^{inka/2} + e^{-inka/2}}{e^{ika/2} - C_n e^{-ika/2}},$$
$$B_n = -A_n C_n \,,$$

where we introduced $C_n \equiv e^{i\omega_n N - \sigma_0 d}$.

Next, we compute the unconjugated norm, $\int \varepsilon E_n^2$, and study its convergence. Introducing the antiderivative function

$$J(x) \equiv \int^x dx' \, \varepsilon (A_n e^{i\omega_n x'} + B_n e^{-i\omega_n x'})^2, \tag{7.39}$$

the unconjugated norm can be written as

$$\mathcal{I}(d) \equiv \int_{\text{all}} dx \, \varepsilon E^2 = \int_{\text{Cav}} dx \, \varepsilon E^2 + 2\left[J\left(\tfrac{L}{2}\right) - J\left(\tfrac{a}{2}\right)\right] + 2\left\{J\left[\widetilde{x}(\tfrac{N}{2})\right] - J\left[\widetilde{x}(\tfrac{L}{2})\right]\right\}. \tag{7.40}$$

We now show that whenever the condition Eq. (7.41) (below) holds, $\mathcal{I}$ is finite and independent of the PML parameters in the limit of $d \to \infty$. Since the coordinate stretching factor is zero at the air-PML boundary [$\widetilde{x}(\frac{L}{2}) = \frac{L}{2}$], the antiderivative terms at $L/2$ cancel ($J\left(\frac{L}{2}\right) = J\left[\widetilde{x}(\frac{L}{2})\right]$). Next, consider the boundary term, $J\left[\widetilde{x}(\frac{N}{2})\right]$. Straightforward integration of Eq. (7.39) yields three terms, all of which decay exponentially as $d \to \infty$, provided that $|C_n|$ decays exponentially. [The first is $\frac{A_n^2 e^{2i\omega_n \widetilde{x}(N/2)}}{2i\omega_n} = \frac{A_n^2 C_n}{2i\omega_n}$, the second term is $\frac{B_n^2 e^{-2i\omega_n \widetilde{x}(N/2)}}{-2i\omega_n} = \frac{A_n^2 C_n}{-2i\omega_n}$, and the last term is $2A_n B_n \widetilde{x}(N/2) = -2A_n^2 C_n \cdot \mathcal{O}(d)$.] Introducing $\omega_n = \omega_n' - i\omega_n''$ and $\alpha = d/L$, one finds from the definition of C_n that it decays exponentially whenever

$$[\omega_n''(\alpha + 2) + \sigma_0]d \gg 1. \tag{7.41}$$

Evaluating the remaining terms in Eq. (7.40), $\int_{\text{Cav}} dx\, \varepsilon E^2$ and $J\left(\frac{a}{2}\right)$, we obtain:

$$\lim_{d\to\infty} \mathcal{I}(d) = \frac{2}{n\omega_n}\left[\sin(n\omega_n a) + n\omega_n a\right] + \frac{4i}{\omega_n}\cos\left(\tfrac{n\omega_n a}{2}\right).$$

The result is finite, and independent of the location of the air-PML interface or the cell boundary, thus completing the proof.

7.9 Appendix D: Forcing EPs in periodic waveguides

In order to force an EP (i.e., an accidental degeneracy of two nearby resonances), we need to satisfy a single complex equation ($\omega_m = \omega_n$), which can be done by searching two real parameters. In the plasmonic example in Sec. 7.3, we search the two-dimensional parameter space spanned by the gain/loss parameter ($|\text{Im}\,\varepsilon|$) and the (real part) of the refraction index in the upper-half of the silica coating. In the periodic example from

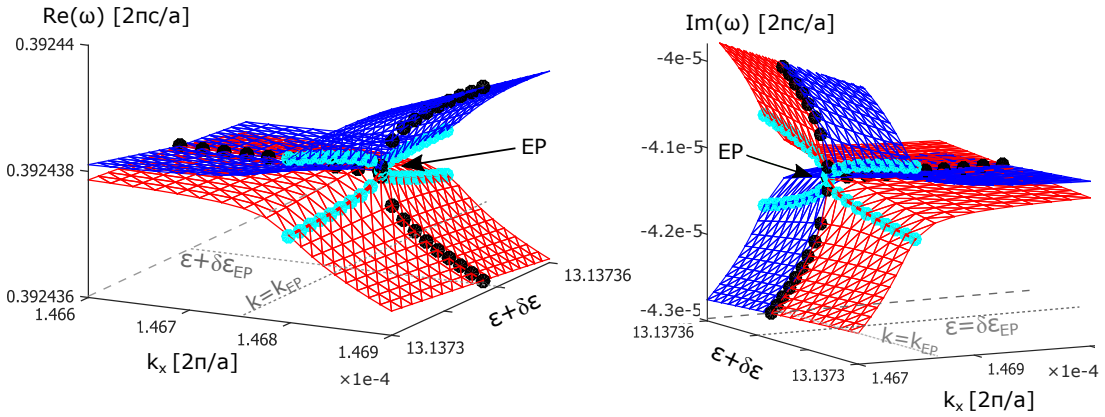

Figure 7.6: Forcing EPs in the periodic waveguides. (a) Real and (b) imaginary parts of the eigenvalues of Maxwell's operator, as a function of the wavevector k_x and the permittivity contrast $\delta\varepsilon \equiv \varepsilon_2 - \varepsilon_1$, for the geometry from Fig. 7.3(a). The EP is found by numerically minimizing the distance between the two eigenvalue sheets (red and blue surfaces). Cyan dots: Eigenvalues for fixed $k_x = k_{\mathrm{EP}}$ and varying $\delta\varepsilon$. Black dots: Eigenvalues for fixed $\delta\varepsilon = \delta\varepsilon_{\mathrm{EP}}$ and varying k_x.

Sec. 7.4, we search the two-dimensional space spanned by the wavevector k_x and the permittivity contrast $\delta\varepsilon$. Figure 7.6 presents our numerical results for the periodic example. As shown, we find a degenerate resonance at $\omega_{\mathrm{EP}} = 0.3924377 - 0.00004119303i$ when $k_{\mathrm{EP}}a/2\pi \approx 1.468 \times 10^{-4}$ and $\delta\varepsilon_{\mathrm{EP}} \approx 1.137$.

7.10 Appendix E: Reduced 2×2 model for the LDOS

In this section, we derive Eq. (7.11) from the main text, which provides a simplified formula for the LDOS in Sec. 7.3. Our approach is similar to coupled-mode theory, originally developed for photonic waveguides [218, 219]. Our derivation consists of projecting Maxwell's operator [describing the coupled-rod system from Fig. 7.1(a)] onto the subspace spanned by the modes of the corresponding uncoupled-system (i.e., a

system in which the rod–rod separation is infinite).

The field of the (original) coupled system satisfies Maxwell's equation:

$$\hat{\mathcal{A}}\,\mathbf{E} \equiv \tfrac{1}{\varepsilon}\nabla\times\nabla\times\mathbf{E} = \omega^2\mathbf{E}. \tag{7.42}$$

Denoting by ε_ℓ the permittivity of a system that contains only a single rod [where $\ell = 1$ (2) indicates the upper (lower) rod in Fig. 7.1(a)], the right eigenvectors of the uncoupled system satisfy

$$\tfrac{1}{\varepsilon_\ell}\nabla\times\nabla\times\mathbf{E}_\ell^R = \omega_\ell^2\mathbf{E}_\ell^R, \tag{7.43}$$

with a similar definition for left eigenvectors.

Next, let us compute the projection of $\mathcal{A}$ onto the subspace spanned by $\mathbf{E}_1$ and $\mathbf{E}_2$, denoted by $\hat{A}$. The diagonal terms of $\hat{A}$ are

$$\int \mathbf{E}_j^L \tfrac{1}{\varepsilon}\nabla\times\nabla\times\mathbf{E}_j^R \approx \int \mathbf{E}_j^L \tfrac{1}{\varepsilon_j}\nabla\times\nabla\times\mathbf{E}_j^R = \omega_j^2. \tag{7.44}$$

The first approximation follows from the fact that the mode profile $\mathbf{E}_j^R$ is significant only in close proximity to resonator j, and in that region $\varepsilon = \varepsilon_j$. The second equality follows from Eq. (7.43). Now, let us define $\Delta\varepsilon_j \equiv \varepsilon - \varepsilon_j$. The off-diagonal terms of $\hat{A}$ are

$$\begin{aligned}\int \mathbf{E}_i^L \tfrac{1}{\varepsilon}\nabla\times\nabla\times\mathbf{E}_j^R = \int \mathbf{E}_i^L \tfrac{\varepsilon_j}{\varepsilon}\tfrac{1}{\varepsilon_j}\nabla\times\nabla\times\mathbf{E}_j^R = \\ \omega_j^2\int \mathbf{E}_i^L \tfrac{\varepsilon-\Delta\varepsilon_j}{\varepsilon}\mathbf{E}_j^R = 2\omega_j\left(-\tfrac{\omega_j}{2}\int \mathbf{E}_i^L\tfrac{\Delta\varepsilon_j}{\varepsilon}\mathbf{E}_j^R\right) \equiv 2\omega_j\kappa_{ij}\end{aligned} \tag{7.45}$$

Assuming that the structure is approximately symmetric in the $\hat{y}$ direction (i.e., under

exchanging $i \leftrightarrow j$), we have $\kappa_{ij} \approx \kappa_{ji} \approx \kappa$. In the limit of low losses/gain, $\gamma \ll \Omega_{\mathrm{EP}}$, we obtain Eq. (7.11):

$$\hat{A} = V^T \hat{\mathcal{A}} U = \begin{pmatrix} (\omega_{\mathrm{EP}} - i\eta)^2 & 2\Omega_{\mathrm{EP}}\kappa \\ 2\Omega_{\mathrm{EP}}\kappa & (\omega_{\mathrm{EP}} + i\eta)^2 \end{pmatrix}. \tag{7.46}$$

where U is the matrix whose columns are $\mathbf{E}_1^R$ and $\mathbf{E}_2^R$ and V is the matrix whose columns are $\mathbf{E}_1^L$ and $\mathbf{E}_2^L$

7.11 Appendix F: Giant enhancement in periodic systems

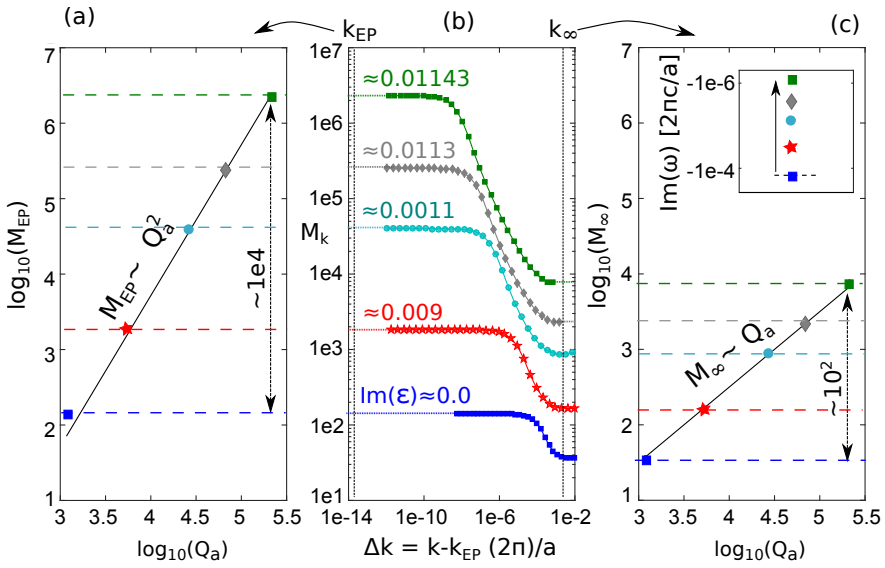

Figure 7.7: LDOS enhancement in active periodic waveguides. Middle: LDOS peak (M_k) vs. Δk for increasing amounts of gain in the waveguide from Fig. 7.3(a). Left: $\log_{10}(M_{\mathrm{EP}})$ vs. $\log_{10}(Q_a)$ for the data from the middle panel near k_{EP}, showing quadratic scaling with Q_a. Right: $\log_{10}(M_\infty)$ vs. $\log_{10}(Q_a)$ for the data from the middle panel at k_∞, showing linear scaling with Q_a. Inset: Eigenvalues move vertically in the complex plane upon adding gain.

In this section, we demonstrate substantial LDOS enhancements by forcing EPs in

periodic waveguides with significant amounts of gain. Similar to Sec. 7.3 in the text, we consider a waveguide with periodic index modulation along $\hat{x}$ and outgoing boundary conditions in the transverse y-direction [Fig. 7.3(a)]. The parameters of the system, prior to adding gain, are $\varepsilon_1 = 12$, $\varepsilon_2 \approx 14.43$, and $d = 0.4807a$.

Figure 7.7 shows our numerical results. At each wavevector, we compute the LDOS_k peak value (M_k) vs. deviation from the EP ($\Delta k \equiv k - k_{\text{EP}}$) when adding increasing amounts of gain to the waveguide (i.e., fixing Q_p while increasing Q_a). The LDOS is evaluated at $\mathbf{r}_0$ [Fig. 7.3(a)] by direct inversion of Maxwell's equations. We show here enhancements of ≈ 400, while higher values can easily be obtained; the enhancement is essentially not bounded in this computational model. However, in reality, it is bounded by quantum noise near threshold [16]. The side panels in the figure demonstrate that the LDOS peak scales quadratically with Q_a near the EP [Fig. 7.7(a)] and linearly with Q_a away from the EP [Fig. 7.7(c)]. Finally, we note that when evaluating the LDOS near the center of the computational cell (i.e., at $x \approx 0$), the lineshape changes dramatically, and it actually has a minimum at the resonance frequency and two side peaks, whose amplitude scales as Q_a^2 (not shown).

7.12 Appendix G: Limit of LDOS enhancement at an EP

In this section, we derive Eq. (7.18) in the text. Let us first define an effective mode amplitude $\langle \mathbf{E}, \mathbf{E} \rangle \equiv \int_C dx \, |\mathbf{E}|^2$, where C denotes a finite region containing the geometry (e.g., the last scattering surface). In order to obtain an upper bound on the LDOS enhancement at the EP, we need to estimate the quantities $\left\langle \mathbf{E}_0^R, \mathbf{E}_0^R \right\rangle / \left\langle \mathbf{J}_0^R, \mathbf{J}_0^R \right\rangle$ and $\left\langle \mathbf{E}_0^L, \mathbf{E}_0^L \right\rangle / \left\langle \mathbf{J}_0^L, \mathbf{J}_0^L \right\rangle$, which determine the relative magnitude of the two terms in the expansion formula for G at the EP [Eq. (7.9)]. Let us decompose the complex-symmetric

Maxwell's operator into: $\hat{\mathcal{A}} = \hat{\mathcal{A}}' + i\hat{\mathcal{A}}''$, where $\hat{\mathcal{A}}' \equiv \frac{\hat{\mathcal{A}}+\hat{\mathcal{A}}^*}{2}$ and $\hat{\mathcal{A}}'' \equiv \frac{\hat{\mathcal{A}}-\hat{\mathcal{A}}^*}{2i}$, and the asterisk denotes complex conjugation. In many cases of interest, one can assume $\left\|\hat{\mathcal{A}}''\right\| \ll \left\|\hat{\mathcal{A}}'\right\|$ (under an appropriate matrix norm). In such cases, one can use defective perturbation theory (Sec. 7.2.2) to expand the eigenmodes $\mathbf{E}_{\pm}^R$ and eigenvalues $\omega_{\pm}$ of $\hat{\mathcal{A}}'$ in terms $\mathbf{E}_0^R$, $\mathbf{J}_0^R$ and λ_{EP}. Using Eq. (7.6), we obtain

$$\mathbf{E}_0^R \approx (\mathbf{E}_+^R + \mathbf{E}_-^R)/2 \tag{7.47}$$

$$\mathbf{J}_0^R \approx (\mathbf{E}_+^R - \mathbf{E}_-^R)/(2\lambda_1 p^{\frac{1}{2}}). \tag{7.48}$$

Since $\hat{\mathcal{A}}'$ is a real Hermitian operator, it has real and orthogonal eigenvectors $\mathbf{E}_{\pm}$. Using Eqs. (7.47) and (7.48) and assuming $\langle \mathbf{E}_+, \mathbf{E}_+ \rangle \approx \langle \mathbf{E}_-, \mathbf{E}_- \rangle$ and $\langle \mathbf{E}_-, \mathbf{E}_+ \rangle = 0$, one obtains

$$\begin{aligned} \left\langle \mathbf{E}_0^R, \mathbf{E}_0^R \right\rangle &\approx \langle \mathbf{E}_+, \mathbf{E}_+ \rangle /2 \\ \left\langle \mathbf{J}_0^R, \mathbf{J}_0^R \right\rangle &\approx \langle \mathbf{E}_+, \mathbf{E}_+ \rangle /2|\lambda_1|^2 p. \end{aligned} \tag{7.49}$$

Substituting the explicit perturbative expansion Eq. (7.7), we find

$$\frac{\left\langle \mathbf{E}_0^R, \mathbf{E}_0^R \right\rangle}{\left\langle \mathbf{J}_0^R, \mathbf{J}_0^R \right\rangle} \approx |\lambda_1|^2 p \approx \left| \frac{(\mathbf{E}_0^L, \hat{\mathcal{A}}'', \mathbf{E}_0^R)}{(\mathbf{J}_0^L, \mathbf{E}_0^R)}, \right| \tag{7.50}$$

(with an equivalent expression for the left eigenvector). Next, recall the definition of $\hat{\mathcal{A}} \equiv \frac{1}{\varepsilon}\nabla \times \nabla \times$. In the limit of low losses, $\|\mathrm{Im}\,\varepsilon/\varepsilon\| \ll 1$, we can approximate $\hat{\mathcal{A}}'' \approx$

$-\frac{\mathrm{Im}\,\varepsilon}{\varepsilon^2}\,\nabla\times\nabla\times$ and, consequently

$$|(\mathbf{E}_0^L, \hat{\mathcal{A}}'', \mathbf{E}_0^R)| \approx \left|\omega_{\mathrm{EP}}^2 \int \mathbf{E}_0^L (\mathrm{Im}\,\varepsilon/\varepsilon)\mathbf{E}_0^R\right| =$$
$$\left|\omega_{\mathrm{EP}}^2 \int \mathrm{Im}\,\varepsilon\, \mathbf{E}_0^{R\,2}\right| \approx \left|\omega_{\mathrm{EP}}^2 \int \mathrm{Im}\,\varepsilon\, |\mathbf{E}_0^R|^2\right| \leq |\omega_{\mathrm{EP}}|^2 \max|\mathrm{Im}\,\varepsilon|\,, \tag{7.51}$$

where, in going from the first to the second line, we used the relation $\mathbf{E}_0^R = \varepsilon^{-1}\mathbf{E}_0^L$ (which holds for Maxwell's eigenvalue problem) and, in the following approximations, we used the property $\mathbf{E}_0^2 \approx |\mathbf{E}_0|^2$ (valid for low-loss systems) and the normalization condition $\int |\mathbf{E}_0|^2 = 1$. This completes the proof of Eq. (7.18).

Chapter 8

Applications of LDOS enhancement at exceptional points

In the previous chapter, we showed that the LDOS can increase dramatically when two non-Hermitian resonances merge at an exceptional point (EP). In this chapter, we generalize and explore applications of this effect. The work in this chapter was done in collaboration with Prof. Alejandro Rodriguez from Princeton University and Zin Lin from Harvard University. In Sec. 8.1, we extend our theory from Ch. 7 to higher-order EPs, which form when multiple resonances merge, and demonstrate LDOS enhancement in a realistic structure with a third-order EP (shown in Fig. 8.1).[§] Then, in Sec. 8.2, we study higher-harmonic generation in nonlinear media with EPs.[†] We use a coupled-mode theory (CMT) approach to analyze the enhancement near the EP.

8.1 LDOS enhancement near third-order EPs

In this section, we exploit a powerful inverse-design method [241] to design a triply degenerate Dirac point (DP), formed out of modes belonging to different symmetry

[§]The results were published in [51]. I was mainly involved in the analytic calculations.

[†]An online version of our manuscript can be found at [52]. My contribution is in deriving CMT near EPs in nonlinear media and in showing that the CMT equations can lead to enhanced frequency-conversion rates.

representations. In particular, we show that such higher-order DPs can be exploited to create third-order exceptional points (EP3). In addition, we exploit coupled-mode theory to derive conditions under which such EP3s can exist and extend recent work [44] to consider the possible enhancements and spectral modifications in the SE rate of emitters. Specifically, we show that an EP3 can produce 8-fold enhancement in the LDOS of passive structures, and can lead to a cubic Lorentzian spectrum. More generally, we find that the enhancement factor scales as $\sqrt{n^3}$ for n-fold degenerate EPs. Even larger enhancements are expected when introducing gain [44]. Our findings provide the foundations for future discoveries of complex structures with unusual and exotic modal properties currently out of the reach of conventional, intuitive design principles.

Structures with EPs are designed by exploiting degeneracies between modes of different symmetry representations, often in simple geometries involving cylindrical pillars or holes on a square or triangular lattice [242, 243]. These singularities are typically of order two (comprising two interacting modes) and arise partly out of some underlying lattice symmetry (e.g. C_{4v} or C_{3v}) and through the fine-tuning of a few geometric parameters [242, 244]. For instance, in [38], it was recently demonstrated that a Dirac point (DP) at the Γ point of a photonic crystal (PhC) with C_{4v} symmetry can give rise to a ring of EP2s. Such a DP is formed by a degeneracy involving modes of both monopolar (M) and dipolar (D) nature, which transform according to A and E representations of the C_{4v} group [242, 244]. Even though the degeneracy consists of one monopole and two dipoles, the induced EP is of the second order, with only the monopole and one of the dipoles colliding, while the coalescence of the dipole partner is prevented by their symmetry [38]. Below, we show that an EP3 can be induced by a completely "accidental" third-order degeneracy (D3) at Γ, involving modes of monopolar (M), dipolar (D) and quadrupolar (Q) nature arising in a novel, inverse-designed PhC structure lacking

C_{4v} symmetry.

8.1.1 Coupled-mode analysis

The band structure in the vicinity of such a D3 can be modeled by an approximate Hamiltonian of the form [243]:

$$\mathcal{H} = \begin{pmatrix} \omega_0 & v_{\mathrm{MD}}k_x & 0 \\ v_{\mathrm{MD}}k_x & \omega_0 & v_{\mathrm{QD}}k_y \\ 0 & v_{\mathrm{QD}}k_y & \omega_0 \end{pmatrix} \tag{8.1}$$

Here, $v_{ij},\ i,j \in \{\mathrm{M},\mathrm{D},\mathrm{Q}\}$ characterizes the mode mixing away from the Γ point, to first order in $\mathbf{k}$ [243]. Note that the diagonalization of this Hamiltonian yields a completely real band structure comprising a Dirac cone and a flat band,

$$\omega = \omega_0,\ \omega_0 \pm \sqrt{v_{\mathrm{MD}}^2 k_x^2 + v_{\mathrm{QD}}^2 k_y^2} \tag{8.2}$$

To induce an EP, non-Hermiticity can be introduced by the addition of a small imaginary perturbation to the Hamiltonian,

$$\mathcal{H} = \begin{pmatrix} \omega_0 + i\gamma_{\mathrm{M}} & v_{\mathrm{MD}}k_x & 0 \\ v_{\mathrm{MD}}k_x & \omega_0 + i\gamma_{\mathrm{D}} & v_{\mathrm{QD}}k_y \\ 0 & v_{\mathrm{QD}}k_y & \omega_0 + i\gamma_{\mathrm{Q}} \end{pmatrix} \tag{8.3}$$

with $\gamma > 0$ (< 0) representing a small amount of absorption (amplification) or radiation. An EP3 is obtained by demanding that the characteristic polynomial of Eq. (8.3) has

vanishing derivatives up to second order,

$$\det\left(\mathcal{H}-\omega\mathbb{I}\right)=P(\omega)=0, \tag{8.4}$$

$$P'(\omega)=0, \tag{8.5}$$

$$P''(\omega)=0. \tag{8.6}$$

Solving the above equations for ω, k_x, and k_y yields the EP3 condition:

$$\omega^{\mathrm{EP3}}=\omega_0+\frac{i}{3}\left(\gamma_{\mathrm{M}}+\gamma_{\mathrm{D}}+\gamma_{\mathrm{Q}}\right) \tag{8.7}$$

$$k_x^{\mathrm{EP3}}=\pm\frac{1}{3v_{\mathrm{MD}}}\sqrt{\frac{\left(\gamma_{\mathrm{D}}+\gamma_{\mathrm{Q}}-2\gamma_{\mathrm{M}}\right)^3}{3\left(\gamma_{\mathrm{Q}}-\gamma_{\mathrm{M}}\right)}} \tag{8.8}$$

$$k_y^{\mathrm{EP3}}=\pm\frac{1}{3v_{\mathrm{QD}}}\sqrt{\frac{\left(2\gamma_{\mathrm{Q}}-\gamma_{\mathrm{M}}-\gamma_{\mathrm{D}}\right)^3}{3\left(\gamma_{\mathrm{Q}}-\gamma_{\mathrm{M}}\right)}} \tag{8.9}$$

where any choice of distinct γ leading to real $\mathbf{k}$ induces an EP3. In this work, we used a novel topology optimization (TO) based design method, which can discover PhC geometries with "accidental" and tunable D3s, formed by degenerate modes with different symmetries.

8.1.2 Numerical example

We used our novel inverse-design tool to create triply degenerate DPs in binary dielectric/air square lattices. Fig. 8.1(left) shows two such structures, involving materials of either low ($n = 2$, upper) or high ($n = 3$, lower) refractive indices (in air) and periodicities $a = 1.05\ \lambda$ and $a = 0.6\ \lambda$, respectively, where λ is the design wavelength in vacuum. Note that such refractive indices are typical for common materials such as

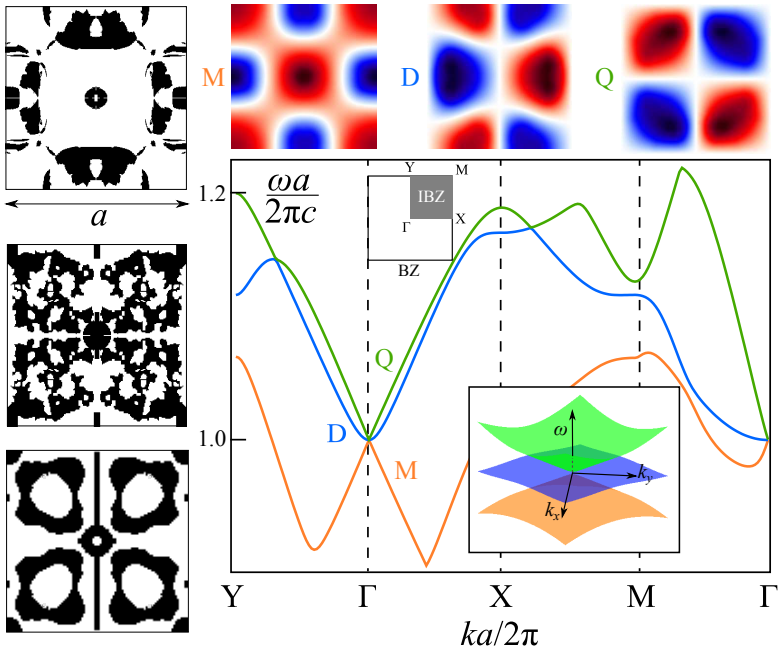

Figure 8.1: Inverse-designed 2d square lattices comprising refractive indices $= \{2, 3, 1.82\}$ (upper, middle, and lower schematics) materials in air (white regions), with periodicity $a = \{1.05, 0.6, 1\}\lambda$. Lower right: band structure of the lattice with refractive index $= 2$ (upper schematic), revealing a Dirac point induced by the presence of an *accidental* third-order degeneracy (D3) of monopolar (M), dipolar (D), and quadrupolar (Q) modes (upper insets). A schematic of the Brillouin zone (BZ) denoting high-symmetry $\mathbf{k}$ points $(\mathrm{Y}, \Gamma, \mathrm{X}, \mathrm{M})$ is also shown. Due to the lack of C_{4v} symmetry, the dispersion along the X and Y directions differ.

silicon nitride, lithium niobate, diamond, silicon, alumina, or many low and high-index ceramics at optical, microwave, and terahertz frequencies. We focus our discussion on the low-index structure (more details can be found in [51]). Noticeably, the band structure of the low-index lattice exhibits a D3 comprising M, D and Q modes at the Γ point, shown in Fig. 8.1 (lower right). Note that since the optimized PhC lacks C_{4v} symmetry (but possesses C_{2v}), there is only one dipolar mode at the designated frequency and hence, the degeneracy of the three modes is completely *accidental*. In the vicinity of the tri-modal degeneracy, the band structure exhibits conical Dirac dispersion accom-

panied by a quadratic flat band. While general rules regarding the occurrence of Dirac point (DP) dispersion in the vicinity of a modal degeneracy are well understood from group theoretic considerations, e.g. as arising from *two* different irreducible representations [244], to our knowledge our TO-designed PhC is the first demonstration of a DP formed by *three* degenerate modes belonging to *three* different representations, namely the A_1, A_2 and B_1 representations of the C_{2v} group.

The third order Dirac degeneracy of Fig. 8.1 can be straightforwardly linked to an EP3 through the introduction of non-Hermiticity, i.e. material loss, gain, or open boundaries (radiation). Here, we consider such an EP3 by introducing a small imaginary part in the dielectric constant, $\kappa = \sqrt{\mathrm{Im}[\epsilon]} = 0.005$, representing intrinsic material loss and resulting in small decay rates $\{\gamma_\mathrm{M}, \gamma_\mathrm{D}, \gamma_\mathrm{Q}\}/\omega_0 \approx \{3.6, 4.3, 4.2\} \times 10^{-4}$. From Eqs. (8.8) and (8.9), it follows that there exists an EP3 at $\mathrm{Re}[\omega_{\mathrm{EP3}}] \approx \omega_0$, $\mathrm{Im}[\omega_{\mathrm{EP3}}] \approx 4{\times}10^{-4}(\frac{2\pi c}{a})$, $k_x^{\mathrm{EP3}} \approx 7 \times 10^{-5}$ $(\frac{2\pi}{a})$ and $k_y^{\mathrm{EP3}} \approx 1.8 \times 10^{-5}$ $(\frac{2\pi}{a})$.

A defining signature of non-Hermitian systems is that eigenvectors are no longer orthogonal. Rather, they are bi-orthogonal [245] in the sense of an unconjugated "inner product" between left and right eigenvectors, $\left(\Psi_n^{\mathrm{L}}\right)^{\mathrm{T}} \Psi_m^{\mathrm{R}} = \delta_{nm}$, defined such that $A\Psi^{\mathrm{R}} = \omega^2\Psi^{\mathrm{R}}$ and $A^{\mathrm{T}}\Psi^{\mathrm{L}} = \omega^2\Psi^{\mathrm{L}}$, where A is the Maxwell operator $\hat{\epsilon}^{-1}(\nabla + i\mathbf{k})\times\frac{1}{\mu}(\nabla + i\mathbf{k})\times$ under Bloch boundary conditions at a specific $\mathbf{k}$, $\hat{\epsilon}$ is the diagonal permittivity tensor $\epsilon(\mathbf{r})$. At our EP3 , the three eigenmodes coalesce and become self-orthogonal [246], leading to vanishing inner products $\left(\Psi_n^{\mathrm{L}}\right)^{\mathrm{T}} \Psi_n^{\mathrm{R}} = 0,\ n \in \{1, 2, 3\}$, as characterized by the so-called Petermann factor (PF),

$$\mathrm{PF}_n = \frac{||\Psi_n^{\mathrm{L}}||^2 ||\Psi_n^{\mathrm{R}}||^2}{|\left(\Psi_n^{\mathrm{L}}\right)^{\mathrm{T}} \Psi_n^{\mathrm{R}}|^2} \tag{8.10}$$

where $||...||^2$ is the usual L_2 norm given by $||\Psi||^2 = \Psi^{\mathrm{T}*}\Psi$.

Local density of states.— The divergence of the Petermann Factor (PF) in open systems can lead to many important effects [13, 247]. In particular, the SE rate of emitters in resonant cavities is traditionally expressed via the PF (a generalization of the Purcell factor [13]), becoming most pronounced near EPs where the latter diverges [184]. More rigorously, however, the SE rate is given by the LDOS, or electromagnetic Green's function (GF), which though enhanced turns out to be finite even at EPs [44]: coalescent eigenmodes no longer form a complete basis, requiring instead an augmented basis of associated Jordan modes and hence a different definition of LDOS. Such an expansion was recently employed in [44] to demonstrate limits to LDOS at EP2s in both passive and active media; here, we extend these results to the case of EP3s.

The LDOS at an EP3 can be obtained from the diagonal elements of the imaginary part of the dyadic GF:

$$\mathbb{G}_{\mathrm{EP3}} \approx \frac{\Psi^{\mathrm{R}}_{\mathrm{EP3}}(\Psi^{\mathrm{L}}_{\mathrm{EP3}})^T}{(\omega^2-\omega^2_{\mathrm{EP3}})^3} + \frac{\Psi^{\mathrm{R}}_{\mathrm{EP3}}(\Phi^{\mathrm{L}}_{\mathrm{I}})^T + \Phi^{\mathrm{R}}_{\mathrm{I}}(\Psi^{\mathrm{L}}_{\mathrm{EP3}})^T}{(\omega^2-\omega^2_{\mathrm{EP3}})^2} + \frac{\Psi^{\mathrm{R}}_{\mathrm{EP3}}(\Phi^{\mathrm{L}}_{\mathrm{II}})^T + \Phi^{\mathrm{R}}_{\mathrm{I}}(\Phi^{\mathrm{L}}_{\mathrm{I}})^T + \Phi^{\mathrm{R}}_{\mathrm{II}}(\Psi^{\mathrm{L}}_{\mathrm{EP3}})^T}{\omega^2-\omega^2_{\mathrm{EP3}}}. \quad (8.11)$$

Eq. (8.11) involves a complicated sum of cubic, quadratic, and linear Lorentzian profiles weighted by the outer products of the only surviving left (right) eigenmode $\Psi^{(\mathrm{L,R})}_{\mathrm{EP3}}$ and the two associated Jordan vectors $\Phi^{(\mathrm{L,R})}_{(\mathrm{I,II})}$, determined by the third-order Jordan decomposition of the Maxwell eigenproblem,

$$A_{\mathrm{EP3}}\Psi^{\mathrm{R}}_{\mathrm{EP3}} = \omega^2_{\mathrm{EP3}}\Psi^{\mathrm{R}}_{\mathrm{EP3}} \quad (8.12)$$

$$A_{\mathrm{EP3}}\Phi^{\mathrm{R}}_{\mathrm{I}} = \omega^2_{\mathrm{EP3}}\Phi^{\mathrm{R}}_{\mathrm{I}} + \Psi^{\mathrm{R}}_{\mathrm{EP3}} \quad (8.13)$$

$$A_{\mathrm{EP3}}\Phi^{\mathrm{R}}_{\mathrm{II}} = \omega^2_{\mathrm{EP3}}\Phi^{\mathrm{R}}_{\mathrm{II}} + \Phi^{\mathrm{R}}_{\mathrm{I}}, \quad (8.14)$$

and its associated dual. Eq. (8.11) reveals that the LDOS spectrum $\sim -\mathrm{Im}\big[\mathrm{Tr}\big(\mathbb{G}\big)\big]$ can vary dramatically depending on position, frequency, and decay rates.

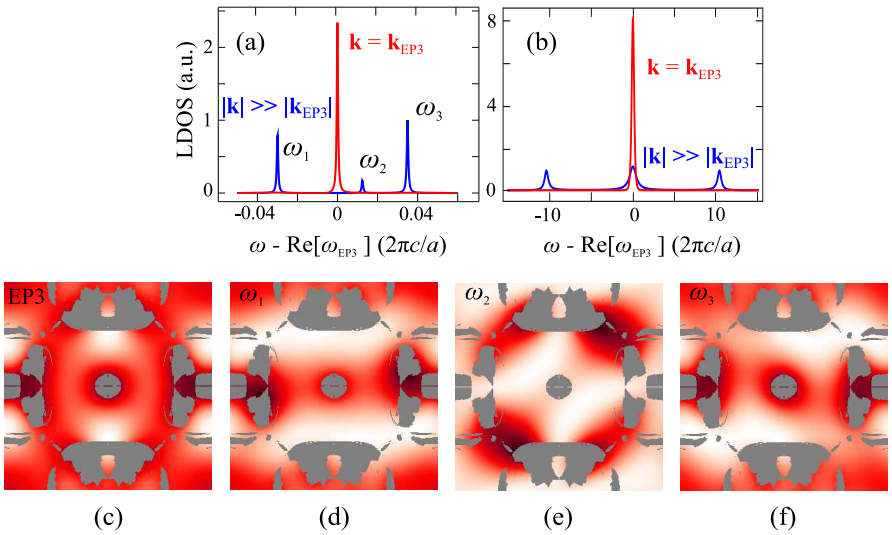

Figure 8.2: (a) Local density of states (LDOS) at the center of the unit cell of the structure in Fig. 8.1, evaluated at either $\mathbf{k}^{\mathrm{EP3}} \approx \{7, 1.8\}\times 10^{-5}(\frac{2\pi}{a})$ (red curves) or $\mathbf{k} = \{7, 1.8\}\times 10^{-2}(\frac{2\pi}{a}) \gg \mathbf{k}^{\mathrm{EP3}}$ (blue curves). (b) Maximum (8-fold) LDOS enhancement associated with a EP3, computed via the reduced 3×3 Hamiltonian model of Eq. (8.3). (c)–(f) LDOS profiles evaluated at either ω_{EP3} or at the non-degenerate frequencies ω_1, ω_2, and ω_3, corresponding to the EP3 and far-away points described in (a). Note that the LDOS is evaluated only in air regions since the LDOS within a lossy medium formally diverges [248].

Figure 8.2(a) shows the LDOS spectra at the center of the unit cell $\mathbf{r}_0$, evaluated at either $\mathbf{k}^{\mathrm{EP3}}$ (red curves) or a point $\mathbf{k} = \{7, 1.8\} \times 10^{-2}(2\pi/a) \gg \mathbf{k}^{\mathrm{EP3}}$ (blue curves) far away from the EP3, demonstrating an enhancement factor of ≈ 2.33 in this geometry. Figure 8.2(c-f) show the corresponding spatial LDOS profiles at and away from the EP3, illustrating the seamless coalescence of the eigenmodes. Even greater enhancements are possible under different loss profiles, i.e., γ_{M}, γ_{D} and γ_{Q}, as illustrated by the following analysis based on the reduced Hamiltonian

framework above. In particular, the GF at a given location in the unit cell can be directly related to the diagonal entries of the resolvent of $\mathcal{H}$, defined as $G \equiv (\mathcal{H} - \omega\mathbb{I})^{-1}$. For example, the third entry of G yields the LDOS at points where the intensity of the quadrupole mode dominates. Consider a scenario in which only the monopole mode has a finite lifetime, i.e., $\gamma_{\mathrm{M}} = \gamma$ while $\gamma_{\mathrm{D}} = \gamma_{\mathrm{Q}} = 0$. It follows from Eq. (8.3) and Eq. (8.11) that the LDOS in this case is given by,

$$
\begin{aligned}
-\operatorname{Im}\{G_{\mathrm{EP3}}[3,3]\} \approx -\frac{2\gamma^2}{27}\frac{\bar{\gamma}^3 - 3\bar{\gamma}(\operatorname{Re}[\omega_{\mathrm{EP3}}] - \omega)^2}{(\operatorname{Re}[\omega_{\mathrm{EP3}}] - \omega)^2 + \bar{\gamma}^2]^3} \\
+ \frac{\gamma}{3}\frac{\bar{\gamma}^2 - (\operatorname{Re}[\omega_{\mathrm{EP3}}] - \omega)^2}{[(\operatorname{Re}[\omega_{\mathrm{EP3}}] - \omega)^2 + \bar{\gamma}^2]^2} - \frac{\bar{\gamma}}{(\operatorname{Re}[\omega_{\mathrm{EP3}}] - \omega)^2 + \bar{\gamma}^2},
\end{aligned}
\tag{8.15}
$$

where $\bar{\gamma} \equiv \gamma/3$. Moreover, the peak LDOS at $\omega = \operatorname{Re}[\omega_{\mathrm{EP3}}]$ is found to be $8/\gamma$, corresponding to an 8-fold enhancement relative to the peak LDOS far away from the EP3. Such an enhancement is illustrated in Fig. 8.2(b), which also reveals the highly non-Lorentzian spectrum associated with this EP3. We remark that this enhancement in LDOS does not lead to additional dissipation, which is made clear upon observing that the loss rates (described by the imginary parts of the complex eigenfrequencies) remain roughly the same at and away from the EP. Instead, it arises from the complex, constructive interference of these modes, as mediated by the decay channels. Note also that similar enhancements can also be realized in non-dissipative media so long as there exist decay channels leading to non-Hermiticity (e.g. radiative or coupling losses).

It is possible to exploit a simple sum rule, namely that the spectrally integrated LDOS is a constant [224], to predict the maximum enhancement possible for an EP

of arbitrary order n. In particular, the integrated LDOS of an order-n Lorentzian of the form $L_n(\omega) = \frac{\gamma^{2n-1}c_n}{[(\omega-\mathrm{Re}[\omega_{\mathrm{EPn}}])^2+\gamma^2]^n}$ is $S_n(\omega) = \int d\omega\, L_n(\omega) = \frac{c_n\sqrt{\pi}\Gamma[n-\frac{1}{2}]}{\Gamma[n]}$, where Γ is the gamma function. It follows from the sum rule that $nS_1(\omega) = S_n(\omega)$ and, consequently, that $c_n/c_1 = \frac{\sqrt{\pi}\Gamma[n+1]}{\Gamma[n-\frac{1}{2}]} \sim \sqrt{n^3}$ for large $n \gg 1$. In the case of an EP3, the maximum enhancement $c_3/c_1 = 8$, which is realized in the scenario discussed above. We now turn to discuss another application of EPs to higher-harmonic generation.

8.2 Nonlinear Frequency conversion at EPs

In this section, we demonstrate that radiative emission at ω_e from a subwavelength particle, e.g. spontaneous emission or fluorescence from atoms or radiation from plasmonic antennas, embedded in a triply resonant nonlinear $\chi^{(2)}$ cavity can be greatly modified and efficiently up-converted to $2\omega_e$ in the vicinity of an EP. The efficiency of such a frequency-conversion process depends strongly on the lifetimes and degree of confinement of the cavity modes [249], which we characterize by deriving a closed-form, analytical formula for the nonlinear Purcell factor: the LDOS or emission rate at $2\omega_e$ from a dipole current source oscillating at ω_e. In particular, we obtain emission bounds applicable to situations involving both monochromatic and broad-bandwidth emitters, showing that the nonlinear Purcell factor in a cavity supporting an EP at ω_e formed out of dark and leaky modes can generally be more two orders of magnitude larger than that of a non-degenerate cavity, depending on the position of the emitter and on complicated but designable modal selection rules. When combined with recently demonstrated

inverse-designed structures optimized to enhance nonlinear interactions [51, 241], the proposed EP enhancements could lead to several orders-of-magnitude larger luminescence efficiencies.

The key to enhancing the LDOS at an EP is to exploit the intricate physics arising from the coalescence of dark and leaky (lossy) resonances. Featuring infinite lifetimes and vanishing decay rates, dark modes are by definition generally inaccessible to external coupling. Consequently, an emitter on resonance with a dark mode cannot radiate unless it is also coupled to a leaky mode. Such a shared resonance underlies the monochromatic LDOS enhancements at EPs described recently in Refs. [44, 51], which showed that the LDOS at an EP exhibits a narrowed, squared Lorentzian lineshape whose peak is four times larger than the maximum LDOS at a non-degenerate resonance. Although such an effect makes it possibile to enhance monochromatic emission near the EP resonance, the existence of a sum rule [224], which forces the frequency-intregrated LDOS over the resonance bandwidth to be a constant, prohibits any enhancement in the case of broadband emitters (e.g. fluorescent molecules). In this section, we exploit a coupled-mode theory framework to show that in contrast to the linear LDOS, both the monochromatic and frequency-integrated radiation rate of a dipolar emitter in a nonlinear medium can be can be enhanced in the presence of an EP.[§]

[§]In our online manuscript [52], we buttress this theoretical prediction with a concrete physical example: a 2D PhC slab designed to support an EP at ω_e and a leaky (phase-matched) resonance at $2\omega_e$. Furthermore, we consider individual emitters as well as uniform distributions of incoherent emitters throughout the crystal, showing that EPs can enhance emission in both cases.

8.2.1 Coupled-mode analysis

To understand the impact of EPs on nonlinear frequency conversion, we consider a generic system involving a degenerate (a_1, b_1) tuple of dark and leaky modes at ω_1 and a single mode a_2 at ω_2. Such a system, shown schematically in Fig. 8.1, is well described by the following coupled-mode equations (CME) [95]:

$$\frac{da_1}{dt} = i\omega_1 a_1 + i\kappa b_1 - i\omega_1 \left(\beta_1 a_2 a_1^* + \beta_3 a_2 b_1^*\right) + s(t) \tag{8.16}$$

$$\frac{db_1}{dt} = i\omega_1 b_1 - \gamma_1 b_1 + i\kappa a_1 - i\omega_1 \left(\beta_2 a_2 b_1^* + \beta_3 a_2 a_1^*\right) \tag{8.17}$$

$$\frac{da_2}{dt} = i\omega_2 a_2 - \gamma_2 a_2 - i\omega_1 \left(\beta_1 a_1^2 + \beta_2 b_1^2 + \beta_3 a_1 b_1\right) \tag{8.18}$$

Mode a_1 is dark while b_1 and a_2 have decay rates γ_1 and γ_2, respectively. The two degenerate modes are coupled to one another via the linear coefficient κ and nonlinearly coupled to a_2 by a parametric $\chi^{(2)}$ nonlinear process characterized by mode-overlap factors βs [249, 95], defined further below in terms of the linear cavity fields. Solving the CMEs in the absence of nonlinearities, one finds that for $\kappa \geq \gamma_1/2$, the frequencies and decay rates of the coupled modes are given by $\omega_\pm = \omega_1 \pm \sqrt{\kappa^2 - \gamma_1^2/4}$ and $\gamma_1/2$, respectively, where the latter is independent of κ. In particular, the two degenerate modes coalesce at $\kappa_{\text{EP}} = \gamma_1/2$, forming an EP at the complex frequency $\omega_1 - i\gamma_1/2$. In the limit $\kappa \to \infty$ of far-apart mode frequencies, one recovers the well-known, non-degenerate (ND), single-mode description of second-harmonic generation [95], which we compare against when

considering any enhancements arising from the EP.[†] Note that in these CMEs, the term $s(t)$ represents a dipole current source positioned in such a way so as to exclusively couple to the dark mode, a situation that is illustrated with a concrete physical example in [52]. Since such a term is meant to model a weak emitter (except in the case of gain media), we primarily focus on the so-called small-signal or non-depletion regime where one can neglect the nonlinear terms responsible for down-conversion (e.g. $\beta_1 a_2 a_1^*$).

Before delving further into the nonlinear equations, it is instructive to briefly review the mechanism of LDOS enhancement in the linear regime of $\beta = 0$. Consider a monochromatic source $s(t) = s_0 e^{i\omega_e t}$ that is on-resonance with the cavity, i.e. $\omega_e = \omega_1$. Solving the CMEs, one finds that the steady-state mode amplitudes at the EP are $a_1^{\mathrm{EP}} = 4s_0/\gamma_1$ and $b_1^{\mathrm{EP}} = 2is_0/\gamma_1$, whereas in the ND limit of $\kappa \to \infty$, $a_1^{\mathrm{ND}} = b_1^{\mathrm{ND}} = s_0/\gamma_1$. Since the LDOS or radiated power is given by $\gamma_1|b_1|^2$, it follows that the EP produces an enhancement factor $\frac{\gamma_1|b_1^{\mathrm{EP}}|^2}{\gamma_1|b_1^{\mathrm{ND}}|^2} = 4$, a result recently derived in [44] by a perturbative expansion of the Green's function based on Jordan eigenvectors but which also follows from the coupled-mode picture above (see supplemental materials). We emphasize that such an enhancement can be realized despite the fact that both the EP and ND resonances exhibit the same effective decay rate $\gamma_1/2$, indicating that the enhancement does not arise from an otherwise trivial increase in resonant lifetimes but rather from a constructive interference of the two modes, which leads to both narrowing and

[†]Note that in principle, coupled-mode theory breaks down in the asymptotic limit of infinite coupling $\kappa \to \infty$. However, as exemplified in the physical example of Fig. 2.2 and as follows from the CMEs, similar enhancements are achieved in the more practical and adequate situation of far-separated and well-defined resonances with $\kappa \gg \gamma_1$.

amplification of the cavity spectrum [44]. Unfortunately, such an enhancement disappears when considering the frequency-integrated emission from a broadband source, a consequence of a general sum rule (derived from causality [224]) which implies that $\int \gamma_1 |b_1^{\mathrm{EP}}(\omega)|^2 \, d\omega = \int \gamma_1 |b_1^{\mathrm{ND}}(\omega)|^2 \, d\omega$. As we show below, however, such a sum rule no longer seems to be valid in the case of finite $\beta \neq 0$.

Consider a typical Lorentzian source, $s(t) = \int_{-\infty}^{\infty} \frac{\sqrt{\gamma_e}}{\gamma_e + i(\omega - \omega_e)} e^{i\omega t} \, d\omega$, of frequency ω_e and decay rate γ_e, and whose Fourier amplitude $s(\omega)$ is normalized so that $\int |s(\omega)|^2 \, d\omega = \pi$. Solving the CMEs in the non-depletion regime yields the amplitude a_2 of the harmonic mode as a convolution,

$$a_2(\omega) = \frac{i\omega_1/2}{i\left(\omega - \omega_2\right) + \gamma_2} \int_{-\infty}^{\infty} dq \, \Big[\beta_1 a_1\left(\omega\right) a_1\left(\omega - q\right) + \beta_2 b_1\left(\omega\right) b_1\left(\omega - q\right) + \beta_3 a_1\left(\omega\right) b_1\left(\omega - q\right) \Big], \quad (8.19)$$

in terms of the mode amplitudes,

$$a_1(\omega) = \frac{s(\omega)\sqrt{\gamma_e}\left(\gamma_1 + i\left(\omega - \omega_1\right)\right)}{\left(\kappa^2 + \left(\omega - \omega_1\right)\left(i\gamma_1 - \omega + \omega_1\right)\right)\left(\gamma_e + i\left(\omega - \omega_e\right)\right)} \quad (8.20)$$

$$b_1(\omega) = \frac{is(\omega)\sqrt{\gamma_e}\kappa}{\left(\kappa^2 + \left(\omega - \omega_1\right)\left(i\gamma_1 - \omega + \omega_1\right)\right)\left(\gamma_e + i\left(\omega - \omega_e\right)\right)}. \quad (8.21)$$

which can be evaluated to yield closed-form, analytical solutions, as we show in Sec. 8.4.

In the particular limit of a monochromatic source with $\gamma_e \ll \gamma_1$, the emission

rate at the harmonic frequency, $\gamma_2|a_2(\delta)|^2$, or nonlinear LDOS can be written as:

$$\gamma_2|a_2^{\mathrm{EP}}(\delta)|^2_{\gamma_e\to 0} = \frac{64\pi^2\zeta|s|^4}{\gamma_1^5\left(4\delta^2+1\right)^4\left(4\delta^2+\zeta^2\right)}\Big[16\beta_1^2\left(\delta^2+1\right)^2+4\beta_3^2\left(\delta^2+1\right) \\ +8\beta_1\left(\beta_2\left(\delta^2-1\right)-2\beta_3\left(\delta^3+\delta\right)\right)-4\beta_2\beta_3\delta+\beta_2^2\Big], \tag{8.22}$$

where $\delta = \frac{\omega_1-\omega_e}{\gamma_1}$ is the normalized frequency detuning of the emitter from the cavity resonance and $\zeta = \gamma_2/\gamma_1$. Evidently, the output spectrum assumes a narrowed and highly non-Lorentzian lineshape, a signature of the EP. In the opposite limit of a broadband source with $\gamma_e \gg \gamma_1$, the relevant quantity to consider is the integrated LDOS near ω_2, given by:

$$\int \gamma_2|a_2^{\mathrm{EP}}(\omega)|^2\,d\omega\Big|_{\gamma_e\gg\gamma_1} \approx \frac{\pi^3|s|^4}{4608\gamma_1^5(\zeta+1)^3}\left(\frac{\gamma_1}{\gamma_e}\right)^2\Big[\beta_1^2\left(237312\zeta^2+638208\zeta+460800\right) \\ -2\beta_2\beta_1\left(29952\zeta^2+89856\zeta+92160\right)+\beta_2^2\left(6912\zeta^2+20736\zeta+18432\right) \\ +\beta_3^2\left(29952\zeta^2+89856\zeta+73728\right)\Big], \tag{8.23}$$

To quantify the impact of these spectral modifications, we compare the emission rates at the EP against those obtained in the ND scenario, given by:

$$\gamma_2|a_2^{\mathrm{ND}}(\delta)|^2_{\gamma_e\to 0} = \frac{4\pi^2\left(\beta_1+\beta_2+\beta_3\right)^2\zeta|s|^4}{\gamma_1^5\left(4\delta^2+1\right)^2\left(4\delta^2+\zeta^2\right)} \tag{8.24}$$

$$\int \gamma_2|a_2^{\mathrm{ND}}(\omega)|^2\,d\omega\Big|_{\gamma_e\gg\gamma_1} = \frac{\pi^3\left(\beta_1+\beta_2+\beta_3\right)^2|s|^4}{\gamma_1^5(\zeta+1)}\left(\frac{\gamma_1}{\gamma_e}\right)^2 \tag{8.25}$$

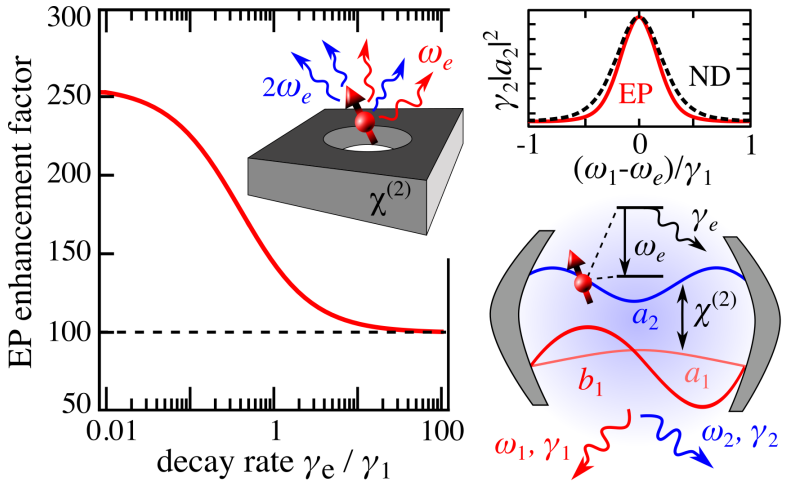

Figure 8.3: Schematic of a dipole emitter (ω_e, γ_e) embedded in a triply resonant $\chi^{(2)}$ nonlinear cavity supporting an exceptional point (EP). The cavity consists of two degenerate resonances (a_1, b_1) at ω_1, one dark and one leaky with decay rate γ_1, that are coupled to one another via a linear coupling rate κ and nonlinearly coupled to a harmonic mode of frequency $\omega_2 = 2\omega_1$ and decay rate γ_2 by the $\chi^{(2)}$ process. An EP is formed when $\kappa = \gamma_1/2$. The EP leads to enhanced emission at the second harmonic frequency over and above that of a non-degenerate (ND) system with a single mode at ω_1 of the same effective decay rate $\gamma_1/2$. The plot summarizes the nonlinear EP enhancement factor, defined as the ratio of nonlinear emission rate at EP to that of ND, as a function of the relative emitter bandwidth γ_e/γ_1, showing the enhancement ratio of 256 in the limit $\gamma_e/\gamma_1 \to 0$ and 100 in the opposite limit $\gamma_e \gg \gamma_1$. The inset (top-right) shows the second-harmonic emission spectra aka nonlinear local density of states $\gamma_2|a_2|^2$ as a function of detuning $\frac{(\omega_e-\omega_1)}{\gamma_1}$ in the limit of a monochromatic emitter, $\gamma_e \to 0$, for both EP (solid) and ND (dashed) systems. For convenience, both emission rates have been normalized to unity, showing narrowed linewidth in the case of EP.

Figure 8.3 shows the nonlinear EP enhancement factor, $\mathcal{F}(\omega, \gamma_e) = \frac{|a_2^{\mathrm{EP}}(\omega,\gamma_e)|^2}{|a_1^{\mathrm{ND}}(\omega,\gamma_e)|^2}$, which is the ratio of the emission rate around ω_2 at the EP to that in the ND scenario for the typical situation of an emitter that is resonantly coupled to the fundamental cavity frequency, i.e. $\omega_e = \omega_1$. In particular, the figure shows $\mathcal{F}$ as a function of the output frequency $(\omega - \omega_2)/\gamma_1$ and for multiple values of γ_e/γ_1 when all of the nonlinear coupling coefficients except the one pertaining to the

dark mode vanish, i.e. $\beta_1 \neq 0,\ \beta_2 = \beta_3 = 0$. Such a nonlinear configuration belies one of the main results of this work, which follows from Eq. (8.24) and Eq. (8.25): the largest radiation rates and therefore Purcell enhancements are achieved when the dipole emitter couples exclusively to the dark mode and when only the latter couples strongly to the harmonic mode. Evaluating $\mathcal{F}$ at $\omega = \omega_2$ and taking the limit of $\gamma_e \to 0$ or equivalently, evaluating the ratio of Eqs. (8.22) and (8.24) in the limit of zero detuning $\delta = 0$, yields a maximum enhancement factor of 256. The (top-right) inset of Fig. 8.3 shows the dependence of the nonlinear LDOS Eq. (8.22) with respect to the emitter detuning δ in the monochromatic regime $\gamma_e \to 0$, showing a slightly narrowed EP spectrum compared to the ND scenario (both spectra are normalized to have the same peak amplitude for clarity). Notably, one finds that compared to the linear scenario discussed above, the nonlinear spectrum undergoes significantly less narrowing, evidence that the frequency-integrated emission can also be enhanced. Indeed, focusing in the case of a broadband emitter with $\gamma_e \gg \gamma_1$, e.g. a fluorescent molecule [250], and taking the ratio of Eqs. (8.23) and (8.25), one finds that the frequency-integrated emission can be enhanced by a factor of 100.

The aforementioned LDOS enhancements at the EP can be understood intuitively from a recently derived sum rule [224]. In the linear regime, causality demands that when two non-degenerate resonances of equal bandwidths γ merge to form an EP, the resulting LDOS spectrum becomes a squared Lorentzian [§] and obeys the sum rule [224], $\sum_i \int \frac{s_i^2 \gamma}{\delta^2+\gamma^2}\, d\delta = \int \frac{2 s_{\mathrm{EP}}^2 \gamma^3}{(\delta^2+\gamma^2)^2}\, d\delta$, where $s_{\mathrm{EP}}^2 = s_1^2 + s_2^2$ and

[§]The optical response of a system near a doubly degenerate leaky resonance can be approximated by a second-order, complex pole [44, 50]

$s_{1,2}$ denote the coupling strengths of a dipole source which generally couples to both modes. It follows from the sum rule that at an EP and in the special case of identical coupling strengths, $s_1 = s_2 = s_{\mathrm{ND}}$, the mode volume of the cavity resonance decreases (and hence the coupling rate of an emitter increases) so that $s_{\mathrm{ND}} = s_{\mathrm{EP}}/\sqrt{2}$, but only at the expense of an effectively narrower cavity bandwidth. Such a multi-modal interference phenomenon also leads to an effective increase in the nonlinear coupling coefficient, with $\beta_{\mathrm{ND}} = 0.5\beta_{\mathrm{EP}}$, as we show in Sec. 8.5. Both effects combine to increase nonlinear emission by two orders of magnitude.

8.3 Concluding remarks

In this section, we explored two applications of LDOS enhancement near EPs in systems with third-order EPs and systems with triply degenerate $\chi^{(2)}$ media. Moreover, we demonstrated that topology optimization can be used to design structures that could demonstrate this enhancement. Although fabrication of the "bar-code" structures in Sec. 8.1 may prove challenging at visible wavelengths using currently available technologies, future experimental realizations are entirely feasible in the mid-infrared to microwave regimes, where complex features can be straightforwardly fabricated in polymers and ceramics with the aid of computerized machining, 3D printing, laser cutting, additive manufacturing, or two-photon lithography [251, 252, 253]. In Sec. 8.2, we have shown that the efficiency of nonlinear frequency conversion processes can be greatly enhanced in cavities featuring EPs. Our derived bounds on the possible nonlinear Purcell factors achievable in

EP systems show that the degree of enhancement depends on complicated but tunable modal selection rules and are optimal when the emission sources couple primarily to dark modes. In combination with recently demonstrated inverse-designed structures optimized to enhance nonlinear overlaps [254], the proposed EP enhancements could lead to orders-of-magnitude larger nonlinear interactions and emission efficiencies. While luminescence enhancements at EPs in linear media are nullified in the case of broadband emitters, nonlinear Purcell factors can be enhanced by two orders of magnitudes even when the emission bandwidth is much larger than the cavity bandwidth. Although we illustrated these ideas by examining a simple proof-of-concept 2d PhC design, these predictions could also be tested in a wide variety of structures, including highly nonlinear mid-infrared quantum wells [255] or microwave super-conducting qubit [256] platforms. Finally, we expect that similar or even potentially larger enhancements can arise in systems supporting higher-order exceptional points [51] or other nonlinear processes, e.g. third-harmonic generation, four-wave mixing, and two-photon down-conversion, with potential applications to quantum information science.

8.4 Appendix A: Nonlinear EP enhancement formula

The nonlinear CMEs describing emission from a dipolar source embedded in the triply resonant cavity above are (in the non-depletion regime):

$$\frac{da_1}{dt} = i\omega_1 a_1 + i\kappa b_1 + s_a(t) \tag{8.26}$$

$$\frac{db_1}{dt} = (i\omega_1 - \gamma_1) b_1 + i\kappa a_1 + s_b(t) \tag{8.27}$$

$$\frac{da_2}{dt} = i\omega_2 a_2 - \gamma_2 a_2 - i\omega_1 \left(\beta_1 a_1^2 + \beta_2 b_1^2 + \beta_3 a_1 b_1\right) \tag{8.28}$$

Here, we assume that the two cavity resonances are frequency-matched for second-harmonic generation, so that $\omega_2 = 2\omega_1$. Assuming a Lorentzian dipole source located at some position $\mathbf{r}$, the coupling amplitudes in Eqs. (8.26) and (8.27) are $s_{a/b}(t) = \left(\frac{E_{a/b}(\mathbf{r})}{2\int \epsilon_r |\mathbf{E}_{a/b}|^2 d\mathbf{r}}\right) \int_{-\infty}^{\infty} \frac{\sqrt{\gamma_e}}{\gamma_e + i(\omega - \omega_e)} e^{i\omega t}\, d\omega$. To obtain an explicit expression for $a_2(\omega)$, it suffices to Fourier transform Eq. (8.28), in which case one finds that the amplitude at the second harmonic depends on a convolution of the linear modes at ω_1. Focusing on the EP scenario ($\kappa = \gamma_1/2$) and defining $\delta = \omega - 2\omega_1$, one

obtains:

$$
\begin{aligned}
a_2^{\mathrm{EP}}(\omega) = -8\pi\gamma_e \Bigg\{ & i\beta_3 \Big[2 s_a s_b \left(\gamma_1^2 \delta + i\gamma_1^3 + \gamma_1 \delta \left(4\gamma_e + i\left(-4\omega_e + 5\omega - 6\omega_1\right)\right) + 2\delta^2 \left(i\gamma_e + \omega_e - \omega + \omega_1\right)\right) \\
& + \gamma_1 s_a^2 \left(2\gamma_1 + i\delta\right)\left(2\gamma_1 + 2\gamma_e + i\left(-2\omega_e + 3\omega - 4\omega_1\right)\right) + \gamma_1 \delta s_b^2 \left(2i\gamma_1 + 2i\gamma_e + 2\omega_e - 3\omega + 4\omega_1\right) \Big] \\
& + \beta_1 \Big[2\gamma_1 s_a s_b \left(2\gamma_1 + i\delta\right)\left(2i\gamma_1 + 2i\gamma_e + 2\omega_e - 3\omega + 4\omega_1\right) \\
& + s_a^2 \left(8\gamma_1^3 + \gamma_1^2 \left(10\gamma_e + i\left(-10\omega_e + 21\omega - 32\omega_1\right)\right) + 4\gamma_1 \delta \left(3i\gamma_e + 3\omega_e - 4\omega + 5\omega_1\right)\right. \\
& \left. -4\delta^2 \left(\gamma_e + i\left(-\omega_e + \omega - \omega_1\right)\right)\right) + \gamma_1^2 s_b^2 \left(-2\gamma_1 - 2\gamma_e + 2i\omega_e - 3i\omega + 4i\omega_1\right) \Big] \\
& - \beta_2 \Big[2\gamma_1 \delta s_a s_b \left(2\gamma_1 + 2\gamma_e + i\left(-2\omega_e + 3\omega - 4\omega_1\right)\right) + \gamma_1^2 s_a^2 \left(2\gamma_1 + 2\gamma_e + i\left(-2\omega_e + 3\omega - 4\omega_1\right)\right) \\
& + s_b^2 \left(\gamma_1^2 \left(-2\gamma_e + 2i\omega_e - i\omega\right) + 4\gamma_1 \delta \left(-i\gamma_e - \omega_e + \omega - \omega_1\right) + 4\delta^2 \left(\gamma_e + i\left(-\omega_e + \omega - \omega_1\right)\right)\right) \Big] \Bigg\} \\
& \Big/ \Bigg\{ \left[\gamma_1 + i\left(\omega - 2\omega_1\right)\right]^3 \left[-i\gamma_2 + \omega - 2\omega_1\right) \left(\gamma_1 + 2\left(\gamma_e + i\left(-\omega_e + \omega - \omega_1\right)\right)\right]^2 \left(-2i\gamma_e - 2\omega_e + \omega\right) \Bigg\}
\end{aligned}
\tag{8.29}
$$

Given this unruly but general expression, we consider two main limiting cases in the main text, corresponding to either a monochromatic ($\gamma_e \to 0$) or broadband ($\gamma_e \gg \gamma_1$) emitter, leading to the simplified expressions in several limits.

8.5 Appendix B: Nonlinear-overlap enhancement

In the main text, we showed and argued that the effectively smaller mode volume associated with an EP also leads to a two-fold increase in the nonlinear overlap coefficients. Here, we show explicitly how such an increase manifests in the CMEs.

The Hamiltonian corresponding to the linear, coupled-mode system above is

given by:

$$\mathcal{H} = \begin{pmatrix} \omega_1 & \kappa \\ \kappa & \omega_1 - i\gamma_1 \end{pmatrix}. \tag{8.30}$$

For $\kappa \neq \gamma_1/2$, $\mathcal{H}$ can be diagonalized such that the mode amplitudes $\mathbf{a}_1 = (a_1, b_1)$ can be transformed into the diagonal basis $\mathbf{a}_1' = (a_1', b_1')$ by a linear, unitary transformation matrix S, such that $\mathbf{a}_1 = S\mathbf{a}_1'$. In the strong-coupling limit $\kappa \to \infty$ of ND resonances, the transformation matrix is $S = \begin{pmatrix} -\frac{1}{\sqrt{2}} & \frac{1}{\sqrt{2}} \\ \frac{1}{\sqrt{2}} & \frac{1}{\sqrt{2}} \end{pmatrix}$. Writing the amplitude of the second-harmonic mode in the non-depletion limit,

$$a_2(\omega) = \frac{-i\omega_1 \left(\beta_1 a_1^2 + \beta_2 b_1^2 + \beta_3 a_1 b_1\right)}{\gamma_2 + i(\omega - \omega_2)},$$

in terms of the ND resonance (i.e. taking $\mathbf{a}_1 \to S\mathbf{a}_1'$), one finds that the amplitude in the ND limit $\kappa \to \infty$ is given by:

$$a_2(\omega) = \frac{-i\omega_1}{\gamma_2 + i(\omega - \omega_2)} \frac{(\beta_1 + \beta_2 + \beta_3)}{2} \left(a_1'\right)^2. \tag{8.31}$$

Thus, the nonlinear overlap coefficient of the ND system is related to the corresponding overlap factors of the system at the EP by the relation:

$$\beta^{\mathrm{ND}} = \frac{(\beta_1 + \beta_2 + \beta_3)}{2}. \tag{8.32}$$

Chapter 9

Outlook

In this chapter, we discuss generalizations and futuer applications of our theory of radiation noise.

9.1 Laser noise at exceptional points

In previous chapters, we focused on the properties of spontaneous-emission noise in two kinds of systems: *non-degenerate lasers* on the one hand and *degenerate non-lasing* systems with EPs on the other hand. A natural question that comes to mind is what happens to spontaneous emission in lasers which operate at EPs? This problem is not trivial for several reasons. First, laser equations are nonlinear, while EPs are traditionally analyzed in linear systems. Most importantly, self-orthogonality, which was the culprit for the apparent divergence of the linewidth in the linear theory, follows from the bi-orthogonality relations, but the modes of nonlinear equations are no longer orthogonal [257]. Additionally, the definition of "Jordan vectors," which we use to compute the limiting behavior at linear EPs (in Ch. 7), changes in nonlinear eigenvalue problems [34]. From a numerical perspective, we need new tools for computing Jordan vectors (similar to those presented

in appendix A) and for forcing EPs. Secondly, even after correctly formulating and finding nonlinear EPs, one still needs to show that the nonlinear solution is a stable one (i.e., small perturbations relax to the solution). The question of stability in lasers can be a rather subtle issue [258], even near ordinary modal degeneracies [259] and, therefore, cannot be taken for granted at EPs. Last, even after correctly formulating the EP solution and proving its stability, there remains the question of computing the linewidth. In the simpler case of non-degenerate (and spectrally separated) resonances, we were able to compute the spectrum semi-analytically by treating the phases of the modes as independent Brownian variables. However, near the EP, the phases of the degenerate eigenmode and associated Jordan vectors are likely to be dependent, and it is not obvious that a semi-analytic solution even exists.

9.2 Linewidth reduction

In Ch. 3, we presented a new comprehensive theory for the laser linewidth. It is naturally interesting to apply our new linewidth formula [Eq. (3.3)] to the practical problem of linewidth reduction. Narrow-linewidth high-power lasers are highly desirable for many applications, such as laser cooling [260] and precision spectroscopy [261]. The challenge of narrowing the linewidth involves achieving stable single-mode steady-state operation with low noise levels. The existing literature on linewidth optimization typically makes many simplifying approximations [262], and we believe that more accurate modeling (along the lines of our work) could greatly advance this field. Note that our current theory applies only

to the Schawlow-Townes limited linewidth, i.e., when external noise influences are lower than internal noise (from spontaneous emission in the gain medium), but can be generalized to include external noise as well. Additional generalizations are required in order to account for external-cavity coupling and seeding, which are commonly used in narrow-linewidth sources [263, 264].[§] Last, we mention that the full generality of our approach is only revealed when applied to complex-cavity realistic structures, and therefore requires efficient tools for solving the steady-state (noise-free) laser equations. The recent algorithm in [18] is already more efficient than the original SALT formulation [56], but our group is developing a new generation of Anderson-acceleration-based software, which can handle complex three-dimensional lasers efficiently.

9.3 Noise-driven relaxation oscillations in other fields

Noise-driven relaxation oscillations (ROs) are not restricted to lasers, and appear, more generally, in complex systems with a nonlinear steady state and multiple time scales: a nonlinear restoring force and a time delay. As such, we think that the tools developed in Ch. 5 could apply to problems in other areas of research. For example, ROs in the neuron network of the brain were suggested as a possible mechanism for gamma oscillations [168]—neural oscillations, typically at 40Hz, which (hypothetically) relate the activity in different areas of the brain and may play a central role in human perception. A neural network is somewhat analogous to the atoms in a laser in the sense that the network consists of coupled elements

[§]For an extension of SALT to seeded lasers, see [265].

(neurons/atoms) which alternate stochastically between two states (active and quiescent neurons/excited and depleted atoms). Another example can be found in geophysics. An earthquake is commonly described as an instability occurring along preexisting crustal faults [170]. The seismic cycle of earthquake recurrence is characterized by long periods of quasi-static evolution which precede sudden slip events accompanied by elastic wave radiation: the earthquake. This succession of processes over two well distinguished time scales recalls the behavior of nonlinear relaxation oscillations. Other examples include predator-prey models in population dynamics [169] and mesoscopic oscillatory chemical reactions [266].

9.4 Theory for LEDs and high-gain amplifiers

Another possible extension of our laser-noise theory is to gain amplifiers or lasers with strong amplified spontaneous emission (ASE). As mentioned in Ch. 6, a strong ASE field may deplete the atomic inversion and affect lasing properties such as output power and threshold. Since SALT in its current form treats only the steady-state "deterministic field," it does not account for ASE. However, the effect of ASE can be incorporated into the theory by using the fluctuation-dissipation theorem to relate the variance of the ASE field to the steady-state Green's function, similar to our general approach for handling laser noise.

9.5 Applications of LDOS enhancement at EPs

In the second part of the thesis, we studied a new striking feature of EPs: a dramatic increase in the "local density of states" (LDOS) near specially designed structures. We explored two applications of this property: enhanced spontaneous emission rates (Ch. 7) and enhanced frequency conversion in nonlinear media (Ch. 8). From a practical standpoint, it is important to understand how to maximize the enhancement and whether it is bounded at all. The answer to the latter question is yes, and recent work [233] shows that existing resonant structures fall orders-of-magnitude short from the theoretical bound. It would be interesting to explore whether EPs may be used to attain (or get closer to) the bound. This hypothesis can be tested with the numerous experimental realizations of EPs in optical systems: waveguides [176], periodic photonic structures (with [267] or without [38] gain), coupled whispering-gallery mode resonators [192] and coupled quantum cascade lasers [178], to name a few. In fact, EPs occur in a wide variety of other systems (such as exciton–polariton billiard-shaped traps [35], optomechanical systems [36], laser-induced autoionized atoms [268], and acoustical systems [181]) and LDOS enhancement in those systems may have additional applications.

Appendix A

Scalable Computation of Jordan Chains

A.1 Introduction

In this appendix, we present algorithms to find approximate Jordan vectors of nearly defective matrices, designed to be scalable to large sparse/ structured matrices (e.g., arising from discretized partial differential equations), by requiring only a small number of linear systems to be solved. This project was lead by Felipe Hernandez, and was motivated by our work in chapter X and, more generally, by the recent explosion of interest in the physics of "exceptional points" (EPs), in which a linear operator $A(p)$ that depends on some parameter(s) p becomes defective at $p = p_0$, almost always with a 2×2 Jordan block [188, 189, 190, 176, 36, 178, 38]. A variety of interesting phenomena arise in the vicinity of the EP. The limiting behavior at the EP [40, 44], as well as perturbation theory around it [34], is understood in terms of the Jordan chain relating an eigenvector x_0 and a Jordan vector j_0:

$$A_0 x_0 = \lambda_0 x_0, \tag{A.1}$$

$$A_0 j_0 = \lambda_0 j_0 + x_0, \tag{A.2}$$

where $A_0 = A(p_0)$. Typically in problems that arise from modeling realistic physical systems, one does not know A_0 precisely, but only has a good approximation μ for the degenerate eigenvalue λ_0 and a matrix $A_\varepsilon = A(p_0 + \varepsilon)$ *near* to A_0, limited both by numerical errors and the difficulty of tuning p to find the EP exactly. Given A_ε and μ, the challenge is to approximately compute x_0, λ_0, and j_0 to at least $O(\varepsilon)$ accuracy.

Existing algorithms to approximate the Jordan chain [269, 270] rely on computing the dense SVD of A_ε, which is not scalable, or have other problems described below. Instead, we want an algorithm that only requires a scalable method to solve linear systems $(A_\varepsilon - \mu\mathbb{1})x = y$ ("linear solves"), and such algorithms are readily available (e.g. they are needed anyway to find the eigenvalues away from the EP that are being forced to coincide). Using only such linear solves, we show that we can compute the Jordan chain to $\mathcal{O}(\varepsilon)$ accuracy (Sec. A.3), or even $\mathcal{O}(\varepsilon^2)$ accuracy if dA/dp is also supplied (Sec. A.5), which we find is similar to the previous dense algorithms (whose accuracy had not been analyzed) [270]. Our algorithm consists of two key steps. First, in Sec. A.2, we compute an orthonormal basis for the span of the two nearly defective eigenvectors of A_ε, using a shift-and-invert–like algorithm with some iterative refinement to circumvent conditioning problems for the second basis vector. Second, in Sec. A.3, we use this basis to project to a 2×2 matrix, find a defective matrix within $\mathcal{O}(\varepsilon)$ of that, and use this nearby defective matrix to approximate the Jordan chain of A_0 to $\mathcal{O}(\varepsilon)$. We have successfully applied this method to study EPs of large sparse matrices arising from discretizing the Maxwell equations of electromagnetism [23], and include an

example calculation in Sec. A.4.

In this sort of problem, we are *given* the existence of a 2×2 Jordan block of an unknown but *nearby* matrix A_0, and we want to find the Jordan chain. (Larger Jordan blocks, which rarely arise in practice for large matrices [51], are discussed in Sec. A.6.) To uniquely specify the Jordan vector j_0 (to which we can add any multiple of x_0 [270]), we adopt the normalization choice $\|x_0\| = 1$ and $x_0^* j_0 = 0$. Our algorithm finds approximations with *relative* errors $\|\lambda_\varepsilon - \lambda_0\|/\|\lambda_0\|$, $\|x_\varepsilon - x_0\|/\|x_0\|$, and $\|j_\varepsilon - j_0\|/\|j_0\|$ which are $\mathcal{O}(\varepsilon)$. The nearly degenerate eigenvalues and eigenvectors of A_ε are given via perturbation theory [33] by Puiseux series:

$$x^\pm = x_0 \pm c\varepsilon^{1/2} j_0 + \varepsilon w \pm \mathcal{O}(\varepsilon^{3/2}) \tag{A.3}$$

for some constant c and a vector w, and similarly for the eigenvalues $\lambda^\pm$. This means that a naive eigenvalue algorithm to find x_ε by simply computing an eigenvector of A_ε will only attain $\mathcal{O}(\varepsilon^{1/2})$ accuracy, and furthermore that computing both $x^\pm$ eigenvectors is numerically problematic for small ε because they are nearly parallel. In contrast, the invariant subspace *spanned* by $x^\pm$ varies smoothly around A_0 [as can easily be seen by considering $x^+ + x^-$ and $\varepsilon^{-1/2}(x^+ - x^-)$] and, with some care, an orthonormal basis for this subspace can be computed accurately by a variant of shifted inverse iteration (Sec. A.2). From that invariant subspace, we can then compute x_ε and so on to $\mathcal{O}(\varepsilon)$ accuracy, which is optimal: because the set of defective matrices forms a continuous manifold, there are infinitely many defective matrices within $\mathcal{O}(\varepsilon)$ of A_ε, and hence we cannot determine A_0 to better accuracy without some additional information about the desired A_0, such as

dA/dp.

An algorithm to solve this problem was proposed by Mailybaev [270], which uses the SVD to approximate the perturbation required to shift A_ε onto the set of defective matrices, but the dense SVD is obviously impractical for large discretized PDEs and similar matrices. Given A_0, Leung and Chang [269] suggest computing x_0 by either an SVD or a shifted inverse iteration, and then show that j_0 can be computed by solving an additional linear system (which is sparse for sparse A). Those authors did not analyze the accuracy of their algorithm if it is applied to A_ε rather than A_0, but we can see from above that a naive eigensolver only computes x_0 to $\mathcal{O}(\varepsilon^{1/2})$ accuracy, in which case they obtain similar accuracy for j_0 (since the linear system they solve to find j_0 depends on x_0). If an $\mathcal{O}(\varepsilon)$ algorithm is employed to compute x_0 accurately (e.g. via our algorithm below), then Leung and Chang's algorithm computes j_0 to $\mathcal{O}(\varepsilon)$ accuracy as well, but requires an additional linear solve compared to our algorithm. It is important to note that our problem is very different from Wilkinson's problem [271], because in our case the Jordan structure (at least for the eigenvalue of interest) is known, making it possible to devise more efficient algorithms than for computing an unknown Jordan structure. (The latter also typically involve dense SVDs, Schur factorizations, or similar [272, 273, 274].) Our algorithm differs from these previous works in that it relies primarily on inverse iteration (and explicitly addresses the accuracy issues thereof), and thus is suitable for use with the large (typically sparse) matrices arising in physical applications. Moreover we perform an analysis of the error in terms of ε (i.e., the distance between A_ε and A_0), which was absent

from previous works.

A.2 Finding the invariant subspace

In this section, we describe two algorithms for computing the invariant subspace of A_ε spanned by the eigenvectors whose eigenvalues are near λ_0. Both algorithms begin by using standard methods (e.g., Arnoldi or shifted inverse iteration [275]) to find u_1 as an eigenvector of A_ε. Then, we find an additional basis vector u_2 as an eigenvector of $P^\perp A_\varepsilon$, where $P^\perp \equiv \mathbb{I} - u_1 u_1^*$ is the orthogonal projection onto the subspace perpendicular to u_1. We denote by U_ε the matrix whose columns are the orthonormal basis vectors, u_1 and u_2. In Algorithm 1, u_2 is found by performing inverse iteration on the operator $P^\perp A_\varepsilon$ (lines 3–8). Since $P^\perp A_\varepsilon$ does not preserve the sparsity pattern of A_ε, this algorithm is scalable only when using matrix-free iterative solvers (that is, solvers which only require fast matrix-vector products).

Algorithm 1 for finding the invariant subspace U_ε using matrix-free iterative solvers

1: Find an eigenvector u_1 of A_ε with eigenvalue near μ (e.g., using inverse iteration).
2: $P^\perp \leftarrow \mathbb{I} - u_1 u_1^*$
3: $\lambda' \leftarrow \mu$
4: $u_2 \leftarrow$ a random vector orthogonal to u_1.
5: **while** $\|(P^\perp A_\varepsilon - \lambda' \mathbb{I}) u_2\| > \text{tol}$ **do**
6: $\quad v \leftarrow (P^\perp A_\varepsilon - \lambda' \mathbb{I})^{-1} u_2$
7: $\quad u_2 \leftarrow v / \|v\|$
8: $\quad \lambda' \leftarrow u_2^* P^\perp A_\varepsilon u_2$
9: Set $U_\varepsilon = (u_1, u_2)$.

Note that this iteration could easily be changed from Rayleigh-quotient inverse

iteration to an Arnoldi Krylov-subspace procedure. In practical applications where the matrix parameters were already tuned to force a near EP, however, the estimate μ is close enough to the desired eigenvalue λ_2 that convergence only takes a few steps of Algorithm 1.

Alternatively, when using sparse-direct solvers, one can implement Algorithm 2, which performs inverse iteration on A_ε and only then applies $P^\perp$. In order to see the equivalence of the two algorithms, let us denote the nearly degenerate eigenvectors of A_ε by u_1 and x_2 [i.e., $A_\varepsilon u_1 = \lambda_1 u_1$ and $A_\varepsilon x_2 = \lambda_2 x_2$, with $\lambda_1 \approx \lambda_2$]. While Algorithm 1 finds the eigenvector u_1 and then computes an eigenvector of $P^\perp A_\varepsilon$, Algorithm 2 computes in the second step the orthogonal projection of the second eigenvector of A_ε, $P^\perp x_2$. The equivalence of the Algorithms follows from the fact that the orthogonal projection of x_2 is precisely an eigenvector of $P^\perp A_\varepsilon$ [since $(P^\perp A_\varepsilon)(P^\perp x_2) = (P^\perp A_\varepsilon)(\mathbb{1} - u_1 u_1^*)x_2 = P^\perp(A_\varepsilon x_2) - P^\perp(A_\varepsilon u_1)u_1^* x_2 = \lambda_2 P^\perp x_2 - \lambda_1 P^\perp u_1 u_1^* x_2 = \lambda_2(P^\perp x_2)$]. Note, however, that a subtlety arises when using Algorithm 2 since the vector $(A_\varepsilon - \mu\mathbb{1})^{-1}u_2$ (line 3) is nearly parallel to u_1 and, consequently, the roundoff error in the projection $P^\perp$ is significant. To overcome this difficulty, we use an iterative refinement procedure [276] (lines 5–7) before continuing the inverse iteration.

The importance of the invariant subspace U_ε is that it is, in fact, quite close to the invariant subspace for the defective matrix A_0. Thus it is possible to find good approximants of the eigenvector and Jordan vector of A_0 within the column space of U_ε, as stated in the following lemma.

Lemma 1 *Let A_ε be near to a defective matrix A_0 (i.e., $\|A_\varepsilon - A_0\| = \mathcal{O}(\varepsilon)$), and*

Algorithm 2 for finding the invariant subspace U_ε using sparse-direct solvers

Do steps 1-4 in Algorithm 1.
while $\|(P^\perp A_\varepsilon - \lambda' \mathbb{I})u_2\| > \text{tol}$ **do**
    $v \leftarrow P^\perp (A_\varepsilon - \lambda' \mathbb{I})^{-1} u_2$
    $e \leftarrow u_2 - P^\perp (A_\varepsilon - \lambda' \mathbb{I}) v$
    while $\|e\| > \text{tol}$ **do**
        $v \leftarrow v + P^\perp (A_\varepsilon - \lambda' \mathbb{I})^{-1} e$
        $e \leftarrow u_2 - P^\perp (A_\varepsilon - \lambda' \mathbb{I}) v$
    $u_2 \leftarrow v/\|v\|$
    $\lambda' \leftarrow u_2^* P^\perp A_\varepsilon u_2$
$U_\varepsilon \leftarrow (u_1, u_2)$.

U_ε be the invariant subspace of its nearly degenerate eigenvalue. Then there exists a matrix U_0 which spans the invariant subspace for A_0 such that $\|U_0 - U_\varepsilon\| = \mathcal{O}(\varepsilon)$.

This Lemma establishes that the invariant subspace of nearly degenerate eigenvalues varies smoothly at the vicinity of the EP, a property that has been previously established (e.g., [245, Chapter 2.1.4]) and can be easily proven using the following proposition:

Proposition 1 *Let v_0 be any vector in the invariant subspace of A_0. Then there exists a vector v in the column space of U_ε such that $\|v - v_0\| = \mathcal{O}(\varepsilon \|v_0\|)$.*

Proof. Expand v_0 in the basis $\{x_0, j_0\}$ consisting of the eigenvector and Jordan vector for A_0, so that

$$v_0 = \alpha x_0 + \beta j_0.$$

According to perturbation theory near A_0, the eigenvectors $x^\pm$ of A_ε can be expanded in a Puiseux series [Eq. (A.3)]. Let us choose $v = ax^+ + bx^-$ with

$a = (\alpha + \beta\varepsilon^{-1/2}/c)/2$ and $b = (\alpha - \beta\varepsilon^{-1/2}/c)/2$. By construction, v is in the invariant subspace of A_ε and, therefore, also in the column space of U_ε. Moreover,

$$\|v_0 - v\| = \varepsilon\alpha w + \mathcal{O}[(|\alpha| + |\beta|\varepsilon^{-1/2})\varepsilon^{3/2}] = \mathcal{O}(\varepsilon\|v_0\|).$$

Proposition 1 allows us to approximate vectors in U_0 (the invariant subspace of A_0) with vectors in U_ε (the invariant subspace in A_ε). To prove Lemma 1, we need to show that the converse is also true, i.e., that vectors in U_0 can be approximated by vectors in U_ε. Since U_0 and U_ε have equal dimensions, this follows as a corollary.

A.3 Computing the Jordan chain

In this section we introduce vectors, x_ε and j_ε, in the column space of U_ε, which approximate the Jordan chain vectors, x_0 and j_0, with $\mathcal{O}(\varepsilon)$ accuracy. Since the first and second columns of U_ε are eigenvectors of A_ε and $P^\perp A_\varepsilon$ respectively, a naive guess would be to set $x_\varepsilon = u_1$ and $j_\varepsilon \propto u_2$. However, we know from perturbation theory that such an approach leads to relatively large errors since $\|u_1 - x_0\| = O(\varepsilon^{1/2})$, and we show below that we can obtain a more accurate approximation. Algorithm 3 presents a prescription for constructing x_ε and j_ε.

In the remainder of this section, we prove the following theorem:

Theorem 1 *Suppose A_0 is a defective matrix with Jordan chain vectors x_0 and j_0, and A_ε is a nearby matrix such that $\|A_\varepsilon - A_0\| = \mathcal{O}(\varepsilon)$. The vectors x_ε and j_ε, constructed via Algorithms 1–3, satisfy $\|x_0 - x_\varepsilon\|, \|j_0 - j_\varepsilon\| = \mathcal{O}(\varepsilon)$.*

Algorithm 3 for finding approximate Jordan chain vectors.

1: Introduce $S_\varepsilon = U_\varepsilon^* A_\varepsilon U_\varepsilon$ (denote entries of S_ε by s_{ij}).
2: Set $\lambda_\varepsilon = (s_{22} + s_{11})/2$.
3: Set $\gamma = (s_{22} - s_{11})/2s_{12}$.
4: Set $x_\varepsilon = u_1 + \gamma u_2$ and $j_\varepsilon = u_2/s_{12}$.
5: Normalize x_ε and j_ε.

To prove Theorem 1, we first introduce the 2×2 defective matrix

$$\tilde{S} = \begin{pmatrix} s_{11} & s_{12} \\ -\frac{(s_{11}-s_{22})^2}{4s_{12}} & s_{22} \end{pmatrix}. \tag{A.4}$$

The vectors x_ε and j_ε, constructed above, are related to the Jordan chain vectors x'_ε and j'_ε of $\tilde{S}$ via $x_\varepsilon = U_\varepsilon x'_\varepsilon$ and $j_\varepsilon = U_\varepsilon j'_\varepsilon$. [More explicitly, one can verify that the vectors $x'_\varepsilon = [1; \gamma]$ and $j'_\varepsilon = [0; s_{12}^{-1}]$ satisfy the chain relations: $\tilde{S}x'_\varepsilon = \lambda_\varepsilon x'_\varepsilon$ and $\tilde{S}j'_\varepsilon = \lambda_\varepsilon j'_\varepsilon + x'_\varepsilon$.] Using this observation, we prove Theorem 1 in two steps: First, we introduce the 2×2 defective matrix $S_0 \equiv U_0^* A_0 U_0$, and show that the Jordan chain vectors of S_0 and $\tilde{S}$ are within $\mathcal{O}(\varepsilon)$ of each other (Lemma 2). Then, we use Lemma 3 to show that the proximity of the Jordan chains of S_0 and $\tilde{S}$ implies the proximity of $\{x_\varepsilon, j_\varepsilon\}$ and the Jordan chain vectors of A_0. In the remainder of this section, we prove Lemmas 2–3.

Lemma 2 *The Jordan chains of S_0 and $\tilde{S}$ are within $\mathcal{O}(\varepsilon)$ of each other.*

Proof. Any defective matrix is similar to a 2×2 defective matrix of the form

$$S = \begin{pmatrix} \lambda + \alpha\beta & \alpha^2 \\ -\beta^2 & \lambda - \alpha\beta \end{pmatrix}, \tag{A.5}$$

with appropriate complex parameters α, β, λ [272]. The Jordan chain vectors of S are

$$x' = \frac{1}{\sqrt{|\alpha|^2 + |\beta|^2}} \begin{pmatrix} \alpha \\ -\beta \end{pmatrix}, \quad j' = \frac{1}{|\alpha|^2 + |\beta|^2} \begin{pmatrix} \beta \\ \alpha \end{pmatrix}. \tag{A.6}$$

The matrix $\tilde{S}$ can be recast in the form of Eq. (A.5) with $\tilde{\alpha}^2 = s_{12}$, $\tilde{\beta}^2 = \frac{(s_{22}-s_{11})^2}{4s_{12}}$, and $\tilde{\lambda} = (s_{11} + s_{22})/2$. To rewrite S_0 in the form of Eq. (A.5), we introduce α_0, β_0 and λ_0. From Eq. (A.6), in order to prove the proximity of the Jordan chains, it remains to show that $|\tilde{\alpha} - \alpha_0|$ and $|\tilde{\beta} - \beta_0|$ are both $\mathcal{O}(\varepsilon)$.

Since u_1 is an eigenvector of A_ε and is also orthogonal to u_2, S_ε is upper triangular (i.e. $s_{21} = 0$). By construction, the matrices $\tilde{S}$ [Eq. (A.4)] and $S_\varepsilon \equiv U_\varepsilon^* A_\varepsilon U_\varepsilon$ differ only in the lower-left entry, which has the form $(s_{11} - s_{22})^2/4s_{12}$. Since s_{11} and s_{22} are the nearly degenerate eigenvalues of A_ε, they differ by $\varepsilon^{1/2}$, so this entry is of size $\mathcal{O}(\varepsilon)$, which implies $\|\tilde{S} - S_\varepsilon\| = \mathcal{O}(\varepsilon)$. From Lemma 1 we have $\|U_\varepsilon - U_0\| = \mathcal{O}(\varepsilon)$, which implies that $\|S_\varepsilon - S_0\| = \mathcal{O}(\varepsilon)$, and it follows that $\|\tilde{S} - S_0\| = \mathcal{O}(\varepsilon)$. Then, using Eq. (A.5), we conclude that $|\tilde{\alpha}^2 - \alpha_0^2| = \mathcal{O}(\varepsilon)$, so that either $|\tilde{\alpha} - \alpha_0| = \mathcal{O}(\varepsilon)$ or $|\tilde{\alpha} + \alpha_0| = \mathcal{O}(\varepsilon)$ and we may choose the sign of α_0 so that $|\tilde{\alpha} - \alpha_0| = \mathcal{O}(\varepsilon)$. To prove that $|\tilde{\beta} - \beta_0| = \mathcal{O}(\varepsilon)$, we first bound

$$2|\tilde{\alpha}\tilde{\beta} - \alpha_0\beta_0| \leq |(\tilde{\alpha}\tilde{\beta} + \tilde{\lambda}) - (\alpha_0\beta_0 + \lambda_0)| + |(\tilde{\alpha}\tilde{\beta} - \tilde{\lambda}) - (\alpha_0\beta_0 - \lambda_0)| = \mathcal{O}(\varepsilon),$$

where the two terms on the right are bounded by $\mathcal{O}(\varepsilon)$ as they are terms contributing to $\|\tilde{S} - S_0\|$. Now since $|\tilde{\alpha} - \alpha_0| = \mathcal{O}(\varepsilon)$, the above inequality implies that $|\tilde{\beta} - \beta_0| = \mathcal{O}(\varepsilon)$.

Lemma 3 *Given that the Jordan chains of S_0 and $\tilde{S}$ are within $\mathcal{O}(\varepsilon)$ of each other, it follows that the Jordan chain of A_0 and the vectors $\{x_\varepsilon, j_\varepsilon\}$ are within $\mathcal{O}(\varepsilon)$ of each other.*

Proof. The Jordan chain vectors of the 2×2 matrix S_0 are related to the Jordan chain vectors of the large matrix A_0 via: $x_0 = U_0 x_0'$, $j_0 = U_0 j_0'$. Using the standard triangle inequality, we have $\|x_0 - x_\varepsilon\| = \|U_0 x_0' - U_\varepsilon x_\varepsilon'\| \leq \|U_0 x_0' - U_0 x_\varepsilon'\| + \|U_0 x_\varepsilon' - U_\varepsilon x_\varepsilon'\|$. It follows that $\|x_0 - x_\varepsilon\| \leq \|U_0\|\|x_0' - x_\varepsilon'\| + \|U_0 - U_\varepsilon\|\|x_0\|$. Both terms on the right-hand side are quantities that we already know are $\mathcal{O}(\varepsilon)$. The same argument can be used to prove that $\|j_0' - j_\varepsilon'\| = \mathcal{O}(\varepsilon)$.

A.4 Implementation

In this section, we analyze the accuracy of our shift-and-invert-based algorithm and compare it with the SVD-based algorithm presented by Mailybaev [270]. We apply both algorithms to dense defective 50×50 matrices, which are randomly perturbed by an amount ε. Figure A.1 shows the relative errors in eigenvalues and Jordan vectors as a function of ε. We find that both methods are $\mathcal{O}(\varepsilon)$ accurate. However, our method is scalable for large defective matrices (as demonstrated below), whereas the SVD-based method becomes impractical.

When the derivative of the matrix dA/dp is known, the accuracy of both algorithms can be improved. This can happen, for example, when A is an operator arising from a physical problem which depends on p in a known way. An extension of the SVD-based algorithm to incorporate the knowledge of dA/dp is given in [270]. Our algorithm can be improved as follows. First, we employ the adjoint

method to find the value p for which $\mathcal{A}_\varepsilon \equiv A_\varepsilon + p\, dA/dp = A_0 + O(\varepsilon^2)$. More explicitly, we compute the derivative dg/dp, where g is a function constructed to be equal to 0 at the exceptional point, and then take a single Newton step in p to obtain $\mathcal{A}_\varepsilon$. More details are given in the Sec. A.5, (where it is assumed that the matrices A_0 and A_ε are real, but the resulting formula works for both real and complex matrices). Then, by applying Algorithms 1–3 to $\mathcal{A}_\varepsilon$, we obtain a Jordan vector to accuracy ε^2, with the additional cost of a single linear solve compared to the first-order method. Therefore, we refer to the modified algorithm as a second-order method.

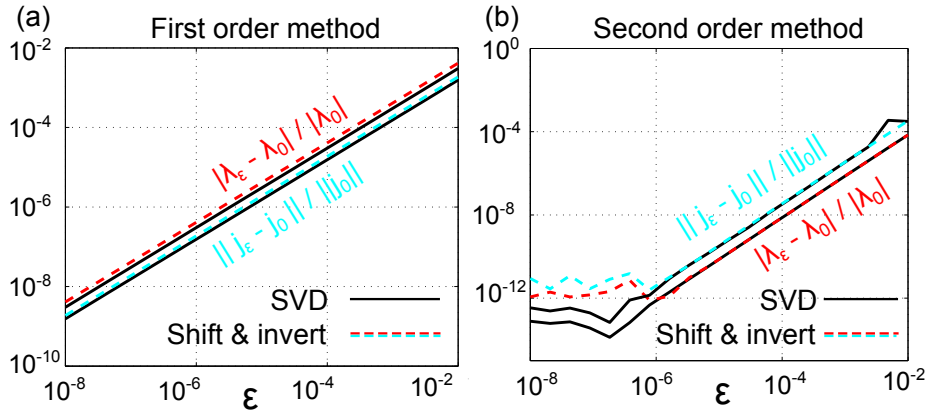

Figure A.1: Relative errors in eigenvalues ($|\lambda_\varepsilon - \lambda_0|/|\lambda_0|$) **and Jordan vectors** ($\|\mathbf{j}_\varepsilon - \mathbf{j_0}\|/\|\mathbf{j_0}\|$)**.** (a) Comparison of our shift-and-invert based first-order method (red and cyan dashed lines) and the previous SVD-based algorithm [270] (black lines). All algorithms demonstrate $\mathcal{O}(\varepsilon)$ convergence. (b) Comparison of our second-order algorithm, which uses the adjoint method (red and cyan dashed lines), and the second-order SVD-based algorithm (black lines). Both methods demonstrate $\mathcal{O}(\varepsilon^2)$ convergence.

The accuracy of our second-order method and a comparison with the SVD-based second-order method are presented in Fig. 1b. Both methods show $\mathcal{O}(\varepsilon^2)$

convergence. Note that a floor of 10^{-12} in the relative error is reached due to rounding errors in the construction of the exactly defective matrix A_0.

In the remainder of this section, we show an application of our algorithm to a physical problem of current interest: Computing spontaneous emission rates from fluorescent molecules which are placed near electromagnetic resonators with EPs [44]. The resonant modes of a system can be found by solving Maxwell's equations, which can be written in the form of an eigenvalue problem: $\hat{A}x_n = \lambda_n x_n$ [23]. Here, Maxwell's operator is $\hat{A} \equiv \varepsilon^{-1}\nabla\times\nabla\times$ (where ε is the dielectric permittivity of the medium), x_n are the eigenmodes (field profiles) and the eigenvalues $\lambda_n \equiv \omega_n^2$ are the squares of the resonant frequencies. We discretize Maxwell operator, $\hat{A}$, using finite differences [217, 44] to a matrix A. As recently shown in [44], the spontaneous emission rate at an EP can be accurately computed using a simple formula that includes the degenerate mode x_n, Jordan vector j_n, and eigenvalue λ_n. To demonstrate our algorithm, we computed x_n, j_n and λ_n for the numerical example of two coupled plasmonic resonators (Fig. A.2a). The system consists of two rectangular silver (Ag) rods covered by a silica (SiO_2) coating, with commensurate distributions of gain and loss in the coating. When adding gain and loss, the eigenvalues move in the complex plane (blue and red lines in Fig. A.2b) and, at a critical amount of gain and loss, they merge at an EP (orange dot). Fig. A.2c presents approximate eigenvector x_ε and Jordan vector j_ε, computed via our shift-and-invert-based algorithm, and normalized so that $x_0^* j_0 = 1$ and $j_0^* j_0 = 0$. (Only the real parts of the vectors are shown in the figure.) The matrix A_ε in this example is $212^2 \times 212^2$. An SVD-based approach would require enor-

mous computational resources for this relatively small two-dimensional problem, whereas our algorithm required only a few seconds on a laptop. The result was validated in [44] by comparing the Jordan-vector perturbation-theory predictions to explicit eigenvector calculations near the EP.

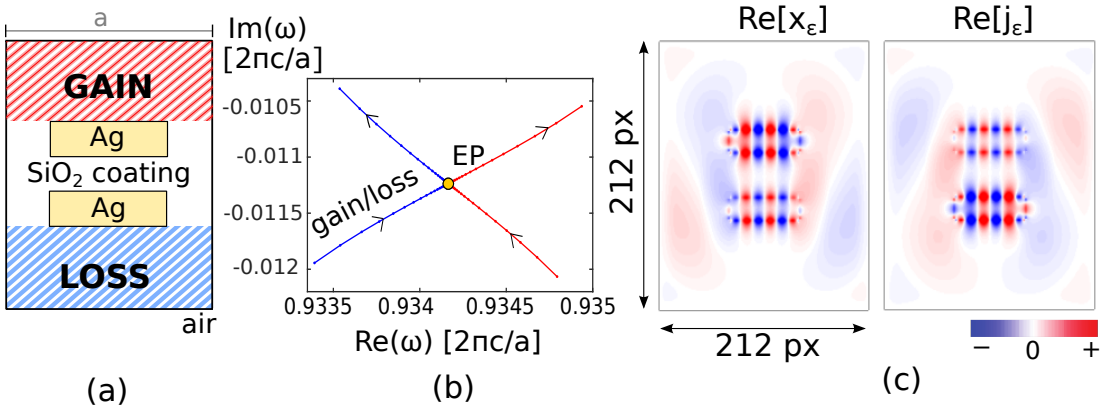

Figure A.2: Application of the algorithm for problems in electromagnetism. (a) Schematics of the structure. Two silver rods (Ag) covered by a silica coating (SiO_2). Gain and loss are added to the outer sides of the coating. (b) By adding gain and loss, the eigenvalues move in the complex plane (blue and red curves) and merge at an EP (orange dot). (c) The approximate degenerate eigenvector x_ε and Jordan vector j_ε. (a) and (b) are borrowed from [44].

A.5 Adjoint method

In this section we suppose we know how to compute the derivaive of the matrix dA/dp and we explain how to use the adjoint method [277, 278] in order to find the value p for which $A_\varepsilon + pdA/dp = A_0 + O(\varepsilon^2)$. The derivation in this section assumes that all matrices are real but, with slight generalizations (some complex conjugations) summarized in Algorithm 5, the formula we provide in the end works both for real and complex matrices.

To find the exceptional point, we consider the matrices U and S as depending on the parameter p. To do this, we would like to define $U(p)$ and $S(p)$ by the equations

$$A(p)U(p) = U(p)S(p)$$
$$U(p)^T U(p) = Id_2,$$

but these do not have a unique solution because of the possibility of rotating the basis U. When U is complex, there are also phase degrees of freedom. To fix this, we can enforce that the first column of U, u_1, is orthogonal to some vector w. We will actually choose w such that when $p = 0$, the matrix S is upper triangular. Thus $U(p)$ and $S(p)$ solve $f(U, S, p) = 0$, where

$$f(U,S,p) = \begin{pmatrix} Au_1 - s_{11}u_1 - s_{21}u_2 \\ Au_2 - s_{12}u_1 - s_{22}u_2 \\ u_1^T u_1 - 1 \\ u_1^T u_2 \\ u_2^T u_2 - 1 \\ u_1^T w \end{pmatrix}.$$

Now we would like to find the value of p such that $S(p)$ is defective and therefore satisfies

$$g(S) = (\text{trace}(S)/2)^2 - \det(S) = 0.$$

By computing $g(0)$ and dg/dp, we can find the correct value of p at which $g(p) = 0$

and we accomplish this task by using the adjoint method, as explained below.

Using the chain rule, we have

$$dg/dp = (\partial g/\partial S)(dS/dp). \tag{A.7}$$

The derivative dS/dp can be found from differentiating $f(U, S, p)$; it satisfies

$$\partial f/\partial p + (\partial f/\partial U)dU/dp + (\partial f/\partial S)dS/dp = 0.$$

Combining the unknowns into a single variable $X = (u_1, u_2, s_{11}, s_{12}, s_{21}, s_{22})$, the equation simplifies to

$$\partial f/\partial p + (\partial f/\partial X)dX/dp = 0.$$

Substituting this into Eq. A.7, we obtain

$$dg/dp = -(\partial g/\partial X)(\partial f/\partial X)^{-1}(\partial f/\partial p).$$

To compute this, we let $\Lambda^T = (\partial g/\partial X)(\partial f/\partial X)^{-1}$, so that

$$(\partial f/\partial X)^T \Lambda = (\partial g/\partial X).$$

The matrix $\partial f/\partial X$ takes the form

$$\partial f/\partial X = \begin{pmatrix} A - s_{11} & -s_{21} & -u_1 & 0 & -u_2 & 0 \\ -s_{12} & A - s_{22} & 0 & -u_1 & 0 & -u_2 \\ 2u_1^T & 0 & 0 & 0 & 0 & 0 \\ u_2^T & u_1^T & 0 & 0 & 0 & 0 \\ 0 & 2u_2^T & 0 & 0 & 0 & 0 \\ 0 & 0 & 0 & 0 & 1 & 0 \end{pmatrix}.$$

Moreover the vector $\partial g/\partial X$ has the form $\partial g/\partial X = (0, 0, h_{11}, h_{12}, h_{21}, h_{22})^T$ (the zeros reflecting the fact that g is independent of U), where

$$\partial g/\partial S = \begin{pmatrix} h_{11} & h_{12} \\ h_{21} & h_{22} \end{pmatrix} = \begin{pmatrix} (s_{11} - s_{22})/2 & s_{21} \\ s_{12} & (s_{22} - s_{11})/2 \end{pmatrix}. \tag{A.8}$$

Expanding the adjoint variables as $\Lambda = (\lambda_1^T, \lambda_2^T, \sigma_{11}, \sigma_{12}, \sigma_{22}, \sigma_{21})^T$, we obtain the adjoint equations

$$(A^T - s_{11})\lambda_1 = s_{12}\lambda_2 - 2\sigma_{11}u_1 - \sigma_{12}u_2 \tag{A.9}$$

$$(A^T - s_{22})\lambda_2 = -\sigma_{12}u_1 - 2\sigma_{22}u_2, \tag{A.10}$$

and the normalization equations

$$-u_1^T \lambda_1 = h_{11} \tag{A.11}$$

$$-u_1^T \lambda_2 = h_{12} \tag{A.12}$$

$$-u_2^T \lambda_2 = h_{22}. \tag{A.13}$$

To solve this system, we first take the dot product of Eq. A.9 with u_1, resulting in

$$g_1^T u_1 + s_{12} \lambda_2^T u_1 - 2\sigma_{11} = 0.$$

Now applying Eq. A.12, this simplifies to

$$\sigma_{11} = \frac{-h_{12} s_{12}}{2}. \tag{A.14}$$

Similarly, taking the dot product of Eq. A.10 with u_2 and using Eq. A.13, we find that

$$\sigma_{22} = \frac{h_{12} s_{12}}{2}. \tag{A.15}$$

To find σ_{21}, we take the dot product of Eq. A.10 equation with u_1 and apply Eq. A.11,

$$-(s_{11} - s_{22}) h_{12} = (s_{11} - s_{22}) \lambda_2^T u_1 = \lambda_2^T (A - s_{22}) u_1 = -\sigma_{12}.$$

This yields

$$\sigma_{12} = (s_{11} - s_{22})h_{12}. \tag{A.16}$$

Now that σ_{ij} are known, we can solve for λ_2 and then for λ_1 using the first two equations. Then we must add back some multiple of the left eigenvectors of A^T to λ_2 and λ_1 so that they satisfy the other two normalization conditions. These steps are summarized in Algorithm 4.

Algorithm 4 The adjoint method for finding p

1: $\sigma_{12} \leftarrow -(s_{11} - s_{22})h_{12}$ (h is defined in Eq. A.8)
2: $\sigma_{22} \leftarrow -s_{12}h_{12}$
3: Solve $(A - s_{22})^T\lambda_2 = \sigma_{12}u_1 - \sigma_{22}u_2$.
4: Add a multiple of the left eigenvector of A to λ_2 so that $u_2^T\lambda_2 = -h_{22}$.
5: Solve $(A - s_{11})^T\lambda_1 = s_{12}\lambda_2 - \sigma_{22}u_1 - \sigma_{12}u_2$.
6: Add a multiple of the left eigenvector of A to λ_1 so that $u_2^T\lambda_1 = -h_{21}$.
7: Compute $dg/dp = -\lambda_1^T(dA/dp)u_1 - \lambda_2^T(dA/dp)u_2$.
8: Set $p = -g(0)/(dg/dp)$.

To derive the adjoint method for complex A, one can split the problem into real and imaginary parts. The resulting computation is described in Algorithm 5.

A.6 Concluding remarks

In this appendix, we presented efficient algorithms for computing Jordan chains of large matrices with a 2×2 Jordan block. These tools can be readily applied to study the limiting behavior of physical systems near second-order exceptional points. The presented algorithm can be easily generalized to handle larger Jordan

Algorithm 5 The adjoint method with complex A

1: Solve $2\alpha_1 - s_{12}\beta_4 i = -s_{12}(g_S)_{12}$ for real α_1 and β_4.
2: Set $a = -\overline{s_{11} - s_{22}}(-(g_S)_{12} + \beta_4 i)$.
3: Set $\overline{b} = (s_{12}(g_S)_{11} - (g_S)_{22} - \overline{a}$.
4: Solve $2\alpha_4 - \beta_3 i = s_{12}(g_S)_{12} + i\beta_4$ for real α_4 and β_3.
5: Solve $(A - \overline{s_{22}})^*\lambda_2 = -au_1 - (2\alpha_4 + \beta_3 i)u_2$.
6: Add a left eigenvector of A to λ_2 so that $u_2^*\lambda_2 = -(g_S)_{22}$.
7: Solve $(A - \overline{s_{11}})^*\lambda_1 = s_{12}\lambda_2 - 2\alpha_1 u_1 - (\overline{a+b})u_2$.
8: Add a left eigenvector of A to λ_1 so that $u_2^*\lambda_1 = -(g_S)_{21}$
9: Compute $dg/dp = -\lambda_1^*(dA/dp)u_1 - \lambda_2^*(dA/dp)u_2$.
10: Set $p = -g(0)/(dg/dp)$.

blocks by first finding an N-dimensional degenerate subspace and a reduced $N \times N$ eigenproblem, and then computing the Jordan chain of its nearest $N \times N$ defective matrix. Since N (the algebraic multiplicity of the eigenvalue) will in practice be very small, existing SVD-based methods [269, 270] can be applied to find this nearby defective $N \times N$ matrix. Moreover, defective nonlinear eigenproblems can be handled using a similar approach with proper modification of the chain relations at the EP [279].

Acknoledgement

The authors would like to thank Gil Strang and Alan Edelman for helpful discussions. This work was partially supported by the Army Research Office through the Institute for Soldier Nanotechnologies under Contract
No. W911NF-13-D-0001.

References

[1] A. I. Sabra, *Theories of light: From Descartes to Newton*. CUP Archive, 1981. (cit. on p. 1)

[2] J. C. Maxwell, "A dynamical theory of the electromagnetic field," *Philos. Trans. R. Soc. Lond.*, vol. 155, pp. 459–512, 1865. (cit. on p. 1)

[3] J. D. Jackson, *Classical Electrodynamics, Edition III*. John Wiley and Sons, 1999. (cit. on pp. 1, 10, 91, 99, and 159)

[4] A. Einstein, "Zur quantentheorie der strahlung (the quantum theory of radiation)," *Phys. Zeit.*, vol. 18, p. 121, 1917. (cit. on p. 1)

[5] A. L. Schawlow and C. H. Townes, "Infrared and optical masers," *Phys. Rev.*, vol. 112, pp. 1940–1949, 1958. (cit. on pp. 1, 3, 26, 30, and 96)

[6] E. Hecht, "Optics, 4th," *International edition, Addison-Wesley, San Francisco*, vol. 3, 2002. (cit. on p. 2)

[7] C. F. Bohren and D. R. Huffman, *Absorption and scattering of light by small particles*. John Wiley & Sons, 2008. (cit. on p. 2)

[8] J. W. Strutt, "Xv. on the light from the sky, its polarization and colour," *Philos. Mag.*, vol. 41, no. 271, pp. 107–120, 1871. (cit. on p. 2)

[9] S. V. Gaponenko, *Introduction to nanophotonics*. Cambridge University Press, 2010. (cit. on p. 2)

[10] J. Arnaud, "Natural linewidth of anisotropic lasers," *Opt. Quant. Elect.*, vol. 18, pp. 335–343, 1986. (cit. on pp. 3, 32, and 71)

[11] H. Haken, *Laser Light Dynamics*. North-Holland, 1985. (cit. on pp. 3, 26, 29, 31, 92, 105, 107, and 111)

[12] A. Cerjan and A. D. Stone, "Why the laser linewidth is so narrow: a modern perspective," *Phys. Scripta*, vol. 91, no. 1, p. 013003, 2015. (cit. on pp. 3, 4, and 110)

[13] K. Petermann, "Calculated spontaneous emission factor for double-heterostructure injection lasers with gain-induced waveguiding," *IEEE J. Quant. Elect.*, vol. 15, no. 7, pp. 566–570, 1979. (cit. on pp. 3, 27, 96, 157, and 203)

[14] C. H. Henry, "Theory of the linewidth of semiconductor lasers," *IEEE J. Quant. Elect.*, vol. 18, pp. 259–264, 1982. (cit. on pp. 3, 27, 32, 49, 60, and 118)

[15] C. H. Henry, "Theory of spontaneous emission noise in open resonators and its application to lasers and optical amplifiers," *J. Light. Tech.*, vol. 4, no. 3, pp. 288–297, 1986. (cit. on p. 3)

[16] A. Pick, A. Cerjan, D. Liu, A. W. Rodriguez, A. D. Stone, Y. D. Chong, and S. G. Johnson, "*Ab initio* multimode linewidth theory for arbitrary inhomogeneous laser cavities," *Phys. Rev. A*, vol. 91, p. 063806, Jun 2015. (cit. on pp. 4, 26, 110, 111, 113, 117, 118, 119, 129, 142, 145, 148, and 194)

[17] A. Cerjan, A. Pick, Y. D. Chong, S. G. Johnson, and A. D. Stone, "Quantitative test of general theories of the intrinsic laser linewidth," *Opt. Express*, vol. 23, no. 22, pp. 28316–28340, 2015. (cit. on pp. 4, 93, and 111)

[18] S. Esterhazy, D. Liu, M. Liertzer, A. Cerjan, L. Ge, K. G. Makris, A. D. Stone, J. M. Melenk, S. G. Johnson, and S. Rotter, "Scalable numerical approach for the steady-state ab-initio laser theory," *Phys. Rev. A*, vol. 90, no. 2, p. 023816, 2014. (cit. on pp. 4, 18, 26, 27, 36, 61, 66, 67, 73, 91, 120, and 221)

[19] K. Vahala, C. Harder, and A. Yariv, "Observation of relaxation resonance effects in the field spectrum of semiconductor lasers," *App. Phys. Lett.*, vol. 42, no. 3, pp. 211–213, 1983. (cit. on pp. 5, 95, 102, 110, and 111)

[20] W. A. H. M. P. Van Exter, J. P. Woerdman, and B. R. P. Zeijlmans, "Spectral signature of relaxation oscillations in semiconductor lasers," *IEEE J. Quantum Electron.*, vol. 28, no. 6, pp. 1470–1478, 1992. (cit. on pp. 5, 110, 111, 112, 113, 117, 118, 119, 120, and 121)

[21] M. Lax, "Classical noise. v. noise in self-sustained oscillators," *Phys. Rev.*, vol. 160, no. 2, pp. 290–301, 1967. (cit. on pp. 5, 27, 28, 30, 43, 48, 66, 71, 114, 142, 144, 145, and 150)

[22] W. Jin, C. Khandekar, A. Pick, A. G. Polimeridis, and A. W. Rodriguez, "Amplified and directional spontaneous emission from arbitrary composite bodies: A self-consistent treatment of purcell effect below threshold," *Physical Review B*, vol. 93, no. 12, p. 125415, 2016. (cit. on p. 5)

[23] J. D. Joannopoulos, S. G. Johnson, J. N. Winn, and R. D. Meade, *Photonic Crystals: Molding the Flow of Light*. Princeton University Press, 2011. (cit. on pp. 6, 9, 10, 12, 13, 23, 161, 169, 171, 187, 225, and 236)

[24] C. F. Guo, T. Sun, F. Cao, Q. Liu, and Z. Ren, "Metallic nanostructures for light trapping in energy-harvesting devices," *Light Sci. Appl.*, vol. 3, no. 4, p. e161, 2014. (cit. on p. 6)

[25] S. S. Wang and R. Magnusson, "Theory and applications of guided-mode resonance filters," *Appl. Opt.*, vol. 32, no. 14, pp. 2606–2613, 1993. (cit. on p. 6)

[26] P. A. Franken, A. E. Hill, C. W. Peters, and G. Weinreich, "Generation of optical harmonics," *Phys. Rev. Lett.*, vol. 7, pp. 118–119, Aug 1961. (cit. on p. 6)

[27] T. Baba, "Slow light in photonic crystals," *Nat. photonics*, vol. 2, no. 8, pp. 465–473, 2008. (cit. on p. 6)

[28] A. Taflove, A. Oskooi, and p. . S. G. Johnson, *Advances in FDTD Computational Electrodynamics: Photonics and Nanotechnology*. Artech House, 2013. Readable online at http://arxiv.org/ftp/arxiv/papers/1301/1301.5366.pdf. (cit. on pp. 6, 16, 90, 91, 159, 160, and 166)

[29] E. M. Purcell, "Spontaneous emission probabilities at radio frequencies," *Phys. Rev.*, vol. 69, pp. 681—681, 1946. (cit. on pp. 6, 157, 162, 171, and 177)

[30] S. Jain, D. G. Hirst, and J. M. O'sullivan, "Gold nanoparticles as novel agents for cancer therapy," *Br. J. Radiol.*, vol. 85, no. 1010, pp. 101–113, 2012. (cit. on p. 6)

[31] J. A. Guicheteau, a. D. C. M. E. Farrell, A. W. F. III, P. M. Pellegrino, E. D. Emmons, A. Tripathi, P. Wilcox, and D. Emge, "Surface-enhanced raman scattering (sers) evaluation protocol for nanometallic surfaces," *Appl. Spectrosc.*, vol. 67, no. 4, pp. 396–403, 2013. (cit. on p. 6)

[32] T. J. Kippenberg, S. M. Spillane, and K. J. Vahala, "Demonstration of ultra-high-q small mode volume toroid microcavities on a chip," *Applied Physics Letters*, vol. 85, no. 25, pp. 6113–6115, 2004. (cit. on p. 6)

[33] N. Moiseyev, *Non-Hermitian Quantum Mechanics*. Cambridge University Press, 2011. (cit. on pp. 6, 9, 11, 14, 22, 24, 35, 71, 79, 156, 157, 159, 181, and 226)

[34] A. P. Seyranian and A. A. Mailybaev, *Multiparameter Stability Theory With Mechanical Applications*. World Scientific Publishing, 2003, vol. XIII. (cit. on pp. 6, 9, 23, 24, 158, 163, 164, 219, and 224)

[35] T. Gao, E. Estrecho, K. Y. Bliokh, T. C. H. Liew, M. D. Fraser, S. Brodbeck, M. Kamp, C. Schneider, S. Hofling, Y. Yamamoto, F. Nori, Y. S. Kivshar, A. G. Truscott, R. G. Dall, and E. A. Ostrovskaya, "Observation of non-hermitian degeneracies in a chaotic exciton-polariton billiard," *Nature*, vol. 526, no. 7574, pp. 554–558, 2015. (cit. on pp. 7, 156, 158, 180, and 223)

[36] H. Xu, D. Mason, L. Jiang, and J. G. E. Harris, "Topological energy transfer in an optomechanical system with exceptional points," *Nature*, vol. 537, no. 7618, pp. 80–83, 2016. (cit. on pp. 7, 156, 157, 158, 180, 223, and 224)

[37] L. Feng, Z. J. Wong, R.-M. Ma, Y. Wang, and X. Zhang, "Single-mode laser by parity-time symmetry breaking," *Science*, vol. 346, no. 6212, pp. 972–975, 2014. (cit. on pp. 7, 157, 158, 169, and 179)

[38] B. Zhen, C. W. Hsu, Y. Igarashi, L. Lu, I. Kaminer, A. Pick, S.-L. Chua, J. D. Joannopoulos, and M. Soljacic, "Spawning rings of exceptional points out of dirac cones," *Nature*, vol. 525, pp. 354–358, 09 2015. (cit. on pp. 7, 22, 23, 156, 158, 178, 198, 223, and 224)

[39] M. Liertzer, L. Ge, A. Cerjan, A. D. Stone, H. E. Türeci, and S. Rotter, "Pump-induced exceptional points in lasers," *Phys. Rev. Lett.*, vol. 108, p. 173901, 2012. (cit. on p. 7)

[40] A. A. Mailybaev, A. P. O. N. Kirillov, and Seyranian, "Geometric phase around exceptional points," *Phys. Rev. A*, vol. 72, no. 1, p. 014104, 2005. (cit. on pp. 7 and 224)

[41] A. Guo, G. J. Salamo, D. Duchesne, R. Morandotti, M. Volatier-Ravat, V. Aimez, G. A. Siviloglou, and D. N. Christodoulides, "Observation of $\mathcal{PT}$-symmetry breaking in complex optical potentials," *Phys. Rev. Lett.*, vol. 103, p. 093902, 2009. (cit. on p. 7)

[42] S. Y. Lee, J. W. Ryu, J. B. Shim, S. B. Lee, S. W. Kim, and K. An, "Divergent petermann factor of interacting resonances in a stadium-shaped microcavity," *Phys. Rev. A*, vol. 78, p. 015805, 2008. (cit. on pp. 7, 71, 156, and 157)

[43] K. J. Vahala, "Optical microcavities," *nature*, vol. 424, no. 6950, p. 839, 2003. (cit. on p. 7)

[44] A. Pick, B. Zhen, O. D. Miller, C. W. Hsu, F. Hernandez, A. W. Rodriguez, M. Soljačić, and S. G. Johnson, "General theory of spontaneous emission near exceptional points," *Opt. Express*, vol. 25, no. 11, pp. 12325–12348, 2017. (cit. on pp. 7, 16, 156, 198, 203, 207, 209, 210, 213, 224, 236, and 237)

[45] A. P. F. Hernàndez and S. G. Johnson., "Scalable computation of jordan chains," *arXiv:1704.05837*, 2017. (cit. on pp. 7 and 174)

[46] L. N. Trefethen and M. Embree, *Spectra and Pseudospectra: The Behavior of Nonnormal Matrices and Operators*. Princeton University, 2005. (cit. on pp. 7, 156, 160, 163, and 176)

[47] W. J. Firth and A. M. Yao, "Giant excess noise and transient gain in misaligned laser cavities," *Phys. Rev. Lett.*, vol. 95, no. 7, p. 073903, 2005. (cit. on pp. 8 and 157)

[48] G. D'Alessandro and C. B. Laforet, "Giant noise amplification in synchronously pumped optical parametric oscillators," *Opt. Lett.*, vol. 34, no. 5, pp. 614–616, 2009. (cit. on pp. 8, 156, and 160)

[49] G. D'Alessandro and F. Papoff, "Giant subthreshold amplification in synchronously pumped optical parametric oscillators," *Phys. Rev. A*, vol. 80, no. 2, p. 023804, 2009. (cit. on pp. 8, 156, and 160)

[50] G. Yoo, H.-S. Sim, and H. Schomerus, "Quantum noise and mode nonorthogonality in non-Hermitian $\mathcal{PT}$-symmetric optical resonators," *Phys. Rev. A*, vol. 84, no. 6, p. 063833, 2011. (cit. on pp. 8, 156, 157, 159, and 213)

[51] Z. Lin, A. Pick, M. Lončar, and A. W. Rodriguez, "Enhanced spontaneous emission at third-order dirac exceptional points in inverse-designed photonic crystals," *Phys. Rev. Lett.*, vol. 117, no. 10, p. 107402, 2016. (cit. on pp. 8, 176, 197, 201, 207, 215, and 226)

[52] A. Pick, Z. Lin, W. Jin, and A. W. Rodriguez, "Enhanced frequency conversion and nonlinear purcell effect at exceptional points," (cit. on pp. 8, 180, 197, 207, and 209)

[53] H. Haken, *Laser Theory*. Springer-Verlag, 1984. (cit. on pp. 9, 17, 18, 26, 29, 32, 38, 43, 72, 92, 107, and 150)

[54] K. Petermann, *Laser diode modulation and noise*, vol. 3. Springer Science & Business Media, 2012. (cit. on pp. 9 and 111)

[55] W. E. Lamb, "Theory of an optical maser," *Phys. Rev.*, vol. 134, p. A1429, 1964. (cit. on pp. 9, 17, 27, and 72)

[56] H. E. Tureci, A. D. Stone, and B. Collier, "Self-consistent multimode lasing theory for complex or random lasing media," *Physical Review A*, vol. 74, no. 4, p. 043822, 2006. (cit. on pp. 9, 18, 26, 27, 30, 33, 39, 73, 92, 111, 114, 117, 120, 144, 147, 161, and 221)

[57] L. Ge, Y. D. Chong, and A. D. Stone, "Steady-state ab initio laser theory: Generalizations and analytic results," *Phys. Rev. A*, vol. 82, p. 063824, 2010. (cit. on pp. 9, 27, 30, 33, 39, 73, and 92)

[58] H. B. Callen and T. A. Welton, "Irreversibility and generalized noise," *Phys. Rev.*, vol. 81, no. 1, p. 34, 1951. (cit. on pp. 9, 26, 27, 45, and 154)

[59] S. M. Rytov, *Principles of Statistical Radiophsics II: Correlation Theory of Random Processes*. Springer-Verlag, 1989. (cit. on pp. 9, 20, 27, and 45)

[60] L. D. Landau, E. M. Lifshitz, and L. P. Pitaevskii, *Electrodynamics of Continuous Media, vol. 8*. Pergamon Press, Oxford, 1960. (cit. on pp. 11 and 19)

[61] S. Gasiorowicz, *Quantum Physics*. John Wiley & Sons, 2003. (cit. on p. 12)

[62] G. Strang, *Introduction to linear algebra*, vol. 3. Wellesley-Cambridge Press Wellesley, MA, 1993. (cit. on pp. 12, 14, and 15)

[63] W. Aaron, A. Yehuda, and S. G. Johnson, "Speed-of-light limitations in passive linear media," *Phys. Rev. A*, vol. 90, p. 023847, Aug 2014. (cit. on p. 14)

[64] J. Hu and C. R. Menyuk, "Understanding leaky modes: slab waveguide revisited," *Adv. Opt. Photonics*, vol. 1, no. 1, pp. 58–106, 2009. (cit. on pp. 15 and 187)

[65] E. Hernàndez, A. Jàuregui, and A. Mondragòn, "Jordan blocks and Gamow-Jordan eigenfunctions associated with a degeneracy of unbound states," *Phys. Rev. A*, vol. 67, p. 022721, 2003. (cit. on pp. 16 and 159)

[66] S. G. Johnson, "Numerical methods for computing casimir interactions," in *Casimir physics*, pp. 175–218, Springer, 2011. (cit. on p. 19)

[67] H. B. G. Casimir and D. Polder, "The influence of retardation on the london-van der waals forces," *Phys. Rev.*, vol. 73, no. 4, p. 360, 1948. (cit. on p. 20)

[68] A. W. Rodriguez, F. Capasso, and S. G. Johnson, "The casimir effect in microstructured geometries," *Nat. photonics*, vol. 5, no. 4, pp. 211–221, 2011. (cit. on p. 20)

[69] S. Basu, Z. M. Zhang, and C. J. Fu, "Review of near-field thermal radiation and its application to energy conversion," *Int. J. Energy Res.*, vol. 33, no. 13, pp. 1203–1232, 2009. (cit. on p. 20)

[70] W. Eckhardt, "First and second fluctuation-dissipation-theorem in electromagnetic fluctuation theory," *Opt. Comm.*, vol. 41, no. 5, pp. 305–309, 1982. (cit. on pp. 20, 27, 45, 103, 117, and 154)

[71] J. Andreasen and H. Cao, "Finite-difference time-domain formulation of stochastic noise in macroscopic atomic systems," *J. Lightwave Technol.*, vol. 27, no. 20, pp. 4530–4535, 2009. (cit. on pp. 21 and 95)

[72] C. H. Henry and R. F. Kazarinov, "Quantum noise in photonics," *Rev. Mod. Phys.*, vol. 68, no. 3, pp. 801–853, 1996. (cit. on pp. 21, 36, 46, 90, 91, and 104)

[73] J. R. Jeffers, N. Imoto, and R. Loudon, "Quantum optics of traveling-wave attenuators and amplifiers," *Phys. Rev. A*, vol. 47, no. 4, pp. 3346–3359, 1993. (cit. on pp. 21 and 36)

[74] J. V. Sengers and M. J. Z. Ortiz, "Thermal fluctuations in non-equilibrium thermodynamics," *J. Non-Equilib. Thermodyn.*, vol. 32, no. 3, pp. 319–329, 2007. (cit. on p. 21)

[75] M. Sargent, M. O. Scully, and W. E. J. Lamb, *Laser Physics*. Westview Press, 1974. (cit. on pp. 26 and 29)

[76] O. Svelto, *Principles of Lasers*. Springer, 1976. (cit. on pp. 26, 29, 30, and 31)

[77] P. W. Milonni and J. H. Eberly, *Laser Physics*. Wiley, 2010. (cit. on pp. 26, 29, and 31)

[78] J. P. Gordon, H. J. Zeiger, and C. H. Townes, "The maser—new type of microwave amplifier, frequency standard, and spectrometer," *Phys. Rev.*, vol. 99, pp. 1264–1274, 1955. (cit. on pp. 26 and 30)

[79] M. Lax, *Quantum noise v: Phase noise in a homogeneously broadened maser, in Physics of Quantum Electronics*. McGraw-Hill, New York, 1966. (cit. on pp. 27, 32, 43, 60, 105, 115, and 118)

[80] M. P. van Exter, S. J. M. Kuppens, and J. P. Woerdman, "Theory for the linewidth of a bad cavity laser," *Phys. Rev. A*, vol. 51, no. 1, pp. 800–816, 1995. (cit. on pp. 27, 30, and 32)

[81] M. Osinski and J. Buus, "Linewidth broadening factor in semiconductor lasers-an overview," *IEEE J. Quant. Elect.*, vol. 23, no. 1, pp. 9–29, 1987. (cit. on p. 27)

[82] Y. Chong and A. D. Stone, "General linewidth formula for steady-state multimode lasing in arbitrary cavities," *Phys. Rev. Lett.*, vol. 109, p. 063902, 2012. (cit. on pp. 27, 33, 35, 38, 59, 94, 97, 109, and 110)

[83] J. C. Pillay, N. Yuki, A. D. Stone, and Y. D. Chong, "Generalized sub-schawlow-townes laser linewidths via material dispersion," *Phys. Rev. A*, vol. 89, p. 033840, 2014. (cit. on pp. 27, 33, 35, 38, 49, 59, 88, 89, and 98)

[84] L. He, S. K. Özdemir, and L. Yang, "Whispering gallery microcavity lasers," *Laser Photonics Rev.*, vol. 7, no. 1, pp. 60–82, 2013. (cit. on pp. 27 and 70)

[85] O. Painter, R. K. Lee, A. Scherer, A. Yariv, J. D. O'Brien, P. Dapkus, and I. Kim, "Two-dimensional photonic band-gap defect mode laser," *Science*, vol. 284, pp. 1819–1821, 1999. (cit. on pp. 27 and 70)

[86] M. Loncar, T. Yoshie, A. Scherer, P. Gogna, and Y. Qiu, "Low-threshold photonic crystal laser," *Appl. Phys. Lett.*, vol. 74, pp. 7–9, 1999. (cit. on pp. 27 and 70)

[87] H. G. Park, S. H. Kim, S. H. Kwon, Y. G. Ju, J. K. Yang, J. H. Baek, S. B. Kim, and Y. H. Lee, "Electrically driven single-cell photonic crystal laser," *Science*, vol. 305, pp. 1444–1447, 2004. (cit. on pp. 27 and 70)

[88] I. E. Dzyaloshinkii, E. M. Lifshitz, and L. P. Pitaevskii, "General theory of van der waals' forces," *Sov. Phys. Usp.*, vol. 4, pp. 153–176, 1961. (cit. on pp. 27 and 45)

[89] E. M. Lifshitz and L. P. Pitaevskii, *Statistical Physics: Part 2*. Pergamon-Oxford, 1980. (cit. on pp. 27, 45, 107, and 108)

[90] C. H. Henry, "Theory of spontaneous emission noise in open resonators and its application to lasers and optical amplifiers," *J. Lightwave Tech.*, vol. LT-4, p. 288, 1986. (cit. on pp. 27, 28, 30, 32, 35, 42, 46, and 50)

[91] H. A. Haut, *Waves and Fields in Optoelectronics*. Englewood Cliffs, NJ:Prentice-Hall, 1984. (cit. on p. 27)

[92] H. A. Haus and W. Huang, "Coupled-mode theory," *Proc. of the IEEE*, vol. 79, no. 10, pp. 1505–1991, 1991. (cit. on p. 27)

[93] W. Suh, Z. Wang, and S. Fan, "Temporal coupled-mode theory and the presence of non-orthogonal modes in lossless multimode cavities," *IEEE J. Quant. Elect.*, vol. 40, no. 10, pp. 1511–1518, 2004. (cit. on p. 27)

[94] J. D. Joannopoulos, S. G. Johnson, J. N. Winn, and R. D. Meade, *Photonic Crystals, Molding the Flow of Light*. Princeton University Press, 2008. (cit. on pp. 27, 29, 31, 61, 62, and 79)

[95] A. Rodriguez, M. Soljačić, J. D. Joannopoulos, and S. G. Johnson, "$\chi(2)$ and $\chi(3)$ harmonic generation at a critical power in inhomogeneous doubly resonant cavities," *Opt. Exp.*, vol. 15, pp. 7303–7318, 2007. (cit. on pp. 27 and 208)

[96] F. T. Arecchi, G. L. Lippi, G. P. Puccioni, and J. R. Tredicce, "Deterministic chaos in laser with injected signal," *Opt. Comm.*, vol. 51, no. 5, pp. 308–313, 1984. (cit. on pp. 28, 43, 44, and 100)

[97] G. L. Oppo, A. Politi, G. L. Lippi, and F. T. Arecchi, "Frequency pushing in lasers with injected signal," *Phys. Rev. A*, vol. 34, no. 5, pp. 4000–4007, 1986. (cit. on pp. 28, 43, and 44)

[98] L. A. Lugiato, P. Mandel, and L. M. Narducci, "Adiabatic elimination in nonlinear dynamical systems," *Phys. Rev. A.*, vol. 29, no. 3, pp. 1438–1452, 1984. (cit. on pp. 28, 43, 44, and 76)

[99] M. P. van Exter, W. A. Hamel, J. P. Woerdman, and B. R. P. Zeijlmans, "Spectral signature of relaxation oscillations in semiconductor lasers," *IEEE J. Quant. Elect.*, vol. 28, no. 6, pp. 1470–1478, 1992. (cit. on pp. 28, 42, 53, 54, 55, and 58)

[100] W. Elsasser, "Multimode effects in the spectral linewidth of semiconductor lasers," *IEEE J. Quant. Elect.*, vol. 21, no. 6, pp. 687–692, 1985. (cit. on pp. 28, 64, 65, and 142)

[101] R. Hui, S. Benedetto, and I. Montrosset, "Near threshold operation of semiconductor lasers and resonant-type laser amplifiers," *IEEE J. Quant. Elect.*, vol. 29, no. 6, pp. 1488–1496, 1993. (cit. on pp. 28, 34, 40, 48, 66, 71, and 150)

[102] A. Cerjan, and A. Pick, and Y. D. Chong, and S. G. Johnson, and A. D. Stone. "Quantitative test of general theories of the intrinsic laser linewidth," arXiv:1505.01884. (cit. on pp. 29 and 70)

[103] D. S. Wiersma, "The physics and applications of random lasers," *Nat. Phys.*, vol. 4, no. 5, pp. 359–367, 2008. (cit. on p. 30)

[104] H. E. Türeci, L. Ge, S. Rotter, and A. D. Stone, "Strong interactions in multimode random lasers," *Science*, vol. 320, pp. 643–646, 2008. (cit. on pp. 30, 70, and 92)

[105] G. H. Duan, P. Gallion, and G. Debarge, "Analysis of the phase-amplitude coupling factor and spectral linewidth of distributed feedback and composite-cavity semiconductor lasers," *IEEE J. Quant. Elect.*, vol. 26, no. 1, pp. 32–44, 1990. (cit. on pp. 30, 32, and 61)

[106] A. E. Siegman, *Lasers*. University Science Books, 1986. (cit. on pp. 31, 54, and 111)

[107] M. Patra, *On Quantum Optics in Random Media*. PhD thesis, University of Leiden, Sept 2005. (cit. on pp. 31 and 45)

[108] S. J. M. Kuppens, "Measurement of the spontaneous emission factor of a 3.39 μm hene laser," *Opt. Comm.*, vol. 107, pp. 249–254, 1994. (cit. on pp. 31 and 68)

[109] S. J. M. Kuppens, M. A. van Eijkelenborg, M. P. v. E. C. A. Schrama, and J. P. Woerdman, "Incomplete inversion and double-valued fundamental linewidth of infrared hene and hexe lasers," *IEEE J. Quant. Elect.*, vol. 32, no. 3, pp. 383–387, 1996. (cit. on p. 31)

[110] A. E. Siegman, "Excess spontaneous emission in non-hermitian optical systems. ii. laser oscillators," *Phys. Rev. A*, vol. 39, no. 3, pp. 1264–1268, 1989. (cit. on pp. 31, 32, and 157)

[111] S. J. M. Kuppens, M. P. van Exter, and J. P. Woerdman, "Quantum-limited linewidth of a bad-cavity laser," *Phys. Rev. Lett.*, vol. 72, p. 3815, 1994. (cit. on pp. 32 and 59)

[112] S. J. M. Kuppens, M. P. van Exter, M. van Duin, and J. P. Woerdman, "Evidence of nonuniform phase-diffusion in a bad-cavity laser," *IEEE J. Quant. Elect.*, vol. 31, no. 7, pp. 1237–1241, 1995. (cit. on p. 32)

[113] K. Vahala, L. C. Chiu, S. Margalit, and A. Yariv, "On the linewidth enhancement factor α in semiconductor injection lasers," *Appl. Phys. Rev.*, vol. 42, pp. 631–633, 1983. (cit. on pp. 32 and 112)

[114] L. D. Westbrook and M. J. Adams, "Simple expressions for the linewidth enhancement factor in direct-gap semiconductors," *IEE Proc. J. Optoelectron.*, vol. 134, no. 4, pp. 209–214, 1987. (cit. on pp. 32 and 112)

[115] R. J. Lang and A. Yariv, "Semiclassical theory of noise in multielement semiconductor lasers," *IEEE J. Quant. Elect.*, vol. 22, no. 3, pp. 436–449, 1986. (cit. on p. 32)

[116] H. Schomerus, K. M. Frahm, M. Patra, and C. W. J. Beenakker, "Quantum limit of the laser linewidth in chaotic cavities and statistics of residues of scattering matrix poles," *Phyisca A*, vol. 278, pp. 469–496, 2000. (cit. on p. 33)

[117] H. Schomerus, "Excess quantum noise due to mode non-orthogonality in dielectric microresonators," *Phys. Rev. A*, vol. 79, p. 061801(R), 2009. (cit. on pp. 33 and 36)

[118] H. E. Türeci, A. D. Stone, L. Ge, S. Rotter, and R. J. Tandy, "Quantitative verification of ab initio self-consistent laser theory," *Nonlinearity*, vol. 22, p. C1, 2008. (cit. on p. 34)

[119] A. E. Siegman, "Excess spontaneous emission in non-hermitian optical systems. i. laser amplifiers," *Phys. Rev. A*, vol. 39, no. 3, pp. 1253–1263, 1989. (cit. on pp. 34, 40, and 157)

[120] M. O. Scully, G. Süssmann, and C. Benkert, "Quantum noise reduction via maser memory effects: Theory and applications," *Phys. Rev. Lett.*, vol. 60, no. 11, pp. 1014–1017, 1988. (cit. on pp. 34, 46, and 72)

[121] M. Scully, M. Zubairy, and K. Wódkiewicz, "Atomic memory effects in the quantum theory of laser," *Opt. Comm.*, vol. 65, no. 6, pp. 440–444, 1988. (cit. on pp. 34, 46, and 72)

[122] C. Benkert, M. O. Scully, A. A. Rangwala, and W. Schleich, "Quantum-noise suppression in lasers via memory-correlation effects," *Phys. Rev. A*, vol. 42, no. 3, pp. 1487–1502, 1990. (cit. on pp. 34, 46, and 72)

[123] C. Benkert, M. O. Scully, and G. Süssmann, "Memory correlation effects on quantum noise in lasers and masers," *Phys. Rev. A*, vol. 41, no. 11, pp. 6119–6128, 1990. (cit. on pp. 34, 46, and 72)

[124] M. I. Kolobov, L. Davidovich, E. Giacobino, and C. Fabre, "Role of pumping statistics and dynamics of atomic polarization in quantum fluctuations of laser sources," *Phys. Rev. A*, vol. 47, no. 2, pp. 1431–1446, 1993. (cit. on pp. 34, 46, and 72)

[125] A. E. Siegman, *Frontiers of Laser Physics and Quantum Optics*. Springer, 2000. (cit. on p. 35)

[126] R. Matloob, R. Loudon, M. Artoni, S. M. Barnett, and J. Jeffers, "Electromagnetic field quantization in amplifying dielectrics," *Phys. Rev. A*, vol. 55, no. 3, p. 1623, 1997. (cit. on p. 36)

[127] M. Patra and C. W. J. Beenakker, "Excess noise for coherent radiation propagating through amplifying random media," *Phys. Rev. A*, vol. 60, p. 4059, 1999. (cit. on p. 36)

[128] L. D. Landau and E. M. Lifshitz, *Statistical Physics, 3rd edition, Part I.* Elsevier Ltd., 1980. (cit. on pp. 36 and 90)

[129] C. Kittel and H. Kroemer, *Thermal Physics*. W. H. Freeman and Company, 1980. (cit. on pp. 36 and 90)

[130] A. Cerjan, Y. Chong, L. Ge, and A. D. Stone, "Steady-state ab initio laser theory for n-level lasers," *Opt. Exp.*, vol. 20, no. 1, pp. 474–488, 2012. (cit. on pp. 39, 68, 69, 72, and 94)

[131] A. Cerjan, Y. D. Chong, and A. D. Stone, "Steady-state ab initio laser theory for complex gain media," *Opt. Exp.*, vol. 23, pp. 6455–6477, 2015. (cit. on pp. 39 and 72)

[132] B. Dana, L. Lobachinsky, and A. Bahabad, "Spatiotemporal coupled-mode theory in dispersive media under a dynamic modulation," *Opt. Comm.*, vol. 324, 2014. (cit. on p. 40)

[133] A. Raman and S. Fan, "Perturbation theory for plasmonic modulation and sensing," *Phys. Rev. B*, vol. 83, p. 205131, 2011. (cit. on p. 44)

[134] W. Feller, "The fundamental limit theorems in probability," *Bull. Amer. Math. Soc.*, vol. 51, pp. 800–832, 1945. (cit. on p. 45)

[135] W. Feller, *An Introduction to Probability Theory and Its Applications*, vol. 1. New York: Willey, 3rd ed., 1968. (cit. on p. 45)

[136] See Eq. 45 in Ref. [29]. (cit. on p. 45)

[137] A. Demir, A. Mehrotra, and J. Roychowdhury, "Phase noise in oscillators: A unifying theory and numerical methods for characterization," *IEEE Trans. Circuits Syst. I, Fundam. Theory Appl.*, vol. 47, no. 5, pp. 655–674, 2000. (cit. on p. 48)

[138] See Eq. A4 in Ref. [20]. (cit. on p. 49)

[139] W. H. Press, S. A. Teukolsky, W. T. Vetterling, and B. P. Flannery, *Numerical Recipes, the art of scientific computing*. Cambridge University Press, 2007. (cit. on p. 50)

[140] B. E. A. Saleh and M. C. Teich, *Fundamentals of Photonics, 2nd Edition*. Wiley, 2007. (cit. on p. 62)

[141] S. Y. Lin, E. Chow, S. G. Johnson, and J. D. Joannopoulos, "Direct measurement of the quality factor in a two-dimensional photonic-crystal microcavity," *Opt. Lett.*, vol. 26, p. 1903, 2001. (cit. on pp. 66 and 68)

[142] W. D. Heiss, "The physics of exceptional points," *J. Phys. A: Math. Theor.*, vol. 45, p. 444016, 2010. (cit. on pp. 71 and 79)

[143] M. Liertzer, L. Ge, A. Cerjan, A. D. Stone, H. E. Türeci, and S. Rotter, "Pump-induced exceptional points in lasers," *Phys. Rev. Lett.*, vol. 108, p. 173901, 2012. (cit. on p. 71)

[144] M. Brandstetter, M. Liertzer, C. Deutsch, P. Klang, J. J. Schöberl, H. E. Türeci, G. Strasser, K. Unterrainer, and S. Rotter, "Reversing the pump dependence of a laser at an exceptional point," *Nat. Comm.*, vol. 5, p. 4034, 2014. (cit. on p. 71)

[145] G. B. Arfken and H. J. Weber, *Mathematical Methods for Physicists*. Elsevier Academic Press, 2006. (cit. on p. 79)

[146] A. Bultheel and M. V. Bare, *Linear Algebra, Rational Approximation and Orthogonal Polynomials*. North-Holland, 1997. (cit. on p. 86)

[147] G. B. Arfken and H. J. Weber, *Mathematical Methods for Physicists*. Elsevier Academic Press, 2006. (cit. on pp. 87, 161, and 181)

[148] J. R. Schulenberger and C. H. Wilcox, "The limiting absorption principle and spectral theory for steady-state wave propagation in homogeneous anisotropic media," *Arch. Ration. Mech. Anal.*, vol. 41, pp. 46–65, 1971. (cit. on pp. 90 and 91)

[149] H. E. Türeci, A. D. Stone, and L. Ge, "Theory of the spatial structure of nonlinear lasing modes," *Phys. Rev. A*, vol. 76, p. 013813, 2007. (cit. on p. 92)

[150] J. Andreasen, H. Cao, A. Taflove, P. Kumar, and C. Cao, "Finite-difference time-domain simulation of thermal noise in open cavities," *Phys. Rev. A*, vol. 77, no. 2, p. 023810, 2008. (cit. on pp. 92 and 95)

[151] P. D. Drummond and M. G. Raymer, "Quantum theory of propagation of nonclassical radiation in a near-resonant medium," *Phys. Rev. A*, vol. 44, no. 3, p. 2072, 1991. (cit. on p. 94)

[152] B. Bidégaray, "Time discretizations for maxwell-bloch equations," *Numer. Methods Partial Differ. Equ.*, vol. 19, no. 3, pp. 284–300, 2003. (cit. on p. 94)

[153] D. Marcuse, "Computer simulation of laser photon fluctuations: Theory of single-cavity laser," *IEEE J. Quant. Elect.*, vol. 20, no. 10, pp. 1139–1148, 1984. (cit. on p. 95)

[154] G. Gray and R. Roy, "Noise in nearly-single-mode semiconductor lasers," *Phys. Rev. A*, vol. 40, no. 5, p. 2452, 1989. (cit. on p. 95)

[155] H. F. Hofmann and O. Hess, "Quantum maxwell-bloch equations for spatially inhomogeneous semiconductor lasers," *Phys. Rev. A*, vol. 59, no. 3, p. 2342, 1999. (cit. on p. 95)

[156] C. Luo, A. Narayanaswamy, G. Chen, and J. D. Joannopoulos, "Thermal radiation from photonic crystals: a direct calculation," *Phys. Rev. Lett.*, vol. 93, no. 21, p. 213905, 2004. (cit. on p. 95)

[157] J. Andreasen and H. Cao, "Numerical study of amplified spontaneous emission and lasing in random media," *Phys. Rev. A*, vol. 82, no. 6, p. 063835, 2010. (cit. on p. 95)

[158] A. Pusch, S. Wuestner, J. M. Hamm, K. L. Tsakmakidis, and O. Hess, "Coherent amplification and noise in gain-enhanced nanoplasmonic metamaterials: A maxwell-bloch langevin approach," *ACS Nano.*, vol. 6, no. 3, pp. 2420–2431, 2012. (cit. on p. 95)

[159] S. Wuestner, J. M. Hamm, A. Pusch, F. Renn, K. L. Tsakmakidis, and O. Hess, "Control and dynamic competition of bright and dark lasing states in active nanoplasmonic metamaterials," *Phys. Rev. B*, vol. 85, no. 20, p. 201406, 2012. (cit. on p. 95)

[160] J. Ohtsubo, *Semiconductor lasers: stability, instability and chaos*, vol. 111. Springer, 2012. (cit. on pp. 96 and 145)

[161] K. Vahala and A. Yariv, "Semiclassical theory of noise in semiconductor lasers-part i," *IEEE J. Quant. Elect.*, vol. 19, no. 6, p. 1096–1101, 1983. (cit. on p. 111)

[162] K. Vahala and A. Yariv, "Semiclassical theory of noise in semiconductor lasers-part ii," *IEEE J. Quant. Elect.*, vol. 19, no. 6, pp. 1102–1109, 1983. (cit. on pp. 111, 113, 116, 119, and 130)

[163] C. Kittel, *Elementary Statistical Physics*, p. 133. Courier Corporation, 2004. (cit. on p. 114)

[164] S. Piazzolla and P. Spano, "Analytical evaluation of the line shape of single-mode semiconductor lasers," *Opt. Commun.*, vol. 51, no. 4, pp. 278–280, 1984. (cit. on p. 115)

[165] J. S. Cohen and D. Lenstra, "Spectral properties of the coherence collapsed state of a semiconductor laser with delayed optical feedback," *IEEE J. Quant. Elect.*, vol. 25, no. 6, pp. 1143–1151, 1989. (cit. on pp. 115 and 121)

[166] N. J. Champagne, J. G. Berryman, and H. M. Buettner, "Fdfd: A 3d finite-difference frequency-domain code for electromagnetic induction tomography," *J. Comput. Phys.*, vol. 170, no. 2, pp. 830–848, 2001. (cit. on p. 120)

[167] C. Henry, "Theory of the phase noise and power spectrum of a single mode injection laser," *IEEE J. Quant. Elect.*, vol. 19, no. 9, pp. 1391–1397, 1983. (cit. on p. 124)

[168] G. Dumont, G. Northoff, and A. Longtin, "Linear noise approximation for oscillations in a stochastic inhibitory network with delay," *Phys. Rev. E*, vol. 90, no. 1, p. 012702, 2014. (cit. on pp. 130 and 221)

[169] W. Liu, D. Xiao, and Y. Yi, "Relaxation oscillations in a class of predator–prey systems," *J. Differential Equations*, vol. 188, no. 1, pp. 306–331, 2003. (cit. on pp. 131 and 222)

[170] T. Putelat, J. R. Willis, and J. H. P. Dawes, "On the seismic cycle seen as a relaxation oscillation," *Philos. Mag.*, vol. 88, no. 28-29, pp. 3219–3243, 2008. (cit. on pp. 131 and 222)

[171] A. E. Siegman, *Lasers*. University Science Books, 1986. (cit. on pp. 143 and 161)

[172] I. Okuda and M. J. Shaw, "Gain depletion due to amplified spontaneous emission in multi-pass laser amplifiers," *Appl. Phys. B*, vol. 54, no. 6, pp. 506–512, 1992. (cit. on p. 143)

[173] K. Ertel, C. Hooker, S. J. Hawkes, B. T. Parry, and J. L. Collier, "Ase suppression in a high energy titanium sapphire amplifier," *Opt. Express*, vol. 16, no. 11, pp. 8039–8049, 2008. (cit. on p. 143)

[174] J. G. Fujimoto, C. Pitris, S. A. Boppart, and M. E. Brezinski, "Optical coherence tomography: An emerging technology for biomedical imaging and

optical biopsy," *Neoplasia*, vol. 2, no. 1, pp. 9–25, 2000. (cit. on pp. 143 and 179)

[175] M.-C. Amann and J. Boeck, "High-efficiency superluminescent diodes for optical-fibre transmission," *Elect. Lett.*, vol. 15, no. 2, pp. 41–42, 1979. (cit. on p. 143)

[176] J. Doppler, A. A. Mailybaev, J. Böhm, A. G. U. Kuhl and, F. Libisch, T. J. Milburn, P. Rabl, N. Moiseyev, and S. Rotter, "Dynamically encircling an exceptional point for asymmetric mode switching," *Nature*, vol. 537, no. 7618, pp. 76–79, 2016. (cit. on pp. 156, 157, 158, 223, and 224)

[177] D. Heiss, "Mathematical physics: Circling exceptional points," *Nat. Phys.*, vol. 12, no. 9, p. 823–824, 2016. (cit. on pp. 156 and 157)

[178] M. Brandstetter, M. Liertzer, C. Deutsch, P. Klang, J. Schöberl, H. E. Türeci, G. Strasser, K. Unterrainer, and S. Rotter, "Reversing the pump dependence of a laser at an exceptional point," *Nat. comm.*, vol. 5, no. 4034, p. 1, 2014. (cit. on pp. 156, 157, 158, 169, 179, 223, and 224)

[179] K. Ding, G. Ma, M. Xiao, Z. Q. Zhang, and C. T. Chan, "Emergence, coalescence, and topological properties of multiple exceptional points and their experimental realization," *Phys. Rev. X*, vol. 6, no. 2, p. 021007, 2016. (cit. on pp. 156 and 176)

[180] M. Liertzer, L. Ge, A. Cerjan, A. D. Stone, H. E. Türeci, and S. Rotter, "Pump-induced exceptional points in lasers," *Phys. Rev. Lett.*, vol. 108, no. 17, p. 173901, 2012. (cit. on pp. 156 and 157)

[181] A. L. Shuvalov and N. H. Scott, "On singular features of acoustic wave propagation in weakly dissipative anisotropic thermoviscoelasticity," *Acta. Mechanica*, vol. 140, no. 1, pp. 1–15, 2000. (cit. on pp. 156 and 223)

[182] H. Yokoyama and K. Ujihara, *Spontaneous Emission and Laser Oscillation in Microcavities*. CRC Press, 1995, vol. X. (cit. on p. 157)

[183] S. V. Gaponenko, *Introduction to Nanophotonics*. Cambridge University, 2010. (cit. on p. 157)

[184] M. V. Berry, "Mode degeneracies and the Petermann excess-noise factor for unstable lasers," *J. Mod. Opt.*, vol. 50, no. 1, pp. 63–81, 2003. (cit. on pp. 157, 162, and 203)

[185] M. A. van Eijkelenborg, Å. M. Lindberg, M. S. Thijssen, and J. P. Woerdman, "Resonance of quantum noise in an unstable cavity laser," *Phys. Rev. Lett.*, vol. 77, no. 21, p. 4314, 1996. (cit. on p. 157)

[186] A. M. van der Lee, N. J. van Druten, A. L. Mieremet, M. A. van Eijkelenborg, Å. M. Lindberg, M. P. van Exter, and J. P. Woerdman, "Excess quantum noise due to nonorthogonal polarization modes," *Phys. Rev. Lett.*, vol. 79, no. 22, p. 4357, 1997. (cit. on p. 157)

[187] W. D. Heiss, "The physics of exceptional points," *J. Phys. A - Math. Theo.*, vol. 45, no. 44, p. 444016, 2012. (cit. on pp. 157 and 159)

[188] Z. Lin, H. Ramezani, T. Eichelkraut, T. Kottos, H. Cao, and D. N. Christodoulides, "Unidirectional invisibility induced by PT-symmetric periodic structures," *Phys. Rev. Lett.*, vol. 106, no. 21, p. 213901, 2011. (cit. on pp. 157 and 224)

[189] B. Peng, Ş. K. Özdemir, F. Lei, F. Monifi, M. Gianfreda, G. L. Long, S. Fan, F. Nori, C. M. Bender, and L. Yang, "Parity-time-symmetric whispering-gallery microcavities," *Nat. Phys.*, vol. 10, no. 5, pp. 394–398, 2014. (cit. on pp. 157, 169, and 224)

[190] L. Feng, Y.-L. Xu, W. S. Fegadolli, M.-H. Lu, J. E. Oliveira, V. R. Almeida, Y.-F. Chen, and A. Scherer, "Experimental demonstration of a unidirectional reflectionless parity-time metamaterial at optical frequencies," *Nat. Mater.*, vol. 12, no. 2, pp. 108–113, 2013. (cit. on pp. 157, 158, 169, and 224)

[191] H. Hodaei, M.-A. Miri, M. Heinrich, D. N. Christodoulides, and M. Khajavikhan, "Parity-time–symmetric microring lasers," *Science*, vol. 346, no. 6212, pp. 975–978, 2014. (cit. on pp. 157, 158, 169, and 179)

[192] B. Peng, Ş. K. Özdemir, S. Rotter, H. Yilmaz, M. Liertzer, F. Monifi, C. M. Bender, F. Nori, and L. Yang, "Loss-induced suppression and revival of lasing," *Science*, vol. 346, no. 6207, pp. 328–332, 2014. (cit. on pp. 157 and 223)

[193] W. D. Heiss and G. Wunner, "Fano-Feshbach resonances in two-channel scattering around exceptional points," *Eur. Phys. J. D*, vol. 68, no. 10, pp. 1–6, 2014. (cit. on p. 157)

[194] A. M. van den Brink, K. Young, and M. H. Yung, "Eigenvector expansion and Petermann factor for ohmically damped oscillators," *J. Phys A: Math. Gen.*, vol. 39, no. 14, p. 3725, 2006. (cit. on p. 157)

[195] M. D. Zoysa, T. Asano, K. Mochizuki, A. Oskooi, T. Inoue, and S. Noda, "Conversion of broadband to narrowband thermal emission through energy recycling," *Nat. Photon.*, vol. 6, no. 8, pp. 535–539, 2012. (cit. on p. 157)

[196] X. Liu, T. Tyler, T. Starr, A. F. Starr, N. M. Jokerst, and W. J. Padilla, "Taming the blackbody with infrared metamaterials as selective thermal emitters," *Phys. Rev. Lett.*, vol. 107, no. 4, p. 045901, 2011. (cit. on p. 157)

[197] M. Laroche, R. Carminati, and J.-J. Greffet, "Coherent thermal antenna using a photonic crystal slab," *Phys. Rev. Lett.*, vol. 96, no. 12, p. 123903, 2006. (cit. on p. 157)

[198] C. Khandekar, W. Jin, O. D. Miller, A. Pick, and A. W. Rodriguez, "Giant frequency-selective near-field heat transfer in $\mathcal{PT}$-symmetric structures," *Phys. Rev. B*, vol. 94, no. 11, p. 115402, 2016. (cit. on p. 157)

[199] T. Søndergaard, S. M. Novikov, T. Holmgaard, R. L. Eriksen, J. Beermann, Z. Han, K. Pedersen, and S. I. Bozhevolnyi, "Plasmonic black gold by adiabatic nanofocusing and absorption of light in ultra-sharp convex grooves," *Nat. Comm.*, vol. 3, p. 969, 2012. (cit. on p. 157)

[200] W. Wan, Y. Chong, L. Ge, H. Noh, A. D. Stone, and H. Cao, "Time-reversed lasing and interferometric control of absorption," *Science*, vol. 331, no. 6019, pp. 889–892, 2011. (cit. on p. 157)

[201] Y. D. Chong, L. Ge, H. Cao, and A. D. Stone, "Coherent perfect absorbers: time-reversed lasers," *Phys. Rev. Lett.*, vol. 105, no. 5, p. 053901, 2010. (cit. on p. 157)

[202] Y. Sun, W. Tan, H.-Q. Li, J. Li, and H. Chen, "Experimental demonstration of a coherent perfect absorber with pt phase transition," *Phys. Rev. Lett.*, vol. 112, no. 14, p. 143903, 2014. (cit. on p. 157)

[203] H. Linnenbank, Y. Grynko, J. Förstner, and S. Linden, "Second harmonic generation spectroscopy on hybrid plasmonic/dielectric nanoantennas," *Light Sci. Appl.*, vol. 5, no. 1, p. e16013, 2016. (cit. on p. 157)

[204] D. C. Brody and E.-M. Graefe, "Information geometry of complex hamiltonians and exceptional points," *Entropy*, vol. 15, no. 9, pp. 3361–3378, 2013. (cit. on p. 158)

[205] G. W. Hanson, A. I. Nosich, and E. M. Kartchevski, "Green's function expansions in dyadic root functions for shielded layered waveguides," *Prog. Electromagn. Res.*, vol. 39, pp. 61–91, 2003. (cit. on p. 159)

[206] E. Hernandez, A. Jauregui, and A. Mondragon., "Degeneracy of resonances in a double barrier potential," *J. Phys. A*, vol. 33, pp. 4507–4523, 2000. (cit. on p. 159)

[207] S. Longhi, "Enhanced excess noise in laser cavities with tilted mirrors," *Opt. Lett.*, vol. 25, no. 11, pp. 811–813, 2000. (cit. on p. 160)

[208] F. Wijnands, J. B. Pendry, F. J. Garcia-Vidal, P. M. Bell, and a. L. M. M. P. J. Roberts, "Green's functions for Maxwell's equations: Application to spontaneous emission," *Opt. Quant. Elect.*, vol. 29, no. 2, pp. 199–216, 1997. (cit. on p. 160)

[209] Y. Xu, R. K. Lee, and A. Yariv, "Quantum analysis and the classical analysis of spontaneous emission in a microcavity," *Phys. Rev. A*, vol. 61, no. 3, p. 033807, 2000. (cit. on p. 160)

[210] K. Sacked, *Optical Properties of Photonic Crystals*. Springer Science & Business Media, 2004, vol. LXXX. (cit. on p. 160)

[211] A. Lagendijk and B. A. V. Tiggelen, "Resonant multiple scattering of light," *Phys. Rep.*, vol. 270, no. 3, pp. 143–215, 1996. (cit. on p. 160)

[212] P. M. Morse and H. Feshbach, *Methods of Theoretical Physics*. New York: McGraw-Hill, vol. I, 1953. (cit. on p. 161)

[213] R. G. Newton, *Scattering Theory of Waves and Particles*. Springer Science & Business Media, 2013. (cit. on p. 162)

[214] S. H. Weintraub, "Jordan canonical form: Application to differential equations," *Synthesis Lectures on Mathematics and Statistics*, vol. 1, no. 1, pp. 1–85, 2008. (cit. on p. 163)

[215] S. A. Maier, *Plasmonics: Fundamentals and Applications*. Springer Science & Business Media, 2007. (cit. on p. 166)

[216] C. E. Rüter, K. G. Makris, R. El-Ganainy, D. N. Christodoulides, M. Segev, and D. Kip, "Observation of parity–time symmetry in optics," *Nat. Phys.*, vol. 6, no. 3, pp. 192–195, 2010. (cit. on p. 166)

[217] A. Christ and H. L. Hartnagel, "Three-dimensional finite-difference method for the analysis of microwave-device embedding," *IEEE Trans. Microw. Theory Techn.*, vol. 35, pp. 688–696, 1987. (cit. on pp. 167 and 236)

[218] W. P. Huang, "Coupled-mode theory for optical waveguides: an overview," *J. Opt. Soc. Am. A*, vol. 11, no. 3, pp. 963–983, 1994. (cit. on pp. 168, 173, and 191)

[219] K. Okamoto, *Fundamentals of Optical Waveguides*. Academic Press, 2010. (cit. on pp. 168, 173, and 191)

[220] N. W. Ashcroft and N. D. Mermin, *Solid State Physics*. Holt, Rinehart and Winston, 1976. (cit. on p. 173)

[221] R. C. McPhedran, L. C. Botten, J. McOrist, A. A. Asatryan, C. M. de Sterke, and N. A. Nicorovici, "Density of states functions for photonic crystals," *Phys. Rev. E*, vol. 69, no. 1, p. 016609, 2004. (cit. on p. 173)

[222] F. Capolino, D. R. Jackson, and a. B. F. D. R. Wilton, "Comparison of methods for calculating the field excited by a dipole near a 2-d periodic material," *IEEE Trans. Antennas Propag.*, vol. 55, no. 6, pp. 1644–1655, 2007. (cit. on p. 173)

[223] H. Benisty, D. Labilloy, C. Weisbuch, C. J. M. Smith, T. F. Krauss, D. Cassagne, A. Beraud, and C. Jouanin, "Radiation losses of waveguide-based two-dimensional photonic crystals: Positive role of the substrate," *App. Phys. Lett.*, vol. 76, no. 5, pp. 532–534, 2000. (cit. on p. 175)

[224] S. M. Barnett and R. Loudon, "Sum rule for modified spontaneous emission rates," *Phys. Rev. Lett.*, vol. 77, no. 12, p. 2444, 1996. (cit. on pp. 176, 205, 207, 210, and 213)

[225] E. M. Graefe, H. J. Korsch, and A. E. Niederle, "A non-hermitian symmetric bose? hubbard model: eigenvalue rings from unfolding higher-order exceptional points," *J. Phys. A. Math. Theor.*, vol. 41, no. 25, p. 255206, 2008. (cit. on p. 176)

[226] J.-W. Ryu, S.-Y. Lee, and S. W. Kim, "Analysis of multiple exceptional points related to three interacting eigenmodes in a non-hermitian hamiltonian," *Phys. Rev. A*, vol. 85, no. 4, p. 042101, 2012. (cit. on p. 176)

[227] W. D. Heiss and G. W. G, "Resonance scattering at third-order exceptional points," *J. Phys. A. Math. Theor.*, vol. 48, no. 34, p. 345203, 2015. (cit. on p. 176)

[228] N. Colthup, *Introduction to Infrared and Raman Spectroscopy*. Elsevier, 2012. (cit. on p. 179)

[229] J. D. McKinney, M. A. Webster, K. J. Webb, and A. M. Weiner, "Characterization and imaging in optically scattering media by use of laser speckle and a variable-coherence source," *Opt. Let.*., vol. 25, no. 1, pp. 4–6, 2000. (cit. on p. 179)

[230] P. Miao, Z. Zhang, J. Sun, W. Walasik, S. Longhi, N. M. Litchinitser, and L. Feng, "Orbital angular momentum microlaser," *Science*, vol. 353, no. 6298, pp. 464–467, 2016. (cit. on p. 179)

[231] D. R. Jackson and A. A. Oliner, *Leaky-Wave Antennas*. Wiley Online Library, 2008. (cit. on p. 180)

[232] F. Monticone and A. Alù, "Leaky-wave theory, techniques, and applications: From microwaves to visible frequencies," *Proc. IEEE*, vol. 103, no. 5, pp. 793–821, 2015. (cit. on p. 180)

[233] O. D. Miller, A. G. Polimeridis, M. T. H. Reid, C. H. H. Chia, B. G. DeLacy, J. D. Joannopoulos, M. Soljačić, and S. G. Johnson, "Fundamental limits to optical response in absorptive systems," *Opt. express*, vol. 24, no. 4, pp. 3329–3364, 2016. (cit. on pp. 181 and 223)

[234] A. E. Siegman, *Frontiers of Laser Physics and Quantum Optics*. Springer, 2000. "Excess quantum noise in nonnormal oscillators". (cit. on p. 182)

[235] B. Vial, F. Zolla, A. Nicolet, and M. Commandré, "Quasimodal expansion of electromagnetic fields in open two-dimensional structures," *Phys. Rev. A*, vol. 89, no. 2, p. 023829, 2014. (cit. on p. 183)

[236] M. Perrin, "Eigen-energy effects and non-orthogonality in the quasi-normal mode expansion of maxwell equations," *Opt. Express*, vol. 24, no. 24, pp. 27137–27151, 2016. (cit. on p. 183)

[237] C. Sauvan, J.-P. Hugonin, I. S. Maksymov, and P. Lalanne, "Theory of the spontaneous optical emission of nanosize photonic and plasmon resonators," *Phys. Rev. Lett.*, vol. 110, no. 23, p. 237401, 2013. (cit. on pp. 183, 184, and 187)

[238] R. E. Collin, *Field theory of guided waves*. McGraw-Hill, 1960. (cit. on p. 187)

[239] P. T. Leung, S. Y. Liu, and K. Young, "Completeness and orthogonality of quasinormal modes in leaky optical cavities," *Phys. Rev. A*, vol. 49, no. 4, p. 3057, 1994. (cit. on p. 187)

[240] W. C. Chew and W. H. Weedon, "A 3d perfectly matched medium from modified maxwell's equations with stretched coordinates," *Microw. Opt. Technol. Lett.*, vol. 7, no. 13, pp. 599–604, 1994. (cit. on p. 188)

[241] Z. Lin, X. Liang, M. Lončar, S. G. Johnson, and A. W. Rodriguez, "Cavity-enhanced second-harmonic generation via nonlinear-overlap optimization," *Optica*, vol. 3, no. 3, pp. 233–238, 2016. (cit. on pp. 197 and 207)

[242] X. Huang, Y. Lai, Z. H. Hang, H. Zheng, and C. T. Chan, "Dirac cones induced by accidental degeneracy in photonic crystals and zero-refractive-index materials," *Nat Mater*, vol. 10, pp. 582–586, 08 2011. (cit. on p. 198)

[243] J. Mei, Y. Wu, C. T. Chan, and Z.-Q. Zhang, "First-principles study of dirac and dirac-like cones in phononic and photonic crystals," *Phys. Rev. B*, vol. 86, p. 035141, 2012. (cit. on pp. 198 and 199)

[244] K. Sakoda, "Proof of the universality of mode symmetries in creating photonic dirac cones," *Opt. Express*, vol. 20, no. 22, pp. 25181–25194, 2012. (cit. on pp. 198 and 202)

[245] T. Kato, *Perturbation Theory for Linear Operators*, vol. 132. Springer Science & Business Media, 2013. p. 68. (cit. on pp. 202 and 230)

[246] M. C. Zheng, D. N. Christodoulides, R. Fleischmann, and T. Kottos, "$\mathcal{PT}$ optical lattices and universality in beam dynamics," *Phys. Rev. A*, vol. 82, p. 010103, 2010. (cit. on p. 202)

[247] M. V. Berry, "Physics of nonhermitian degeneracies," *Czechoslovak Journal of Physics*, vol. 54, no. 10, 2004. (cit. on p. 203)

[248] S. Scheel, L. Knöll, and D.-G. Welsch, "Spontaneous decay of an excited atom in an absorbing dielectric," *Phys. Rev. A*, vol. 60, pp. 4094–4104, 1999. (cit. on p. 204)

[249] R. W. Boyd, *Nonlinear optics*. Academic press, 2003. (cit. on pp. 206 and 208)

[250] B. Zhen, S. L. Chua, J. Lee, A. W. Rodriguez, X. Liang, S. G. Johnson, J. D. Joannopoulos, M. Soljačić, and O. Shapira, "Enabling enhanced emission and low-threshold lasing of organic molecules using special fano resonances of macroscopic photonic crystals," *Proc. Natl. Acad. Sci. U.S.A.*, vol. 110, no. 34, pp. 13711–13716, 2013. (cit. on p. 213)

[251] R. Borisov, G. Dorojkina, N. Koroteev, V. Kozenkov, S. Magnitskii, D. Malakhov, A. Tarasishin, and A. Zheltikov, "Fabrication of three-dimensional periodic microstructures by means of two-photon polymerization," *Applied Physics B*, vol. 67, no. 6, pp. 765–767, 1998. (cit. on p. 214)

[252] A. Clausen, F. Wang, J. S. Jensen, O. Sigmund, and J. A. Lewis, "Topology optimized architectures with programmable poisson's ratio over large deformations," *Advanced Materials*, vol. 27, no. 37, pp. 5523–5527, 2015. (cit. on p. 214)

[253] C. Pouya, J. T. B. Overvelde, M. Kolle, J. Aizenberg, K. Bertoldi, J. C. Weaver, and P. Vukusic, "Characterization of a mechanically tunable gyroid photonic crystal inspired by the butterfly parides sesostris," *Advanced Optical Materials*, vol. 4, no. 1, pp. 99–105, 2016. (cit. on p. 214)

[254] Z. Lin, X. Liang, M. Lončar, S. G. Johnson, and A. W. Rodriguez, "Cavity-enhanced second-harmonic generation via nonlinear-overlap optimization," *Optica*, vol. 3, pp. 233–238, Mar 2016. (cit. on p. 215)

[255] E. Rosencher, A. Fiore, B. Vinter, and V. Berger, "Quantum engineering of optical nonlinearities," *Science*, vol. 271, no. 5246, p. 168, 1996. (cit. on p. 215)

[256] G. Kirchmair, B. Vlastakis, Z. Leghtas, S. E. Nigg, H. Paik, E. Ginossar, M. Mirrahimi, L. Frunzio, S. M. Girvin, and R. J. Schoelkopf, "Observation of quantum state collapse and revival due to the single-photon kerr effect," *Nature*, vol. 495, no. 7440, pp. 205–209, 2013. (cit. on p. 215)

[257] H. Voss, "Nonlinear eigenvalue problems," *Handbook of Linear Algebra. Chapman & Hall/CRC, FL*, 2013. (cit. on p. 219)

[258] S. Burkhardt, M. Liertzer, D. Krimer, and S. Rotter, "Steady-state ab initio laser theory for fully or nearly degenerate cavity modes," *Phys. Rev. A*, vol. 92, no. 1, p. 013847, 2015. (cit. on p. 220)

[259] D. Liu, B. Zhen, L. Ge, F. Hernandez, A. Pick, S. Burkhardt, M. Liertzer, S. Rotter, and S. G. Johnson, "Symmetry, stability, and computation of degenerate lasing modes," *Phys. Rev. A*, vol. 95, no. 2, p. 023835, 2017. (cit. on p. 220)

[260] S. S. Sané, S. Bennetts, J. E. Debs, C. C. N. Kuhn, G. D. McDonald, P. A. Altin, J. D. Close, and N. P. Robins, "11 w narrow linewidth laser source at 780nm for laser cooling and manipulation of rubidium," *Opt. Express*, vol. 20, no. 8, pp. 8915–8919, 2012. (cit. on p. 220)

[261] A. Wicht, N. Strauss, K. Doringshoff, I. Ernsting, B. Roth, J. Koelemeij, S. Schiller, R. H. Rinkleff, and K. Danzmann, *Narrow linewidth diode laser system for coherent precision spectroscopy*. Optical Society of America, 2007. (cit. on p. 220)

[262] T. P. Nguyen, M. Schiemangk, S. Spießberger, H. Wenzel, A. Wicht, A. Peters, G. Erbert, and G. Tränkle, "Optimization of 780 nm dfb diode lasers for high-power narrow linewidth emission," *Appl. Phys. B*, vol. 108, no. 4, pp. 767–771, 2012. (cit. on p. 220)

[263] M. Fleming and A. Mooradian, "Spectral characteristics of external-cavity controlled semiconductor lasers," *IEEE J. Quant. Elect.*, vol. 17, no. 1, pp. 44–59, 1981. (cit. on p. 221)

[264] F. J. Duarte, *Tunable laser applications*, vol. 150. CRC press, 2008. (cit. on p. 221)

[265] A. Cerjan and A. D. Stone, "Steady-state ab initio theory of lasers with injected signals," *Phys. Rev. A*, vol. 90, no. 1, p. 013840, 2014. (cit. on p. 221)

[266] R. Ramaswamy and I. F. Sbalzarini, "Intrinsic noise alters the frequency spectrum of mesoscopic oscillatory chemical reaction systems," *Sci. Rep.*, vol. 1, p. 154, 2011. (cit. on p. 222)

[267] A. Regensburger, C. Bersch, M.-A. Miri, G. Onishchukov, D. N. Christodoulides, and U. Peschel, "Parity-time synthetic photonic lattices," *Nature*, vol. 488, no. 7410, pp. 167–171, 2012. (cit. on p. 223)

[268] O. Latinne, N. J. Kylstra, M. Dorr, J. Purvis, M. Terao-Dunseath, C. J. Joachain, P. G. Burke, and C. J. Noble, "Laser-induced degeneracies involving autoionizing states in complex atoms," *Phys. Rev. Lett.*, vol. 74, no. 1, p. 46, 1995. (cit. on p. 223)

[269] A. Leung and J. Chang, "Null space solution of Jordan chains for derogatory eigenproblems," *J. Sound Vib.*, vol. 222, no. 4, pp. 679–690, 1999. (cit. on pp. 225, 227, and 243)

[270] A. A. Mailybaev, "Computation of multiple eigenvalues and generalized eigenvectors for matrices dependent on parameters," *Numer. Linear Algebra Appl.*, vol. 13, no. 5, pp. 419–436, 2006. (cit. on pp. 225, 226, 227, 234, 235, and 243)

[271] G. H. Golub and J. H. Wilkinson, "Ill-conditioned eigensystems and the computation of the Jordan canonical form," *SIAM review*, vol. 18, no. 4, pp. 578–619, 1976. (cit. on p. 227)

[272] A. Edelman, E. Elmroth, and B. Kågström, "A geometric approach to perturbation theory of matrices and matrix pencils. part I: Versal deformations," *SIAM J. Matrix Anal. Appl.*, vol. 18, no. 3, pp. 653–692, 1997. (cit. on pp. 227 and 233)

[273] R. A. Lippert and A. Edelman, "The computation and sensitivity of double eigenvalues," *Advances in Computational Mathematics, Lecture Notes in Pure and Appl. Math*, vol. 202, pp. 353–393, 1999. (cit. on p. 227)

[274] B. Kågström and A. Ruhe, "An algorithm for numerical computation of the jordan normal form of a complex matrix," *ACM Trans. Math. Softw.*, vol. 6, no. 3, pp. 398–419, 1980. (cit. on p. 227)

[275] L. N. Trefethen and D. Bau III, *Numerical Linear Algebra*, vol. 50. SIAM, 1997. (cit. on p. 228)

[276] J. H. Wilkinson, *Rounding Errors in Algebraic Processes*. Courier Corporation, 1994. (cit. on p. 229)

[277] R. M. Errico, "What is an adjoint model?," *Bull. Am. Meteorol. Soc.*, vol. 78, no. 11, pp. 2577–2591, 1997. (cit. on p. 237)

[278] G. Strang, *Computational Science and Engineering*, vol. 791. Wellesley-Cambridge Press, 2007. (cit. on p. 237)

[279] D. B. Szyld and F. Xue, "Several properties of invariant pairs of nonlinear algebraic eigenvalue problems," *IMA J. Numer. Anal.*, p. drt026, 2013. (cit. on p. 243)